

ISSN 2367-7570

Workshop
**"Solar Influences on the Magnetosphere,
Ionosphere and Atmosphere"**

Book
of
Proceedings

Eleventh Workshop
Primorsko, Bulgaria, June 3÷7, 2019

Organized by:
**Space Research and Technologies Institute
Bulgarian Academy of Sciences**

Scientific Organizing Committee

Katya Georgieva (Space Research and Technologies Institute, Bulgaria) - *Chair*
Crisan Demetrescu (Institute of Geodynamics, Romanian Academy)
Ana G. Elias (Universidad Nacional de Tucuman, Argentina)
Petra Koucká-Knižová (Institute of Atmospheric Physics, Czech Republic)
Olga Malandraki (IAASARS, National Observatory of Athens, Greece)
Dibyendu Nandi (Indian Institute for Science Education and Research, Kolkata, India)
Vladimir Obridko (IZMIRAN, Moscow, Russian Federation)
Atila Özgüc (Kandilli Observatory, Turkey)
Dragan Roša (Zagreb Astronomical Observatory, Croatia)
Jean-Pierre Rozelot (Université de la Côte d’Azur, Grasse, France)

Editors: Katya Georgieva, Boian Kirov, Dimitar Danov

CONTENT

Sun and Solar Activity	
<i>Bazilevskaya G.A., Logachev Yu.I., Daibog E.I., Ginzburg E.A., Ishkov V.N., Lazutin L.L., Nguyen M.D., Surova G.M., Vlasova N.A., Yakovchouk O.S.</i>	
Dynamic of the Occurrence Rate of the Solar Energetic Particle Events During Solar Activity Cycles 21-24	01
<i>Daibog E. I., Kecskemety K., Logachev Yu. I.</i>	
Fluxes of Jovian Electrons and Galactic Protons in the Minimum of 23-24 Cycles of Solar Activity	07
<i>Dechev M. Ts., Koleva K., Duchlev P., Miteva R.</i>	
Double Filament Eruption and Associated Ribbon Flare and Halo Coronal Mass Ejection	13
<i>V.N. Ishkov</i>	
Evolutionary and Flare Characteristics of Prolonged Phases of Solar Minimum	17
<i>Kilcik A., Ozguc A., Yesilyaprak H., Pektas R..</i>	
Comparison of FI and the MCMESI for the Last two Solar Cycles	23
<i>Kilcik A., Sarp V..</i>	
Possible Interactions between Some Solar Activity Indicators for the Last two Cycles	28
<i>Krastev K., Semkova J., Koleva R., Bankov N., Benghin V., Drobishev S.</i>	
The Shading Effect for Doses and Galactic Cosmic Rays Fluxes Measured by Liulin Instrument, Depending on Liulin - Mars Geometry	31
<i>Sarp V., Kilcik A.</i>	
Investigation of Sunspot Area Dynamics in Different Categories	35
<i>Shevchuk M., Melnik V., Dorovskyy V., Brazhenko A., Frantsuzenko A., Konovalenko A., Poedts S., Magdalenic J.</i>	
On Polarization of Solar Decameter Spikes	40
<i>Stanislavsky A.A., Burnecki K., Janczura J., Niczyj K., Weron A.</i>	
Solar X-ray Variability in two Distinct States and Its Real-Time Analysis Based on a Fractionally Time-Series Model With a Heteroskedastic Component	44
<i>Filip Šterc, Darije Maričić, Dragan Roša</i>	
Morphology of Coronal Hole Based on SDO/AIA Data in May 2010 ÷ December 2013	50
<i>Tsvetkov Ts., Petrov, N., Miteva, R., Ivanov, E., Popov, V.</i>	
Research on Active Solar Processes During 2019 July 2 Total Solar Eclipse	56
<i>Krasimira Yankova</i>	
RS Ophiuchi and ADVECTION	60
<i>Zagainova Iu.S., Fainshtein V.G., Rudenko G.V.</i>	
Comparing the Height Dependences of the Magnetic Field Overlying the Initial Areas of Fast and Slow Coronal Mass Ejections	65

Solar Wind-Magnetosphere-Ionosphere Interactions

<i>Bojilova R., Mukhtarov P.</i> Global and Regional Response of the Total Electron Content to Geomagnetic Storms Occurred in January 2005	71
<i>Dachev T., Tomov B., Matviichuk Y., Dimitrov P., Semkova J., Koleva, R., Jordanova M., Bankov N., Shurshakov V., Benghin V.</i> Long-Term Variations of the Galactic Cosmic Rays Dose Rates	77
<i>Derevyagin V. G., Kravetz R. O., Lytvynenko O. A., Panishko S. K.</i> Regular Observations of the Power Cosmic Radio Sources on the Radio Telescope URAN-4. Processing Method, Results Keeping System and their Applying in Ionosphere Investigations	84
<i>Despirak I.V., Lubchich A.A., Kleimenova N.G.</i> Supersubstorms, High-Latitude Substorms and Space Weather Conditions	89
<i>Gromova L.I., Kleimenova N.G., Gromov S.V., Malysheva L.M.</i> Dayside Polar Magnetic Bays under Different Interplanetary Magnetic Field Direction	95
<i>Ishkova L.M., Ruzhin Yu.Ya., Bershadskaya I.N.</i> Anomalous TEC Disturbances of the South American Ionosphere before and after the Main Shocks of Some Powerful Chilean Earthquakes	101
<i>Kleimenova N.G., Gromova L.I., Gromov S.V., Malysheva L.M.</i> Strong Magnetic Storm on 25-26 August 2018 with Reference to the Solar Cycle 24 Declining	107
<i>Manninen J., Kleimenova N.G., Gromova L.I., Turunen T.</i> Auroral VLF Hiss as a Signature of the Growth Phase of the Magnetic Substorm	113
<i>Nikitenko A.S., Lebed O.M., Fedorenko Yu.V., Manninen J., Kleimenova N.G., Gromova L.I., Turunen T.</i> Ground-Based Auroral Hiss: Wave Direction Finding	119
<i>Shagimuratov I.I., Chernouss S.A., Despirak I.V., Tepenitsyna N.Yu., Filatov M.V., Efishov I.I., Yakimova G.A.</i> TEC Response to the Solar Flare on 6 September 2017	123

Data Processing and Modeling

<i>Dashkevich Zh.V., Ivanov V.E.</i> The Nitric Oxide Density in the Polar Region from Ground-Based Photometer Data	129
<i>Dashkevich Zh.V., Ivanov V.E.</i> The Efficiencies of O(¹S) and O(¹D) Excitation Mechanisms in Aurora	134
<i>Kupryakov Yu.A., Dodin A.V., Schwartz P., Kashapova L.K.</i> The Calculation of the Intensity of The Mg I Spectral Lines in Solar Prominences Using the Cloudy code Model	139
<i>Sarp V., Kilcik A.</i> State Space Reconstruction for Sunspot Area Time Series	143
<i>Werner R., Petkov B., Valev D., Guinevav V., Atanassov A., Kirillov A.</i> Scheme to Forecast the Local UV-index over Bulgaria	147

Solar Influences on the Lower Atmosphere and Climate

<i>Ya. Chapanov</i> ENSO Variations Driven by Solar Cycles, Expressed by N-S Solar Asymmetry	152
<i>Ya. Chapanov</i> Water Transport and Earth Rotation Variations Due to Solar Cycles	158
<i>Tonev P.T.</i> Observations supporting hypothesis for global electrical circuit as mediator between solar events and weather	165

Instrumentation for Space Weather Monitoring	
<i>Dachev T., Dimitrov P., Tomov B., Matviichuk Y., Saganti P. Holland D., Okuyama K.-I., Fajardo I. Analysis of the First Space Radiation Data, Obtained by Liulin Ten-Koh Instrument on the Japanize Ten-Koh Satellite</i>	171
 SEP Origin Project	
<i>Bogomolov A.V., Myagkova I.N., Miteva R., Danov D., Kashapova L.K. Parameters of Thermal and Non-thermal X-ray and Gamma Ray Emission of Solar Flares, Observed onboard CORONAS-F</i>	179
<i>Kashapova L.K., Meshalkina N.S., Miteva R., Zhukova A.V., Myagkova I.N. Study on the Features of the SEP Solar Origin Based on Microwave Observations</i>	185
<i>Miteva R., Samwel S.W. Radio Signatures of in Situ Observed ACE/EPAM Electron Fluxes</i>	191
<i>Miteva R., Samwel S. W., Veronig A., Koleva K., Dechev M., Dissauer K., Temmer M., Kozarev K., Zabunov S. EVE Flare Diagnostics of in situ Observed Electron Events</i>	196
<i>Myagkova I.N., Miteva R., Kashapova L., Bogomolov A.V., Danov D. Features of Solar Energetic Particle Events During the 23rd Cycle of Solar Activity and their Relationship with Solar X-ray, Gamma-Emission and Coronal Mass Ejections</i>	201
<i>Tsvetkov Ts., Miteva, R., Temmer, M., Petrov, N. STEREOCat Speed de-projection of SEP-Related CMEs</i>	207
<i>Zhdanov D.A., Kashapova L.K., Myshyakov I.I., Miteva R. About Productivity of the Solar Energetic Particle Events</i>	211
Author's index	223

P r e f a c e

The Eleventh Workshop "**Solar Influences on the Magnetosphere, Ionosphere and Atmosphere**" was held in Primorsko, Bulgaria, from June 3 to 7, 2019. It was attended by 78 participants from 12 countries. Eighty-seven oral and poster presentations were given during the five working days. Forty papers based on these presentations with a total of one hundred and thirteen authors are included in this Book of proceedings.

The Scientific Organizing Committee and the Editors of the Proceedings thank all the participants in the Workshop and contributors to the Proceedings.

Dynamic of the Occurrence Rate of the Solar Energetic Particle Events During Solar Activity Cycles 21-24

Bazilevskaya G.A.¹, Logachev Yu.I.², Daibog E.I.², Ginzburg E.A.³, Ishkov V.N.⁴,
Lazutin L.L.², Nguyen M.D.², Surova G.M.², Vlasova N.A.², Yakovchouk O.S.²

¹ Lebedev Physical Institute, RAS, Moscow, Russia

² Skobeltsyn Institute of Nuclear Physics, Lomonosov State University, Moscow, Russia

³ Fedorov Institute of Applied Geophysics, Rosgidromet, Moscow, Russia

⁴ Pushkov IZMIRAN, Moscow, Russia

E-mail: bazilevskayaga@lebedev.ru

Abstract

The Catalogues of the solar proton events [Logachev, ed., 1982-2016] provide the homogeneous data series of events with maximum intensity of > 10 MeV solar protons $J \geq 1 \text{ cm}^{-2}\text{s}^{-1}\text{sr}^{-1}$ beginning from 1970 up to now. The event rates behavior is rather smooth: the total number of such events, relative to accumulated sunspot number, is almost constant in the solar cycles 21-23 and even slightly growing in the solar cycle 24. Contrary, the total number of the most powerful (GLE) events per cycle was constant within statistical errors in the cycles 21-23, and it fell abruptly in cycle 24. Considering the conventional sources of GLEs we found that production of GLEs by X-class bursts was 3 times less in cycle 24 than in cycle 23, while production of GLEs by the >1000 km/s halo-type CMEs was 5 times lower.

Introduction

Energetic charged particles of solar origin were discovered almost 80 years ago [Forbush, 1946], in the solar cycle 17; their observation covers more than seven 11-year solar cycles. Solar energetic particles (SEPs) coming to the Earth are a product of multiple processes on the Sun and in the space where they are generated and modulated. The SEP features bear signatures of mechanisms of their acceleration and propagation. In spite of the long history of observations, the contribution of various sources in the process of SEP generation remains a long-standing question. During the period of SEP investigation, Sun mostly demonstrated high activity but cycle 24 opened an epoch of lowered solar activity with a complete rearrangement of physical conditions, both on the Sun and in the inner heliosphere [Ishkov, 2018]. The aim of this work is to examine changes in the SEP occurrence rate due to the decrease of solar activity in cycle 24, which may shed some light to the SEP origin.

Catalogs of the solar proton events

In 1940ies-1950ies, a SEP appearance could be recorded only by the ground-based instruments, mainly by ionizing chambers, i.e. their energy exceeded several GeV. They are rather rare events and received the name of the ground level enhancements (GLEs). Development of neutron monitors [Simpson, 1957] did not strongly increase the observed GLE rate: until now, there are only 72. Balloon measurements [Charakhch'yan, 1964] doubled the observed number of solar energetic particle (SEP) events, and space observations in 1970ies increased it by an order of magnitude. Energies of SEPs cover more than 4 orders of magnitude and intensities, more than 8 orders of magnitude, therefore a SEP event cannot be recorded by a single instrument. A need to compile the data of various observations was recognized and led to the issue of the first Catalog of Solar Particle Events 1955-1969 [Svestka and Simon, ed., 1975].

Beginning from early 1980ies an informal group of experts in solar physics, particle physics, and geophysics collected the data on solar particle observations and accompanying phenomena trying to form the homogeneous data sets, a Catalog of solar proton events which is a continuation of the Catalog [Svestka and Simon, ed., 1975]. The group is working under

the leadership of professor Yu.I. Logachev from Moscow State University. The Catalog compiles the data of the solar energetic particle (SEP) events with the ≥ 10 MeV proton flux $J_{10} \geq 1 \text{ cm}^{-2}\text{s}^{-1}\text{sr}^{-1}$ (pfu) in the maximum of the intensity-time profile (TOM flux). All available data of various spacecraft, balloons, and neutron monitors were included in the issues [Logachev, ed., 1982, 1986, 1989, 1990, 1998, 2016].

An uniform approach to the data collection enables us to compare the solar proton activity in the last solar cycles. The Catalogs ed. by Yu.I. Logachev started in January 1970, i.e. in the middle of the 20th solar cycle. Therefore, we took for comparison three full solar cycles 21-23 and the last almost finished cycle 24. In this work, we examine changes in the solar proton generation rate against the weakening of solar activity during the last solar cycles. In particular, we focus on the total number of SEP events with ≥ 10 MeV protons (J_{10} series) and the number of the most powerful SEP events, GLEs. Figure 1 demonstrates the timeline of J_{10} proton fluxes in the maximum of the intensity-time profile of a SEP event against the background of the sunspot number. GLEs are marked by the red color.

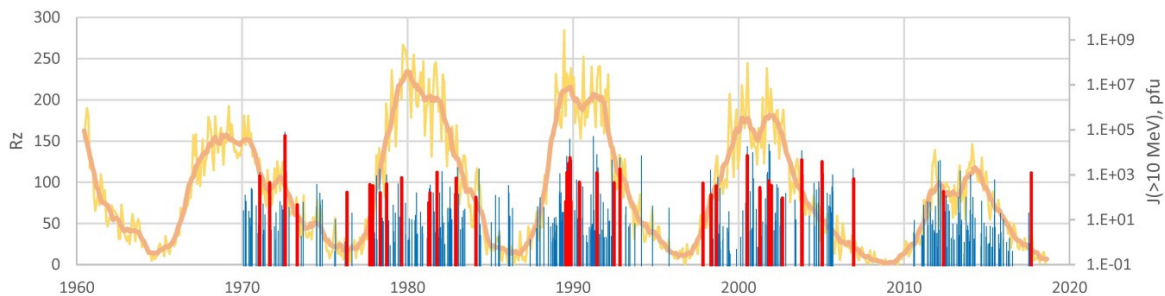


Fig. 1 Time dependence of ≥ 10 MeV solar proton intensities in the maximum of the intensity-time profile of a SEP event. Orange lines are monthly and smoothed sunspot numbers R_z , bars are intensities of ≥ 10 MeV solar protons. GLEs are marked by red color.

Accumulated number of SEP events

An approach implemented here is an analysis of the accumulated number of parameters for each solar cycle: the data for each month of a solar cycle are summarized beginning from the cycle start. Figure 2 demonstrates the accumulated values of sunspot number R_z and of SEP events numbers vs. ordinal month number in solar cycle. The R_z vs. time is shown for clarifying of accumulation approach. It is seen that R_z number decreased from cycle 21 to cycle 24 faster than J_{10} . The accumulated values are convenient for the study of the summarized values of the solar activity parameters, duration of the sunspot cycles and of the active periods within the cycles when SEPs were generated. The sunspot number was decreasing persistently from cycle 21 to cycle 24 but the cycle duration, not. Note, that cycle 24 in June 2019 is the second in duration, and it is not finished yet at the moment of the paper writing. Although SEPs do not repeat the ranking of sunspot number, cycle 24 is the weakest in all aspects with the exception of the duration of the GLE active period. The maximum number and longest duration of J_{10} were in cycle 21, and GLEs, in cycle 23, which was the second in strength for J_{10} .

Keeping in view weakening of solar activity it is interesting to look at the relative value of SEP parameters, i.e. ratio of the accumulated number of SEP events to accumulated R_z . Contrary to absolute values, the relative number of J_{10} SEP event number increased by 20% from cycles 21-22 to cycle 24. At the same time, the relative number of GLEs fell from 5-7% to less than 1.5%. In the cycles 21-23 the total number of J_{10} SEP events was ~ 9 -12 times larger than that of the GLE events. In cycle 24 this factor was ~ 55 .

The average rate of SEP events per month may be defined as the ratio of accumulated SEP event number to the duration of an R_z cycle, or to the duration of SEP generation period

within a cycle. In the first case, the *J10* rate slowly decreased from cycle 21 to cycle 24, while the GLE rate was constant in cycles 21-23 and strongly decreased in cycle 24. In the second case, the *J10* rate remained constant in cycles 21-23 and slightly decreased in cycle 24; the GLE rate had maximum in cycle 22 and fell dramatically in cycle 24.

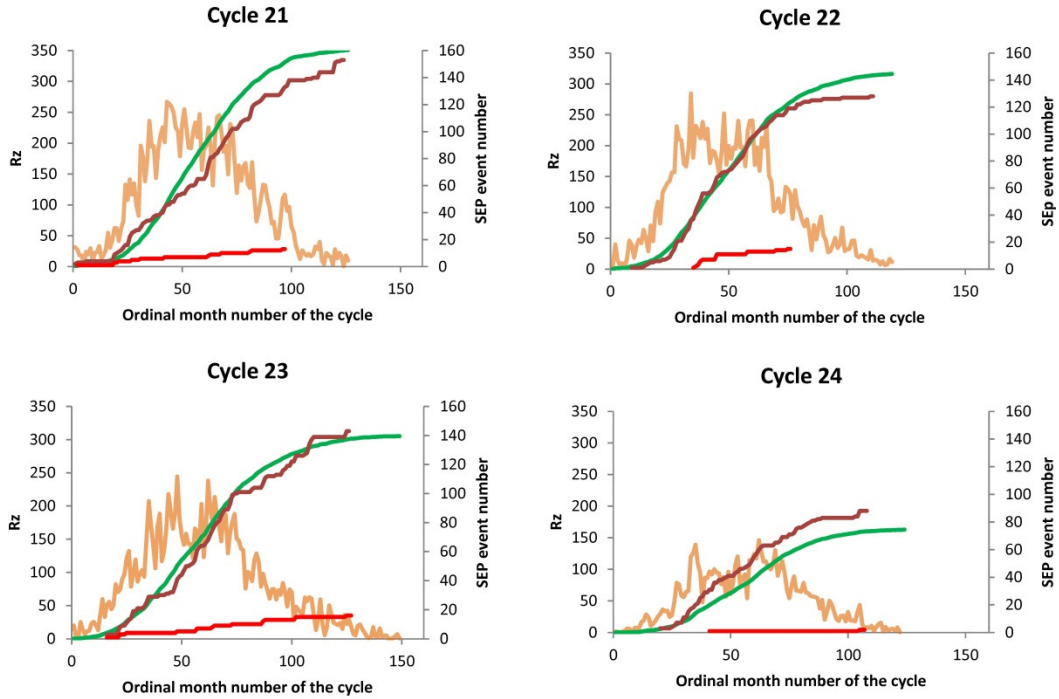


Fig. 2. Accumulated numbers of sunspots *Rz* (green lines), SEP events *J10* (brown lines), and GLEs (red lines). Orange lines show *Rz* vs. ordinal month number of the cycle.

Sources of SEPs in cycles 21-24

The most striking phenomenon in cycle 24 is dramatic fell in the rate of GLEs. It is natural to examine the GLE sources, namely X-ray flares and coronal mass ejections (CMEs) [e.g., Klein and Dalla, 2017]. Only reliable sources according to the Catalogs ed. by Yu.I. Logachev were taken into account. Relationship between GLEs and X-ray flares was considered for 1971-2017 (URL flares). There were 52 GLEs during the period 1971-2017, among them 49 with a reliable flare source. Two events (28 May 1990 and 18 April 2001) with a back side solar flare sources were excluded from consideration. Around 81% of GLEs originated from the X-ray flares of the class $> X$, 15 %, of the class M. Numbers of X-class bursts relative to M-class ones in the cycles 21-14 were virtually constant – 7.8%, 7.6%, 8.7%, and 6.8%, respectively. Figure 3 demonstrates the accumulated number of X-class X-ray bursts and accumulated GLE number for cycles 21-24. In cycles 21 and 22 both data series are similar. However, in cycle 23 the number of GLEs increased faster than the X-class burst number while in cycle 24 a situation was the opposite. The number of X-class flares for one GLEs was ~ 8 in cycle 23, and it was 24 in cycle 24.

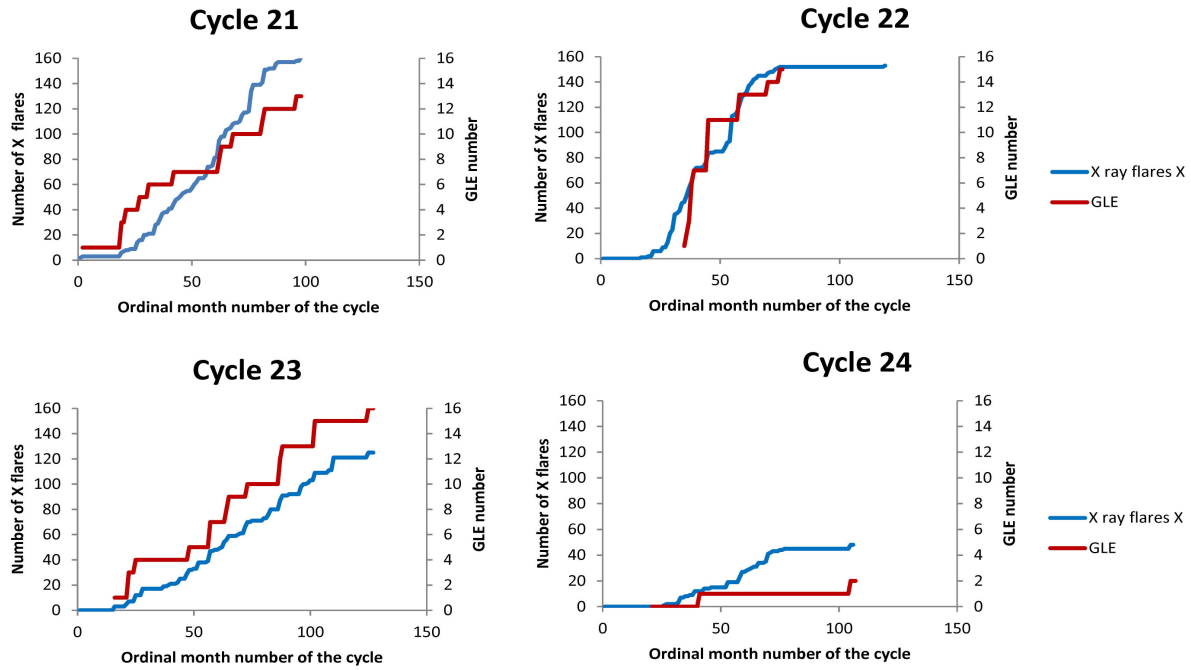


Fig. 3. Accumulated numbers of X-ray flares of X class (blue lines) and GLEs (dark-red lines).

An additional or an alternative source of GLEs are CMEs, information of which is available for cycles 23 and 24 [URL CME]. There were 18 GLEs during this period, information for 17 events being available. More than 94% of the GLE-related CMEs had velocity > 1000 km/s, more than 76% - > 1500 km/s. More than 82% of GLE-related CMEs were of the halo type. We have examined the accumulated number of the halo-type CMEs with velocity more than 1000 km/s and compared them with those of the GLE number (see Figure 4).

The numbers of the halo-type CMEs with $V \geq 1000$ km/s for one GLE in the cycles 23 and 24 was 11 and 55, respectively.

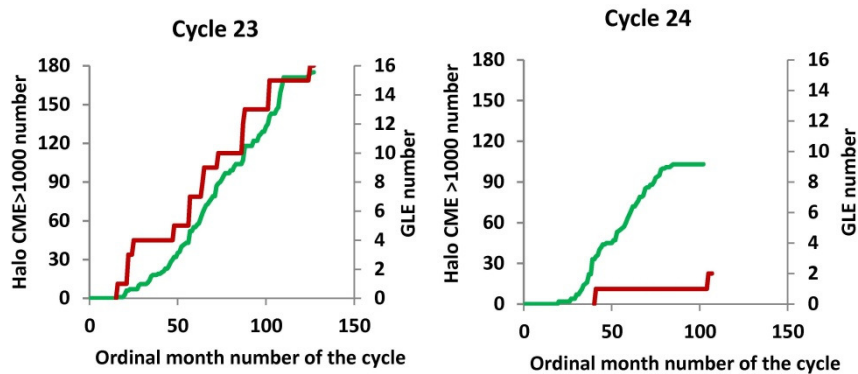


Fig. 4. Accumulated numbers of the halo-type CMEs with $V \geq 1000$ km/s (green lines) and GLEs (dark red lines).

While considering sources of $J10$ SEP events, GLEs were excluded from the analysis. In cycles 23 and 24 more than 95% of the $J10$ SEP associated flares belonged to class $> M$, differences between cycles 23 and 24 being quite small. More than 95% of the $J10$ related CMEs had velocity above 500 km/s and more than 70% were of the halo type. Figure 5 shows comparison between the accumulated numbers of the $J10$ SEP events and those of the sum of M and X classes flares (upper panels) and between $J10$ and CMEs of the halo type with

velocity > 500 km/s (lower panels). From cycle 23 to 24 the number of powerful solar flares decreased stronger than the number of the *J10* SEP events. On the contrary, the number of CMEs diminished less than the *J10* SEP event number. The numbers of M+X-class flares for one *J10* event was 12.3 in cycle 23, and 8.7 in cycle 24. Similar values for the halo-type CMEs with $V > 500$ km/s were 2.6 and 3.1.

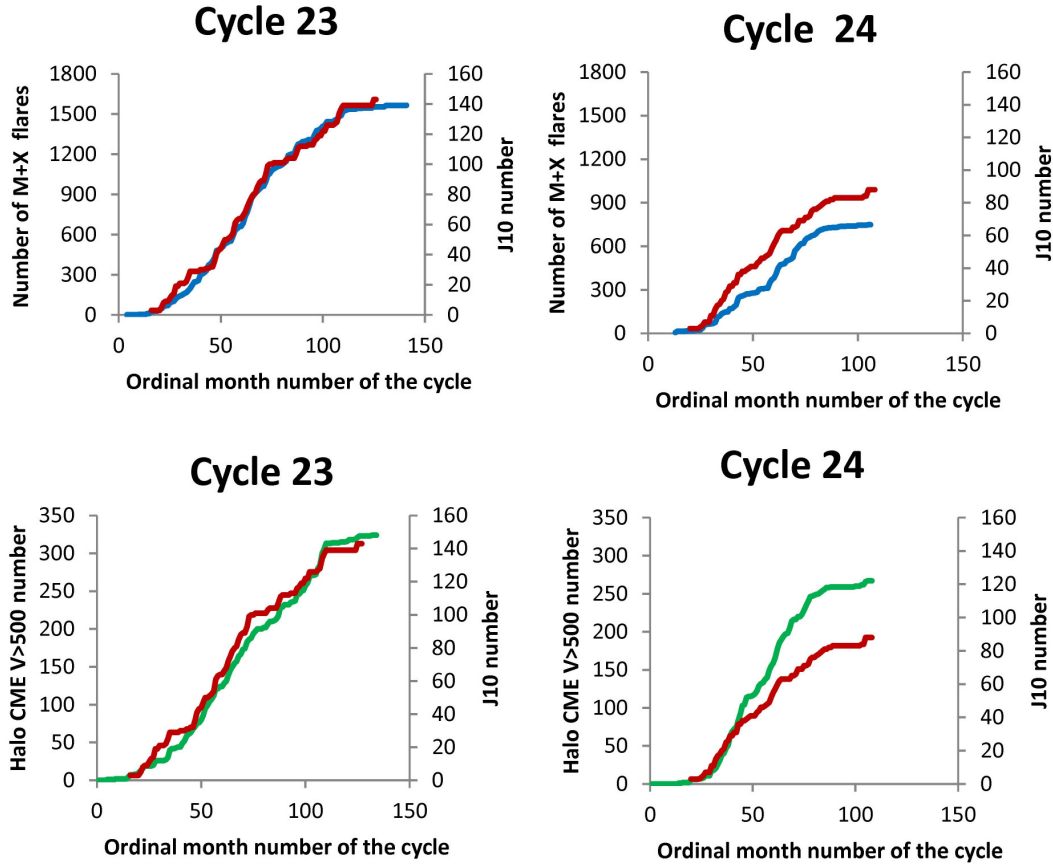


Fig. 5. Upper panels: accumulated numbers of the flares of M+X classes (blue lines) and *J10* SEP events (dark red lines). Bottom panes: accumulated numbers the halo-type CMEs with $V \geq 500$ km/s (green lines) and *J10* SEP events (dark red lines)

Conclusion

A series of Catalogs [Logachev, ed., 1982, 1986, 1989, 1990, 1998, 2016] being continued nowadays provides a homogeneous data set on the SEP events from 1971 up to the present. We separated all the events in two groups, one containing events with energies of 10 - ~ 500 MeV (*J10* series), and another, containing GLEs.

The occurrence rate of GLEs was almost constant in cycles 21-23. It diminished by a factor > 5 in cycle 24. The majority of GLEs are connected with the X-ray flares of the class $\geq X$ and the CMEs with velocity ≥ 1000 km/s and angular width of 360 deg (halo). Our analysis proves that, basing on relations between the total number of recorded GLEs and the total number of the assumed sources, the production of GLEs by X-class bursts was 3 times less in cycle 24 than in cycle 23, while production of GLEs by the > 1000 km/s halo-type CMEs was 5 times lower.

Nevertheless, it should be stressed that this result is purely statistical. A real complex of solar phenomena leading to the GLE occurrence needs further study.

The number of SEP events with ≥ 10 MeV protons diminished with the weakening of solar activity in cycles 21-24 but less than the sunspot number. The majority of *J10* SEPs are connected to solar flares $> M$ class and the halo type CMEs with velocity ≥ 500 km/s. The occurrence rate of $\geq M$ flares decreased from cycle 23 to cycle 24 more than the occurrence rate of the *J10* SEP event number. The number of the *J10* SEPs related CME decreased less than the *J10* SEP number. This result confirms that the CME role is bigger for the less powerful SEP events [Dierckxsens et al. 2015].

Striking difference in the timeline of the rate occurrence of the GLEs and the less energetic events may suggest that the GLEs are a special class of SEP events.

Acknowledgments

Thanks are due to all researchers providing their data on solar activity, interplanetary space, and energetic charged particles (from spacecraft, balloon, and ground-based instruments) via Internet. This work is supported by the RFBR grant 19-02-00264. G.A.B. has benefited from discussions at the meeting of the ISSI International Team "High EneRgy sOlar parTICle events analysis (HEROIC)" led by Dr. A. Papaioannou.

References

- Charakhch'yan, A.N. (1964), Investigation of stratosphere cosmic ray intensity fluctuations induced by processes on the Sun. *Sov. Phys. Uspekhi* 7 (3), 358–374.
- Dierckxsens, M. et al. (2015), Relationship between solar energetic particles and properties of flares and CMEs: statistical analysis of solar cycle 23 events. *Sol. Phys.* 290,841–874 (2015). doi:10.1007/s11207-014-0641-4.
- Forbush, S.E. (1946), Three unusual cosmic-ray increases possibly due to charged particles from the Sun. *Phys. Rev.*, 70, 771–772.
- Ishkov, V.N. (2018), Space Weather and Specific Features of the Development of Current Solar Cycle. *Geomagnetism and Aeronomy*, 58(6), 753–767, Doi: 10.1134/S0016793218060051
- Klein, K.-L. and Dalla, S. (2017), Acceleration and Propagation of Solar Energetic Particles. *Space Sci. Rev.* 212:1107–1136, DOI 10.1007/s11214-017-0382-4
- Logachev, Yu.I., ed., (1982) Catalog of solar proton events 1970-1979, Moscow, IZMIRAN, 1982, 184 pp.
- Logachev, Yu.I., ed., (1986) Catalog of energy spectra of solar proton events 1970-1979, Moscow, IZMIRAN, 1986, 236 pp.
- Logachev, Yu.I., ed., (1989) Catalog of solar proton events 1980-1986, Data on particles and electromagnetic emission, Moscow, WDC B., 1989, 160 pp.
- Logachev, Yu.I., ed., (1990) Catalog of solar proton events 1980-1986, Plots of the time profile and energetic spectra of protons, synoptic charts and schemes of sunspot groups Moscow, WDC B., 1990, 204 pp.
- Logachev, Yu.I., ed., (1998) Catalog of solar proton events 1987-1996, Moscow University Press, 248 pp.
- Logachev, Yu.I., ed., (2016) Catalog of solar proton events in the 23rd cycle of solar activity (1996-2008). ESDB repository, GC RAS, Moscow, doi: 10.2205/ESDB-SAD-001. <https://www.ngdc.noaa.gov/stp/space-weather/interplanetary-data/solar-proton-events/documentation/>
- Simpson J.A. (1957) Cosmic-radiation neutron intensity monitor. // *Annals of the IGY*. 4. 351–373.
- Svestka, Z. and Simon, P., eds., (1975), Catalog of Solar Particle Events 1955–1969, ed. Reidel, 430 pp..
- URL flares: <https://www.ngdc.noaa.gov/stp/space-weather/solar-data/solar-features/solar-flares/x-rays/goes/xrs/>
- URL CME https://cdaw.gsfc.nasa.gov/CME_list/

Fluxes of Jovian Electrons and Galactic Protons in the Minimum of 23-24 Cycles of Solar Activity

Daibog E. I.¹, Kecskemety K.², Logachev Yu. I.¹

¹ SINP MSU Moscow, Russia

² Wigner Research Centre for Physics, Budapest, Hungary

E-mail: daibog@srd.sinp.msu.ru

Abstract

In the minimum of solar activity 2007–2008, there was an extremely long stable state of the structures of the solar wind speed, which persisted for 14 rotations of the Sun. According to the neutron monitor (Apatity), which registered galactic protons with energy > 500 MeV, and the integral channel $E_p > 50$ MeV of the EPHIN, SOHO instrument, quasi-27-day variations in the fluxes of galactic protons were studied. Periods of their variations turned out to coincide with the periods of the long-lived structures of the solar wind, 27.1 days, and anti-correlated with them. Simultaneously periodic increases in the fluxes of Jovian electrons ($J_e > 1$ MeV) were observed. At the beginning of the cycle of these variations, the fluxes of Jovian electrons and galactic protons correlated, then, a small phase shift of correlation took place at each rotation of the Sun, so that by the middle of the cycle already complete anti-correlation of these fluxes took place. This difference in the behavior of Jovian electrons and galactic protons indicates the different nature of the observed quasi-27-day variations. While for galactic protons, the explanation is in modulation of charged particle fluxes by an interplanetary magnetic field associated with periodic variations in the solar wind, for Jovian electrons, the relative position of the electron source (Jupiter magnetosphere) and the Earth and electron propagation process in Jupiter-Earth space must be taken into account.

Introduction

In their near-Jupiter flight, the Pioneer-10 and Pioneer-11 spacecraft detected fluxes of MeV electrons accelerated in the Jovian magnetosphere and ejected into the surrounding space [Chenette D.L., et al, 1974; Trainor J.H., et al, 1974]. Measurements of Jovian electrons were also conducted using the IMP-8 [Chenette D.L., et al, 1977; Eraker J.H. and Simpson J.A., 1979], MARS-7 [Alekseev N.V., et al, 1982, 1983], PROGNOZ-3 [Alekseev N.V., et al, 1983], SOHO [del Peral L., et al, 2003; Gomez-Herrero R., et al, 2008], and ULYSSES [Simpson J.A., et al, 1993] spacecraft. Under favorable interplanetary conditions, fluxes of Jovian electrons can reach the Earth's orbit. Differences in the properties of Jovian electrons and electrons originating on the Sun include differences in their energy spectra, with solar electrons having much softer spectrum. Beginning from the first observations of Jovian electrons and comparisons with other components of the cosmic rays and with the characteristics of the solar wind and solar magnetic field, the diffusion model [Chenette D.L., et al, 1977] has mainly been used. This model was then used together with the Corotating Interaction Region (CIR) model [del Peral L. et al, 2003; Barns K.V., et al, 1977; Chenette D.L., 1980; Conlon T.F., 1978; Richardson I.G., 2004; Kuhl P., et al, 2013;], developed to describe overtaking collisions of solar-wind fluxes with different speeds. If the magnetic field near Jupiter is strongly perturbed, the longitudinal and perpendicular diffusion coefficients K_{\parallel} and K_{\perp} will be small, and electrons cannot move to substantial distances from Jupiter. Since light charged particles, and especially electrons, propagate along magnetic-field lines, it is natural to expect the appearance of Jovian electrons near the Earth when the Earth and Jupiter are located along the same solar magnetic-field line; i.e., when they are optimally magnetically connected. If the structure of the solar magnetic field is in a strictly stationary state, the optimal magnetic connection between the Earth and Jupiter will arise only once

every 13 months (the synodic period of the Earth–Jupiter system). Over a full orbit of the Earth around the Sun, or more precisely over 13 months, an optimal solar magnetic-field line passes near the Earth 14–15 times (the number of rotations of the Sun over 13 months), “sampling” the flux of Jovian electrons at all longitudes near Jupiter.

Data

Trustworthy observations of Jovian electrons at the Earth’s orbit are possible only during quiet solar periods because their flux is very small, $J_e(1\text{MeV}) \approx 10^{-2} \text{ cm}^{-2} \text{ s}^{-1} \text{ sr}^{-1} \text{ MeV}^{-1}$, so that they can be detected only when the background of solar, interplanetary, and galactic electrons is low. More often this situation occurs during minima of the 11-year solar activity cycle, when the flare activity of the Sun and the substorm activity in the Earth’s magnetosphere die down. Another important factor is the stability of the solar wind structure, when Jovian electrons can be detected near the Earth during several solar rotations. Since the solar-wind structure is inhomogeneous, periodicities appear in the fluxes of Jovian electrons, due to rotation of the Sun and its magnetic field. An especially prolonged period of stability of the solar wind structure and detection of Jovian electrons was observed during the solar-activity minimum of 2007–2009 by SOHO (EPHIN), which had a very low level of background electron counting, which made it possible to register their very small fluxes. Fig. 1 shows the total cycle of registration of Yu-electrons by the SOHO, EPHIN, consisting of 14 consecutive risings of flux at each rotation of the Sun and Fig. 2 - high stability of solar wind structures.

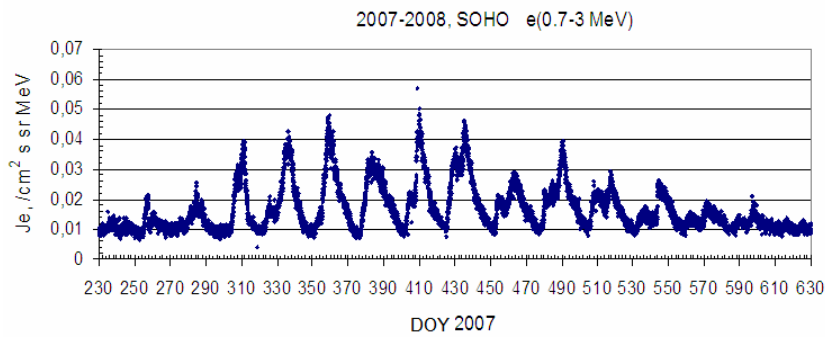


Fig.1. 27-day variations of Jovian electrons registered by SOHO, EPHIN at the Lagrange point L1 in the minimum of 23-24 solar activity cycle

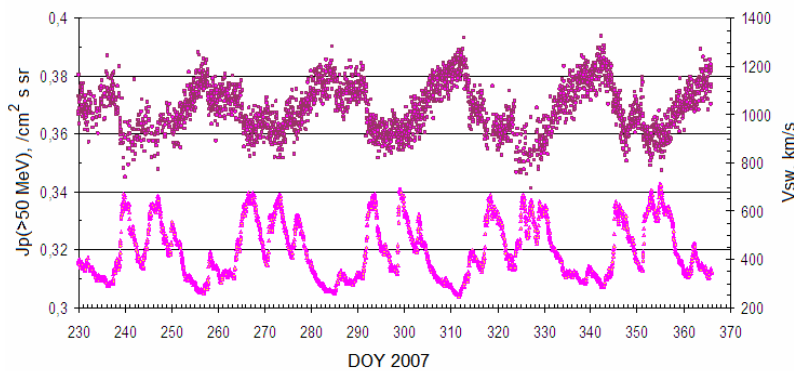


Fig.2. The structure of solar wind speed is almost preserved from rotation to the rotation of the Sun.

The last solar flare with the flux of protons $E_p > 10 \text{ MeV}$ exceeded $J_p \geq 1(\text{cm}^2 \cdot \text{s} \cdot \text{sr})^{-1}$ before this period occurred, according to our Catalog of Solar Proton Events [Logachev Yu.I., et al, 2016], on December 14, 2006, the first one after that – on August 03, 2010.

Simultaneously periodic variations in the fluxes of galactic cosmic rays, which are always present in the heliosphere, were also observed.. Galactic cosmic rays (GCR) - energetic charged particles, accelerated, as believed, by such objects as supernovae and

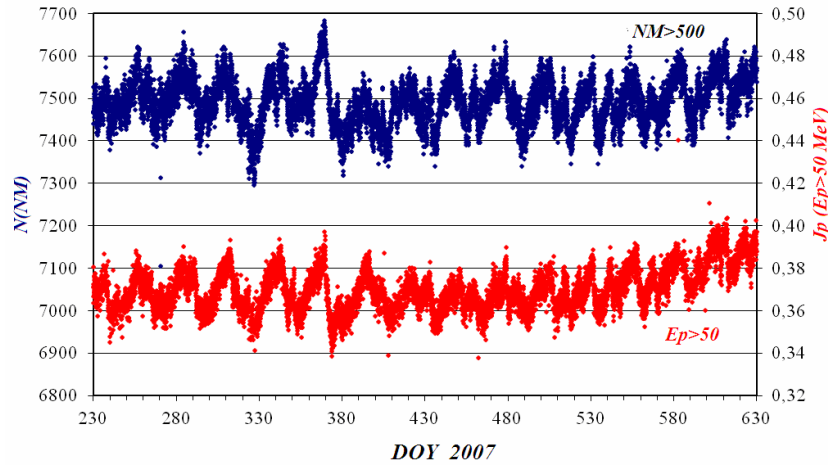


Fig. 3. Neutral monitor ($E > 500$ MeV) and EPHIN (SOHO) $E > 50$ MeV data in 2007-2008

supernova remnants, pulsars, compact objects in close binary systems and stellar winds with energies $E_p > 500$ MeV. Usually neutron monitors data are used for registration of GCR. In this paper we mainly use the data of the integral channel $E_p > 50$ MeV of the EPHIN, SOHO instrument. The advantage of this consideration compared with the NM data is that both electron and proton data were obtained at the same instrument.

Fig. 3 demonstrates that galactic protons, which differ greatly in energy, are almost identical in variations, although the percentage variation of proton fluxes for energies > 500 MeV = 1.3%, and for > 50 MeV = 4.5%. Both GCR and Jovian electrons experienced quasi-27-day variations associated with the rotation of the Sun. The periods of GCR variations turned out to be the same with the periods of long-lived structures of the solar wind, 27.1 days. During all this time, variations in the flux of galactic protons of high and low energy ($J_p > 50$ and > 500 MeV) anti-correlated with variations in the solar wind speeds (see Fig. 4). This permits to consider these variations as depressions, caused by enhanced convection and adiabatic deceleration during the increase of solar wind speed [Richardson I.G., et al, 1996].

At the same time, the electrons behaved somewhat differently. As shown in Fig. 5, anti-correlation of the solar wind velocity and MeV electrons in 2007 gradually changed to a positive correlation in 2008. This led to the following effect: at the beginning of the observed cycle, variations in the fluxes of Jovian electrons and galactic protons correlated, then at each rotation of the Sun a small phase shift of the correlation took place, so that by the middle of the cycle (by the 7 rotation) there was already a complete anti-correlation of the Jovian electrons and galactic protons (Fig. 6). As mentioned above, all this time, the galactic protons anti-correlated with the solar wind.

We find an explanation for this fact in our proposed trap model, shown in Fig. 7 (left). It was noted in [Daibog E.I., et al, 2013], that the periodicity of increases in the fluxes of electrons in 2007–2008, differed from the periodicity of the solar wind structures and was 26.1 days, which represents a significant deviation from the Sun-Earth synodic period of 27.3 days. An explanation of this effect was proposed in [Daibog E.I., et al, 2017], which, in particular, took into account the influence of the mutual position in space of the Earth and Jupiter and the time of their stay in the magnetic trap. When both Jupiter and Earth stay inside the magnetic trap, then their relative location is important.

Before an optimum magnetic connection (Fig. 7, right (a)), when both Jupiter and the Earth located on the same field line, the trap first reaches the Earth, then Jupiter. The period between successive fillings of the trap is 25.6 days (the synodic period of the Sun-Jupiter system) and at each solar rotation the electron flux increases before the rise of galactic protons by about 1.7 days, which is independent of the Earth-Jupiter phase.

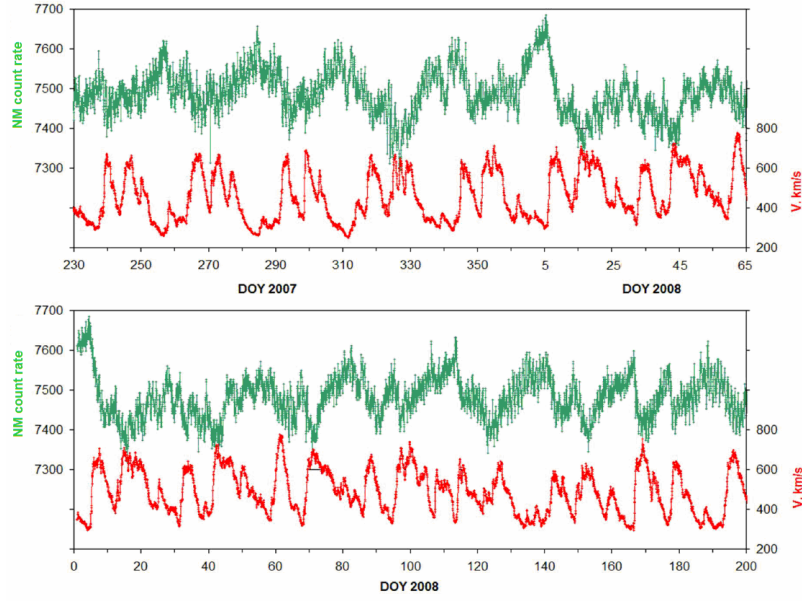


Fig. 4. Apatity neutron monitor count rate and solar wind speed: constant anticorrelation

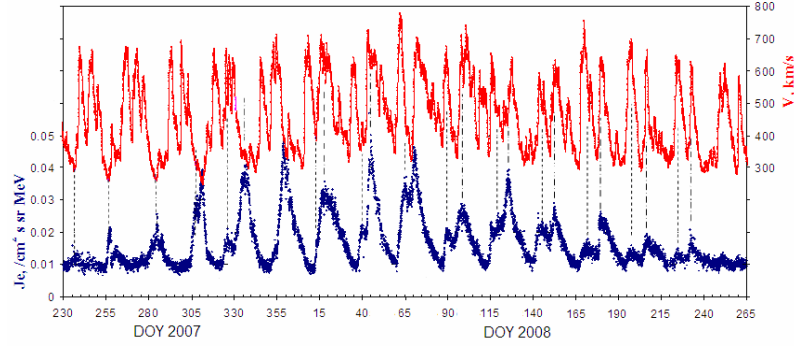


Fig.5. Correlation of solar wind speed and flux of 0.3-7 MeV electrons. Anticorrelation in 2007 and positive correlation in 2008

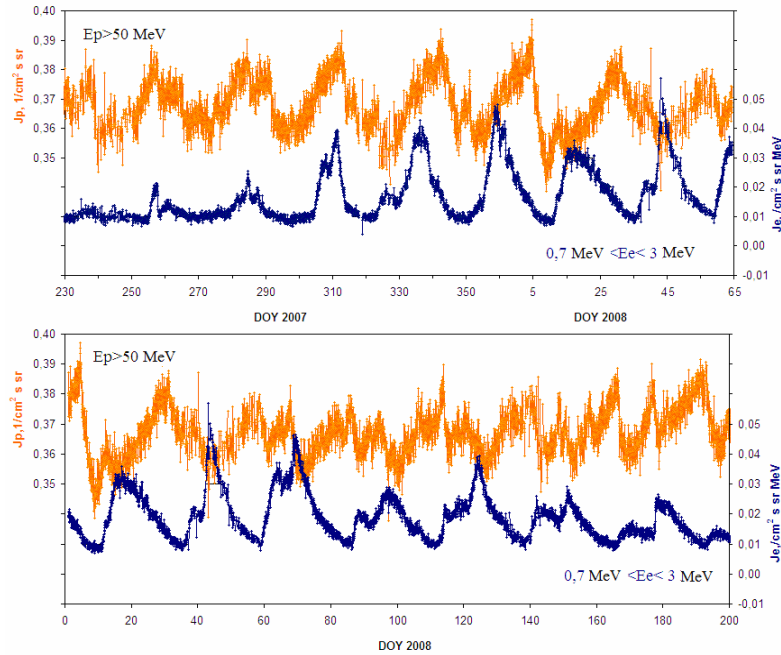


Fig. 6. Galactic protons $E_p > 50$ MeV and Jovian electrons E_e 0.7-3 MeV (EPHIN, SOHO), (top) positive correlation ; (bottom) anticorrelation

After an optimum magnetic connection (Fig. 7 right (b)) the trap first reaches Jupiter, which fills the trap with electrons, then the trap approaches the Earth where electrons are observed. Observed period: 27.3 days (Sun-Earth synodic period).

Galactic proton fluxes anticorrelate with solar wind speed.

Total duration of the cycle $T_e = nT_{\text{Sun-J}} + mT_{\text{Sun-E}} = 399$ days (J-E synodic cycle), resulting average period $\langle T_e \rangle = \{nT_{\text{Sun-J}} n + mT_{\text{Sun-E}} m\} / (n + m)$, where $T_{\text{Sun-J}} = 25.6$ days, $T_{\text{Sun-E}} = 27.3$ days, n and m are the numbers of increases before and after the optimum connection, and thus the range of $\langle T_e \rangle$ is between 25.6 to 27.3 days. For 2007-2008 $\langle T_e \rangle = 26.1$ days.

This leads to a gradual phase shift of the correlation between the Jovian electrons and GCR.

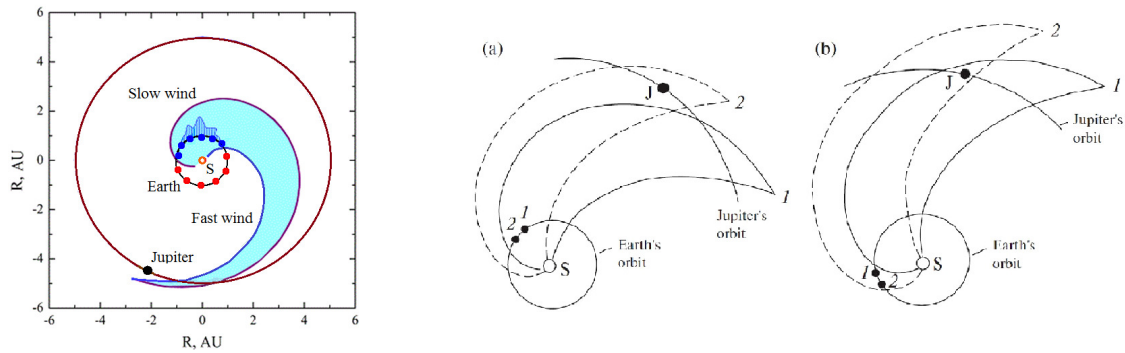


Fig. 7. Left. Schematic of the magnetic trap, existing over several rotations of the Sun. Blue and red points –favorable and unfavorable Jupiter-Earth positions for observation of Jovian electrons. Right. Schematic of the successive relative positions 1 (solid curves) and 2 (dashed curves) of the Earth (E) and Jupiter (J). (a) before and (b) after their optimal magnetic connection. S denotes the Sun. Before their optimal connection, the Earth is located inside a trap at positions 1 and 2, which reaches Jupiter only at position 2, when it is filled with electrons that are registered at the Earth. After their optimal connection, Jupiter is located inside the trap at position 1 and fills it with electrons, while the Earth is outside the trap; both the Earth and Jupiter are inside the trap at position 2, and Jovian electrons are registered.

Conclusions

1. In the presence of periodic structures of the solar wind of a certain configuration, forming a magnetic trap, variations in the fluxes of galactic protons and Jupiter electrons are due to various mechanisms:
 - Protons - flux depressions due to enhanced convection and adiabatic deceleration during the increase of solar wind speed;
 - Electrons - flux increases due to their trapping in a closed magnetic structure.
2. The model of the magnetic trap, taking into account that both Jupiter and the Earth can stay inside it simultaneously, and considering their relative position, explains that:
 - during the 2007-2008 solar minimum the average period of Jovian electron peaks was 26.1 days, significantly shorter than the expected 27.3 days of the Sun-Earth synodic period
 - solar wind speed increases and galactic proton flux peaks are in anticorrelation
 - change in the regime from the initially positive correlation (until the optimum Earth-Jupiter connection) between the variations of galactic protons and Jovian electrons to anticorrelation after the optimal connection.

Acknowledgment

This work was supported by grant RFBR № 19-02-00264

References

- Alekseev N.V., P.V. Vakulov, N.I. Vologdin, and Yu.I. Logachev (1982). Investigation of the flux of Jupiter electrons with energy not less than 40 keV by the Mars-7 interplanetary probe *Izv. Akad. Nauk SSSR, Ser. Fiz.* 46, 1695.
- Alekseev N.V., P.V. Vakulov, N.I. Vologdin, and Yu.I. Logachev (1983). Some features characterizing the intensity variations of electrons with energies of 40-500 keV in interplanetary space *Izv. Akad. Nauk SSSR, Ser. Fiz.* 47, 1810.
- Barns K.V., D. L. Chenet, T.F. Conlon, K.R. Pail, and Dzh. A.S. Simpson (1977). Acceleration of nucleons in the interplanetary space and the modulation of Jupiter electrons in the interval from 1 to 10 A.U. by corotating regions of solar origin *Izv. Akad. Nauk SSSR, Ser. Fiz.* 41, 303.
- Chenette D.L., T.F. Conlon, and J.A. Simpson (1974). Bursts of relativistic electrons from Jupiter observed in interplanetary space with the time variation of the planetary rotation period. *J. Geophys. Res.* 79, 3551.
- Chenette D.L., T.F. Conlon, K.R. Pyle, and J.A. Simpson (1977). Observations of Jovian electrons at 1 AU throughout the 13 month Jovian synodic year. *Astrophys. J.* 215, L95.
- Chenette D.L. (1980). The propagation of Jovian electrons to earth. *J. Geophys. Res.*, 85, 2243.
- Conlon T.F. (1978). The interplanetary modulation and transport of Jovian electrons. *J. Geophys. Res.* , 83(A2), 541.
- Daibog E.I., K. Kecskemety, and Yu.I. Logachev (2013). Jovian Electrons and the Solar Wind during the Minimum of the 23rd–24th Solar Activity Cycle. *Bull. Russ. Acad. Sci.: Phys.* 77, 554.
- Daibog E.I., K. Kecskemety, L.L. Lazutin, Yu I. Logachev, G.M. Surova (2017). A 27-Day Period in the Flux of Jovian Electrons at the Earth's Orbit. *Astronomy Reports*, 61, 1073.
- Eraker J. H. and J.A. Simpson (1979). Jovian electron propagation close to the sun /at about 0.5 AU *Astrophys. J.* 232, L131.
- Gomez-Herrero R., D. Rodriguez-Frias, G. Hebrero, R. Cruz, L. del Peral, R. Muller-Mellin, B. Heber and R. Wimmer-Schweingruber (2008). An overview of Soho 12 years after. *Lect. Notes Essays Astrophys.* 3, 213.
- Kuhl P., N. Dresing, P. Dunzlaff, H. Fichtner, et al. (2013). Simultaneous analysis of recurrent Jovian electron increases and galactic cosmic ray decreases. *Centr. Eur. Astrophys. Bull.* 37, 643.
- Logachev Yu.I., G.A. Bazilevskaya G.A., Vashenyuk E.V., et al., (2016). Catalog of Solar Proton Events in the 23rd Cycle of Solar Activity (1996 – 2008). ESDB repository, GC RAS, Moscow, doi: 10.2205/ESDB-SAD-001. http://www.wdcb.ru/stp/data/SPE/Catalog_SPE_23_cycle_SA.pdf, <https://www.ngdc.noaa.gov/stp/space-weather/interplanetary-data/solar-proton-events/documentation>.
- del Peral L., R. Gomez-Herrero, M.D. Rodriguez-Frias, J. Gutierrez, R. Muller-Mellin, and H. Kunow (2003). Jovian electrons in the heliosphere: New insights from EPHIN on board SOHO. *Astropart. Phys.* 20, 235.
- Richardson I.G., G. Wibberenz, H.V. Cane, (1996) The relationship between recurring cosmic ray depressions and corotating solar wind streams at <1 AU' IMP 8 and Helios 1 and 2 anticoincidence guard rate observations. *J. Geophys. Res.*, 101, 13,483.
- Richardson I.G. 2004. Energetic particles and corotating interaction regions in the solar wind. *Space Sci. Rev.* 111, 267.
- Simpson J.A., D.A Smith., M. Zhang (1993). Jovian electron propagation in three dimensions of the heliosphere: The ULYSSES investigations. *J. Geophys. Res.*, 98, 21,129.
- Trainor J.H., F.B. McDonald, B.J. Teegarden, W.R. Webber, E.C. Roelof (1974). Energetic particles in the Jovian magnetosphere. *J. Geophys. Res.* 79, 129.
- Vogt A., F. Effenberger, H. Fichtner, B. Heber, et al. (2015). Modelling the Influence of Corotating Interaction Regions on Jovian MeV-electrons. *Proceedings of the 24th European Cosmic Ray Symposium, J. Phys.: Conf. Ser.* 632, 012082.

Double Filament Eruption and Associated Ribbon Flare and Halo Coronal Mass Ejection

Dechev M. Ts.¹, Koleva K.², Duchlev P.¹, Miteva R.²

¹ Institute of Astronomy with NAO, Bulgaria

² Space Research and Technoly Institute, Bulgaria

E-mail: mdechev@astro.bas.bg

Abstract.

We observe and study a double filament eruption and associated ribbon flare and halo coronal mass ejection. The filament eruption occurred 31 August 2012. The eruption was followed by a C8.4 two-ribbon flare and second filament eruption. We explore the kinematics of the events and found velocities in the range of 1–151 km/s and accelerations from 0.9 to 125 km/s². The kinematic parameters of the associated CME are also discussed.

Introduction

Prominence/filament eruptions are believed to be one aspect of a more general single eruption that can produce a solar flare and a coronal mass ejection (CME) (e.g. Forbes, 2000; Priest & Forbes, 2002). These three eruptive phenomena may be different manifestations of the same magnetic energy release process in the corona (e.g. Moore et al., 2001; Sterling et al., 2012). Many studies of the relationship between eruptive prominences (EPs), solar flares and CMEs (e.g. Chandra et al., 2010, Dechev et al., 2018) point out to strong relations between EPs, solar flares and CMEs.

In this work we report a rarely observed case of a dual prominence eruption, leading to the solar flare and CME. Our aim was to study time evolution and causal relationships between the observed events in order to analyse in deep the dynamical processes involved in CME initiation and evolution and its impact for space weather and geospace climate.

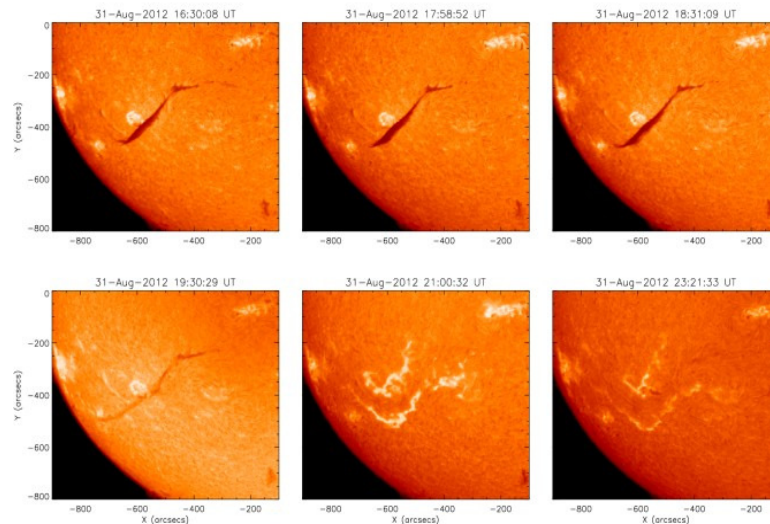


Fig. 1 Evolution of the two-ribbon flare occurred at the base of the erupted filament as seen in KSO Ha images

Observations

A major filament eruption (FE) occurred on 31 August 2012 and was observed in the southeast solar hemisphere close to the solar limb (Figs. 1, 2). During the activation, the filament slowly rose as compact body between 18:00 UT and 19:10 UT. During the eruptive phase, two main flux ropes (FRs) from the filament body erupted consecutively that was well

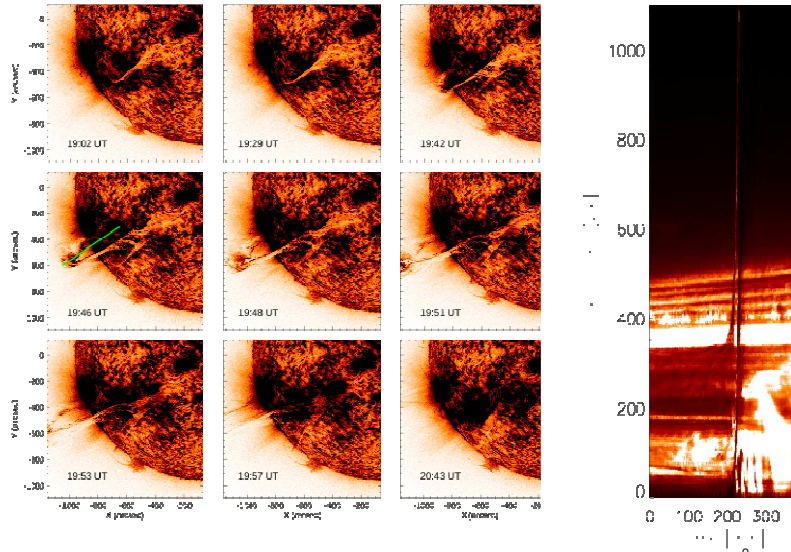


Fig. 2 Evolution of the filament eruption on 2012 Aug 31 in the AIA/SDO 304Å inverted color images (left). The green line shows the slice position. AIA/ 304Å time-distance diagram (right).

observed in the AIA/SDO instrument. First FR eruption started at 19:10 UT and after 19:50 UT, when the upper part of FR was out of AIA field-of view, two ribbon flare began to form at the filament feet.

Later, at 20:20 UT, when two ribbons evolved as C8.4 flare, the eruption of second FR started. Double filament eruption was associated with coronal wave, fast halo CME and solar energetic particles (SEP). The kinematic parameters of two FRs were established. We found causal relationships between all events in the following order: first filament FRs eruption - C8.4 ribbon flare - second filament FRs eruption - coronal wave - fast halo CME - SEP event.

The observations of the FE analyzed here are obtained from the Atmospheric Imaging Assembly (AIA) instrument onboard SDO (Lemen, et al. 2012), that provides high cadence (12") and high spatial resolution (0.6 arcsec/pixel) data, allowing to see more details of the filament eruption. The AIA images were processed through a `aia_prep` routine in IDL SolarSoft data analysis package for SDO AIA. We use data from AIA/SDO 304Å channel to analyze the filament evolution and its kinematics. In order to study the kinematics of the filament eruption, we create a time-slice diagram, showing the eruption evolution in He II 304Å channel.

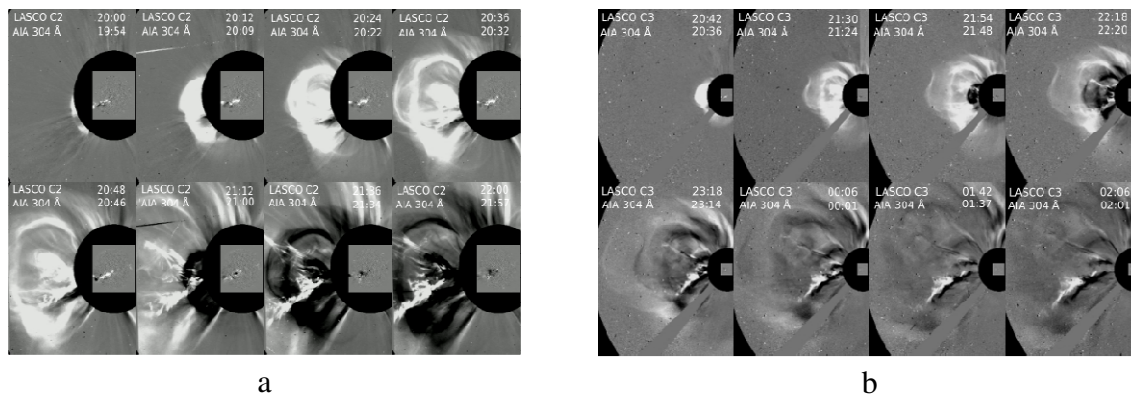


Fig. 3 Composite image of the white-light SOHO/LASCO-C2 running difference images on 2012 August 31 between 20:00 UT and 22:00 UT and the SDO/AIA 304Å images during the same time interval (a) and composite image of the white-light SOHO/LASCO-C3 running difference images from 2012 August 31 between 20:30 UT and 2012 September 1 02:30 UT and the corresponding AIA/SDO 304Å images (b).

We also use LASCO/SOHO (Brueckner, et al. 1995) C2/C3 data to study the kinematics of associated CME and the FE as a CME bright core. Synoptic H α observations by the Kanzelhöhe Solar Observatory (KSO) are also included in the study.

Kinematics

The plot the time evolution of the filament height (Fig. 5) reveals two distinct phases of the FE: acceleration phase followed by constant velocity filament raising.

The acceleration phase is well fitted by an exponential function, while for the second phase the best fit is linear function. The regression error for exponential fit is 230 ± 30 Mm and those for linear fit is 376 ± 14 Mm.

We found that during the acceleration phase the velocity increases in the range of 1–151 km/s and the acceleration increases from 0.9 to 125 km/s^{-2} . During the second phase, the filament rise up with constant velocity of 163 km/s.

The filament eruption is associated with a fast halo CME. According to the LASCO CME catalog (https://cdaw.gsfc.nasa.gov/CME_list/), the CME first appearance in the LASCO/C2 field of view was around 20:00 UT. The linear speed of the CME was 1442 km/s. Second order velocity and the acceleration of the CME were 1454 km s^{-1} and 2 m s^{-2} , respectively.

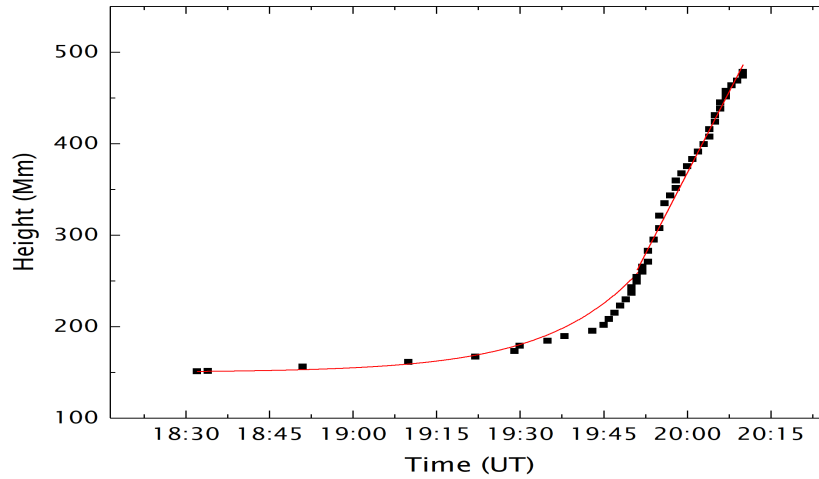


Fig. 4 Height–time plot of the filament leading edge, measured using the SDO/AIA 304Å slice diagram (Fig. 2 right).

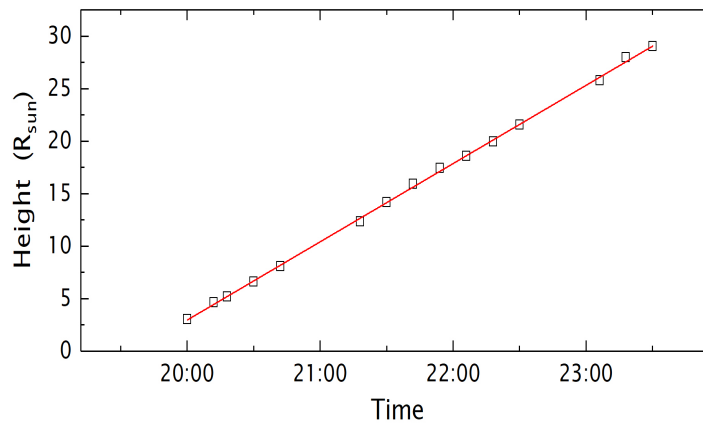


Fig. 5 Height–time plot of the CME, measured in the LASCO C2 and C3 field-of-view (Fig. 3).

Results

The FE showed two distinct eruptive phases: phase with acceleration and constant velocity phase.

- The eruption of the first filament FR triggered two ribbon flare, which acted as a possible trigger for the second filament FR eruption.
- The FE was associated with fast halo CME and it could be traced as a bright CME core up to 20 solar radii in the LASCO C3 field of view.
- The time evolution of all associated events on 31 August 2012 reveals causal relationships between events in the following order: first filament FRs eruption - C8.4 ribbon flare - second filament FRs eruption - coronal wave - fast halo CME - SEP events.

Acknowledgment

This research is co-funded by a bilateral collaborative project NTS/AUSTRIA 01/23, 28.02.17, under agreement between Bulgaria’s National Science Fund and Austria’s OeAD-GmbH. It was also partially funded by Bulgarian National Science Fund under Grants DH 081/13.12.2016 and DN 18/13-12.12.2017. H-alpha data were provided by the Kanzelhöhe Observatory, University of Graz, Austria.

References

- Brueckner, G. E., Howard, R. A., Koomen, M. J., et al. 1995, Sol. Phys., 162, 357
Chandra, R.; Pariat, E.; Schmieder, B.; Mandrini, C. H.; Uddin, W., 2010 ,Sol. Phys., 261, 127
Dechev, M., Duchlev, P., Koleva, K.: 2018, BlgAJ, 28, 60
Forbes T. G., 2000, J. Geophys. Res. 105 , 23153
Lemen, J. R., Title, A. M., Akin, D. J., et al. 2012, Sol. Phys., 275,17
Moore, R. L.; Sterling, A. C.; Hudson, H. S.; Lemen, J. R., 2001, ApJ 552, 833
Priest E. R. & Forbes T. G., 2002, A&AR 10, 313
Sterling, A. C.; Moore, R. L.; Hara, H., 2012, ApJ 761, 69

Evolutionary and Flare Characteristics of Prolonged Phases of Solar Minimum

V.N. Ishkov

Pushkov Institute of Terrestrial Magnetism, Ionosphere and Radio Wave Propagation RAS,
Moscow, Troitsk, Russia
E-mail: ishkov@izmiran.ru

Abstract

The current 24 solar cycle (SC), which opened second epoch of the lowered solar activity (SA) entered the last period of its development ($W^* \leq 5$ to the minimum), which can be prolonged of up to 1.5-2 years. According to the scenario of solar cyclicity the second epoch of lowered SA will overlap two thirds of 21 century. The development of SC in the phases of the minima makes it possible to isolate two groups of the SA decrease with the characteristic times 19 (+10/-6) and 43 (+2/-4) months. The first group (cycles **10-11** and **16-23**) includes all SC of the epochs of increased SA, and 2 SC (**11** and **23**) of transition periods. All SC of second group (**12-15** and **24**) - SC of lowered SA epochs (except SC **16**). The periods of beginning following SC are determined by the strength of new SC: more active (high) cycles, as a rule, begin their increase earlier (through 8-15 months), although there were two noticeable exceptions: SC**17**, and **22**..

Introduction

At the present time the statistics of reliable Wolf number series observations gives an opportunity to investigate the scenario of solar activity (SA) cycles, its property, characteristic and rules of the development on a reliable (1849-2014) series of Wolf numbers at the time scale of more 180 years - 17 complete solar cycles (SCs). It is necessary to note that for such studies of SC characteristics we in principle cannot use the restored series (1755-1848), since the reliable and restored series of the Wolf numbers have quite different spectral characteristics and significantly differ in the statistical parameters [*Ishkov, Shibaev, 2006*].

The reliable series of the relative sunspot numbers shows surprising constancy in the basic manifestations development of separate 11- and 22-year SC, and the structure of its cyclicity, on this statistics (16 SCs), implies periodic changes from the epoch of lowered (SCs 12th-16th) to the increased (SCs 18th-22nd) SA. Between these epochs are observed transition periods (SCs 11th, 23rd and 17th), during which the character of spot-forming activity changes, i.e., regimes of magnetic fields generation in the spot-forming zone of the Sun changes.

Almost all absurdity and artifacts fall only on the restored cycles. At the same time, the statistics reliable solar cycles may be conditionally included cycles 8 and 9, adjacent to reliable, and does not contradict the basic characteristics of reliable solar cycles, thus increasing the statistics up to 17 cycles (~ 185 years) [*Shibaev, Ishkov, 2012*].

The principal differences in the characteristics and main properties of SCs of various SA epochs are determined by the different ranges of variations in the mean background values of the solar general magnetic field, which is manifested in the character of sunspot-forming activity and determines the general characteristics of SCs within the epochs. Studies of the characteristic features and laws of the development of SCs in different epochs made it possible to draw the following conclusions: for the entire series of reliable SCs, regardless of the epoch, patterns associated with the magnetic properties of the Sun, such as the 22-year cycle of the magnetic field polarity reversal during the maximum phase of the 11-year cycle, are strictly fulfilled [*Ishkov, 2018*]. Hence follows Hale's law: the magnetic polarities of leading and trailing sunspots in each hemisphere change to the opposite sign upon the

transition from one cycle to another. The principal difference between epochs well reflects Fig. 1, which shows the difference of epochs in the smoothed areas of sunspots groups.

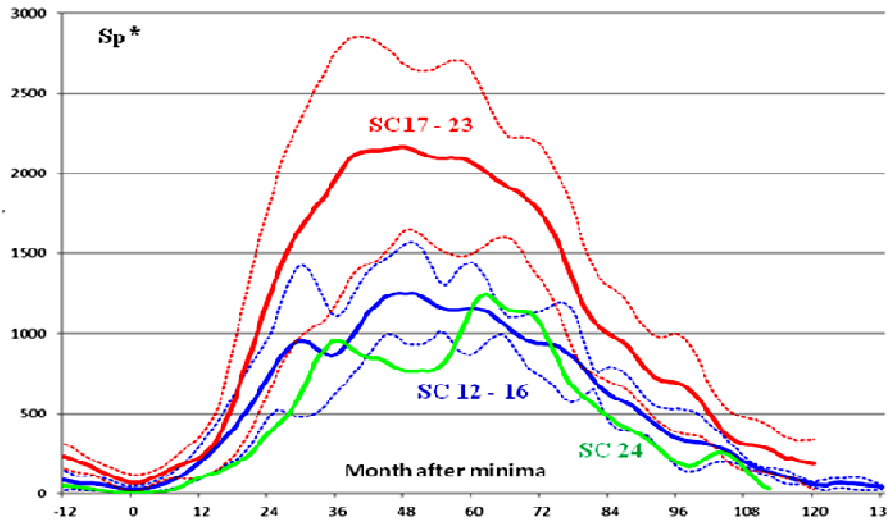


Fig.1. Smoothed average areas of sunspots group for the epochs of increased SA (red thick curve) and for the epochs of lowered SA (dark-blue thick curve) with the boundaries of the spread values. The first curve includes SCs 17-23, that possible can reduces the values of areas increased epoch of SA. Green curve shows current 24 SC. Converted image from [Janssens, 2019].

The same is true for Joy's law: a tilt of the bipolar structures from the leading to the trailing sunspot grows with their heliolatitude (the leading sunspots are closer to the equator). For the Waldmeier rule, the higher the growth rate of the cycle is, the higher is the cycle. The Gnevyshev–Ohl rule is also invariably fulfilled inside the epochs: an odd 11-year cycle is higher than the preceding even cycle. In the available statistics, there were no low cycles during the epochs of increased SA and no high cycles during the epoch of lowered SA. The most powerful flare events (for a given cycle) within the epochs generally occur on the phase of the decrease and, more rarely, in the rise phase of SC.

Long duration solar cycles

There is special interest for understanding of rules governing the general development of SCs and approaches to the forecast of the branches of decrease in a study of the phases of minimums for SCs which duration exceeds 11.25 years (135 months). By phase of the minimum here is understood the interval of the time, when the smoothed values of the relative numbers of sunspots remain within the limits $W^* \leq 30$. The phase of the minimum is, thus, general for current and subsequent SCs; however, the point of the minimum we carry to completed SC. In this work we will distinguish the temporary sections of the phase of the minimum from the beginning of cycle to the point $W^* = 30$ - **the phase of minimum for the increasing branch**, and the subsequent phase of the minimum after the maximum of cycle - **the phase of minimum for the descending branch**.

The study of the development of last two SCs, of transitional SC 23 and SC 24 - first cycle second epoch the lowered by SA [Ishkov 2005, 2017] - showed the imperative need of investigating the regularities such SCs for the approach to the forecast of their evolution and creation of the more precise, real models of SA cycles. In the table 1 are given the main evolutionary characteristics of long-duration solar cycles among that SCs with the tightened phases of the minimums of the descending branch. SCs of the increased SA epochs are marked in cursive. Main SCs of transition periods are marked in bold type. This is all the more relevant because we live in a period of deep minimum of the current solar cycle 24 ($W^* = 4.0$ in November 2018). It should be noted that in terms of duration, all reliable solar cycles are clearly divided into two classes.

Table 1. The main evolutionary characteristics of long-duration reliable solar cycles.

N	T_0	W_m^*	T_M	T_e	W_M^*	$T_Y\uparrow$	$T_Y\downarrow$	$T_{SC} Y$	$T1_m$	$T2_m$	Sp_{less}
9	1843VIII	3.2	1848 II	1855XII	131.6	4.58	7.83	12.42	18 ^m	23 ^m	>322
10	1855XII	3.2	1860 II	1867 II	97.9	4.17	7.25	11.42	38 ^m	34 ^m	402
11	1867 III	5.2	1870 VIII	1878 XI	140.5	3.42	8.50	11.92	2.83	5.41	1025
12	1878XII	2.2	1883 XII	1890II	74.6	5.0	6.3	11.3	5.42	4.92	732
13	1890III	5.0	1894 I	1901II	87.9	4.5	8.2	12.1	4.92	6.42	937
14	1902 I	2.6	1906 II	1913VII	64.2	4.1	7.6	11.7	6.42	4.92	1045
20	1964X	9.6	1968 XI	1976 VI	110.6	4.1	7.8	11.9	3.17	5.75	269
23	1996 VI	8.0	2000 IV	2008 XII	120.7	3.8	8.9	12.7	3.33	5.67	821
24	2009 I	1.7	2014 IV	2020V-IX	81.9	5.3	5.9	12.3	5.67	4.92	

T_0 – beginning of SC; W_m^* – initial value of smoothed Wolf numbers; T_M – the time of SC maximum; W_M^* – maximum value of the smoothed Wolf numbers; $T_Y\uparrow$ – duration of the rising branch; $T_Y\downarrow$ – annual duration of the decreasing branch; $T_{SC} Y$ – annual duration of SC; $T1_m$, $T2_m$ – monthly length of the minimum phase before and after this SC; Sp_{less} – a number of spotless days in the corresponding phases of minima.

The first class includes cycles whose duration exceeds 11.25 years (**135 months**). These are all the cycles of the XIX century and SCs 20 and 23, which were realized in the XX and XXI centuries.

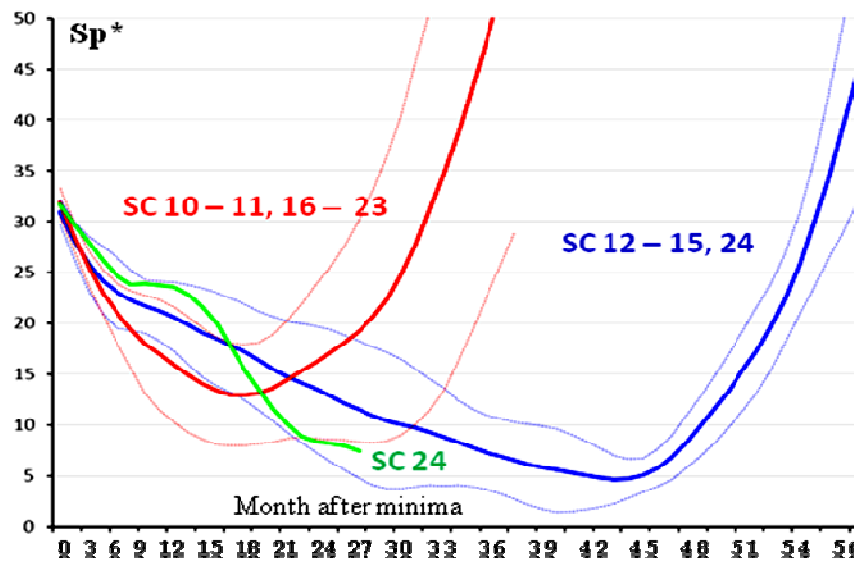


Fig.2. Distribution of durations the phases of minima for the descending branch of reliable SCs. The phases of the minimum can be compared to previous SCs, which have been conveniently grouped into two groups: cycles 10-11 and 16-23 (red curves - the first group), and cycles 12-15 (blue curves - second group), and 24 (green curve). The dashed curves indicate the standard deviation from the average curve (thick lines). Point "0" is the last month with a smoothed sunspot number above $W^*=30$ (April, 2016). Converted image from [Janssens, 2019].

As can be seen from Fig. 2, for the first group of solar cycles, a minimum occurred on the average 19 (+10/-6) months later. However, for the second group this minimum took place only after 43 (+2/-4) months. The timing is mostly determined by the strength (height) of the new cycle: more active cycles tend to start their rise earlier (after 8-15 months; the first group), though there have been 2 notable exceptions: SC17 and SC22. According to belonging to the CA epochs, they are distributed as follows:

- three of them constitute the initial SCs of the first epoch of lowered CA (SCs 12-14)
- two (out of three) solar cycles of transition periods (SC 11 and 23), in both had occurrence the restructuring of the solar general magnetic field to the epochs of lowered SA;
- and two medium solar cycles of the epoch of increased SA (SC 10 and 20).

The second class the solar cycles lasting ≤ 10.5 years (125 months) includes:

- all high (SC 18, 19, 21, 22) solar cycles the second epoch of increased SA;
- transitional SC 17 from the epoch of lowered to increased SC;
- two last solar cycles (15-16) of the first epoch of lowered SA.

The main feature of SCs 20 and 10 of the epoch of increased SA, falling into the first class, is the prolonged phase of decline to the beginning of the phase of minimum and the short itself minimum phase (19 and 20 months). The relatively short duration of the phase of minimum (19–23 months) is a characteristic feature all solar cycles of epochs of increased SA. It should be noted that the flare activity of cycle 20, despite the fact that it was of medium height, was at a very high level, comparable to the flare activity of other high solar cycles of the epoch of increased solar activity. Nothing is possible to say about the SC10 flare activity. However, it should be noted that in the SC10 formally began the processes of the transition period to the first epoch of lowered CA (analog SC 23) and in this SC the most powerful flare event (1.09.1851) took place in the entire history of observation of the Sun.

That is, even for SCs of a long duration for epochs of increased SA, the rule of the short phase of the minimum of the descending branch is preserved. Therefore, in this talk, we will not affect the cycles of epochs of increased SA. But the transition cycles to epochs of lowered SA, as well as itself cycles of lowered SA, belong to cycles of long duration precisely due to the prolonged phase of the minimum of the descending branch. The average interval of the phase of minimum for such cycles is 41-47 months, however, SC 13 has become extremely prolonged-57 months.

Such SCs on this statistics were observed between transitional and first low SCs opening epochs of lowered SA (SCs 11-12, and 23-24), between the cycles lowered SA (SC 12-13, 13-14 and 14-15) and also between average and high SC (20-21) and between formally averages (9-10) in the epochs of increased SA. The fact calls attention to itself that SC 9, falls into this sample due to the phase of decrease ($T_{\max}-T^*_{30}$) anomalously tightened on the time. Since the SC 9 are conditionally reliable cycle, it is possible that this the effect of “poor” data.

For SCs of epochs of increased SA and transitional cycles comparatively short half-phase of the minimum of the rise branch ($T1_m$), determines the long phase of the minimum of the descending branch ($T2_m$). This rule is also correct for three of five SCs of epoch lowered SA, but in 13 and 16 SCs it is disrupted and half-phase of the minimum of the rise branch exceeded the phase of the minimum of the decrease branch. In this case it is necessary to bear in mind, that for all reliable SCs inside epochs the branch of rise in 1.2-2 time is shorter on the time than the decrease branch, and for transition solar cycles (SC11 and SC23) the branch of rise in 2.5 time is shorter on the time than the decrease branch.

For SCs of epochs of increased SA and transitional cycles comparatively short phase of the minimum of the rise branch ($T1_m$), determines the more long phase of the minimum of the fall branch ($T2_m$). This rule is also correct for three of five SCs of epoch lowered SA, but in 13 and 16 SC it is disrupted and the phase of the minimum of the rise branch exceeded the phase of the minimum of the decreasing branch. In this case it is necessary to bear in mind, that for all reliable SCs the branch of rise in 1.5-2 time is shorter on the time than the decreasing branch.

Development of current SC 24 in comparison with SCs of the first epoch lowered SA

After the 23rd SA cycle, the transitional period of the restructuring of the generation of magnetic fields in the solar convective zone passed and entered the stationary mode of alternating low and medium cycles similar to the 12–16 cycles time interval.

According to the scenario of cyclicity for reliable solar cycles, SC24, opened the 2nd epoch of lowered SA, which will cover two-thirds of the XXI century. The first epoch of lowered SA includes 5 SC [Ishkov, 2018], three of which were low ($W^* \leq 80$ - cycles 12th, 14th, 16th) and two were average (SC 13th and 15th). The main averaged SC characteristics of "lowered" SA epoch in comparison with "increased" SA epoch are:

- a ban on high (strong) SCs and the indispensable implementation of basic observational rules, including the rules of Gnevyshev-Ol', according to which the next SC25 should be of an average size;
- lower initial values W^*_{min} (3.38); - their large duration (11.1^y);
- more prolonged rising branch (4.5^y);
- several (≥ 2) peaks in the maximum phase for low cycles and a single peak for cycles of average magnitude;
- shorter decreasing branches (6.5^y);
- narrower zone of sunspot-formation on the latitude of $\pm 35^\circ$;
- a quantity of spotless days around the minimum phase - 781^d;
- the average smoothed area of the sunspot groups ~ 1200 msh (see Fig.1);
- number of the sunspot groups with the areas ≥ 1000 msh in all cycles of the first epoch - 147 [Janssen, 2004];
- tightened phases of the SC minimum phases (61 month on average) and, especially, before low SC, and in two cases of three (SC 23-24 and 14-15) - the most prolonged phases of the minimum, 68 and 77 months respectively;
- the maximum value of the polar magnetic field is ± 100 mT [Svalgaard, 2019].

The current 24th SA cycle, which began in January 2009, has given us a lot of new information about SA since the beginning of the space age. It began and was developed under the conditions, when in a transitional SC23 time, the background values of the overall magnetic field of the Sun decreased more than twice [Ishkov 2018], that it led to complete reconstruction of physical conditions in the Sun, and, as a result, in the heliosphere, and it was reflected in the state of near-earth space. The current SC is developed as the cycle of low value, whose flare activity substantially lower than all previous SCs of the Space Age, and it opens the second epoch of lowered SA. After 10 the years of evolution SC24 it is important to reveal differences in its characteristics with SCs of the first epoch lowered SA. After the first peak in November 2011 after small, but prolonged (15 month) the decrease in the Wolf numbers, SC 24 became confidently grow and by April 2014 it reached its maximum ($W^* = 81.9$). The motion of its development shows that since April 2016 the phase of the minimum realizes ($W^* \leq 30$). A study current SC revealed some fundamental special features of its evolution:

- **the first special feature** lies in the fact that not in one SC of the first epoch of lowered SA (and even for the entire totality of reliable SC) the first peak was manifested so clearly and with such difference in the peak values with the main ($\Delta W^* \sim 15$), and taking into account the decrease of W^* after the first peak, the intermediate section of rise to main peak engage the interval $\Delta W^* \sim 30$;
- **the second feature of the SC 24** became the record duration of the branch of growth, which is the largest and for the first epoch of low solar activity and for the entire reliable series - 5.32 year.

- **the third special** feature became in the smallest quantity of high ($Sp \geq 1000$ mvh), very large ($Sp \geq 1500$ mvh) and gigantic ($Sp \geq 2000$ mvh) the sunspot groups not only among all SCs of the Space Age, but also all SCs of the first epoch lowered SA. By May 2019 on the Sun appeared only 16 the large sunspot groups, of them 5 very large and one gigantic - $Sp \geq 2000$ mvh (16/5/1), whereas into the SC 12 of such sunspot groups it was 23/10/0, in SC13 - 37/9/2, in SC14 - 21/7/2, SC15 - 21/7/2 and SC16 - 33/10/3;

- the smallest lifetime of the sunspot groups became **the fourth special feature**, moreover current SC became leader in a quantity of sunspot groups, that live one day only. The average number of spots in a group, the average size of a single group, as well as the average number of recorded spots and groups are the smallest among all SCs of the Space Age [Otkidychev and Skorbezh, 2013].

Conclusions

The comparison of evolutionary changes of different SCs in the phases of the minimum made it possible to isolate two groups SCs on the rate of the decrease with the characteristic times ($19 \pm 10/-3$) also ($45 \pm 0/-5$) of months (Fig. 2). The first group includes all SCs of epochs of increased SA, all three SC of transition SCs and SC 16 from the first epoch of lowered SA. The second - all the remaining SC of epochs of lowered SA. The times of beginning the following SC, in essence are determined by the height (power) of new SC: more active (high) cycles, as a rule, begin their rise earlier (through 8-15 months).

By August, 2019 the Sun has been without sunspots for 135 days - more than half the time in current year. To find a similar number of blank Suns, we have to go back to 2009 when the Sun was experiencing the deepest solar minimum in a century. Solar minimum has returned, bringing extra cosmic rays, long-lasting coronal holes in the Sun's atmosphere, and strangling pink auroras.

For SCs the epochs of increased solar activity, the duration of cycles is ensured due to protracted the phase of decline to the point of the beginning of the phase of minimum.

For solar cycles of epochs of reduced solar activity, the duration of cycles is ensured due to the prolonging the phase of minimum in the current cycle.

The decline curve of the minimum phase of the SC 24 is carried out within the boundaries of the development of the SCs characteristic of the epoch of lowered SA. This gives reason to believe that the minimum point of the current cycle will take place no earlier than mid-2020 and no later than the beginning of 2021

References

- Ishkov, V.N. (2005), Properties of the current 23rd solar-activity cycle, Solar System Research. 39. (60), 453-461.
- Ishkov V.N., (2017), Space Weather Forecast: Principles of the Construction and Boundaries of the Implementation (Experience of Three Cycles) // Cosmic Res., 2017, Vol. 55, No. 6, pp. 381-388., DOI: 10.1134/S0010952517060053.
- Ishkov, V.N. (2018), Space Weather and Specific Features of the Development of Current Solar Cycle. Geomagnetism and Aeronomy, 58(6), 785-800, DOI: 10.1134/S0016793218060051.
- Ishkov, V.N., Shibaev, I.G. (2006), Solar Activity Cycles: General Characteristics and Modern Forecasting Boundaries, Bulletin of the Russian Academy of Sciences: Physics, 70, (10), 2006 p. 1643-1647, Allerton Press, Inc., ISSN:1062-8738.
- Janssens, (2019), <http://users.telenet.be/j.janssens/SC24web/SC24.html>
- Otkidychev P.A., Skorbezh N.N., (2013) Specific features of solar activity cycle 24 and their correlation with general regularities of cycles 19–23, Proceedings of the Pulkovo Conference "Solar and Solar–Terrestrial Physics-2013", Nagovitsin Yu.A., Ed., St. Petersburg: VVM, 2013, pp. 187–190.
- Shibaev I., Ishkov V. (2012). Investigation of the statistical characteristics of Wolf numbers reliable series: signs of solar cycles likelihood, Proceed. of 7th Scientific Conf. "Space, Ecology, Safety–2011". Sofia. Bulgaria. SRTI-BAS. 297-301. 2012.
- Svalgaard, (2019),. <https://www.leif.org/research/>

Comparison of FI and the MCMESI for the Last Two Solar Cycles

Kilcik A. ¹, Ozguc A. ², Yesilyaprak H. ², Pektas R. ²

¹ Akdeniz University Faculty of Science, Department of Space Science and Technologies,
07058, Antalya, Turkey

² Kandilli Observatory and Earthquake Research Institute, Bogazici University, 34684
Istanbul, Turkey

E-mail: alilikcik@akdeniz.edu.tr

Abstract.

Here, we used H α flare index (FI) data taken from Bogazici University Kandilli Observatory for the time period of January 1996– March 2018 (total 8127 days), which covers Cycle 23 completely and almost whole cycle 24 (2009-2018). This data set compared with the maximum CME speed index (MCMESI) data during the studied time period. Then temporal and periodic variations of hemispheric and whole data were analyzed by using the cross-correlation analysis method, Morlet wavelet, MTM period analysis methods and wavelet coherence analysis. It is found that; i) the temporal variation of northern and southern hemisphere FI data sets show remarkable differences, ii) both northern and southern hemisphere FI data show the same level of correlation ($r = 0.48$) which is lower than the total FI data ($r = 0.58$), with the MCMESI, iii) these hemispheric FI data sets also show some cyclic differences in periodicity analysis.

Introduction

Solar flares are very strong explosions observed on the solar atmosphere. They generally are observed as intense variation in brightness and are observed around the sunspot groups and are classified in two different ways; 1) X-ray solar flares are classified in 5 classes (A, B, C, M, and X) according to their X-ray peak fluxes in the 1 to 8 Å wavelength band. Each of these classes is also subdivided into 10 subclasses, while the X-class is open-ended. 2) Solar flares are also classified in Hydrogen alpha (H α , 6563 Å) according to their brightness and the size of brightening area in 15 different classes such as Sn, 4b, 2f etc. According to flaring area brightness there are three main groups as faint (f), normal (n), and bright (b). And for the size of the flaring area there are also five groups as S, 1, 2, 3, and 4.

To describe the solar activity Kleczek J, (1952) introduced a daily flare index (FI) parameter after the regular H α observations beginning as follows

$$FI = i \times t$$

where i is the flare importance which is a function of a combination of flaring area brightness and size, and t is the duration of flare in minutes. Also the number of observed flares in both X-Ray and H α classifications can be used as a solar activity indicator.

Coronal Mass Ejections (CMEs) are also another intensive solar events observed in the solar corona. Huge amount of plasma and accompanying magnetic field releases from the solar corona during a CME. Some of them are related to solar flares and prominence eruption. Both solar flare and CME frequencies also follow the solar activity cycle and they have strong geoeffectiveness (Dumbovic M, et al., 2015).

Kilcik A, et al., (2011) introduced a new solar and geomagnetic activity index called the Maximum CME Speed Index (MCMESI) which is a measure of the linear speed of the fastest CME observed in a day.

In this study we investigate the temporal and periodic relationship between the MCMESI and hemispheric and full disc FI data sets.

Data and Methods

H α flare index (FI) data are taken from Bogazici University Kandilli Observatory as daily values. The CME data are taken from SOHO/LASCO CME catalog (Gopalswamy, et al. 2009) and the maximum CME speed index are calculated as daily values (Kilcik A, et al., 2011). Then monthly values are produced. H α flare index (FI) data are used for the time period of January 1996–March 2018 (total 8127 days), which covers Cycle 23 completely and almost whole cycle 24 (2009–2018). The temporal variations of hemispheric and full disc FI data sets are compared with the MCMESI data. Cross correlation analyses were applied to hemispheric and full disc FI and the MCMESI data sets. Periodic variations of hemispheric and full disc data were obtained by using the Morlet wavelet (Torrence C and Compo G P, 1998) and MTM (Ghil M et al., 2002) period analysis methods. Coherencies of periodicities are obtained by applying the wavelet coherence analysis method.

Results

We presented the temporal variations (left panel) and cross-correlation analysis results (right panel) in Figure 1. As shown in the left panel of this figure the temporal variation of hemispheric FI data sets show remarkable differences that the northern hemisphere flare index data access to its maximum around the year 2000, while the southern hemisphere FI data access to its maximum around the year 2002 during solar cycle 23. Full disc FI data generally follows the northern hemisphere temporal behavior during the same solar cycle (cycle 23). This result shows that the northern hemisphere was dominant during this cycle. Contrary, the MCMESI data reach to its maximum around 2002 as similar to southern hemisphere FI data. During solar cycle 24 the situation is completely opposite; the MCMESI slightly higher during the first peak of FI at 2012, the southern hemisphere FI is dominant and the hemispheric asymmetry also exists. Again the full disc FI data behave as a combination of hemispheric FI data. When we look at the correlation between FI and the MCMESI data sets we found that both northern and southern hemisphere FI show the same level of correlation ($r=0.48$) without any time delay, while full disc FI data show higher correlation ($r=0.58$) with the MCMESI compared to hemispheric FI data.

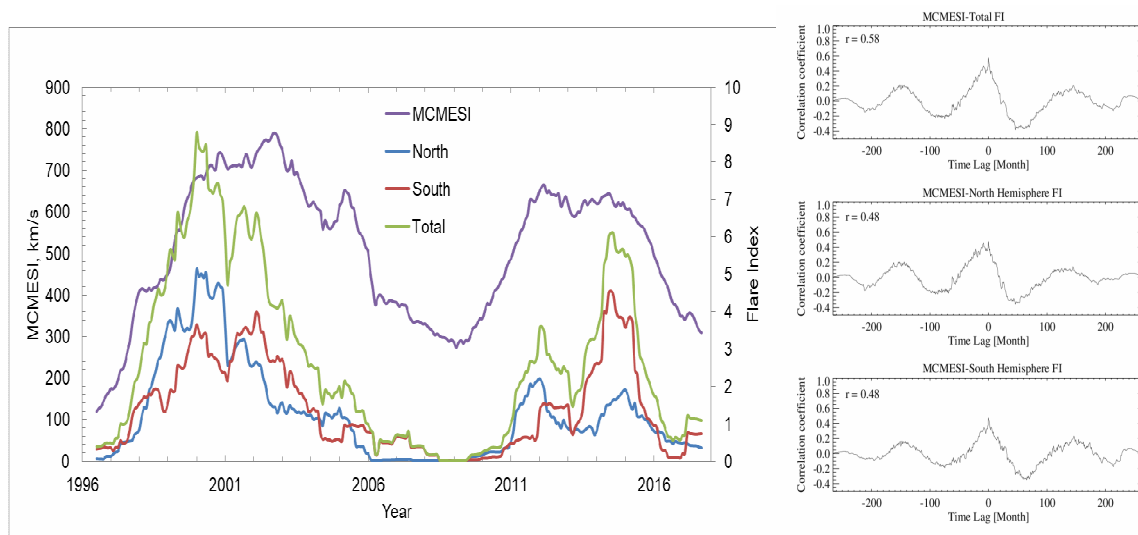


Figure 1. Temporal variations of the hemispheric and total flare index and the MCMESI (left panel) and the cross correlation analysis results for the hemispheric and full disc FI data sets (right panel).

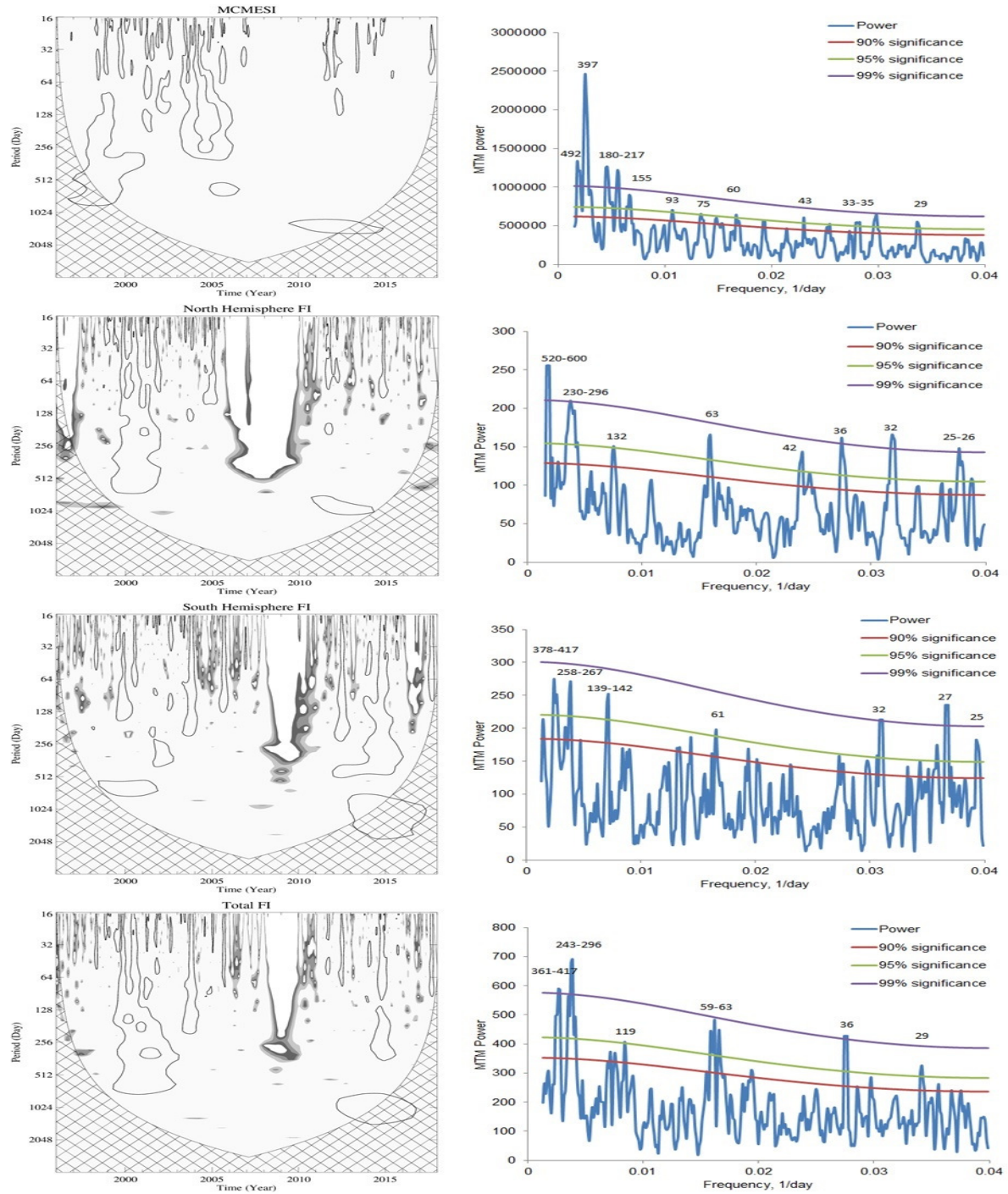


Figure 2. Wavelet (left panel) and MTM (right panel) period analysis results for the MCMESI and FI data sets during the investigated time period (1996-2018).

Figure 2 left panels / right panels show wavelet scalograms / MTM spectra for all data sets used in this study for the investigated time period. From the wavelet power spectrums there are some interesting results i) all periods appear generally during the maximum phases of solar cycles, ii) the MCMESI and the northern hemisphere FI data show similar behavior, while southern hemisphere FI data behave quite differently; during solar cycle 23 the northern hemisphere was dominate, but during solar cycle 24 the situation was opposite, iii) Full disc solar FI data show the combination of northern and southern hemispheres FI data periodic behavior.

In the right panels we presented MTM analysis results that it gives exact periodicities and their significance levels according to the red noise approximation. It is interesting to note that solar rotation periodicity is detected in all cases without any exception. But northern and southern hemispheres solar FI data show some small differences. Note that the periodic behavior of the MCMESI show serious differences from all FI data sets.

As shown in Figure 3 about 11 years periodicity (Schwabe cycle) are in phase in all cases. But the other short term periodicities show some phase differences and these differences also clearly seen in the hemispheric data sets.

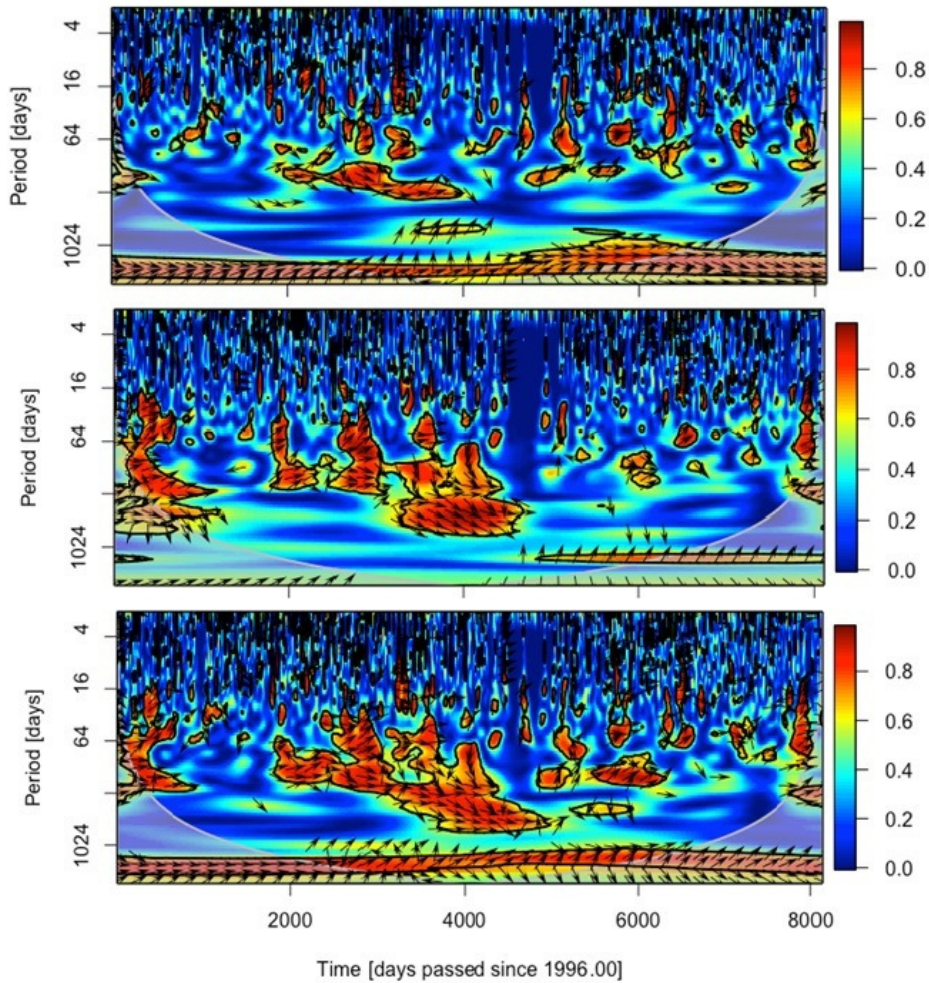


Figure 3. Wavelet coherence of North hemisphere (upper panel), South hemisphere (middle panel) and full disc (lower panel) $H\alpha$ FI versus the MCMESI during the investigated time period (1996-2018).

Conclusions

Here we compared hemispheric and full disc $H\alpha$ solar flare index data with the MCMESI for the last two solar cycles and found the followings;

1. The temporal behavior of northern and southern hemispheres FI data show different variations during the investigated time period.
2. Both northern and southern hemispheres FI data show the same level of correlation ($r = 0.48$) which is lower than the total FI data ($r = 0.58$) with the MCMESI.
3. Hemispheric FI data sets also show some cyclic differences in both wavelet and MTM periodicity analysis.
4. The wavelet coherence analysis also reveals some differences between hemispheric data sets

Acknowledgment

Solar FI data are taken from Bogazici University Kandilli Observatory and the CME data are taken from SOHO/LASCO CME catalog. This study was supported by the Scientific and Technical Council of Turkey by the Project of 115F031.

References

- Dumbovic, M., Devos, A., Vrsnak, B., Sudar, D., Rodriguez, L., Ruzdjak, D., Leer, K., Vennerstrøm, S., and Veronig, A., 2015, *Solar Phys.* 290, 579.
- Ghil, M., Allen, M.R., Dettinger, M.D., Ide, K., Kondrashov, D., Mann, M.E., Robertson, A.W., Saunders, A., Tian, Y., Varadi, F., Yiou, P.: 2002, *Rev. Geophys.* 40, 3.1.
- Gopalswamy, N., Yashiro, S., Michalek, G., Stenborg, G., Vourlidas, A., Freeland, S., & Howard, R. 2009, *Earth Moon Planets*, 104, 295.
- Kilcik, A., Yurchyshyn, V.B., Abramenko, V., Goode, P.R., Gopalswamy, N., Ozguc, A., Rozelot, J.P.: 2011, *Astrophys. J.* 727, 44.
- Kleczeck J., 1952, *Publ. Cent. Inst. Astron*, No. 22, Prague
- Torrence, C., Compo, G.P.: 1998, *Bull. Am. Meteorol. Soc.* 79, 61.

Possible Interactions between Some Solar Activity Indicators for the Last two Cycles

Kilcik A.¹, Sarp V.¹

¹ Akdeniz University, Faculty of Science, Space Science and Technologies Department,
Antalya/Turkey

E-mail: alikilcik@akdeniz.edu.tr

Abstract

In this study we investigated the possible linear and nonlinear interaction between some solar activity indicators which are MCMESI, FI, SSA, SSN, F10.7 and TSI for the time period of 1996-2018. Here, we used Convergent Cross Mapping (CCM) to examine the non-linear relationship and cross-correlation analysis to examine the linear relationship between the MCMESI and all other solar activity indicators. We found that FI, SSN, F10.7 and SSA show symmetrical relationship while the only TSI data show moderate asymmetric relationship with the MCMESI. The highest nonlinear relationship with the MCMESI is obtained for F10.7 data. This relationship is a symmetrical bidirectional coupling; when the library sample size gets smaller CCM score is increasing up to about 50 then it decreasing sharply. As a result, we can get information about the future of both data sets from each other's manifold. From the cross correlation analysis we also found that the F10.7 has the strongest correlation with the MCMESI. Thus, we may argue that this relationship can be used for further dynamical modelling and prediction approaches.

Introduction

It is important to analyze the causal understanding of solar activity cycle indicators to interpret and to predict solar activity variations. Balogh A. et al. (2014) reviewed correlations and causal relations of a selection of solar activity indicators and concluded that important pieces in the puzzle of solar activity variation are still missing. The Maximum CME Speed index (MCMESI) was introduced by Kilcik A. et al. (2011) and found as a strong indicator of geoeffective solar disturbances. Later, Ozguc A. et al. (2012) analyzed its hysteresis effects with typical solar activity indices during Solar Cycle 23.

In this study we focused on the possible non-linear interactions of the MCMESI with Flare Index (FI), Sunspot Area (SSA), Sunspot Number (SSN) version 2.0 (Clette F. and Lefèvre L., 2016) 10.7 cm Solar Radio Flux (F10.7) and Total Solar Irradiance (TSI) during Solar Cycles 23 and 24. Causal relationship between two dynamical variables can be established if they belong to a common dynamical system, which can be reconstructed from time-delay embedding of each observed time series. For this purpose, we applied the method called Convergent Cross Mapping (Sugihara G. et al. 2012) to above mentioned time series so that we can reveal their interactions during the investigated time period.

Data

The CME data are taken from SOHO/LASCO CME catalog and the maximum CME speed index (MCMESI) are calculated as daily values and then the monthly values were produced as introduced by Kilcik A. et al. (2011). The ISSN data are taken from the WDC-SILSO, Royal Observatory of Belgium, Brussels, as a monthly mean values. Here we used the second version ISSN data. H α flare index (FI) data are taken from Bogazici University Kandilli Observatory as daily values. Then, monthly average values were calculated. F10.7 data are downloaded from NASA OMNIWeb system as a daily values and the monthly values were calculated. SSA data are taken from Debrecen Photoheliographic Data (DPD) sunspot catalogue as a daily data, and then the monthly values were calculated. The TSI data are taken

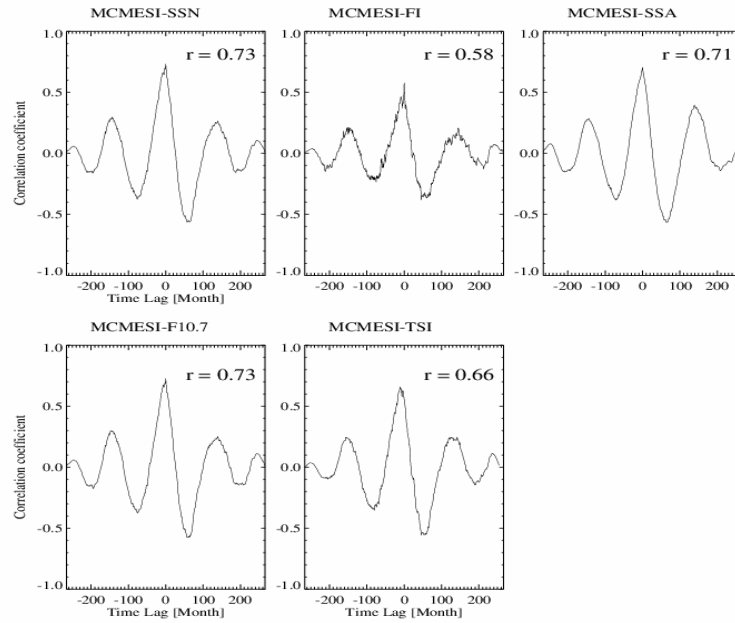


Figure 1 - Cross correlation analysis results between the MCMESI and all other solar indices.

from <ftp://ftp.pmodwrc.ch/pub/data/irradiance/composite> as a daily values and the monthly values were calculated.

Results

In order to investigate the linear relations between the MCMESI and other data sets used in this study, cross correlation analysis were applied. Results of cross-correlation analysis are given in Figure 1.

Optimal value for the embedding dimension and corresponding prediction performances are determined to use in CCM analysis. Simplex projection results for the MCMESI are given in Figure 2. It is also calculated for all other solar indices used in this study by the same method. The determined values are used to cross-map the indices to each other in order to analyze their non-linear interactions. These CCM results are given in Figure 3.

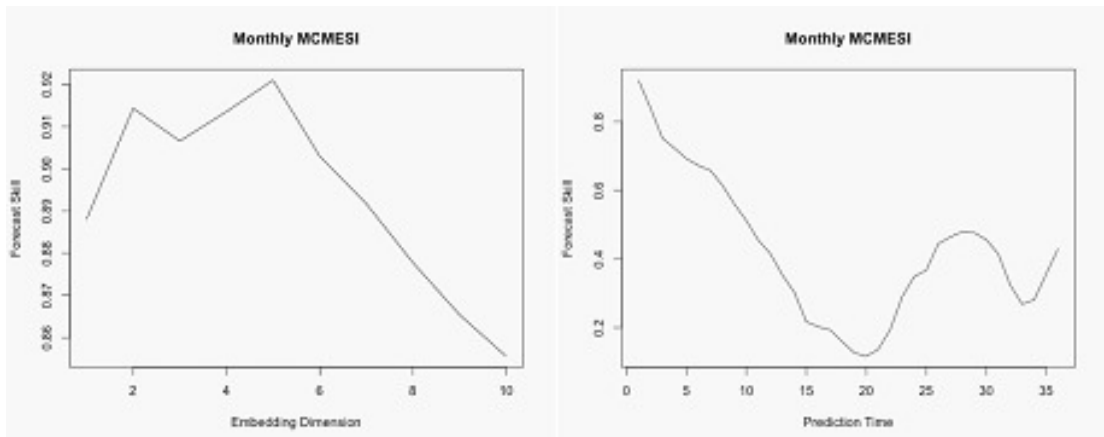


Figure 2- Simplex Projection results of MCMESI to calculate optimal embedding dimension and prediction decay

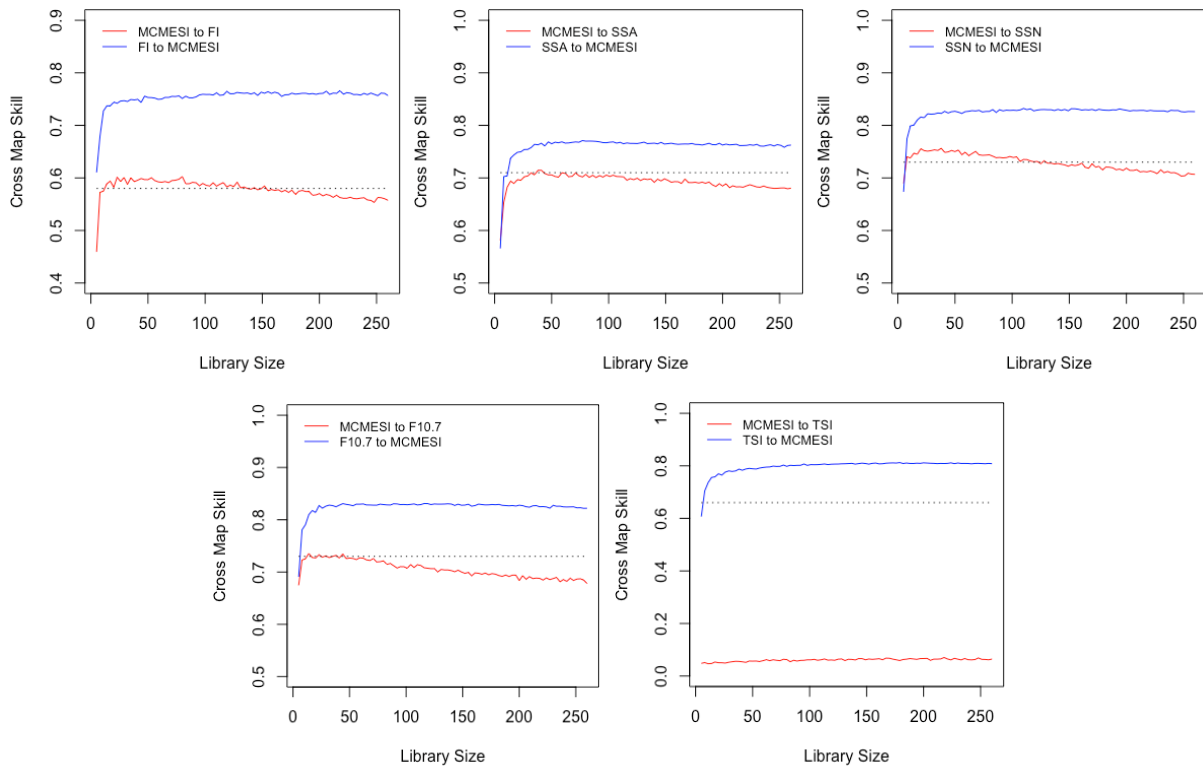


Figure 3 - CCM results for MCMESI cross mapped with other solar indices used in this study

Conclusions

1. The most complicated data are the MCMESI which has the highest embedding dimension ($E = 5$)
2. Forecast skills decrease with increasing time in a short duration. This indicates that all data sets used in this study can be approximated by deterministic chaos rather than stochastic process.
3. CCM results indicate that there are no bidirectional coupling in the long term (more than one cycle). Because one of the CCM curve always under the level of correlation coefficient.
4. In contrast, for the short term there are synchronized relations between two variables.
5. TSI behave differently than other data sets used; it has the weakest coupling with the MCMESI

Acknowledgment

This study was supported by the Scientific Research Projects Coordination Unit of Akdeniz University (Turkey) by the Project of FBG-2019-4914.

References

- Balogh A., Hudson H.S., Petrovay K. and von Steiger R. (2014) Introduction to the Solar Activity Cycle: Overview of Causes and Consequences. *Space Sci Rev.* 186:1–15
- Clette F., and Lefèvre L. (2016) The New Sunspot Number: Assembling All Corrections. *Sol Phys.* 291, pp. 2629-2651
- Kilcik A., Yurchyshyn, V. B., Abramenko, V., Goode, P. R., Gopalswamy, N., Ozguc, A., Rozelot, J. P., (2011) Maximum Coronal Mass Ejection Speed as an Indicator of Solar and Geomagnetic Activities. *ApJ.* 727-1
- Ozguc A., Kilcik A., Rozelot J.P., (2012) Effects of Hysteresis Between Maximum CME Speed Index and Typical Solar Activity Indicators During Cycle 23. *Sol Phys.* 281-2 pp. 839-846
- Sugihara G., May R., Ye H., Hsieh C.H., Deyle E., Fogarty M., Munch S. (2012) Detecting causality in complex ecosystems. *Science* 338, p.496–500
- Sugihara G., and May R.M., (1990) Nonlinear forecasting as a way of distinguishing chaos from measurement error in time series. *Nature.* 344, p.734-741

The Shading Effect on Galactic Cosmic Rays Fluxes and Doses Measured by Liulin-MO Instrument on Near-Mars Orbit

Krastev K.¹, Semkova J.¹, Koleva R.¹, Bankov N.¹, Benghin V.², Drobishev S.²

¹ Space Research and Technologies Institute-BAS, Sofia, Bulgaria

² Institute of Biomedical Problems, RAS, Moscow, Russia

E-mail: krastev.kras@yandex.ru

Abstract.

The paper presents the relation between the galactic cosmic rays fluxes and doses in free space and the measured radiation quantities near Mars. From purely geometric considerations it follows that the measured galactic cosmic ray fluxes close to Mars are strongly dependent on the geometry LIULIN - Mars (the shading effect is 20 - 40 %).

Introduction

In recent years manned interplanetary flights have regained priority. One of the main problems for long duration manned flights is the radiation from the galactic cosmic rays (GCR). The LULIN series instruments are designed to measure cosmic radiation and the radiation risk for the astronauts. FRENDO (Mitrofanov, et al., 2018) dosimetric unit LIULIN - MO (Semkova, et al., 2018) is a part of the ExoMars Trace Gas Orbiter science complex designed to investigate the Martian atmosphere. TGO was inserted into Mars orbit on 19.10.2016. FRENDO was turned on 31.10.2016 ÷ 17.01.2017 in Mars high elliptic orbit (MCO1: 98 000 ÷ 230 km, 4.2 days orbit period). In April 2018, TGO was inserted into its scientific orbit – a near circular orbit at 400 km altitude, 74° inclination and a two hours period. In order to properly estimate doses and fluxes in free space the planet's shading effect and the albedo particles from Mars must be taken into account.

Mars shading effect on GCR flux

Geometry of the problem

Liulin-MO contains two dosimetric telescopes - A&B, and C&D arranged at two perpendicular directions. The geometry and the considerations are one and the same for both telescopes, so we further for simplicity we will present results for only one of them – A&B.

When calculating the effect of shading, we neglect the size of the detector and take into account only its orientation and the distance to Mars. The principal configuration is shown in Figure 1. Let $J(\theta, \varphi)$ denotes the differential flux and F_{sh} - the part of GCR flux shaded by Mars.

Then $F_{sh} = \int_0^{2\pi} \int_0^{\theta_1} J(\theta, \varphi) |\cos \theta'| \sin \theta d\theta d\varphi$, $K_{sh} = \frac{F_{sh}}{2\pi J(\theta, \varphi)}$ where θ' is the angle between the normal to the plane of the detector and the differential flux, $\sin \theta_1 = \frac{\text{Mars radius}}{\text{Distance to Mars}}$, θ_0 is the angle between the normal and the Mars direction and K_{sh} – shading coefficient.

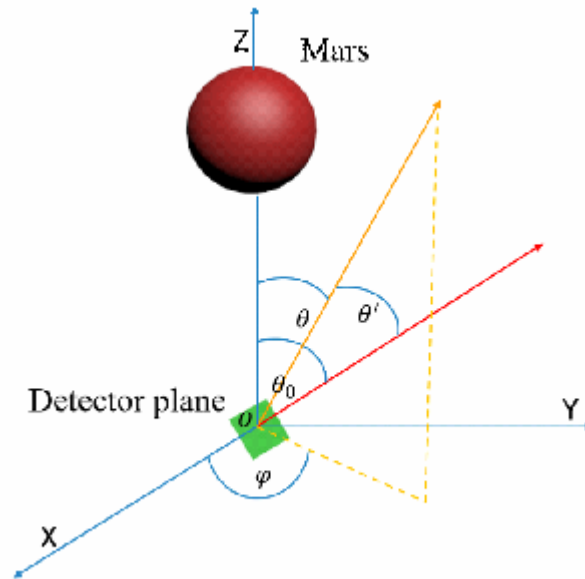


Figure 1. The shading effect for GCR flux. The red line marks the normal to the detector plane, θ' is the angle between the normal and the differential flux.

Distance vs orientation

The dependence of the shading effect on the distance to Mars and the angle between detectors' normal and the nadir to Mars is shown in Figure 2. The data on the high-elliptical orbit are shown on the left. It can be seen that here the main dependence is due to the distance to Mars. Unlike the highly elliptical orbit in scientific orbit the shadow coefficient depends mainly on the orientation.

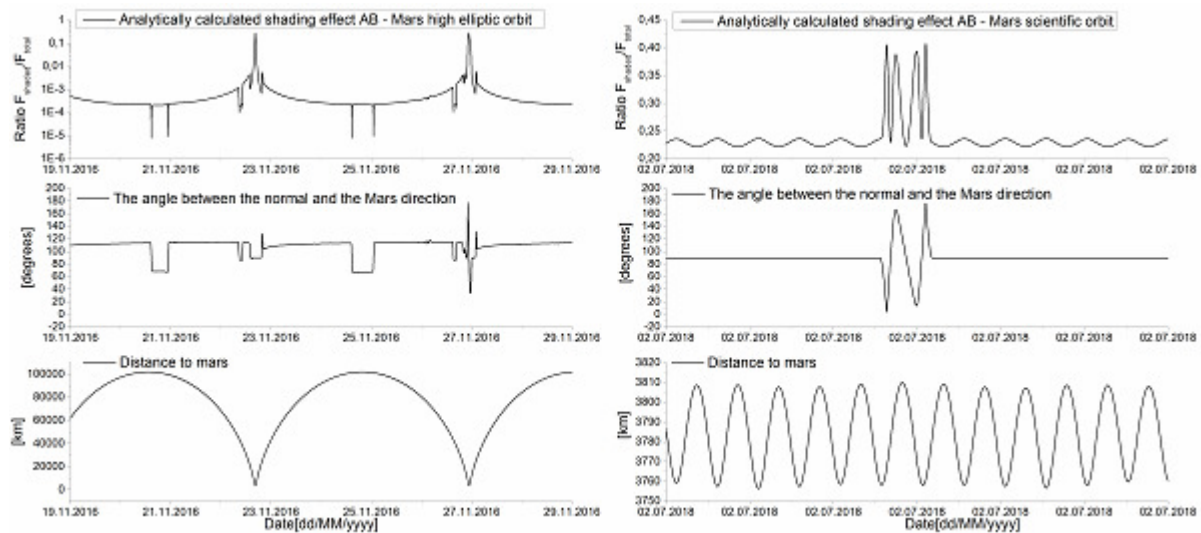


Figure 2. Analytically calculated shading effect for Mars high elliptic orbit – left and Mars scientific (circular) orbit – right.

Comparison with experimental data

The comparison of the experimental flux data with the analytical estimates of the shadow coefficient are shown in Figure 3. The modulation of the flux and consequently the absorbed dose rate is due to the GCR interaction with the solar wind. Mars presence causes the narrow sharp drops of the measured flux (upper panels). These drops coincide with the increases of the shading effect.

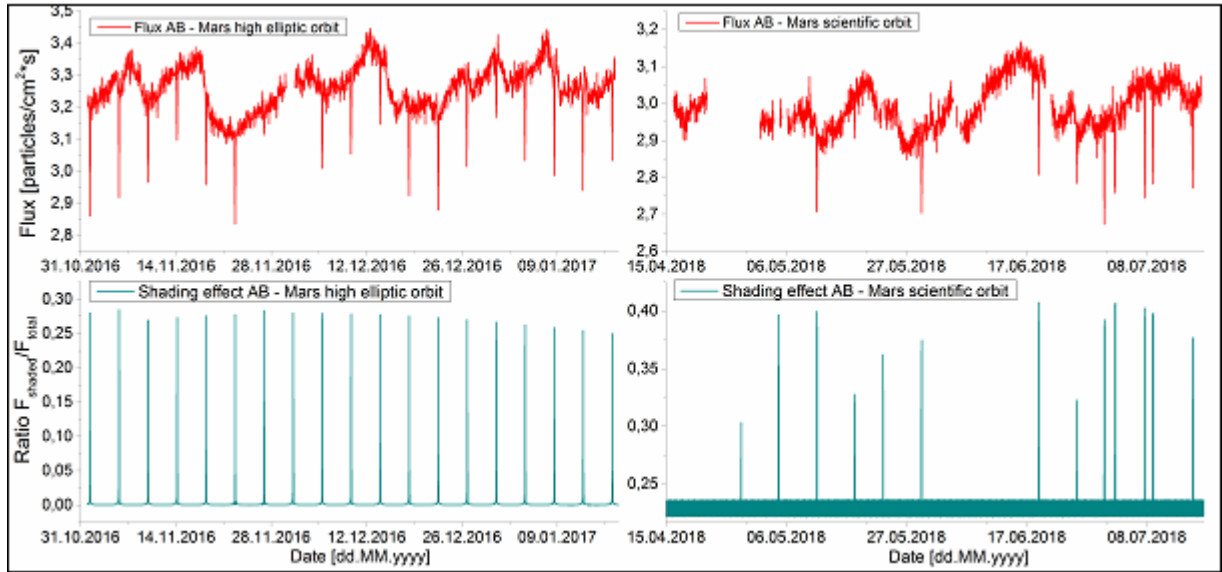


Figure 3. The measured flux (upper panels) compared to the shadow coefficient

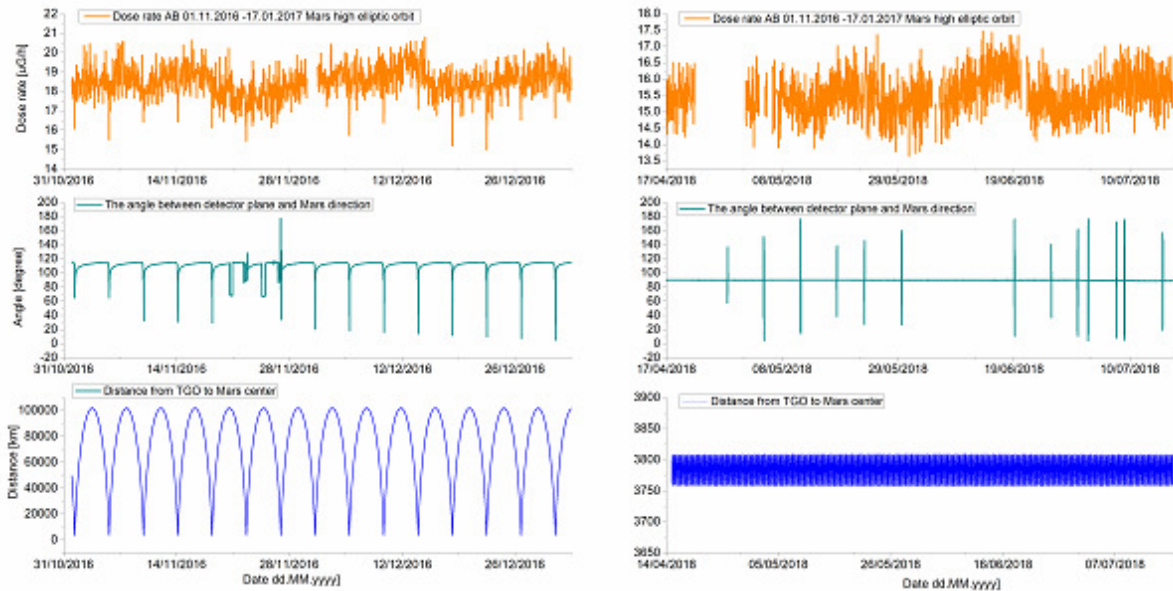


Figure 4. Measured dose rates vs angles and distances

Shading effect on absorbed doses

Figure 4 presents the measured dose rates, the corresponding distance to Mars and the angle between the detectors' normal and the nadir to Mars for the high elliptic orbit (left) and the science circular orbit (right). It can be seen that, as a first approximation, the absorbed dose depends only on the distance. As the planet shades some of the particles hitting the detector at smaller angles, the above peculiarity can be explained by two mutually compensating effects:

1. When the angle between the differential flux GCR and the normal to the plane of the detector increases, then the number of registered particles per unit time decreases.
2. When it falls at a greater angle, the flux passes a large path into the detector and respectively leaves more energy, so contributes for higher dose.

Conclusion

Presented data show a strong dependence of the measured GCR fluxes on the part of the instrument's field of view shadowed by Mars. The dependence on the orientation is valid for all measurements near celestial bodies without magnetic field, performed by detectors with planar geometry. Our estimates show that, depending on the orientation, the shading effect reaches 40 %.

In the first approximation the measured doses depend mainly on the distance to the planet.

References

- Mitrofanov I., A. Malakhov, B. Bakhtin, D. Golovin, A. Kozyrev, M. Litvak, et al. (August 2018 г.). Fine Resolution Epithermal Neutron Detector (FREND) Onboard the ExoMars Trace Gas Orbiter. *Space Science Reviews*, 214(86). doi: 10.1007/s11214-018-0522-5
- Semkova, J., R. Koleva, V. Benghin, T. Dachev, Yu. Matviichuk, B. Tomov, K. Krastev, et al. (2018). Charged particles radiation measurements with Liulin-MO dosimeter of FREND instrument aboard ExoMars Trace Gas Orbiter during the transit and in high elliptic Mars orbit. *Icarus*, 303, 53-66. doi: 10.1016/j.icarus.2017.12.034

Investigation of Sunspot Area Dynamics in Different Categories

Sarp V.¹, Kilcik A.¹

¹ Akdeniz University, Faculty of Science, Space Science and Technologies Department,
Antalya/Turkey

E-mail: volkansarp@akdeniz.edu.tr

Abstract.

In this study, sunspot areas are divided into four empirical categories according to their corrected areas on the solar disk in order to analyze their temporal variations and non-linear dynamics. Complexity parameter (last parameter) of the modified Zurich classification scheme for the last two solar cycles (Solar Cycle 23 and 24) is used as reference to determine the upper and lower bounds for distinct sunspot areas of each empirical group. Simplex Projection and S-Map algorithms are used to determine the embedding dimension and nonlinearity parameter of each category, respectively. Cross-Correlation (CC) and Convergence Cross Mapping (CCM) methods are also applied to determine unidirectional and bidirectional relationships of these classes. Obtained results have shown that smoothing process drastically affects the embedding dimension and nonlinearity of each category. The empirical groups are also found consistent with each other as well as total sunspot number and sunspot area. Thus, we may conclude that the proposed empirical classification can be used for further studies.

Introduction

McIntosh sunspot Classification scheme is formed by three parameters. The first parameter is related to the structure and distribution of penumbra as well as the polarity (unipolar or bipolar) and length of the sunspot group. Second parameter focuses on the largest spot in the group and related to the type and size of its penumbra, and also symmetry of umbra and surrounding penumbra. Final parameter is related to the compactness of the sunspot groups. In other words, combination of this third parameter shows how a sunspot group is distributed on the solar disk (McIntosh P.S., 1990).

There are various studies in the literature that show sunspot related time series display different temporal variations in different groups (Kilcik A. et al., 2011 and references therein). However, there are very good data for the McIntosh Classification and all group information together for the last two solar cycles (Solar Cycle 23 and 24). On the other hand, there exists sunspot photoheliographic data after the year 1872. Therefore, the main motivation of this study is to confirm the possibility of extrapolating classification schemes to the historical measurements by using empirical groups and also investigating possible relationships and/or interactions between the dynamics of these extrapolated groups.

Data

Zurich Classifications and corrected areas for each observed sunspot for the time period between 1996 and 2018 are taken from “NOAA Space Weather Prediction Center”. These data are used as reference values for extrapolating the classification to the historical measurements of corrected sunspot areas observed from 1874 to 2018. Historical measurements are taken from “Revised version of Greenwich Photoheliographic Results (GPR) sunspot catalogue” (1874-1974) and “Debrecen Photoheliographic Data” (1974-2018). The new sunspot number data (Clette and Lefèvre, 2016) are also used to compare the separated time series and analyze their coherency.

Methods

The reference data is separated according to each sunspot’s complexity parameter of the Modified Zurich Classification scheme, namely x, o, i, and c. Therefore 4 empirical groups

are introduced by calculating the mean values of each parameters corrected sunspot are on the solar disk. Upper and lower bounds for empirical groups are determined from the middle values of each consecutive mean area of reference data. These separations can be summarized as in Table 1.

Table 1 – Empirical Classification Scheme

Complexity Parameter	x	i	o	c
Means of reference data [MSH]	51.49	87.24	272.12	561.78
Range for Empirical Classification [MSH]	$69.36 > x \geq 0$	$179.68 > i \geq 69.36$	$416.95 > o \geq 179.68$	$c \geq 416.95$
Empirical Groups	Group 1	Group 2	Group 3	Group 4

In order to determine the embedding dimension parameter of these empirical groups, Simplex Projection (Sugihara and May, 1990) method is used. This method is based on the state space reconstruction of time series data and these reconstructions are assumed to map one-to-one to the original attractor of the comprising dynamic system (Takens, 1981). Thus, we can use prediction skill to identify the optimal embedding dimension.

An approximation of the nonlinearity of these empirical groups is calculated by using S-map (Sugihara, 1994) approach. In addition to the standard parameters of Simplex Projection, S-maps also contain a nonlinearity parameter (θ) that determines the degree to which points are weighted when fitting the model. If θ parameter is equal to zero, the model will be the same for each place in the reconstruction and so it will be identical to an autoregressive model. When values of θ are greater than 0, closer points in the reconstruction will get more weights, and so the local model can vary in state-space to accommodate nonlinear behavior.

A generic property of the reconstructions is that the states of each time series maps one-to-one onto to the states in the original attractor. So, if two variables are dynamically coupled, then local neighborhoods on their reconstructions will map to each other since they are essentially alternative observations of the common original attractor. Thus, we used Convergent Cross Mapping (CCM) method which analyses how well local neighborhoods of two time series correspond to each other (Sugihara et al. 2012) to see the interactions of empirical group

Results

Monthly temporal variations of each empirical group and their comparison with total sunspot number and sunspot area can be seen in Figure 1. It is clear that these empirical groups behave differently especially during the maximum and declining phases of solar activity, although the main peaks are generally determined by the SSA Group 4. Both original versions of these groups and their smoothed versions are tested in the Simplex Projection algorithm (Figure 2). The original time series' embedding dimensions are failed to converge a low dimension, possibly because of their intrinsic noise levels. On the other hand, a small smoothing, 3-month running average, fixed the optimal embedding dimension to 4 for all empirical groups. The same pattern is also revealed in terms of nonlinearity parameter during the S-map analysis.

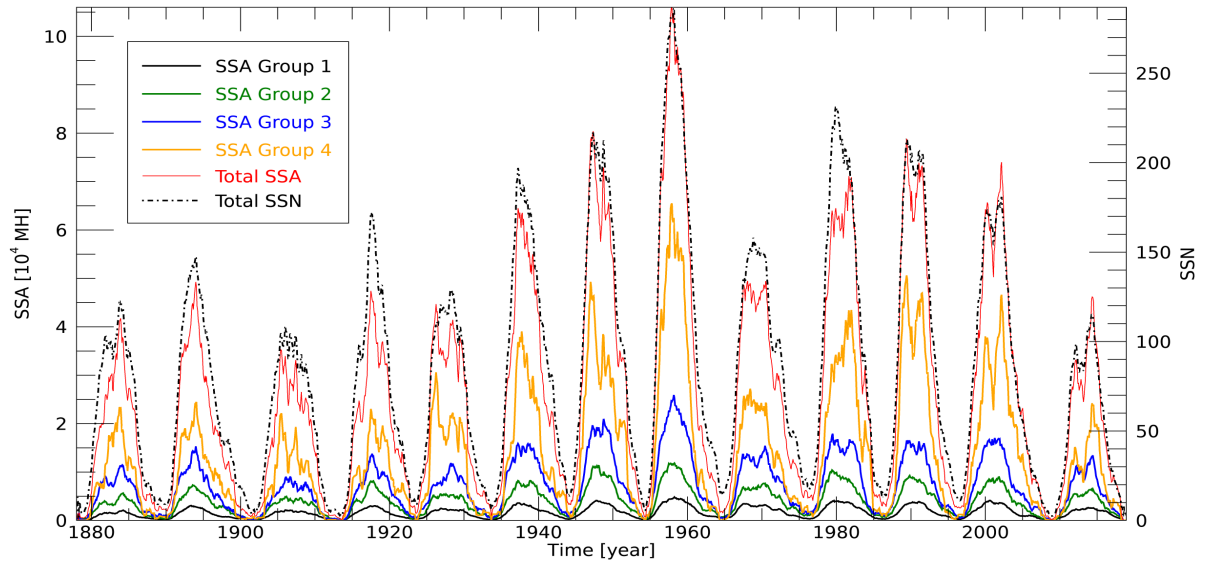


Figure 1 – Monthly temporal variations of 3-month running averaged empirical groups, total sunspot numbers and total sunspot areas.

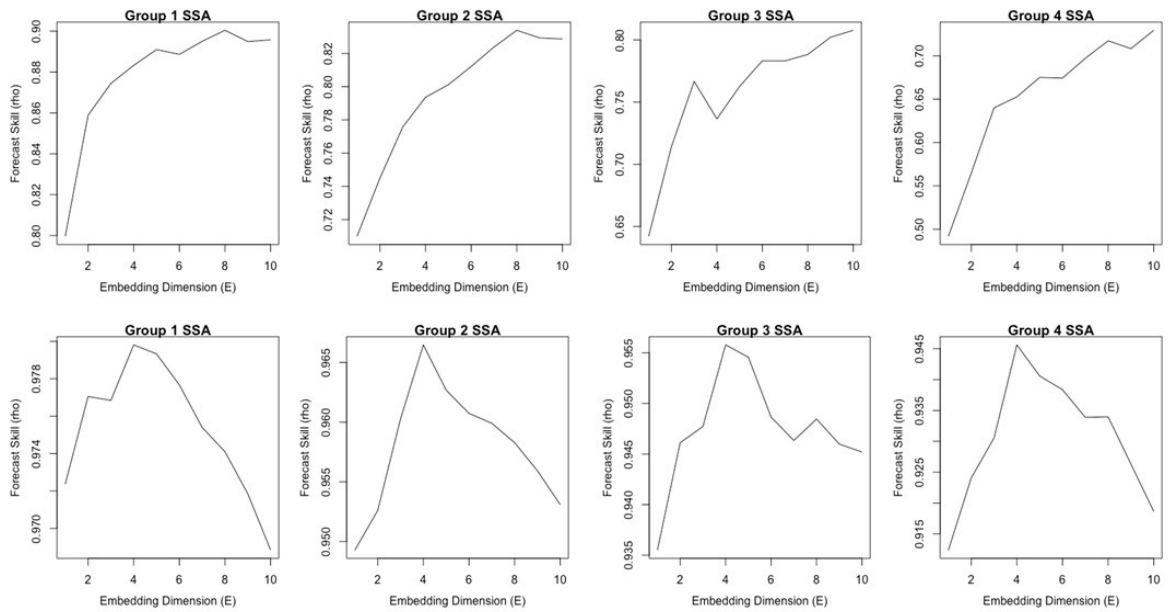


Figure 2 – Forecast skills of each empirical group for varying embedding dimension from 1 to 10. First row represent the original time series while second row represent the smoothed versions of the same time series.

We also calculated the correlation coefficients between the empirical groups and their temporal delays. These results are presented in Table-2. Finally, we analyzed the interaction of these groups with the SSN and SSA time series. The CCM results of this analysis can be seen in in Figure 4.

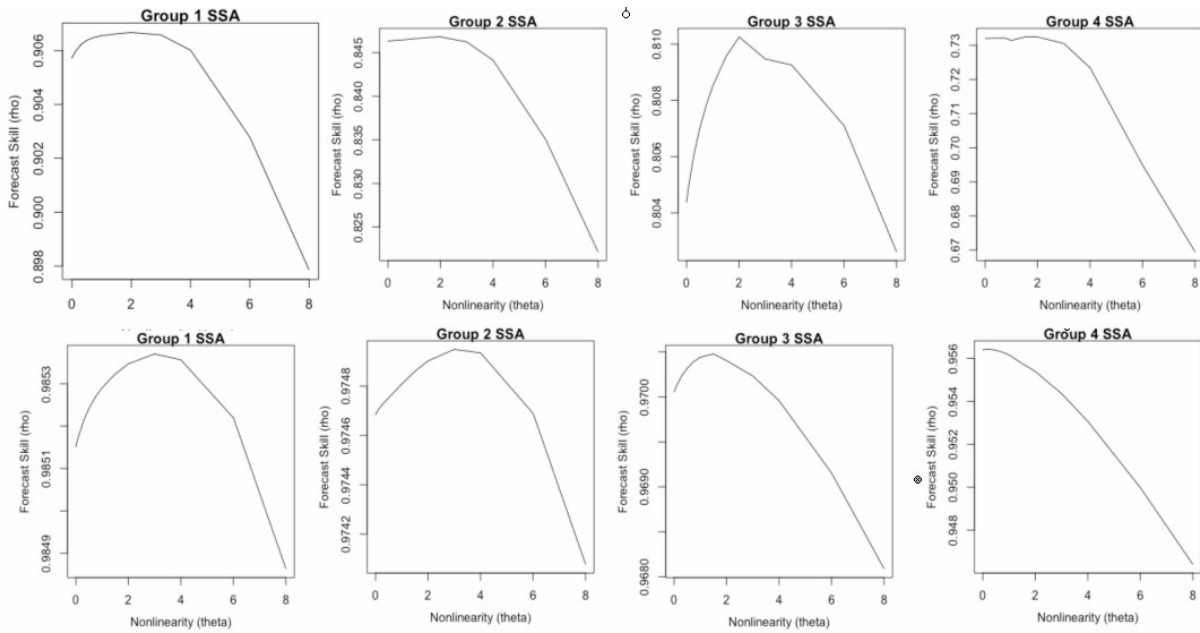


Figure 3 – Forecast skills of each empirical group for varying nonlinearity parameter from 1 to 8. First row represent the original time series while second row represent the smoothed versions of the same time series.

Table 2 – Correlation Coefficients between empirical groups and SSN, SSA time series. The correlation values which marked with bold corresponds to the one month temporal delay.

Group 1	1.00					
Group 2	0.87	1.00				
Group 3	0.81	0.83	1.00			
Group 4	0.71	0.70	0.72	1.00		
Total SSA	0.83	0.82	0.85	0.96	1.00	
Total SSN	0.92	0.91	0.90	0.83	0.95	1.00
	Group 1	Group 2	Group 3	Group 4	Total SSA	Total SSN

Conclusions

1. This empirical classification scheme introduced four consistent sunspot series, that is based on the last parameter of modified Zurich Class and can be used for future studies.
2. All groups have identical embedding dimensions and similar nonlinearity parameters that can be used to reconstruct their state space models.
3. Total SSA has the highest correlation with Group 4, while Total SSN has the lowest correlation and one month temporal delay with this group. Thus we conclude that, there are asymmetrical relationships between these two time series.
4. Each time series used in this study perform a higher CCM score than correlation coefficient values except mapping to Group 4 from Total SSA library. This indicated the uni-directional relation from Group 4 to Total SSA. In other words, Total SSA dynamics are sensitive to the variations in Group 4, but the opposite is not true.

Acknowledgment

This study was supported by the Scientific Research Projects Coordination Unit of Akdeniz University (Turkey) by the Project of FBG-20190-4914.

References

- Clette F., and Lefèvre L. (2016) The New Sunspot Number: Assembling All Corrections. *Sol Phys.* 291, pp. 2629-2651
- Kilcik A., Yurchyshyn V.B., Abramenko V., Goode P.R., Ozguc A., Rozelot J.P. and Cao W. (2011) Time Distributions of Large and Small Sunspot Groups over Four Solar Cycles. *ApJ.* 731-1
- McIntosh P.S. (1990) The Classification of Sunspot Groups. *Solar Physics*, 125, p.251-267.
- Sugihara G., and May R.M., (1990) Nonlinear forecasting as a way of distinguishing chaos from measurement error in time series. *Nature.* 344, p.734-741
- Sugihara G. (1994) Nonlinear forecasting for the classification of natural time series. *Philosophical Transactions of the Royal Society of London. Series A: Physical and Engineering Sciences.* 348-1668
- Sugihara G., May R., Ye H., Hsieh C.H., Deyle E., Fogarty M., Munch S. (2012) Detecting causality in complex ecosystems. *Science* 338, p.496–500
- Takens F. (1981) Detecting Strange Attractors in Turbulence. *Lecture Notes in Math.* Vol. 898, Springer, New York.

On Polarization of Solar Decameter Spikes

*Shevchuk M.*¹, *Melnik V.*¹, *Dorovskyy V.*¹, *Brazhenko A.*², *Frantsuzenko A.*²,
*Konovalenko A.*¹, *Poedts S.*³, *Magdalenic J.*⁴

¹ Institute of Radio Astronomy, Kharkov, Ukraine,

² Institute of Geophysics, Gravimetrical Observatory, Poltava, Ukraine

³ Catholic University of Leuven, Leuven, Belgium

⁴ Royal Observatory of Belgium, Brussels, Belgium

E-mail: mykola.shevchuk@rian.kharkov.ua

Abstract.

In the present paper an analysis of the polarization properties of the solar decameter spikes is performed. We found that decameter spikes can possess both left and right circular polarization which changes from 0 up to 100% with an average value 50%.

Introduction

For more than one decade solar radio spikes attract attention of the researchers in the field of the solar radio astronomy. It is assumed that these bursts have high diagnostic potential for both source of emission generation and surroundings (coronal plasma) in which the emission is generated [Benz A. O., 1986, Melnik V. N., et al., 2014]. Since 60th a great number of papers devoted to spikes in the different wavelength ranges have been published. In those articles the main spectral properties of the spikes and possible models of their generation were described in details. However, such parameter of spikes as polarization remained practically unattended. Nowadays polarization properties of the spikes well enough studied in the meter and decimeter wavelength ranges [Messerotti M., et al., 1985, Benz A. O., et al., 1987, Guedel M., et al., 1991]. Depending on polarization degree solar spikes are divided into three groups: weakly polarized ones (polarization degree less than 20%); intermediately polarized (polarization between 20% and 80%); strongly polarized (polarization higher than 80%) [Messerotti M., et al., 1985]. In most cases spikes with intermediate polarization are observed. In the paper [Guedel M., et al., 1991] it was shown that the degree of spikes polarization depends on location of the active region on the solar disk. Namely, the farer from the meridian is the active region the lower is the degree of polarization of associated spikes. In some cases the sense of spikes polarization and associated with them Type III and IV bursts is the same [Chernov G. P., 1977, Nonino M., et al., 1986] and in other cases the sense of polarization is opposite [Guedel M., et al., 1991].

Until the relatively recent time the question concerning spikes polarization in the decameter wavelength range has not been studied. In the present paper the first results of analysis of spikes polarization in the frequency band 8 - 32 MHz are presented.

Observations

The spikes analyzed in the paper were observed on 14 June 2012 with URAN-2 radio telescope (Ukrainian Radio interferometer of the Academy of Science) in continuous frequency band 8 - 32 MHz with high time - frequency resolution 100 ms and 4 kHz respectively. URAN-2 consists of 512 elements in form of two orthogonal dipoles arranged at an angle 45° to the meridian and has an area of 28,000 m² [Brazhenko A. I., et al., 2005]. Such configuration of the elements gives an opportunity to register simultaneously two linearly or two circularly polarized components of the signal. Registration and identification of spikes on the dynamic spectrum with URAN-2 became possible after equipment of the last with a receiver of new generation DSP-Z (Digital Spectra Polarimeter of Z modification) [Zakharenko V., et al., 2016]. The part of the dynamic spectrum with storm of spikes simultaneously with storm of Type III bursts is presented on Figure 1. This storm lasted

during all day of observations from 04:45 up to 16:00 UT [Shevchuk N. V., et al., 2016]. The dynamic spectrum was recorded with URAN-2 coupled with new receiver DSP-Z.

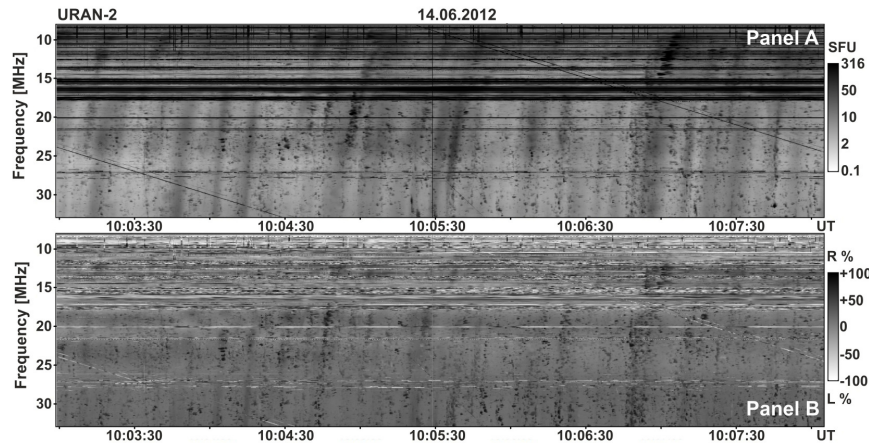


Fig. 1 Storm of spikes bursts simultaneously with storm of Type III bursts recorded on 14 June 2012. Panel A represents power characteristics of the bursts and Panel B shows polarization one.

Spikes are fine structured bursts with duration and bandwidth in the decameter wavelength range about 1s and 60 kHz respectively [Melnik V. N., et al., 2014]. On the Figure 1 spikes are dark spots chaotically located on the dynamic spectrum. Decameter Type III bursts on the dynamic spectrum appear as intense tracks drifting from high towards low frequencies. Duration of these bursts increases with observational frequency decrease. For example, at frequency 16 MHz duration of Type III bursts is about 10s [Melnik V. N., et al., 2018].

Analysis of the observed data

For the analysis of polarization properties of the spikes we chose arbitrary 30 second intervals on the dynamic spectrum where influence of the accompanying bursts (Type IIIb, III, IV bursts) would be minimal. We measured the sense and the degree of polarization for more than 1500 spikes. According to statistical analysis spikes have high degree of circular polarization. On Figure 2 the histogram of spikes distribution on polarization is presented. As can be seen from the presented distribution spikes can have both left and right circular polarization. However, on this particular day the majority of analyzed spikes (approximately 96%) had right circular polarization. At the same time spikes with left circular polarization were not numerous only 4%. Such a numerical advantage on polarization may testify that most probably spikes with left and right circular polarization escaped from different active regions.

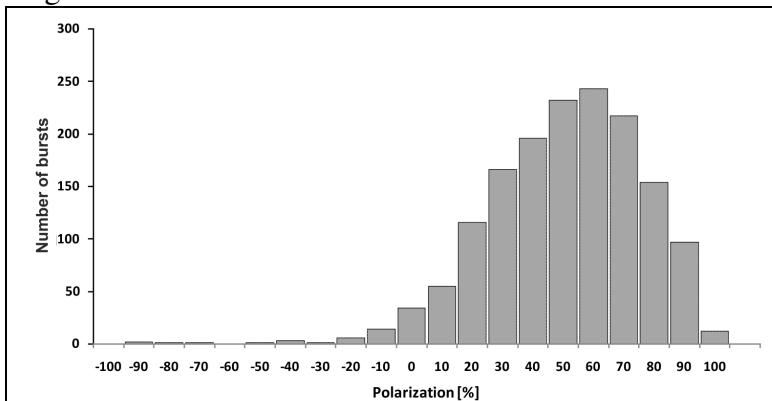


Fig. 2 Histogram of spikes distribution on the polarization.

From the histogram of spikes distribution on the polarization we can conclude that degree of polarization of spikes changes from 0 up to 100% with average value about 50% and 20% for the bursts with right and left polarization respectively. The former value is close to that obtained for the decameter Type IIIb bursts which were observed simultaneously with Type III

bursts and composed so called IIIb-III pairs [Melnik V. N., et al., 2018]. The mean value of Type IIIb bursts polarization is 40% - 60% depending on the time of observations. Also we found that spikes polarization does not depend on observational frequency and changes within interval 40% - 70%. It must be noted that as in the case of Type IIIb bursts in the majority of the cases (70%) the maximums of spikes polarization precede the maximums of emission fluxes (Figure 3). On the Figure 4 the histogram of distribution of time shifts between flux and polarization maxima is presented. The positive and negative values correspond to delay (in average 0.14s) and advance (about 0.25s) of flux maxima with respect to polarization maxima correspondingly.

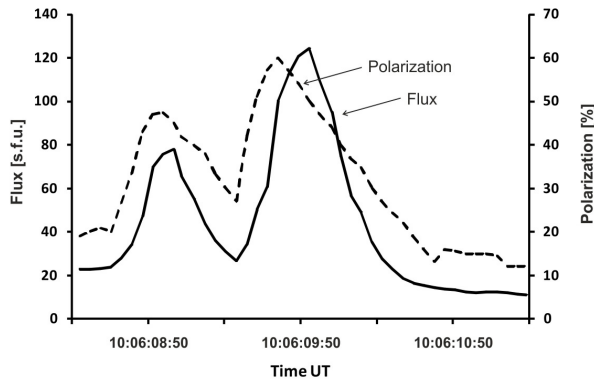


Fig. 3 Power and polarization profiles of the spikes.

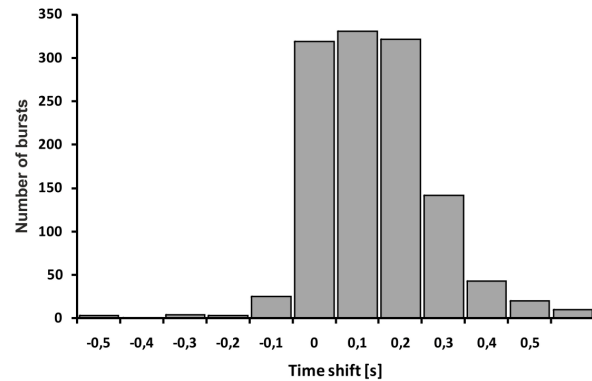


Fig. 4 Histogram of distribution of time shifts between flux and polarization maxima

Leading spot rule

Polarization properties of the spikes can be used to determine or refine their generation mechanism. Apparently from the polarization observations we can judge about preferred mode of emitted wave (ordinary or extraordinary). The "leading spot rule" is often used to determine the wave mode [Benz A. O., et al., 1987, Guedel M., et al., 1991]. In the frames of this rule it is assumed that flare happens above leading spot of the active region which in the majority of the cases dominate the trailing one. Thus the magnetic polarity of the leading spot determines direction of magnetic field of the emission source. Comparing measured degree of circular polarization of the bursts and direction of the magnetic field in the leading spot the mode of the wave can be determined. For example, if the emission has left (right) circular polarization and the magnetic field in the leading spot is directed toward the observer North (from observer South) then the leading spot rule suggests o-mode emission. In our case the majority of spikes (96%) had right circular polarization (see Figure 2). At the same time according to data from SDO satellite (Solar Dynamic Observatory) magnetic fields of the leading spots of the active regions NOAA 11504-11505 and NOAA 11507-11508 with which we associate the enhanced activity in the radio band were directed toward the observer North (Figure 5). Comparing spikes polarization and direction of the magnetic field we can conclude that most probably mode of the emitted wave corresponded to x-mode.

However, Type III bursts observed on this day had right circular polarization (see Figure 1). According to [Guedel M., et al., 1991, Chernov G. P., 1977] the emission of the Type III bursts corresponds to o-mode. To satisfy this statement the Type III bursts should be associated with active region NOAA 11506, where the magnetic field in the leading spot was pointed from observer South (Figure 5). Since Type III bursts and spikes observed on this day have the same sense of circular polarization we may conclude that both types of bursts are emitted on o-mode and can be associated with the same AR NOAA 11506.

Conclusion

In the present article for the first time the analysis of the observational polarization properties of the decameter spikes was performed. It was shown that decameter spikes can have both left and right circular polarization. The degree of their polarization can vary from 0 up to 100% that observed in the case of high frequency spikes as well.

The sense and degree of polarization of decameter spikes agree well with those obtained for the decameter Type IIIb bursts. This fact can be additional evidence that spikes and striae, which form Type IIIb bursts, are the same type of the solar radio bursts [Shevchuk M. V., et al., 2018].

Question concerning usage of the polarization of spikes for determination or confirmation of the possible model of their generation on this stage of our research remains open and needs further study.

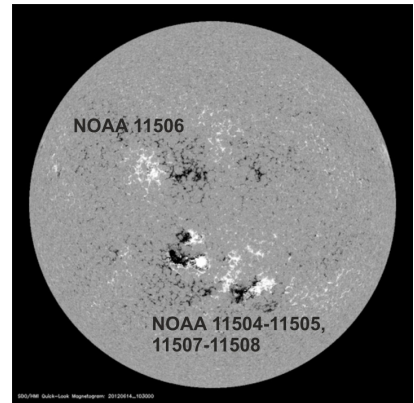


Fig. 5 Magnetogram obtained with SDO satellite showing map of magnetic fields on the solar disk (black spots show direction of the magnetic field from observer and white toward observer). Taken from: <https://www.nasa.gov/content/goddard/sdohmi-magnetogram/>.

Acknowledgements

The work was partially fulfilled in the framework of FP7 project SOLSPANET (FP7-PEOPLE-2010-IRSES-269299) and by project DBOF-12-0261 of the KU Leuven.

References

- Benz A. O. (1986). Millisecond radio spikes, *Solar Physics*, 104, pp. 99–110, doi:10.1007/BF00159950.
- Melnik V. N., N. V. Shevchuk, A. A. Konovalenko, H. O. Rucker, V. V. Dorovskyy, S. Poedts, A. Lecacheux (2014). Solar decameter spikes, *Solar Physics*, 289, pp. 1701 – 1714, doi:10.1007/s11207-013-0434-1.
- Messerotti M., M. Nonino, P. Zlobec (1985). Polarization and brightness temperature of 'spike' bursts related to metric Type IV solar radio events, *Società Astronomica Italiana, Memorie* (ISSN 0037-8720), 56, pp. 795 – 799.
- Benz A. O., M. Guedel (1987). Harmonic emission and polarization of millisecond radio spikes, *Solar Physics*, 111, pp. 175 – 180, doi:10.1007/BF00145450.
- Guedel M., P. Zlobec (1991). Polarization and emission mode of solar radio spikes, *Astronomy and Astrophysics*, 245, pp. 299 – 309.
- Chernov G. P. (1977). Morphological characteristics of solar radio bursts of the 'spike' type, *Soviet Astronomy*, 21, pp. 612 – 625.
- Nonino M., A. Abrami, M. Comari, M. Messerotti, P. Zlobec (1986). The characteristics of type IV associated spikes at metric wavelengths, *Solar Physics*, 104, pp. 111 – 116, doi:10.1007/BF00159951.
- Brazhenko A. I., V. G. Bulatsen, R. V. Vashchishin, A. V. Frantsuzenko, A. A. Konovalenko, I. S. Falkovich, E. P. Abranin, O. M. Ulyanov, V. V. Zakharenko, A. Lecacheux, H. Rucker (2005). New decameter radiopolarimeter URAN-2, *Kinematika i Fizika Nebesnykh Tel*, 5, pp. 43 – 46.
- Zakharenko V., A. Konovalenko, P. Zarka et al. (2016). Digital Receivers for Low-Frequency Radio Telescopes UTR-2, URAN, GURT, *Journal of Astronomical Instrumentation*, 5, p. 738, doi:10.1142/S2251171716410105.
- Shevchuk N. V., V. N. Melnik, S. Poedts, V. V. Dorovskyy, J. Magdalenic, A. A. Konovalenko, A. I. Brazhenko, C. Briand, A. V. Frantsuzenko, H. O. Rucker, P. Zarka (2016). The Storm of Decameter Spikes During the Event of 14 June 2012, *Solar Physics*, 291, pp. 211 – 228, doi:10.1007/s11207-015-0799-4.
- Melnik V. N., A. I. Brazhenko, A. V. Frantsuzenko, V. V. Dorovskyy, H. O. Rucker (2018). Properties of Decameter IIIb-III Pairs, *Solar Physics*, 293, pp. 26, doi:10.1007/s11207-017-1234-9.
- Shevchuk M. V., V. N. Melnik, S. Poedts, V. V. Dorovskyy, J. Magdalenic, A. A. Konovalenko (2018). On the Observational Properties of the Decameter Striae, 2nd URSI Atlantic Radio Science Meeting (AT-RASC), 28 May - 1 June, Gran Canaria, Spain, doi:10.23919/URSI-AT-RASC.2018.8471315

Solar X-ray Variability in two Distinct States and Its Real-Time Analysis Based on a Fractionally Time-Series Model With a Heteroskedastic Component

Stanislavsky A.A.¹, Burnecki K.², Janczura J.², Niczyj K.², Weron A.²

¹ Institute of Radio Astronomy NANU, Kharkiv, Ukraine

² Hugo Steinhaus Center, Wrocław University of Science and Technology,
Wrocław, Poland

E-mail: astex@ukr.net

Abstract.

Soft X-ray emission observed at the current solar cycle in the period July-September, 2017 is analyzed. We have found two different states of the solar activity using a Hidden Markov Model, and we show that in the periods of high solar activity the energy distribution of soft X-ray solar flares is well described by an ARFIMA-GARCH model. Although it is assumed that higher solar activity can contain more states, in the period under study (close to the quiet Sun) this approach allows us to describe both the two states of the solar activity and the emission dynamics within a single state.

Introduction

A pronounced feature of the solar activity is its irregularity, visible in daily changes of the space weather [Usoskin I.G., 2013]. The space weather disturbances are caused mainly by the Sun, through the different types of solar activities. Solar flares and Coronal Mass Ejections (CMEs) are clear indicators of active processes at the Sun among the most energetic and spectacular solar activity events. They are two types of solar eruptions that can spew vast quantities of radiation, solar energy particles and magnetized plasmas into space.

The Sun is a strong X-ray emitter because the solar atmosphere (solar corona) is much hotter than the solar surface and so is a source of thermal (soft) X-rays. Observations of solar flare phenomena in X-rays are held from the 1960s with the space-borne instrumentation. Since 1974 the broadband X-ray emission of the Sun has been recorded almost continuously by the meteorology satellites operated by NOAA first with the Synchronous Meteorological Satellite (SMS) and then with the Geostationary Operational Environment Satellite (GOES) [Garcia H.A., 1994]. The solar X-ray flares data are widely available from the NOAA Space Environment Center site. Therefore, studying the long-term solar variability and predicting the solar activity is an actual problem in solar physics. Two bands of X-rays (1-8 Å, 0.5-4 Å) are measured by GOES, soft and hard. We concentrate on the soft X-ray emission. It is particularly sensitive to high-temperature plasma and is thus an important diagnostic of the coronal temperature distribution.

Recently, autoregressive fractionally integrated moving average (ARFIMA)-type modeling was advertised to address problems in the burgeoning field of time domain astronomy [Feigelson E.D., et.al., 2018]. In particular, the ARFIMA process was considered as a candidate for extensive statistical studies of the soft X-ray solar emission [Stanislavsky A., et.al., 2009]. The ARFIMA model is a discrete-time analog of the fractional Langevin equation that takes into account the non-Gaussian statistics and the long-range dependence (long-term memory), i.e., the events are arbitrarily distant still influence each other exceptionally strong [Magdziarz M., et.al., 2007; Burnecki K., et.al., 2008]. Note that the long memory property represented by ARFIMA processes can be combined with variance changing in time. Bollerslev [Bollerslev T., 1986] generalized the autoregressive conditional heteroskedastic model, named ARCH, proposed in the seminal Nobel Prize winning paper by Engle [Engle R.F., 1982]. The generalized autoregressive conditional heteroskedasticity

(GARCH) process takes into account heteroskedastic effects typically observed in form of clustering of volatilities. Baillie et al. [Baillie R., et.al., 1996] introduced ARFIMA driven by GARCH noise, namely ARFIMA-GARCH processes.

The aim of this paper is to present a proper statistical procedure for analyzing and modeling soft X-ray solar emission activity in the period of the current solar minimum, during July-September of 2017. The analysis of the data reveals two state dynamic of the solar emission. Within the two states the statistical parameters are nearly constant. To account for these findings we introduce a combination of the Hidden Markov Model (HMM) and ARFIMA approaches, which allows us to describe both the two states of the solar activity and the emission dynamic within a single state.

Analysis of X-ray solar flux data

The solar X-ray flux arises from two origins. Firstly, there is flux coming from sunspot regions and other features – the background flux – and it varies slowly from day to day. Secondly, solar flares produce large amounts of X-ray flux, but their duration are usually from minutes to several hours. Our approach was tested using a relatively short, but interesting, interval of soft X-ray data to pinpoint its features. In July, August and September of 2017 the Sun was approaching the minimum of its next 11-year cycle. Despite the fact that a major X-class solar flare erupted peaking as X9.3 at 12:02 UTC on September 6, 2017. Surprisingly, it was the strongest solar flare of the current solar cycle (Cycle 24).

Unfortunately, the solar X-ray data contain gaps (missing data), due to 35 minutes of eclipse per orbit; four transits through the radiation belts per orbit and irregular, short periods of primary payload observation and others. In order to reduce the effect of gaps, we used the data obtained from two satellites (GOES-13 and GOES-15), and for the August data from three satellites (also GOES-14, see <ftp://ftp.swpc.noaa.gov/pub/warehouse>). All the satellites gave very similar data (correlated and close values, see Figure 1). Our strategy in the data preparation was the following. If there are no gaps, we carry out averaging over two (or even three in August) satellite data. For gaps in one of the time series we have taken the best without gaps. As a result, we have three time intervals, namely July, August and September, 2017 with 1-minute steps, which were studied by statistical methods. This leads to a big data set including 132 480 equal sized bins.

Although the time series of solar X-ray data looks like random, it violates the assumption of “independence” in random variables. This is the case when autoregressive modeling can be effective. ARFIMA(p, d, q) seems to be a time series model well-adapted for extensive statistical studies of the soft X-ray solar emission. On the one hand, it quantifies the dependence of current values on recent past values via the parameter p describing how many lags to model. Second, a moving average process accounts for the dependence of current values on recent past random shocks to the system, and the parameter q determines the number of the past noise values. In order to estimate ARFIMA parameters, we follow the procedure described in [Burnecki K., et.al., 2013]. The third parameter d characterizes memory effects caused by the Sun’s magnetic field. The memory of the solar cycle plays an important role in predictions because it determines how much of the past history of solar activity determines its future output. This explains “modulation” of the soft X-ray radiation. When the Sun’s magnetic field gets really twisted, there are lots of sunspots. There are lots of solar storms then. After a while, the Sun’s “messy” magnetic field resets itself into a smoother, more orderly arrangement. Most sunspots go away. The cycle starts all over again. This is a source of long memory. But there are effects making memory shorter: turbulent pumping [Karak B.B., et.al., 2012], random variations in meridional flow amplitude [Hathaway D.H., et.al., 2014], the gravitational action of planets on the solar dynamo [Stefani F., et.al., 2016]. Probably there are others that we do not know yet. Using an ARFIMA model

estimation directly to the entire time series is problematic, as the parameters d , p and q are changing. The result is unstable. Nevertheless, if we take a rolling window of 512 data points and scan the entire segment from beginning to the end, observing how the parameters change, then the parameter estimate becomes a successful procedure. For this purpose we use the methods described in [Kokoszka P.S., et.al., 1996]. Sometimes the algorithm does not converge (exitflag = 0). This can serve as a criterion for model parameters selection. From this point of view the best model is $(2,d,0)$, as it yields no problems with convergence. Moreover, in many cases the values Φ and Θ became too large, except for the case $(1,d,0)$. This means that the solar X-ray data are non-stationary time series, but the short intervals (about 500-1000 minutes) may be similar to a stationary type. The ARFIMA process can be useful, as a fitting model, but it has a piecewise character which should be taken into account.

The resulting time evolution of the obtained ARFIMA parameters is plotted in Figure 2. We can see that the memory parameter d changes in time and has lower values when the X-ray flux is relatively low and higher variance in the opposite situation. In order to investigate heaviness of tails, following [Stanislavsky A., et.al., 2009], we assume that the ARFIMA noise distribution belongs to the domain of attraction of α -stable Lévy law for $0 < \alpha \leq 2$. An evolution of the stability index for the three considered here months is also depicted in Figure 2. We can observe that the α values close to 2 correspond to the low X-ray flux and lower d , whereas α being lower (heavier-tailed case) coincides with high X-ray flux and higher d .

Hidden Markov Model applied to the data

The results of fitting ARFIMA to solar data indicate that ARFIMA model can describe the data well but only if we divide the sample into shorter periods. On the other hand, if one looks at the parameter evolution plots (see Figure 2), it can be observed that the parameters are stable during some periods of time and then change its behavior. Further, those changes are related to changes in the data character, i.e. we observe different parameters for low values of solar activity and different for solar flares (high values of X-ray flux). Hence, it seems to be natural to consider two types of dynamics (states or regimes) of solar X-ray data. A good starting point for a description of such dynamics is a class of regime switching (RS) models. In the RS models one assumes that there exists some (external or/and internal) stochastic process, which governs the switching mechanism between different states (regimes) of the observed data. A prominent examples of this class are the Hidden Markov Models (HMM), sometimes called Markov regime switching models (MRS) (see [Cappe O., et.al., 2005; Rabiner L.R., 1989] for reviews on HMM usage in pattern recognition or [Meyer L., et.al., 2014] for an application of HMM in astrophysics).

Here we apply a 2-state HMM Model with Gaussian distribution having different parameters in different states. In order to stabilize the variance of the estimation results, we apply the model to the logarithm of the analyzed data. As a by-product of the estimation procedure we obtain inferences on state process values S_t , i.e. probabilities $P(S_t = i)$. Based on this values we can classify the X-ray flux data into two different states, namely we put $S_t = i$ if $P(S_t = i) > 0.5$. The identification results are plotted in Figure 3. As can be observed the obtained classification corresponds to the time evolution of the parameter changes plotted in Figure 2, namely we observe lower values of d and values of α close to 2 for State 1 (background dominated) while for State 2 (flare dominated) there are higher values of d and lower values of α . In the background state of our system the noise is close to Gaussian, and the model in its parameters changes slowly. In another state the solar flares result from the rapid release of energy in the solar corona, probably initiated by magnetic reconnection. This release of energy leads to the acceleration of particles, which in turn leads to the formation of high temperature plasma that emits strongly in the soft X-ray wavelength region. The X-ray

emitting plasma becomes exciting and non-equilibrium. This just explains why the parameters of the model change quite quickly and the noise becomes heavy-tailed. Switching from one state to another occurs due to explosive phenomena (solar flares, CMEs and so on).

Fitting ARFIMA-GARCH to selected two states

Having identified two states of the solar activity we now analyze them separately. Since the X-ray emission clearly exhibits a long-range dependence often possibly heavy-tails we choose ARFIMA model as a basic model. We perform the ARFIMA identification and validation procedure in the ITSM package [Brockwell P., et al., 1996] which allows a user-friendly and detail diagnostic of the fitted model. We perform the fitting procedure separately for identified parts of the data in State 1, which is background dominated (a light-tailed case), and identified parts in State 2, which is flare dominated (a heavy-tailed case). It appears that for the whole fragments of the data in State 1 or 2 a single ARFIMA model often cannot be properly fitted. With intervals 500-2000 points (minutes) the Windows-based computer package ITSM works more successfully. This is not a surprise as our analysis of the X-ray solar flux data revealed that the parameters of the process change in time. This suggests that the whole fragments in State 1 or 2 can be described by a piecewise ARFIMA process. We also found that in State 2 well-fitted parts are usually shorter, not more than 1000 observations (minutes). This also coincides with the foresaid analysis shown a more non-stationary behavior in State 2. Furthermore, the ARFIMA model residual diagnostics quite often suggest a bad fit of the model in terms of the independence of the squared values. This clearly suggests that there is a need for allowing the variance change stochastically in time. A natural extension of the ARFIMA process that allows for the (conditional) variance fluctuating in time is the ARFIMA-GARCH process. The GARCH process can explain a slowly changing X-ray background solar emission well.

To sum up, for the first trajectory the ARFIMA model seems quite appropriate but for other trajectories ARFIMA-GARCH is much better than the simple ARFIMA and in general is very well-fitted which clearly indicates a stochastic heteroscedastic pattern.

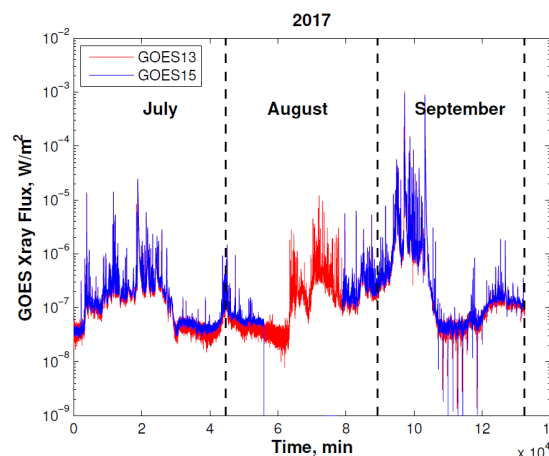


Fig. 1 Data obtained from two satellites, GOES-13 and GOES-15, in July, August and September 2017 (following <ftp://ftp.swpc.noaa.gov/pub/warehouse>)

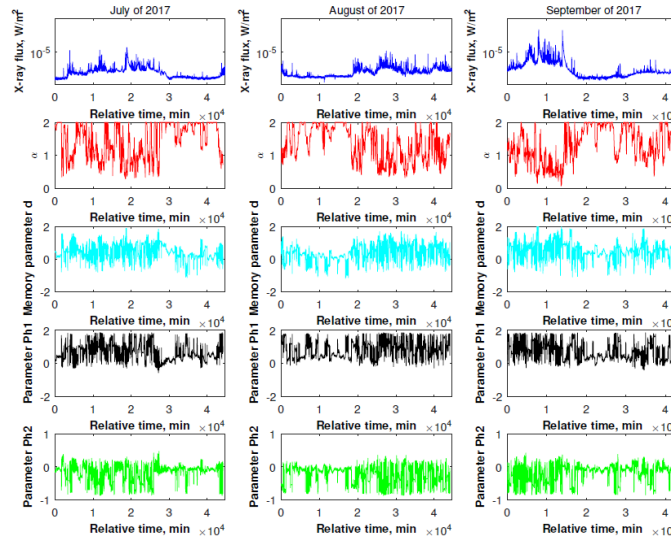


Fig. 2 Evolution of ARFIMA parameters and index obtained in July, August and September 2017

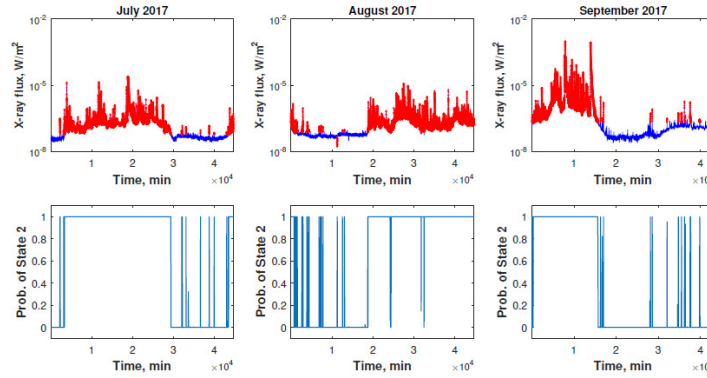


Fig. 3 Results of a 2-state HMM identification in July, August and September of 2017. The points classified to State 2 (i.e. with $P(S_t = 2) > 0.5$) are denoted by red dots. The values of the probabilities $P(S_t = 2)$ are plotted in the corresponding lower panels.

Conclusions

The main results obtained in this study can be summarized in following points:

1. On the base of the GOES satellite instrumental data for the solar soft X-ray emission during July-September of 2017, we have detected several important effects in our empirical studies. Soft X-ray emission demonstrates a long-term dependence, variance changing in time, and heavy-tailed distributions.
2. Evidence for the existence of regime (state) switching behavior was found. The observed flux densities exhibit two states: background dominated and flares dominated.
3. The piecewise ARFIMA and ARFIMA-GARCH models were built separately for both states. In the models the solar X-ray data are considered as a non-stationary time series, whereas the short intervals may be stationary, but their duration is random.
4. Our findings were confirmed by rigorous ARFIMA and ARFIMA-GARCH residual diagnostics which shown that for most of the case a plain ARFIMA model is not enough.
5. In the framework of ARFIMA and ARFIMA-GARCH models the evolution of their parameters is connected with changes of solar activity (in X-ray emission). The correlations are very noticeable.
6. The introduced framework allows one to calculate forecasts along with prediction intervals which may be helpful in predicting potentially catastrophic events.

Acknowledgment

A.S. and A.W. would like to acknowledge a support of Beethoven Grant No. DFG-NCN 2016/23/G/ST1/04083. K.B. and K.N. were supported by NCN Maestro Grant No. 2012/06/A/ST1/00258. We also want to thank the GOES team for developing and operating the instrument as well as for their open data policy.

References

- Baillie R., Ch.-F. Chung, M.A. Tieslau (1996). Analysing inflation by the fractionally integrated ARFIMA-GARCH model. *J. Appl. Econometrics*, 11, 23–40.
- Beran J., Y. Feng, S. Ghosh, R. Kulik (2013). *Long-Memory Processes. Probabilistic Properties and Statistical Methods* (Springer-Verlag, Berlin).
- Bollerslev T. (1986). Generalized autoregressive conditional heteroskedasticity. *J. Econometrics*, 31, 307–327.
- Brockwell P., R. Davis (1996). *Introduction to Time Series and Forecasting* (Springer-Verlag, New York).
- Burnecki K., J. Klafter, M. Magdziarz, A. Weron (2008). From solar flare time series to fractional dynamics. *Phys. A*, 387, 1077–1087.
- Burnecki K., G. Sikora (2013). Estimation of FARIMA parameters in the case of negative memory and stable noise. *IEEE Trans. Signal Process.*, 61, 2825–2835.
- Cappe O., E. Moulines, T. Ryden (2005). *Inference in Hidden Markov Models* (Springer, New York).
- Engle R.F. (1982). Autoregressive conditional heteroscedasticity with estimates of the variance of United Kingdom inflation. *Econometrica* 50, 987–1007.
- Feigelson E.D., G.J. Babu, and G.A. Caceres (2018). Autoregressive times series methods for time domain astronomy. *Front. Phys.*, 6, 80.
- Garcia H.A. (1994). Temperature and emission measure from GOES soft X-ray measurements. *Solar Phys.*, 154, 275–308.
- Hathaway D.H., L. Upton (2014). The solar meridional circulation and sunspot cycle variability. *J Geophys Res (Space Physics)*, 119, 3316–3324.
- Karak B.B., D. Nandy (2012). Turbulent pumping of magnetic flux reduces solar cycle memory and thus impacts predictability of the Sun’s activity. *Astrophys. J.*, 761, L13.
- Kokoszka P.S., M.S. Taqqu (1996). Parameter estimation for infinite variance fractional ARIMA. *Ann. Statist.*, 24, 1880–1913.
- Magdziarz M., A. Weron (2007). Fractional Langevin equation with α -stable noise. A link to fractional ARIMA time series. *Studia. Math.*, 181, 47–60.
- Meyer L., G. Witzel, F.A. Longstaff, A.M. Ghez (2014). A formal method for identifying distinct states of variability in time-varying sources: Sgr A* as an example. *Astrophys. J.*, 791, 24.
- Rabiner L.R. (1989). A tutorial on hidden Markov models and selected applications in speech recognition. *Proc. IEEE.*, 77, 257–286.
- Stanislavsky A., K. Burnecki, M. Magdziarz, A. Weron, K. Weron (2009). FARIMA modeling of solar flare activity from empirical time series of soft X-ray solar emission. *Astrophys. J.*, 693, 1877–1882.
- Stefani F., A. Giesecke, N. Weber, T. Weier (2016). Synchronized helicity oscillations: a link between planetary tides and the solar cycle? *Solar Phys.*, 291, 2197–2212.
- Usoskin I.G. (2013). A history of solar activity over millennia. *Living Rev Sol Phys*, 10, 1.

Morphology of Coronal Hole Based on SDO/AIA Data in May 2010 ÷ December 2013

Filip Šterc¹, Darije Maričić¹ and Dragan Roša¹

¹ Astronomical Observatory Zagreb, Opatička 22, 10000 Zagreb, Croatia.
E-mail: (fsterc@gmail.com, dmaricic@zvjezdarnica.hr, drosa@zvjezdarnica.hr)

Abstract.

We present an analysis of the high speed streams (HSSs) parameters, using *in situ* WIND data recorded from May 2010 to December 2012. For this purpose we made a list of 202 solar wind disturbances incorporated into an online catalogue for general use. Separating the solar wind signatures on: high speed streams, interplanetary coronal mass ejections (ICMEs), complex signatures; we focused our attention on 102 HSSs (52% of all SW signatures) which can be clearly associated with particular stream interface (SI). Furthermore, we analyzed in detail the correlation of solar wind parameters in different parts of HSSs, particularly in front and behind of SI. We found the best correlation between maximum of the magnetic field strength B vs proton density N_p and proton thermal speed v_{th} , 0.65 and 0.62, respectively. As well as between flow speed v and proton thermal speed v_{th} , $cc = 0.64$. While the correlation is significantly lower ($cc = 0.38$) between magnetic field B and flow speed v . Also, the correlation between maximum of the magnetic field B , flow speed v and proton thermal speed v_{th} , in the regions of HSS before and after SI are: $cc = 0.84$, 0.66 and 0.79, respectively. Correlations for the maximum of the proton density N_p between these two HSS regions is significantly lower ($cc = 0.39$) and points out to the possibility of two different HSS families.

Keywords. solar wind disturbance, stream interface, high speed stream

Introduction

Corotating interaction regions (CIRs) are created by the interaction of the high speed solar wind streams (HSSs) and slow solar wind streams (e.g., *Tsuratani et al.*, 2006, and references therein). The slow solar wind speed has a typical speed from 300 to 400 kms^{-1} , while the high-speed solar wind may reach velocities up to 800 kms^{-1} . CIRs originate from a coronal hole on the Sun (*Krieger, Timothy and Roelof*, 1973) and cause recurrent activity in the interplanetary space (e.g. *Gosling*, 1996). Furthermore, at heliocentric distance of around 1 AU, CIRs are usually bounded by magnetohydrodynamic forward and reverse waves, which develop into a forward and reverse shocks at a larger distance, occasionally some events develop already at 1 AU (*Smith and Wolfe*, 1976). CIRs cause geomagnetic storms of medium to weak strenghts (e.g. *Vennerstorm*, 2001; *Verbanec et al.*, 2011a,b; *Hajra et al.*, 2013, *Vršnak et al.*, 2017), although this phenomena is much stronger when it is caused by a single ICME or ICMEs interaction. CIRs occur more common throughout the solar cycle and their cumulative effect is larger than those of ICMEs (*Tsuratani et al.*, 2006). From the measurements of the solar wind at 1 AU, a CIR structure is characterized by the compression region associated with stream interface (SI). Inside the compression region the magnetic field, the temperature and the plasma density are increased (*Dumbović et al.*, 2012, and references therein). Compression region usually lasts typically one day. The whole region contains strong fluctuation and the increase of the southward-directed magnetic field is always present. Fast HSS from coronal holes lasts typically several days and reach flow speeds that can reach values above 800 kms^{-1} . For the evolution and structure of CIRs see articles *Baloghet al.*, 1999 as well as *Gosling and Pizzo*, 1999. The main objective of the analysis presented in this article is the comparison of measured magnetic field and plasma SW parameters in different parts of the CIR. In following Section 2 we describe the data used for our study. Section 3 describes data analysis of the magnetic field and plasma parameters in different parts of HSS,

that were recorded by *in situ* measurements at the Langrangian point L1, focusing on the period from May 2010 to December 2012. In particular, we analyze, in detail, the relationship between: the magnetic field, B ; the flow speed, v ; the thermal proton speed, v_{th} ; and proton density, N_p , in front and behind the SI. The main results and conclusions of the research are summarized and discussed in Section 4.

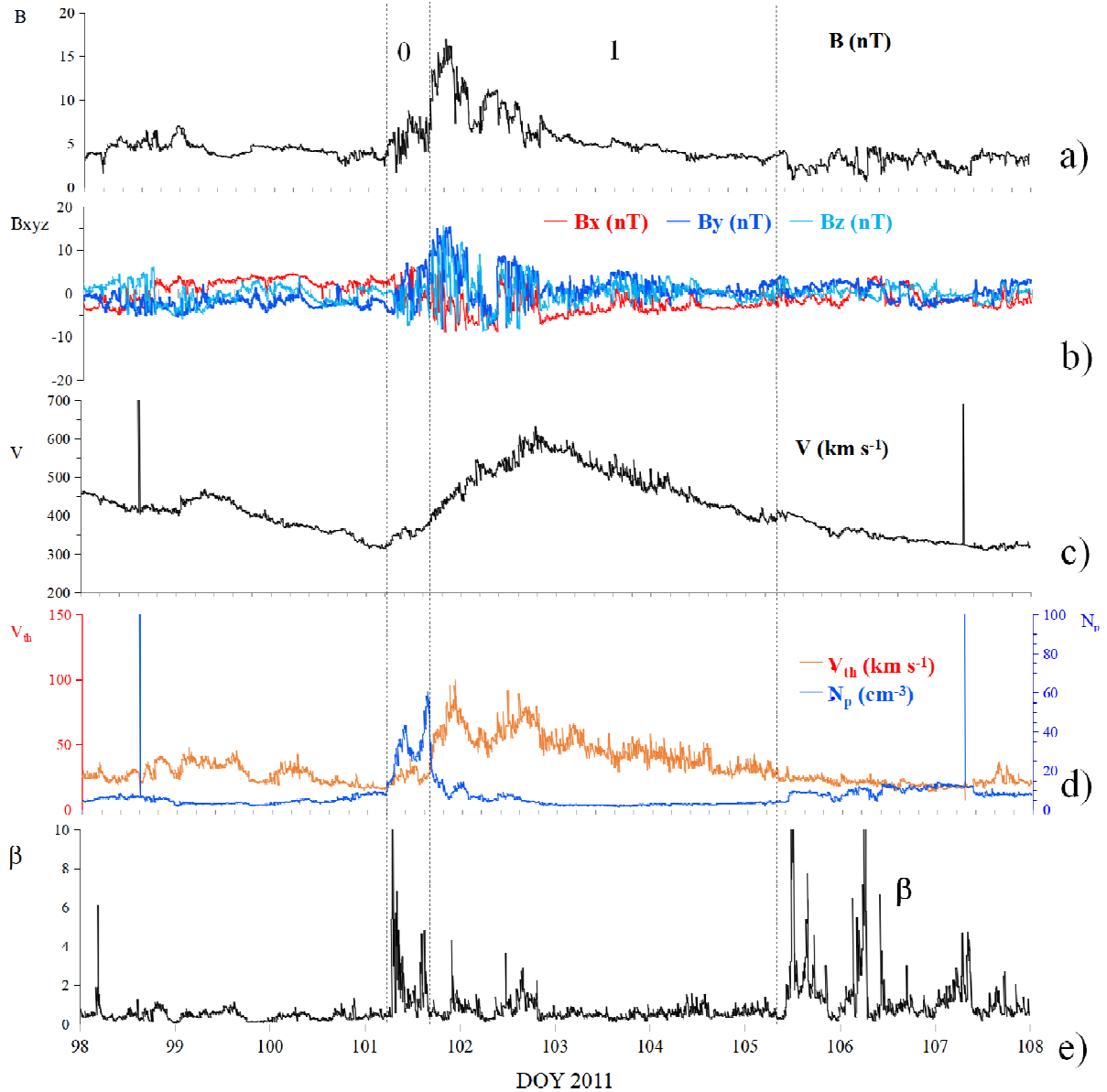


Figure 1. The presented figures the following labels are: a) the magnetic field strength, b) GSE magnetic field components, c) solar-wind speed, d) proton density and thermal velocity and e) plasma-to-magnetic pressure ratio. From a) to e): Example of the HSS *in situ* WIND measurements at L1 (DOY (day of year) = 98 is 8 April 2011). This HSS, measured by WIND satellite occurred on 13 April 2011, represents events with clearly distinctive features of SI (middle dashed vertical line). The morphology of such HSS can be divided into two different parts: part of the HSS between the front wave and SI (which is marked with number 0) and part of the HSS between SI and reverse wave (which is marked with number 1). First and last vertical dashed lines represent forward and reverse waves, while the middle dashed lines represent stream interfaces or interaction region.

The data set

For the measuring of solar wind disturbances at L1 point we used the data recorded by the Magnetic Field Investigation (MFI) and Solar Wind Experiment (SWE) Wind instruments (http://wind.nasa.gov/mfi_swe_plot.php), with 1 minute resolution data in GSE coordinates. The HSS events were separated by a detailed analysis of plasma and the magnetic field structure, as described in Dumbović *et al.* 2012. First we identified the increase of the plasma speed above the current background wind speed level, which corresponds to high-speed streams (for details see Vršnak, Temmer, and Veronig, 2007a). Also, we found the compression region or SI at the rising phase of the HSS from the data of plasma temperature, density and magnetic field (a sharp peak of the density and field strength, as well as sharp increase of temperature). Using the IS we separated the HSS on two parts. The *in situ* data in Figure 1 show that the structure of the HSS consists of two different parts (separated by the vertical dashed lines). Middle vertical dashed line represents stream interface. In both parts we measured the magnetic field strength, change in GSE magnetic field components, flow speed, maximum and minimum values of the flow speed components, temperature, proton density and plasma-to-magnetic field pressure (β). First region, which we marked with 0 (part of the HSS from onset of HSS to the onset SI) is characterized by a gradual increase of magnetic field strength, decrease in temperature and strong increase of proton density. The second region, which we marked with the number 1 (part of the HSS from the onset of SI to the end of the HSS) is characterized by a sharp drop of proton density, increased magnetic field strength, flow speed and temperature. As the end of HSS we took the time when the flow speed returned to the same values, as on the onset of the speed increase. In Figure 1; in every plot the date is expressed as DOY.

For the analyzed period, from 202 solar wind disturbances, 137 have been recognized as HSSs (67% of all SW samples). From the whole HSS sample, 74% of HSSs show a typical field and plasma structure and SI inside the CIR which can be clearly recognized. Between 137 HSS events, 35 events (25% of whole CIR sample) have complex signatures, and have been defined as events with complex signatures. For such HSSs it was not possible to clearly recognize the SI, but it was possible to recognize two or more SI, which can be caused by HSSs or ICME-HSS interaction. These events are excluded from our analysis. Our list of HSS events can be found at <https://zvjezdarnica.hr/pdf/ListSWDs2010.pdf>. For each HSS we provide the following information: no. of event (column 1); date of HSS disturbance (column 2 - 4); column 5 - 7 give information whether the HSS is associated with a change in cosmic ray neutron flux, Dst index and whether it shows a rotation of the magnetic field. For the purpose of this analysis we separated the SWDs into different types: ICMEs, HSSs and complex signatures, and the SWD type is noted in column 8; in columns 9 - 16 we give information on the SWD onset and the maximum values of magnetic field strength and plasma parameters; finally columns 17 - 19 give information about the onset and values of change, maximum and minimum of the Dst index.

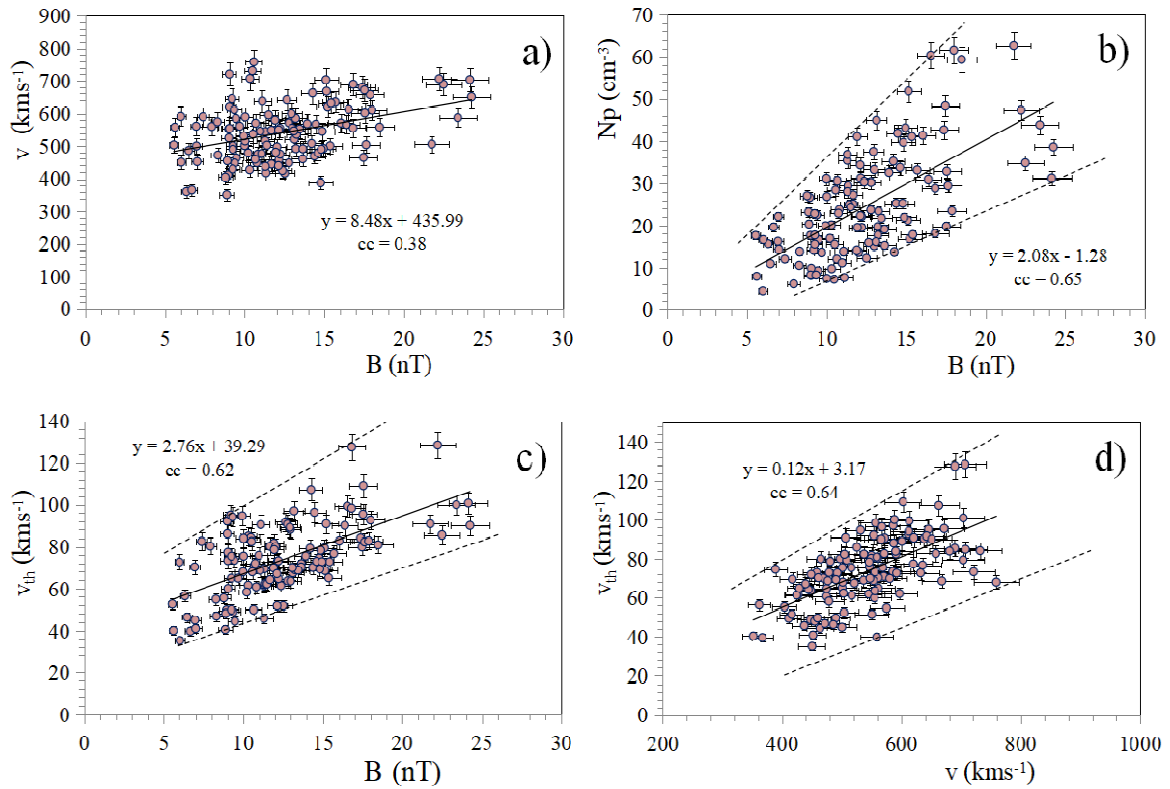


Figure 2. The following labels are: a) flow speed vs magnetic field strength, b) proton density vs magnetic field strength, c) thermal velocity vs magnetic field strength, and d) thermal velocity vs solar-wind speed. Dashed line represents a provisional drawn possible lower and heights values for the specific solar wind parameter.

Analysis

The results presented in this section quantify the previously described behaviour in statistical sense concerning the analysed period (from May 2010 to December 2014), are presented in graphical form in Figures 2 and 3. The correlations between four HSS-related solar wind parameters measured by *in situ* WIND data, are shown in Figure 2a-d. The presented scatter plots relating the correlation between the maximum measured values of the solar wind magnetic field strength B , proton density N_p , flow speed v and proton thermal speed v_{th} , over the analyzed period. The graphs reveal a well defined lower and upper limits to $v(B)$, $N_p(B)$, $v_{th}(B)$ and $v_{th}(v)$, indicated by the dotted line. In every graph we displayed the linear last-squares fit for solar wind parameters related data. We found the best correlations, $cc = 0.65$, 0.62 and 0.64 , between: proton density and magnetic field strength, proton thermal speed and magnetic field strength, as well as proton thermal speed and flow speed, respectively. While a significant lower correlation $cc = 0.38$ was found between the flow speed and magnetic field strength.

In Figures 3a-d we plotted the variation of the four solar wind parameters measured separately in two different parts of the HSS for the same analyzed period (noted as parts 0 and 1 in the Figure 1). There is a high correlation between the maximum of magnetic field strength B , solar wind flow speed and proton thermal speed in HSS parts 0 and 1, with correlation coefficients of $cc = 0.84$, 0.66 and 0.79 , respectively.

While, a very weak correlation ($cc = 0.39$) was found between maximum values of the proton density N_p measured in regions 0 and 1. Inspecting the graphs (Figure 3b), we can distinguish that the variation between maximum of the proton density in HSS parts 0 and 1 show two different correlations or possible two different families of the HSS.

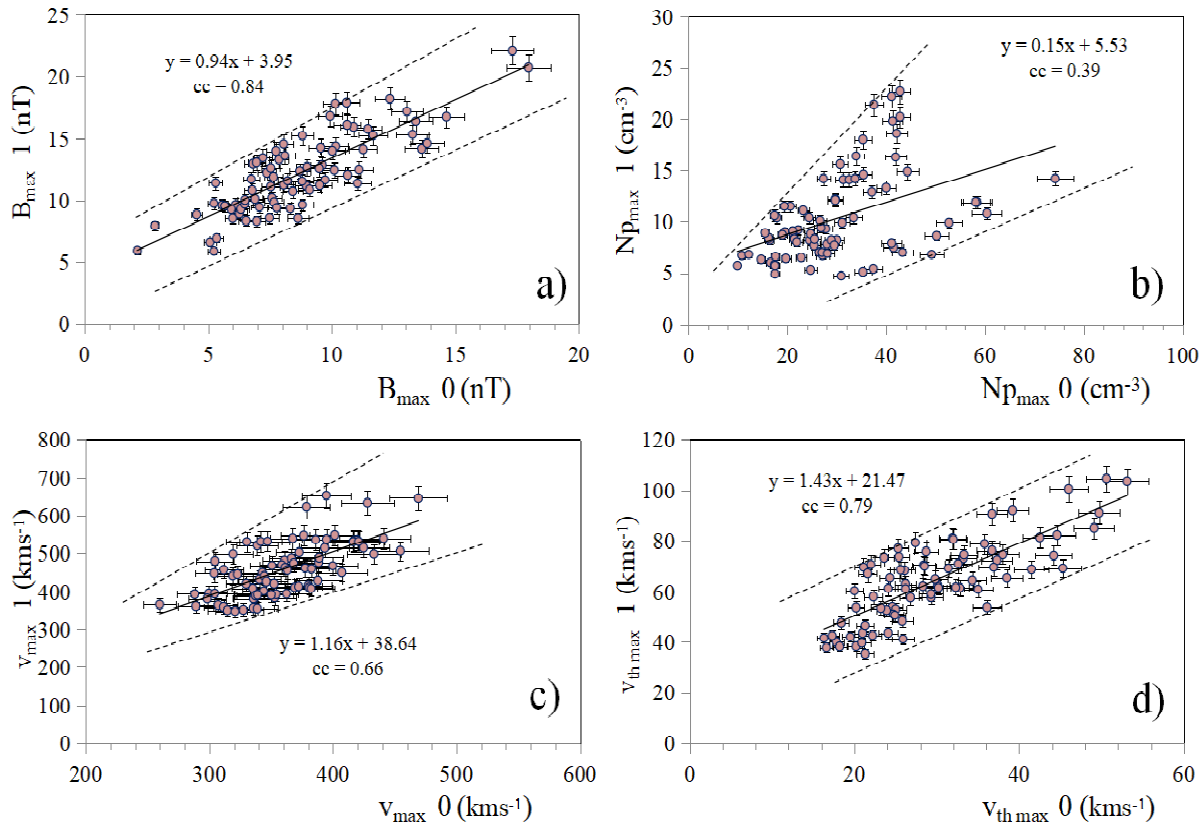


Figure 3. Variation between maximum of: a) magnetic field strength B b) proton density N_p c) solar wind flow speed and d) proton thermal speed, in HSS parts 0 and 1. The dashed line represents a provisionally lower and higher values for the specific solar wind parameter.

Discussion and Conclusion

We summarize the main results of our analysis of the HSS-related solar wind parameters as follows:

- For our analyzed sample of the SWDs, 52% of the whole solar wind disturbances can be recognized as a HSS, which can be clearly associated with a particular stream interface.
- We found high correlations between maximum of the magnetic field strength B vs proton density N_p and proton thermal speed v_{th} , as well as between flow speed v and proton thermal speed v_{th} , with correlation coefficients 0.65, 0.62 and 0.64, respectively. While the correlation is significantly lower ($cc = 0.38$) between magnetic field B and flow speed v .
- Correlation between the maximum of the magnetic field B , flow speed v and proton thermal speed v_{th} , in the regions of HSS behind and after SI are: $cc = 0.84$, 0.66 and 0.79 , respectively. Correlations for maximum of the proton density N_p between these two HSS regions is significantly lower ($cc = 0.39$) and points out to a possibility of two different HSS families.

Acknowledgment

We would like to thank the WIND, ACE, SOHO, STEREO, SDO and Kyoto University teams for developing and operating the instruments and we are grateful for their open data policy.

References

- Balogh, A., Gosling, J.T., Jokipii, J.R., Kallenbach, R., Kunow, H. (1999). Corotating interaction regions. *Space Sci. Rev.* 89, 1.
- Dumbović, M., Vršnak, B., Čalogović, J., Župan, R. (2012). Cosmic ray modulation by different types of solarwind disturbances. *Astron. Astrophys.* 538, A28.
- Gosling, J.T. (1996). Corotating and transient solar wind flows in three dimensions. *Annu. Rev. Astron. Astrophys.* 34, 35.
- Gosling, J.T., Pizzo, V.J.: (1999). Formation and evolution of corotating interaction regions and their threedimensional structure. *Space Sci. Rev.* 89, 21.
- Hajra, R., Echer, E., Tsurutani, B.T., Gonzalez, W.D. (2013). Solar cycle dependence of high-intensity longd uration continuous AE activity (HILDCAA) events, relativistic electron predictors? *J. Geophys. Res.* 118, 5626.
- Krieger, A.S., Timothy, A.F., Roelof, E.C. (1973). A coronal hole and its identification as the source of a high velocity solar wind stream. *Solar Phys.* 29, 505.
- Smith, E.J., Wolfe, J.H. (1976). Observations of interaction regions and corotating shocksbetween one andfive AU – Pioneers 10 and 11. *Geophys. Res. Lett.* 3, 137.
- Tsurutani, B.T., McPherron, R.L., Gonzalez, W.D., Lu, G., Sobral, J.H.A., Gopalswamy, N. (2006). Introductionto special section on corotating solar wind streams and recurrent geomagnetic activity. *J. Geophys. Res.* 111, 1.
- Vennerstroem, S. (2001). Interplanetary sources of magnetic storms: a statistical study. *J. Geophys. Res.* 106, 29175.
- Verbanac, G., Vršnak, B., Veronig, A., Temmer, M. (2011a). Equatorial coronal holes, solar wind high-speedstreams, and their geoeffectiveness. *Astron. Astrophys.* 526, A20.
- Verbanac, G., Vršnak, B., Živković, S., Hojsak, T., Veronig, A.M., Temmer, M. (2011b). Solar wind high-speedstreams and related geomagnetic activity in the declining phase of solar cycle 23. *Astron. Astrophys.* 533, A49.
- Vršnak, B., Temmer, M., Veronig, A.M. (2007a). Coronal holes and solar wind high-speed streams: I. Forecastingthe solar wind parameters. *Solar Phys.* 240, 315.
- Vršnak, B., Dumbović, M., Čalogović, J., Verbanec, G., Poljanić-Beljan, I. (2017). Geomagnetic Effects of Corotating Interaction Region. *Solar Phys.* 292, 140.

Research on Active Solar Processes During 2019 July 2 Total Solar Eclipse

*Tsvetkov Ts.*¹, *Petrov, N.*¹, *Miteva, R.*², *Ivanov, E.*³, *Popov, V.*³

¹ Institute of Astronomy and National Astronomical Observatory, BAS, Bulgaria

² Space Research and Technology Institute, BAS, Bulgaria

³ Konstantin Preslavsky University of Shumen, Bulgaria

E-mail: tstsvetkov@astro.bas.bg

Abstract.

We live in an era where scientific studies of the Sun and the solar-terrestrial interactions, being done by ground-based and orbital observatories, are more improved and wide-spread. However, the total solar eclipses are still a cosmic laboratory impossible to simulate on Earth and they provide a chance for detailed studies of the corona and the active processes which affect our everyday lives.

Our research team is preparing an expedition to observe a total solar eclipse on 2019 July 2 from Chile. The current report gives details on preliminary research of choosing the location, preparing the equipment and scientific tasks to perform.

Introduction

On 2019 July 2 a total solar eclipse will be visible from within a narrow corridor that crosses throughout the Pacific (the totality will be visible from Oeno Island), Chile, and Argentina. The path of the Moon's umbral shadow will first “touch” the land in Chile and leave the mainland, crossing the Argentina. A partial eclipse will be visible from a much wider band of penumbra of the Moon, which includes much of the Pacific Ocean, across South America, and part of the South Atlantic Ocean.

The maximum duration of the total phase of the eclipse will be 4 min 33 s (visible from a territory situated in the Pacific Ocean). For observers from continental land of South America the greatest duration will continue 2 min 36 s (NASA Goddard Space Flight Center:

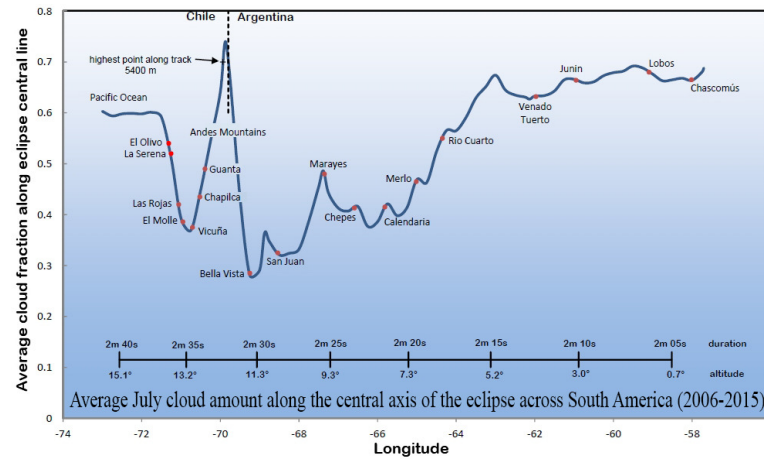
<https://eclipse.gsfc.nasa.gov/SEgoogle/SEgoogle2001/SE2019Jul02Tgoogle.html>).

All preliminary studies regarding the weather conditions confirm that one of the best places for observations of this eclipse is the Atacama Desert, Chile, where our team will be located (Figure 1a). Using the provided information about the average cloud amount in July along the central axis of the eclipse for the territory of Chile and Argentina, our team chose the best observational spot to be located in the surroundings of the town of El Molle (Figure 1b). Eclipse details for the preferred location are listed in Table 1.

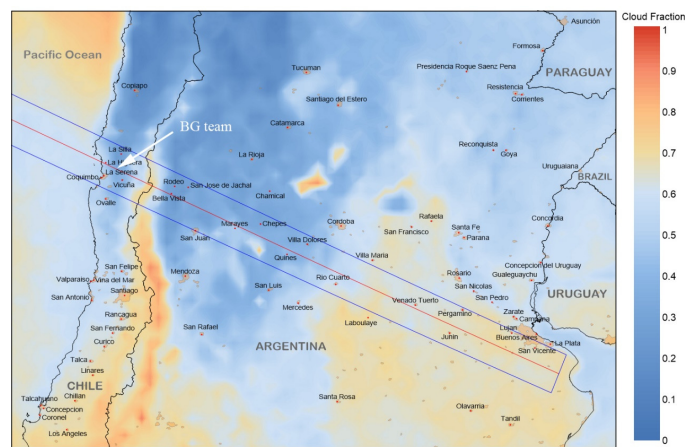
Table 1. Eclipse details for the chosen observational area near El Molle
(<https://www.timeanddate.com/eclipse/solar/2019-july-2>).

Magnitude	Duration [hh:mm:ss]	Duration of the totality [mm:ss]	Maximum [LT]	Sun's altitude at maximum
1.0149	2:23:25	2:32	16:39:47	13.2°

It is important to note that the altitude of the chosen area is in the order of 1000 meters (or more), which contributes to greater transparency of the atmosphere. Our team has chosen a location outside the cities to minimize the effects of light pollution.



a)



b)

Fig. 1 a) Average July cloud amount along the central axis of the eclipse across South America (<http://eclipsophile.com/total-solar-eclipse-july-2-2019/>); b) Average July afternoon fractional cloudiness along the eclipse track over South America. Data are extracted from 14 years (2002-2015) of observations from the Aqua satellite. (<http://eclipsophile.com/total-solar-eclipse-july-2-2019/>).

Planned experiments and tasks

a) White-light observations and polarimetric analysis of the solar corona

Polarimetric measurements conducted during TSEs are an important source of information about the physical conditions in the so called white-light corona. During every TSE such measurements are a fundamental experiment in view of the fact that numerous problems related to polarization of the corona are still unsolved [Badalyan O. G., et al., 1997; Koutchmy S. and Schatten K. H., 1971; Molodensky M. M., et al., 2009].

- Searching for areas of polarization in the inner corona which is at a degree, exceeding the maximum possible one, when considering only the Thomson scattering of photosphere photons.
- Investigating electron distribution in solar corona as function of distance from solar center (especially above active regions).
- Determination of the relationship between the degree of polarization and the wavelength.
- Evaluation of the degree of polarization in polar plumes.

b) Fine structure of white-light solar corona

Due to the progress of observing techniques and the usage of modern detectors we now know that the white-light solar corona drives the formation of small-scale structures in the solar corona like helmet streamers or knots. Over the polar regions we have clearly identified the structures of coronal rays and plumes. Observations with a resolution in the order of one arc sec indicate that the majority of the solar corona is in a dynamic state [Pasachoff J., et al., 2007].

- Photographing the solar corona with couple of cameras with different lenses in order to be able to achieve details of coronal fine structure when combine images with different exposure times.

c) Polarimetry of solar prominences

Investigations of quiescent prominences fine structure as well as these on physical parameters like density, temperature or speed are directly connected with underlying magnetic field. Both its global and local components in the environment of prominences are responsible for their lifetime duration. On the other hand, the magnetic reconnection is key factor in destabilization and eruption of filaments. While it is clear that the basis of the dynamics and evolution of solar prominences is related to the local magnetic fields in the area of their occurrence, lots of questions remain unanswered. The planned experiment includes:

- Determination of the parameters of the magnetic field that supports solar prominences, using a polarizing observational method to determine the Sun's magnetic field parameters.
- Obtaining a picture of the global magnetic structure surrounding and supporting the prominences. We aim at showing the existence of coronal voids and/or coronal cavities near prominences and to prove that they are related to the acceleration of the prominence plasma during eruption.

d) Monitoring and recording of "shadow bands"

A yet not fully studied atmospheric phenomenon observed immediately before and after the full phase of a TSE are the so called “shadow bands” [Codona J. L., 1998]. This phenomenon was familiar to astronomers 200 years ago, but its successful photographing and videotaping became possible only in the last three decades. Shadow bands are visible on a flat white surface in the final few seconds before and after the totality of an eclipse. It is clear that this is an atmospheric phenomenon but the part or layer of the atmosphere involved is not yet known. It is largely accepted that it is a result of the light emitted from a thin solar crescent being refracted by the Earth's turbulent atmosphere. We suggest a relatively new experiment for shadow bands exploration.

- Registering the shadow bands using ultrasound anemometers with 4 times per second frequency for measuring the speed of wind.
- Videotaping and registering infrasound signals of this phenomenon. Registering and analysis of infrasound from natural processes in nature is a relatively new scientific branch.

Each eclipse is accompanied by “eclipse wind”. The wind speed depends mainly on the regional and local topography, including water surfaces and whether the land is covered by desert, forest or mountains. The landscape also determines rapid changes in temperature which decreases 5-15°C.

- Checking if both the wind and the changes in temperature can cause atmospheric turbulence that is capable to generate very low frequency sound in the atmosphere.
- Monitoring the atmosphere at ground level for low frequency sounds, because their existence would infer that shadow bands are associated with turbulence at all levels of the Earth's atmosphere. For the purposes of this experiment, we will employ a highly sensitive infrasound microphone with a frequency response of 0.1 to 10000 Hz.

Conclusions

We present a preliminary program for observations of 2019 July 2 total solar eclipse visible from the territory of South America. Our team chose a location to obtain the observations situated in the surroundings of Chilean town El Molle with altitude higher than 1000 m above the sea level.

The planned experiments include photographing solar corona with different instruments (lenses and filters) and settings (exposure times, diaphragms, light sensitivities, etc.), as well as registering the properties of atmospheric phenomena that accompany the totality – eclipse winds and shadow bands.

The obtained results will be compared with the ones that we have from similar experiments, held at 2017 August 21 total solar eclipse in USA.

Acknowledgment

This study is supported by the National Science Fund of Bulgaria with contracts No.: KP-06-H28/4, the joint project of cooperation between Institute of Astronomy and NAO, BAS and the Department of Astronomy, Faculty of Mathematics, University of Belgrade P-22/04.07.2017, and Ministry of Education and Science project No. 577/17.08.2018.

References

- Badalyan, O. G., Livshits, M. A., Sýkora, J. (1997). *Solar Physics*, 173, Issue 1, 67-80.
Codona J. L., (1998). *Astronomy and Astrophysics*, 164, no. 2, 415-427.
Koutchmy, S. and Schatten, K. H. (1971). *Solar Physics*, 17, Issue 1, 117-128.
Molodensky, M. M., Starkova L. I., Kutvitskii V. A., and Merzlyakov V. L. (2009). *Astronomy Reports*, 53, No. 3, 275–280.
Pasachoff, J., Rušin, V., Druckmüller, M., Saniga, M. (2007) *The Astrophysical Journal*, 665, Issue 1, 824-829.

RS Ophiuchi and ADVECTION

Krasimira Yankova

Space Research and Technology Institute – Bulgarian Academy of Sciences
e-mail: f7@space.bas.bg

Abstract.

Binary systems RS Oph comprise a white dwarf and a closely orbiting Red giant. RS Oph (HD 162214) is a symbiotic recurrent nova which exhibits recurrent nova outbursts approximately every 15-20 years. Matter is transferred from the companion to the white dwarf, forming an accretion disk with corona (Mondal et al. 2018). Advection in the disk contributes to dynamics in internal orbits of the disk. Therefore mechanism can be viewed as a catalyst of an activity from the coronas arches collisions.

Introduction

Advection carries the properties of flow parameters from one area of the medium to another. The mechanism transfers (transports) all disturbances without deformation in them.

We have developed a MHD model of the accretion disc, based on a new specific advective hypothesis, presented in Yankova (2013, 2015a). The unified model we built on the conception to non-deforming advection allows in the field of nonlinear physics to conduct an analytical study of the accretion.

Researching the behavior of the emerging as a consequence of this mechanism direct and reverse connections in the flow on disk, represent a solution to the global model for the radial and vertical disk structures ; the local structure model and adaptation of the model for the emerging corona. Results given in detail in Iankova (2007a, b), Iankova (2009), Yankova (2012a, b, c), Yankova (2015 b, c)

In the papers Yankova (2015c, 2016) is research of the accretion flow in concrete objects: the disks structures in on Cyg X-1 and SgrA * have been modeled. Here we analyze the behavior on the advective hypothesis in the RS Ophiuchi nova-like disk.

Advection mechanism

As we show in our relativistic consideration (Yankova 2017a, b; Yankova 2018a, b), the Advective Operator who consists of Pure Rotation in Time and Rotation + Translation respectively:

$$(\partial_{t_i} + v_{ij} \partial_{x_j}) \nu_{ji} = \beta_{ji} \partial_{t_i} + \delta_{ij} \partial_{t_j} \quad (1)$$

where

$$v_{ij} = \frac{\partial x_i}{\partial t_j} \quad (2)$$

it naturally go to the low-energy boundary of non-deforming advection:

$$\frac{\partial(\rho v_i)}{\partial t} + \frac{\partial}{\partial x_j} (\rho v_i v_j) = \rho \left(\frac{\partial v_i}{\partial t} + v_j \frac{\partial v_i}{\partial x_j} \right) = \rho \frac{Dv_i}{Dt} \quad (3)$$

Earlier in (Yankova 2015-2018) we have noted, incomplete modes of advection deformed the differential by an individual modification of one or another component. But in a case, when the advection is non-dominant mechanism, there are not conditions of flow deformations. Solution is transferred as a whole.

The advective rings in the disk packed the plasma and radiation and transfer them without any changes in theirs parameters. Exactly the ring is the main carrier of the hidden activity. Advection in self-induction mode is due to the self-gravity and transfer of the electro-

magnetic field. (Iankova 2009, Yankova 2015a, b). It builds straight and feedbacks in the stream. The local warming in a ring is an expression of the direct connection and carries information about the development of the instabilities in dependence from the energetics of the disc. Feedback is an expression of the hidden dependence of the internal structure of the flow by non-linear effects in it.

Advection in the RS Ophiuchi disk

In (Yankova and Zamanov 2019) we apply the generalized model of a magnetized accretion disk with non-deforming advection, which preserves the nonlinearity of the problem, to the nova-like accretion disc in RS Ophiuchi. We have determined the corona radius (fig.4), the destruction radius of the disk (fig.3), and its active zone.

Active zone is located in the range $(0.02; 0.3)R_0$, where $R_0 = 100 R_*$ is the radius of the disk and R_* the radius of the star. Advection transports the properties of the flow parameters from one area of the environment to the other without deformations (Yankova 2013, Yankova 2015), so that the Plateau in the Luminosity (see Fig.2) indicate the regions $(0.1; 0.3) R_0$ in which the advection conceals the activity and where the activity becomes observable only at $(0.02; 0.1) R_0$.

The advection controls the flow parameters in both parts of the active zone: in the outer active zone the advection controls the local heating and the disc is cooled very well (Figure 1 and Tabl.1). This is consistent with the theoretical precepts for the very large size of the RS Oph accretion disc (King& Pringle, 2009) and the observations of a low-luminosity accretion disc (Mondal et al. 2018). In the inner region the displacement velocity v_{ji} (eq.1) and v_i (eq.3) is insufficient to hide the activity. It is sufficient, however to contribute to the rapid torsion on ML at the pad of the corona. The annihilation of the shortened part of the magnetic arches in this case is so powerful that the inner zona can reach the luminosity of the white dwarf. White dwarf luminosity is $\sim 1.26 \times 10^{37} \text{ ergs}^{-1}$. (Mondal et al. 2018)

In the layer where azimuthal velocity skips over from one Keplerian curve to another – the disc evaporates $(0.011; 0.02) R_0$. There arcs collision due to the impact of the interacting currents (star wind, disk wind and coronal flow) on the arches dynamics. In this sense the corona contribution there is not directly related to the advection. The luminosity in this case is super-Edington $L \sim 10^{40} \text{ erg / s}$, but it differs from the luminosity supernovas $L \sim 10^{51} \text{ erg / s}$ with of 5-6 orders of magnitude.

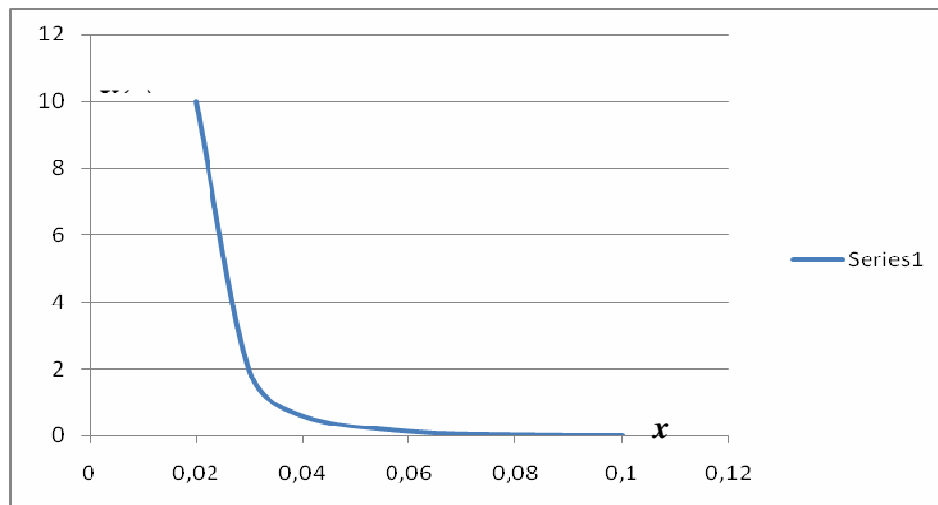


Figure 1: Distribution of the local heating in the inner regions of the of the RS Oph disk.

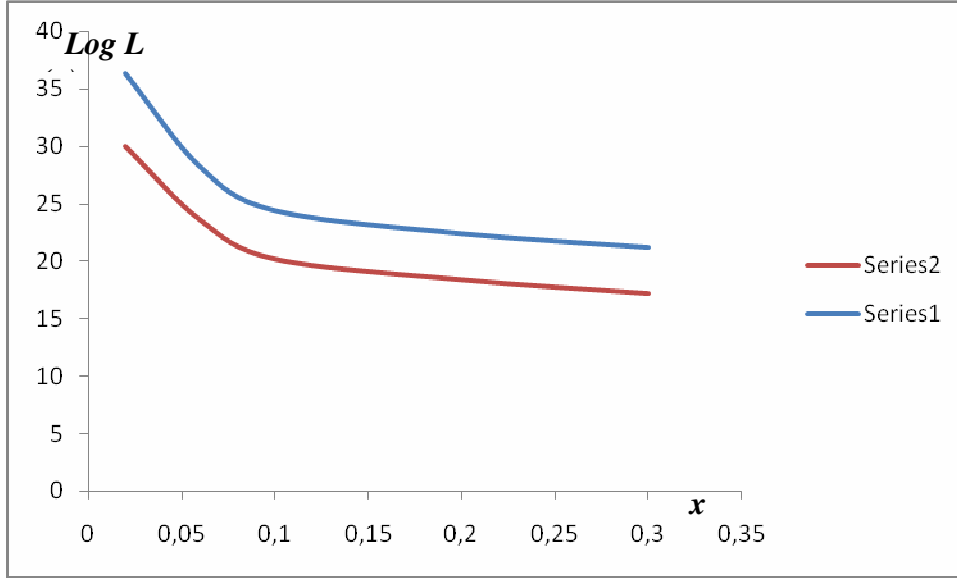


Figure 2: below: Luminosity distribution function of the inner regions of the RS Oph disk; above: L_{fl} – “distribution” of the on the local orbits

Table 1: Significant values of the local heating and Luminosity

X [R ₀]	$K(x) = \frac{\text{warming}}{\text{cooling}}$	L_{id} [erg/s]	L_{fl} [erg/s]
0.3	$(3.0 \pm 0.1) 10^{-4}$	$\approx 2 \cdot 10^{17}$	$\approx 10^{22}$
0.1	$(1.7 \pm 0.1) 10^{-2}$	$\approx 2 \cdot 10^{20}$	$\approx 4 \cdot 10^{24} \approx 2 \cdot 10^4 L_{id}$
0.08	$(4.0 \pm 0.5) 10^{-2}$		
0.06	0.14 ± 0.05	$\approx 6 \cdot 10^{23}$	$\approx 2 \cdot 10^{28} \approx 3 \cdot 10^4 L_{id}$
0.04	0.60 ± 0.05	$K_{cr} = 1$	
0.03	1.95 ± 0.05		
0.02	10 ± 0.1	$\approx 1,5 \cdot 10^{30}$	$\approx 3 \cdot 10^{36} \approx 2 \cdot 10^6 L_{id}$
≤ 0.02		L_{cor}	
0,01	83 ± 0.6	$\approx 2 \cdot 10^{32}$	$\approx 2 \cdot 10^{37}$

x103[cm/s]

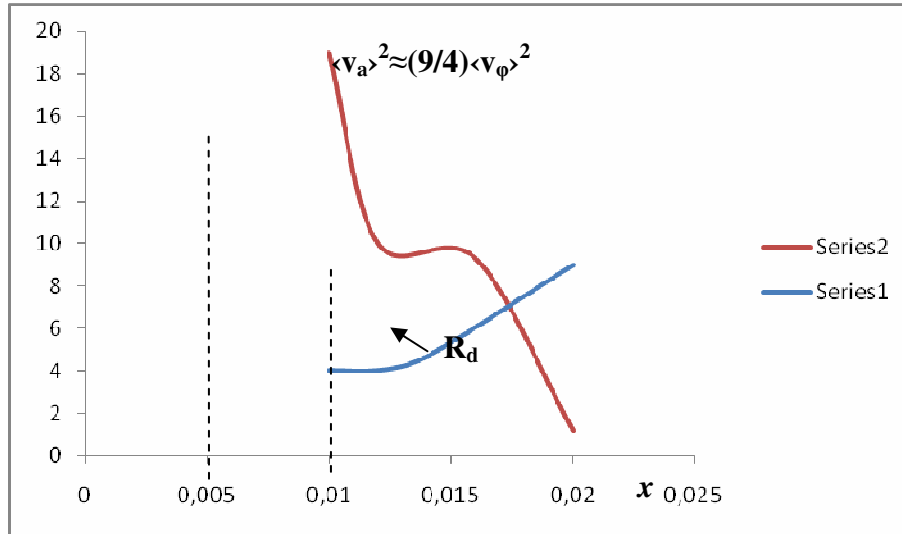


Figure 3: Condition $\langle v_a \rangle^2 \leq (9/4) \langle v_\phi \rangle^2$. Ser.1: Distribution of the Alfvén velocity on the RS Oph disk. Ser.2: Distribution of the azimuthal velocity on the RS Oph disk.

x103[cm/s]

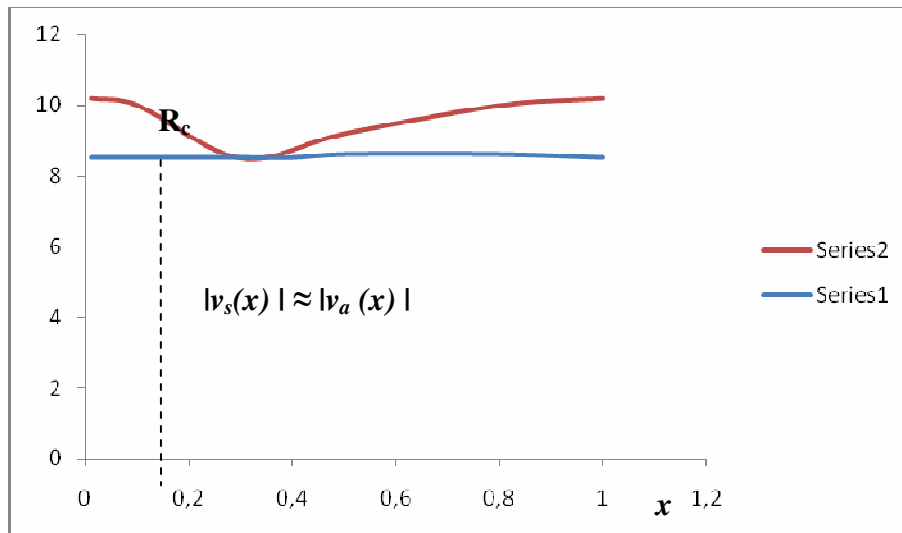


Figure 4: Condition $|v_s(x)| \approx |v_a(x)|$. Ser.1: Distribution of the Alfvén velocity on the RS Oph disk. Ser.2: Distribution of the sound velocity on the RS Oph disk.

Conclusions

In this paper, we used the results of the theoretical model to description of the processes in the nova-like disk. The model is analytical and predicts radial and vertical profiles of all basic physical characteristics of the accretion disc as well as a local survey. Our model may be applied to a large variety of sources such as symbiotic novas, Micro -Quasars; Sleeping Cores and AGN.

Observations of RS Oph show irregular with light variations on timescales of 20yr to a few minutes (Alexander et al. 2011). It cannot be compared to the time required to accumulate to the supernova $\sim 10^5$ yr. We have already proved that the long-run ones are due to the external inflow (Yankova and Zamanov 2019).

Advection mechanism in RS Oph disk can explain the short-lived light variations accompanied by the extreme X-ray variability. Advection catalyses an activity from the

coronas arches collisions. Advective rings which control dynamics in internal orbits and provide the warming of the pad, at RS Oph contribute to form a sharp boundary between the disc and the corona. RS Ophiuchi disk has a very good expressed corona, visible in the observations (Mondal et al. 2018). Probably the corona has subsides periods and therefore it is certain that the dynamics of the arches are not responsible for long-term variability.

References:

- Alexander, R. D., Wynn, G. A., King, A. R., & Pringle, J. E. 2011, MNRAS, 418, 2576
- Iankova Kr.D., 2007a, Accretion disk with advection and magnetic field , BG-Ursi School and Workshop on Waves and Turbulence Phenomena in Space Plasmas, BSSPP Proceedings, Series No. 1, pp 143-146, 2007, <http://sp.phys.uni-sofia.bg/Kiten06/Pres/Iankova.pdf>
- Iankova Krasimira 2007b, ” Evinces of interaction of flow in disk with magnetic field”, Bulg. J. Phys. (2007) vol.34 no.s2 pp. 326-329, [ISSN1310-0157].
- Iankova Kr.D., 2009, Stability and evolution of magnetic accretion disk, Publ. Astron. Soc. "Rudjer Bošković", No. 9, pp 327-333, Belgrade (2009). <http://www.scopus.com/record/display.uri?eid=2-s2.0-84902507488>
- King, A. R., & Pringle, J. E. 2009, MNRAS, 397, L51
- Mondal, A., Anupama, G. C., Kamath, U. S., et al. 2018, MNRAS, 474, 4211
- Yankova Krasimira, 2012, Structure of accretion disk in the presence of magnetic field, Publications of the Astronomical Society "Rudjer Boskovic", vol. 11, pp. 375-383. <http://adsabs.harvard.edu/abs/2012PASRB..11..375Y>
- Yankova Kr. D.: 2012a, SSTRI-BAN, SENS 2011 proceedings, ISSN 1313-3888, 73-78.
- Yankova Kr.D.: 2012b, Publications of the Astronomical Society "Rudjer Boskovic", vol. 11, pp.375-383. <http://adsabs.harvard.edu/abs/2012PASRB..11..375Y>
- Yankova Kr.D.: 2012c, JUBILEE INTERNATIONAL CONGRESS: SCIENCE, EDUCATION, TECHNOLOGIES "40 YEARS BULGARIA – SPACE COUNTRY ", proceedings (ISBN 978-954-577-636-6), Tom1, 152-158.
- Yankova Kr.D.: 2013, Generation and development of the disk corona, Publ. Astron. Soc. “Rudjer Bošković” vol. 12, 375-381. <http://www.scopus.com/authorid/detail.uri?authorId=56206009300>
- Yankova Kr.: 2015a, MHD of accretion-disk flows, BlgAJ, Vol. 22, p. 83. <http://adsabs.harvard.edu/abs/2015BlgAJ..22...83Y>
https://apps.webofknowledge.com/full_record.do?product=WOS&search_mode=CitingArticles&qid=10&SID=F2jjLBQJ8SBI5ml3ndb&page=1&doc=1
- Yankova Kr.: 2015b, Behaviour of the flow on the boundary in the system disk-corona, Publ. Astron. Soc. “Rudjer Bošković” No 15, 2015, 107-115. <https://www.scopus.com/record/display.uri?origin=recordpage&eid=2-s2.0-84954042356>
- Yankova, Kr., 2015c, Analysis of the nonlinear behavior of the accretion flows, SSTRI-BAN, Proceedings Seventh Workshop “Solar Influences on the Magnetosphere, Ionosphere and Atmosphere”, 25-28, ISSN 2367-7570, <http://ws-sozopol.stil.bas.bg/2015Sunny/Proceedings2015S1-2.pdf>
- Yankova, Kr., 2016, Relationships in the system disc-corona, SSTRI-BAN, Proceedings Eighth Workshop “Solar Influences on the Magnetosphere, Ionosphere and Atmosphere”, 31-34, ISSN 2367-7570 <http://ws-sozopol.stil.bas.bg/2016Sunny/Proceedings2016.pdf>
- Yankova Kr.: 2017, Inter-component connections in Quasar, SSTRI-BAN, Sofia, Proceedings SES 2017, ISSN 1313-3888, 85-88, 2017.
- Yankova, Kr., 2017, Unified model of the AGN, SSTRI-BAN, Proceedings Ninth Workshop “Solar Influences on the Magnetosphere, Ionosphere and Atmosphere”, 77-82, ISSN 2367-7570. http://ws-sozopol.stil.bas.bg/2017Sunny/Proceedings2017_V3.pdf
- Yankova, Kr., 2018, Advection and Inter-Component Connections in the Quasar, SSTRI-BAN, Proceedings Tenth Workshop “Solar Influences on the Magnetosphere, Ionosphere and Atmosphere”, 43-46, ISSN 2367-7570. DOI: [10.31401/WS.2018.proc](https://doi.org/10.31401/WS.2018.proc)
http://ws-sozopol.stil.bas.bg/2018Primorsko/Proceedings2018_V2.pdf
<http://adsabs.harvard.edu/abs/2018simi.conf..43Y>
- Yankova Kr.: 2018, Fundamental Advection, Proceedings SES2018, 85-89, ISSN: 1313-3888.
- Yankova Kr., [R K Zamanov](#) , 2019, RS OPH – flickering variability in the depending on the rate of accretion, submit.

Comparing the Height Dependences of the Magnetic Field Overlying the Initial Areas of Fast and Slow Coronal Mass Ejections

Zagainova Iu.S.¹, Fainshtein V.G.², Rudenko G.V.²

¹ Pushkov Institute of Terrestrial Magnetism, Ionosphere and Radio Wave Propagation RAS,
Moscow, Russian Federation

² Institute of solar-terrestrial physics RAS, Irkutsk, Russian Federation
E-mail: yuliazagainova@mail.ru

Abstract.

A relationship is examined between the height distribution of the transverse magnetic-field component in the lower corona, above the polarity inversion line (PIL), in an Active Region (AR), and the speed of the coronal mass ejection (CME) originating from this AR. A three-dimensional (3D) configuration is calculated for the AR magnetic field in terms of the non-linear force-free approximation. Three CME groups are addressed: fast, intermediate-speed and slow CMEs. It is demonstrated that, on average, the faster the decay rate of the transverse component of the magnetic field above the PIL as height-averaged up to about 0.21 solar radii and along the PIL, the higher the linear projected speed of the CME originating from this AR and recorded within the LASCO field of view.

Introduction

Coronal mass ejections (CMEs) are characterised by a wide spectrum of linear projected velocities V_{lin} in the field of view of LASCO coronagraphs [Gopalswamy N., et al., 2009a]. Their velocity varies from several dozen to over 3000 km/s. Despite the many studies of coronal mass ejections (see review by [Webb D.F., et al., 2012]) and suggested mechanisms of their generation [Chen P.F., 2011], however, the question of what determines the speed of each CME is still to be answered. It was suggested in [MacQueen R.M., et al., 1983] that two types of CMEs exist: flare- and filament eruption-related ones. CMEs of the first group are, on average, faster and feature smaller acceleration than those of the second group. Sheeley N.R. with co-authors [Sheeley N.R., et al., 1999] concludes that, depending on their speed, the CMEs can be subdivided into two classes: (1) ‘gradual’, prominence eruption-related CMEs, with speeds of (400 - 600) km/s, which gradually increases to its maximum in the coronagraph field of view; (2) flare-related ‘pulse’ CMEs, featuring speeds of over 750 km/s even before appearing in the LASCO field of view. Later, it became evident that such classification is not ‘absolute’ (see [Vršnak B., et al., 2005] and references therein): a slow CME can turn out to be a ‘pulse’ one, associated with a flare, while a fast CME can be gradual and associated with a filament eruption. Moreover, both fast and slow CMEs can be accompanied by weak or, vice versa, powerful flares.

Török and Kliem [Török T. and Kliem B., 2007] constructed a model of a force-free flux-rope moving in the external magnetic field with a dipole or quadrupole configuration. Those authors conclude that a fast CME forms if magnetic field tension rapidly decreases with height relative to the photospheric level (characteristic of the quadrupole configuration of magnetic field), while a slow CME forms if it decreases slowly (dipole configuration).

This paper compares the magnetic field decay rate above the AR photospheric field PIL vs V_{lin} , for three groups of CMEs of different - fast, intermediate-speed and slow - velocities. We used the “decay index” $n = -(h/B_t) \cdot (dB_t/dh)$ [Bateman G., 1978] as a characteristic of the magnetic field decay with height, where B_t is the transverse component of magnetic field, h is the height as counted from the photosphere. A positive trend is shown to exist between the linear mapped CME velocity V_{lin} and the PIL- and height-averaged “decay index” $\langle n \rangle_{\text{PIL}}$, within the calculation domain.

Data

Three CME groups were selected for analysis, 9 events per each: slow CMEs with $V_{lin} = (400 - 600)$ km/s; CMEs with intermediate speed $V_{lin} = (600 - 1300)$ km/s, and fast CMEs with $V_{lin} > 1300$ km/s. Data on the CME properties was taken from the CME catalogue https://cdaw.gsfc.nasa.gov/CME_list/HALO/index.html. To increase accuracy while treating solar images in the extreme ultraviolet channels and measuring magnetic field, we chose ‘halo’-type CMEs with sources within 45° of the solar disk centre. The mapped CME velocity to be measured in this case is essentially the speed, V_e , with which the CME extends transversally. There is a dependence between V_e and the CME velocity V_r along its path: V_r grows on average as V_e increases (see [Gopalswamy N., et al., 2009b]), which is why detecting a relation between V_e and n would indirectly confirm the fact that V_r and n are related.

CME formation was studied using multi-wave data obtained by high temporal and spatial resolution instruments Atmospheric Imaging Assembly (AIA) [Lemen J.R., et al, 2012] onboard the Solar Dynamics Observatory (SDO) [Pesnell W.D., et al., 2012]. The AIA instruments produce full-disk images of the corona and the transition region up to R_S (R_S is the solar radius) above the solar limb, at a spatial resolution of 1.5 arcseconds and time resolution of 12 seconds. To detect various manifestations of solar activity, we used observations at several spectral channels: 94 Å, 304 Å, 171 Å, 193 Å, 211 Å and 131 Å. To detect the frontal structure (FS) for each CME under study we used difference images of the Sun, in the above spectral channels of the AIA. Additional information on the properties of the ARs where we observed the formation of the CMEs and related flares was taken from the website <https://solarmonitor.org/>.

For 3D calculations of the magnetic field above the PIL in the AR, we used vector measurements of photospheric field by the Helioseismic and Magnetic Imager (HMI) [Schou J., et al, 2012] onboard the SDO. The pixel size of the registering matrix of this instrument ≈ 0.5 arc seconds, the time resolution $\approx 12'$. We used HMI data, in which magnetic field measurements were corrected for the π -ambiguity of the transverse component of the field. The vector measurements of magnetic field allowed three components of the photospheric magnetic field to be found: B_x , B_y (horizontal components) and B_z (vertical component). 3D calculations of the field were based on the non-linear force-free field (NLFFF) approximation.

This study used an effective implementation of the optimisation technique proposed in [Wheatland M.S., et al., 2000] to reconstruct the magnetic field, in the NLFFF approximation. This implementation was detailed in [Rudenko G.V., et al., 2009]. Magnetic field calculations in the NLFFF approximation served to plot the height distributions of the transverse component of magnetic induction $B_r(t) = \sqrt{B_x^2 + B_y^2}$ above the PIL in the AR, up to $\sim 0.21 R_S$ above the photosphere, for all the events examined. Height distributions of the magnetic field decay index $n(h)$ and $\langle n \rangle_{PIL}$ were also plotted above the PIL in each AR. 3D calculations of magnetic field were conducted in a 3D box with a $[0.316 \times 0.316]$ R_S^2 basis and height $h = 0.21 R_S$.

Results

The findings of our research into the CME properties will be exemplified by the halo CME at 09.03.2012 registered in AR NOAA 11429 as moving at intermediate speed $V_{lin} = 950$ km/s. The main stages of the CME at 09.03.2012 formation are shown in Figure 1: stage I – filament eruption (Figure 1a), stage II – formation of loop-like structures of various scales (Figure 1b), stage III - formation of the FS of the mass ejection (Figure 1c). This sequence of the observed structures is similar to those detected earlier and characteristic of generation of CMEs with various velocities [Fainshtein V.G., et al., 2015; Grechnev V.V., et al., 2016].

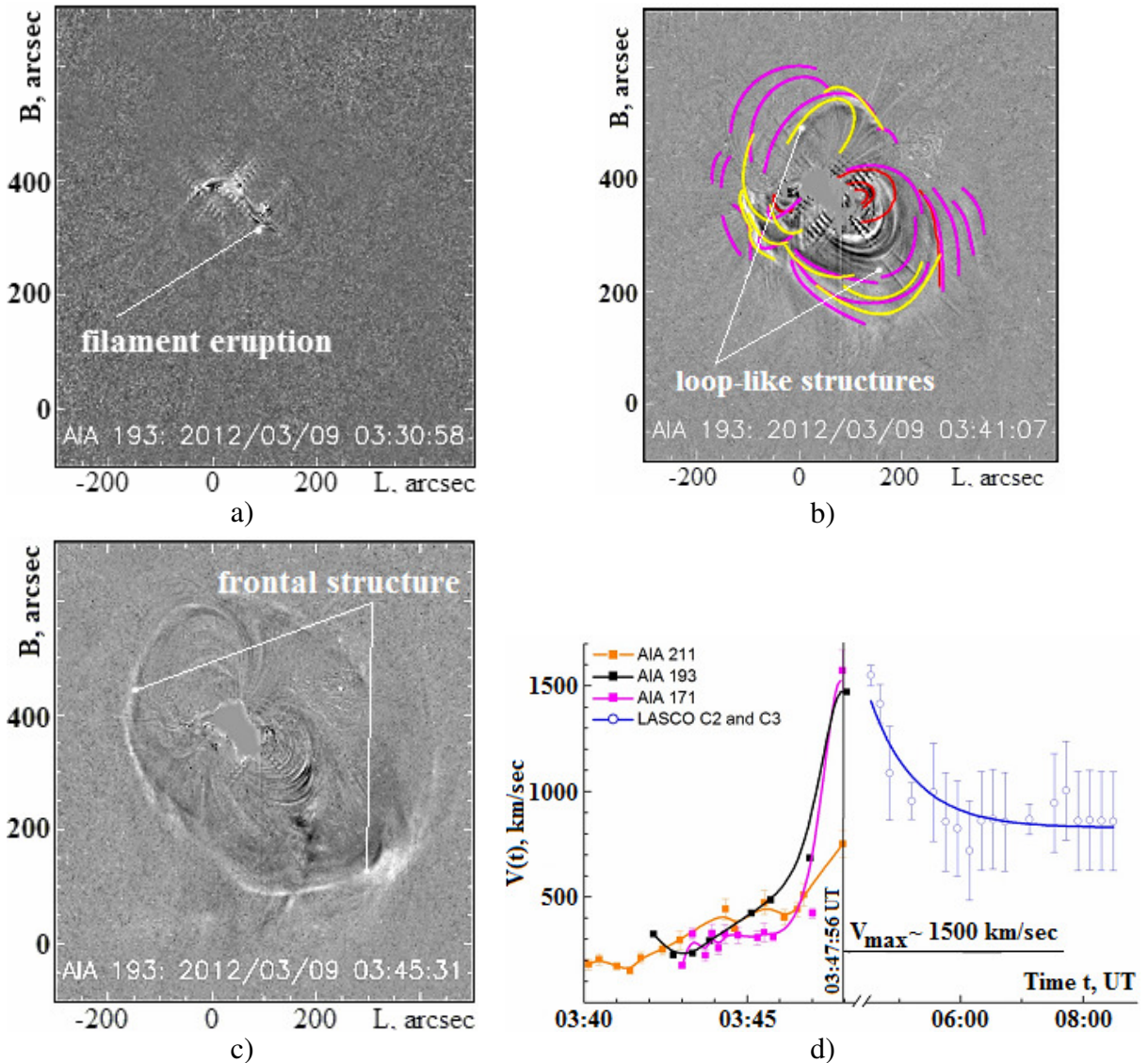


Fig. 1 a) – illustration of a filament eruption; b) – observed loop-like structures; c) – fully-formed FS of the CME; d) – temporal profile of the mapped velocity V_{lin} , reconstructed from observations of the Sun by SDO/AIA and SOHO/ LASCO, for the CME at 09.03.2012

Shown in Figure 1d is the profile of the mapped velocity of the CME at 09.03.2012 FS based on UV observations of the Sun, in different AIA spectral channels, as well as on LASCO data. Note one feature of the CME kinematics: the mass ejection is observed to move at maximum speed in the AIA 171 Å and 193 Å channels, even before it enters the LASCO C2 coronagraph field of view.

Figure 2 is a magnetogram of AR NOAA 11429, where the CME at 09.03.2012 was observed to be forming. This image shows a 2D distribution of the magnetic field radial component, B_r . Areas of higher values of $|B_r|$ are distinct, where the light-colored sites correspond to $B_r > 0$, dark-colored ones to $B_r < 0$. The yellow line in Figure 2 indicates the main PIL of the photospheric magnetic field (where $B_r = 0$) in the AR under study. Small-scale segments with sizes equal to the spatial resolution of the HMI are numbered in the PIL - over these segments we plotted the radial distributions of the field transverse component $B_t(h)$ and "decay index" vs height $n(h)$. The circle highlights the AR area with the PIL where we identified the CME at 09.03.2012 formation source. Magnetograms with the PIL and

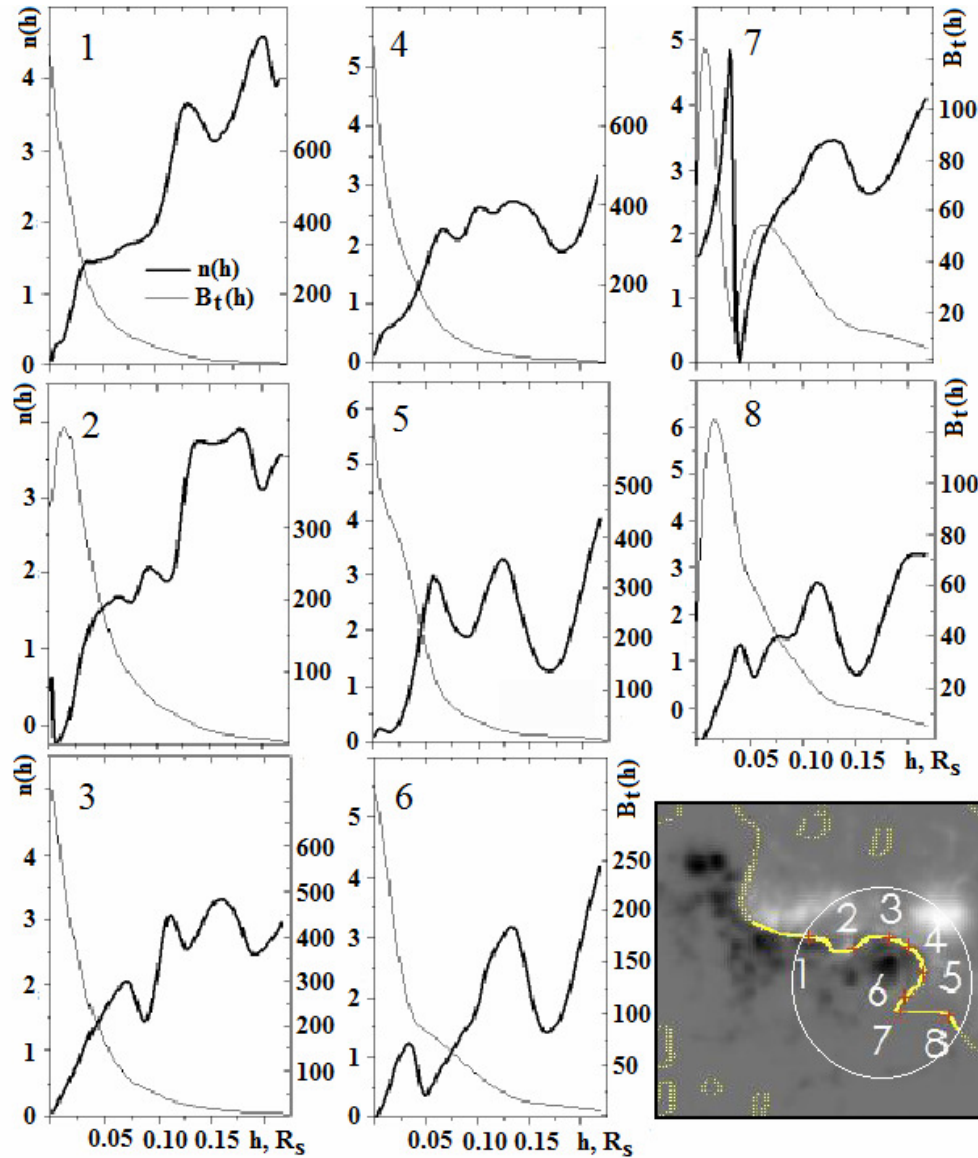


Fig. 2 AR NOAA 11429 magnetogram (at the bottom right) with the PIL and numbered small-scale areas. The radial distributions of the field transverse component $B_t(h)$ and "decay index" $n(h)$ above these areas are plotted in the right-hand panels

$B_t(h)$ and "decay index" distributions vs height $n(h)$ were obtained analogously for all the CMEs under study.

Also shown in Figure 2 are the height distributions of $B_t(h)$ and $n(h)$ above the different small-scale segments of the PIL numbered 1 to 8. After averaging the "decay index" along the highlighted segment of the main PIL of the AR photospheric field and up to $\sim 0.21 R_s$, we obtained the average value of the magnetic field decay with height, $\langle n \rangle_{PIL} = 2.642$.

It can be seen in Figure 2 that the field component $B_t(h)$ decreases monotonously above certain small-scale segments on the PIL, while local extrema are observed in the $B_t(h)$ distribution, above other segments. The behaviour of $n(h)$ above all numbered small-scale PIL segments is complex in character: non-monotonous variations, local maxima and minima are observed. Such a complicated variation of the "decay index" with height appears to reflect the complex 3D structure of the magnetic field above the PIL, including a series of loop-like structures and coronal arcades of various scales located one above another in height.

Finally, a $\langle n \rangle_{PIL}$ vs V_{lin} plot is shown in Figure 3. The V_{lin} relationship with $\langle n \rangle_{PIL}$ obviously demonstrates a positive trend, according to which the projected linear velocity V_{lin} of the CME also increases, on average, as $\langle n \rangle_{PIL}$ increases (the correlation coefficient $\rho = 0.68$).

The circle in Figure 3 highlights the value of the 09.03.2012 CME velocity $V_{lin} = 950$ km/s based on the CME catalog data. At the same time, the red point in this figure indicates the maximum velocity of this CME, ~ 1500 km/s, in the picture plane (see Figure 1d). In future, we plan to use the AIA telescope data to find the maximum velocities V_{max} for all the CMEs in question. We expect that the correlation coefficient of the V_{max} relationship with $\langle n \rangle_{PIL}$ will be higher than that for the V_{lin} relationship with $\langle n \rangle_{PIL}$.

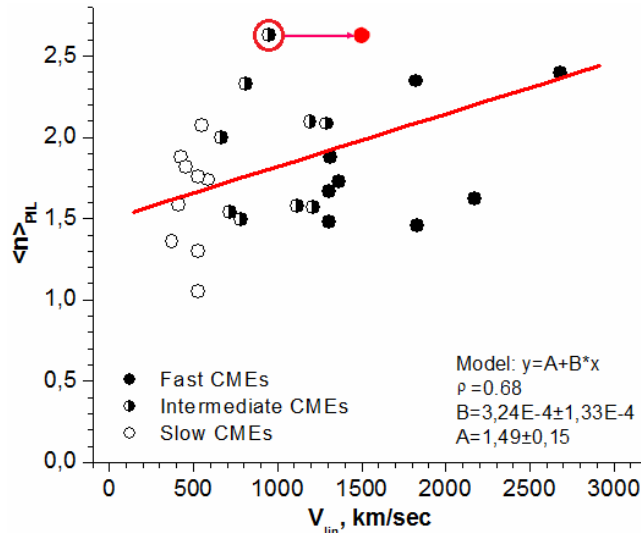


Fig. 3. Linear mapped CME velocity V_{lin} vs "decay index" n , as averaged along the PIL in the AR and over height from the photosphere up to $\sim 0.21 R_S$, denoted as $\langle n \rangle_{PIL}$

Conclusions

Coronal mass ejection (CME) formation processes and the relationship between the CME linear mapped velocity V_{lin} in the LASCO coronagraph field of view and the decay rate of the transverse magnetic-field component above the main polarity inversion line (PIL) of the photospheric field in the AR where the CME originated are studied for three different-velocity CME groups (fast, slow and intermediate-speed). The basic findings can be formulated as follows:

1. For most events, CME formation has been found to involve the following stages: filament eruption, formation of a group of loop-like structures, and formation of the frontal structure of the CME. Based on the example of one event it is shown that the temporal profile of the mapped speed of the coronal mass ejection is characterised by an increasing speed, reaching a maximum before entering the LASCO C2 field of view, and later decreasing.
2. Above most segments of the main PIL of the AR, the transverse magnetic-field component is shown to decrease, the rate of field decay with height (characterised by the decay index $n = -(h/B_t) \cdot (dB_t/dh)$) varying nonmonotonously above various PIL segments, including several local maxima and minima. This suggests a complex magnetic structure of the field above the PIL. There were no significant differences.
3. A positive trend has been found between $\langle n \rangle_{PIL}$ and linear mapped velocity V_{lin} : V_{lin} increases on average with increasing $\langle n \rangle_{PIL}$. Here, $\langle n \rangle_{PIL}$ is the decay index n averaged along the PIL and over height, within the calculation domain (up to $h \sim 0.21 R_S$).

Acknowledgment

The authors are grateful to the LASCO, AIA and HMI teams for making the data of these instruments freely available. The study was done with budgetary funding of Basic Research program II.16. Rudenko G.V. would like to thank Irkutsk Supercomputer Center of SB RAS for providing the access to HPC-cluster Akademik V.M. Matrosov (Irkutsk Supercomputer Center of SB RAS, Irkutsk: ISDCT SB RAS; <http://hpc.icc.ru/>, accessed 16.05.2019).

References

- Bateman G. (1978) MHD Instabilities. Cambridge, Mass., MIT Press.
- Chen P. F. (2011). Coronal Mass Ejections: Models and Their Observational Basis. *Living Rev. Solar Phys.*, 8, 1-92.
- Fainshtein V.G., Ya. I. Egorov (2015). Initiation of CMEs associated with filament eruption, and the nature of CME related shocks. *Advances in Space Res.*, 55, 798-807.
- Gopalswamy N., A. Dal Lago, S. Yashiro, S. Akiyama (2009a). The Expansion and Radial Speeds of Coronal Mass Ejections. *Central European Astrophysical Bulletin*, 33, 115-124.
- Gopalswamy N., S. Yashiro, G. Michalek, et al. (2009b). The SOHO/LASCO CME Catalog. *Earth Moon Planet*, 104, 295-313.
- Grechnev V.V., A. M. Uralov, A. A. Kochanov, et al. (2016). A tiny eruptive filament as a flux-rope progenitor and driver of a large-scale CME and wave. *Solar Phys.*, 291, 1173-1208.
- Lemen J.R., A.M. Title, et al. (2012). The atmospheric imaging assembly (AIA) on the solar dynamics observatory (SDO). *Solar Phys.*, 275, 17-40.
- MacQueen R. M., R. R. Fisher (1983). The kinematics of solar inner coronal transients. *Solar Phys.*, 89, 89-102.
- Pesnell W.D., B. J. Thompson, P. C. Chamberlin (2012). The Solar Dynamics Observatory (SDO). *Solar Phys.*, 275, 3-15.
- Rudenko G.V., I. I. Myshyakov (2009). Analysis of reconstruction methods for nonlinear force-free fields. *Solar Phys.*, 257, 287-304.
- Schou J., P. H. Scherrer, R.I. Bush, et al. (2012). Design and Ground Calibration of the Helioseismic and Magnetic Imager (HMI) Instrument on the Solar Dynamics Observatory (SDO). *Solar Phys.*, 275, 229-259.
- Sheeley N.R., J. H. Walters, Y.-M. Wang, R. A. Howard (1999). Continuous tracking of coronal outflows: Two kinds of coronal mass ejections. *J. Geophys. Res.*, 104, 24767- 24768.
- Török T., B. Kliem (2007) Numerical simulations of fast and slow coronal mass ejections. *Astron. Nachrich.*, 328, 743-746.
- Vršnak B., D. Sudar , D. Ruždjak (2005). The CME-flare relationship: Are there really two types of CMEs? *Astron. Astrophys.*, 435, 1149-1157.
- Webb D.F., T. A. Howard (2012) Coronal Mass Ejections: Observations. *Living Reviews in Solar Physics*, 9, Issue 1, 1-83.
- Wheatland M.S., P. A. Sturrock, G. Roumeliotis (2000). An Optimization Approach to Reconstructing Force-free Fields. *Astrophys. J.*, 540, 1150.

Global and Regional Response of the Total Electron Content to Geomagnetic Storms Occurred in January 2005

Bojilova R., Mukhtarov P.

National Institute of Geophysics, Geodesy and Geography, Sciences, Sofia, Bulgaria

E-mail: rbojilova@geophys.bas.bg

Abstract.

This study presented the global and mid-latitude ionospheric response to three geomagnetic storms occurred in January 2005: the first one on 7-8 January, the second one on 17-19 January, and the last one on 21-22 January. This period has been selected, because no major sudden stratospheric warming (SSW) occurred during this month and according to many scientists this winter is represented as an example of a background reference case corresponding to a 'normal' year. Therefore, the observed ionospheric response to the considered geomagnetic storms could be attributed mainly to the external forcing. The reaction is explored by considering N(h) profiles registered by manually scaled ionosonde measurements at station Sofia, which are used for calculating the total electron content (TEC) up to the F2-layer maximum (bottom-TEC). The full-TEC data are provided by the Center for Orbit Determination of Europe (CODE)-Bern, for the nearest point to Sofia. The basic aim of this work is to compare in detail the temporal variability of the full-TEC with bottom-TEC and top-TEC the F2-layer maximum for each of the considered geomagnetic storms. It is found that for all investigated geomagnetic storms in January 2005 the bottom-TEC is considerably different from bottom-TEC and full-TEC.

Introduction

Geomagnetic storms are associated with high-speed plasma injected into the solar wind from coronal mass ejections or coronal holes that impinges upon Earth's geomagnetic field. The ionospheric structure and variability are related to changes in solar radiation and geomagnetic activity, together with the subsequent response of the thermosphere-ionosphere system (Roble, 1995). The ionosphere also varies in response to neutral winds (Schunk *et al.*, 2009), electrodynamical coupling with the overlying plasmasphere and magnetosphere (Huba *et al.*, 2005), and dynamical coupling with the underlying atmosphere particularly effective during low solar activity conditions (Mendillo *et al.*, 2002; Rishbeth, 2006). It is well known that during geomagnetic storms the dynamics, electrodynamics and chemistry of the atmosphere-ionosphere system are modified on a global scale and cause positive and/or negative phases of ionospheric response. The latitude and longitude, season, as well as the both storm onset time and maximum are the main factors which define the positive/negative response (Mukhtarov *et al.*, 2013a; Mukhtarov and Bojilova, 2017).

Three main reasons have been proposed to explain the observed storm phases: thermospheric composition changes, neutral wind perturbations and the electric fields of magnetospheric origin (Mendillo, 2006). The total electron content (TEC) is one of the particularly important physical quantities of the ionosphere. The main reason for the TEC importance is that the trans-ionospheric radio signals, used by the Global Navigation Satellite Systems (GNSS), may experience quite large range errors and these errors are proportional to the integral of the electron density along the ray path, i.e. proportional to slant TEC. It is measured by TEC Unit (TECU) as one TECU is equal to 10^{16} electrons/m². Therefore the ionospheric effect has become the largest error source in GNSS positioning, timing and navigation. The geomagnetic storms significantly change the ionosphere especially the electron density and its vertical distribution, as well as the total electron content (TEC). The

serious problems in the ground-based HF radio communications during negative ionospheric storm are caused because the electron density and TEC decrease much below their "quiet-time" levels. The positive ionospheric storms in which electron density and TEC increase much above their "quiet-time" levels can cause serious problems in satellite communication and navigation. Because the GPS signals are used by wide range of applications, any geomagnetic storm event which makes GPS signal unreliable could have significant impact on the society. That is why a detailed study of the ionospheric response to forcing from above and below is among the important mission of the ionosphere studies.

The idea of this study is to compare the temporal variability of the full-TEC with below (bottom-TEC) and up (top-TEC) the F2- layer maximum for each of the considered geomagnetic storms in January 2005. It is found that for all cases examined in this study the bottom-TEC is considerably different from both the top-TEC and the full-TEC. An explanation of the main mechanisms responsible for the observed difference has been proposed.

Data

The geomagnetic activity is described by the planetary Kp-index is received from: <https://omniweb.gsfc.nasa.gov/>. The TEC values for the nearest point to Sofia are obtained by the Center for Orbit Determination of Europe (CODE) at Astronomical and Physical Institutes of the University of Bern: <ftp://ftp.unibe.ch/aiub/CODE/>. The reason for using the closest to Sofia point with coordinates (42.5°N, 25°E) is that the TEC data have a grid spacing of 5° x 2.5° in longitude and latitude. The N(h) profiles up to the F2-layer maximum are derived from the manually scaled ionograms (Mukhtarov et. al, 2013b) of the ionosonde station Sofia-SQ143 (42.4°N, 23.2°E). The considered quantity bottom-TEC in this paper is defined as an integral of the electron density profile while the top-TEC is the difference between the full-TEC and the bottom-TEC. The TEC response to the geomagnetic storms is described by relative deviations of the considered all three quantities (the top-TEC, bottom-TEC and full-TEC) from their stationary diurnal course.

Results

The first geomagnetic storm occurs on 7-8 January 2005 and the TEC response is presented in Fig. 1. In order to have a general idea of what the global response to this storm is Fig. 1a presents the latitude-time cross-section of the relative TEC at a longitude of 25°E for the period of 7-10 January. This storm begins in the late hours on 7 January and slightly after the midnight on 8 January the Kp-index reaches to ~ 7.5-8 (see Fig. 1c). Then a clear positive response is seen for all latitudes as the relative TEC is the largest at around 60°N. The summer Southern Hemisphere (SH) reacts predominantly negatively after the midnight on 8 January Fig. 1a. Such negative TEC response is typical for geomagnetic storms in summer (Pancheva et. al., 2016). The TEC response in the Northern Hemisphere (NH) is more complex (Fig. 1a). After the positive response seen at all latitudes in the late hours on 7 January it follows a negative response which can be traced only between 15°N and 50°N. At the same time a positive response is formed that is seen first at equatorial latitudes and later with some time delay it appears at mid-latitudes during the day-time on 8 January when the Kp-index is below 5 (see Fig. 1c). While the positive response at high-mid latitudes during the late hours on 07 January is apparently associated with the direct ionization under the action of the charged particle precipitations into the night-side of the Earth's atmosphere the positive response during the day-time conditions is probably connected with electrodynamic effects. After the decay of the positive response during the afternoon hours on 8 January a long duration negative TEC reaction has been established (Fig. 1a); the latter is related to the change of the [O] / [N₂] ratio. Fig. 1b shows the relative values of the full-TEC (upper plot), top-TEC (middle plot) and bottom-TEC (bottom plot) for the period of 7-10 January. The

bottom plot of Fig. 1c displays the Kp-index for the considered period. Considering the variability of the relative TEC (Fig. 1b) it is seen that all three quantities have first a positive response that is followed by a negative and then again a positive response. The largest changes of the relative values are as follow: (i) from -0.6 to +0.6 for the full-TEC; (ii) from -0.5 to +0.5 for the top-TEC, and (iii) from -0.8 to +1 for the bottom-TEC. These results clearly reveal that the bottom-TEC ionospheric changes are larger than those of both the top-TEC and the full-TEC.

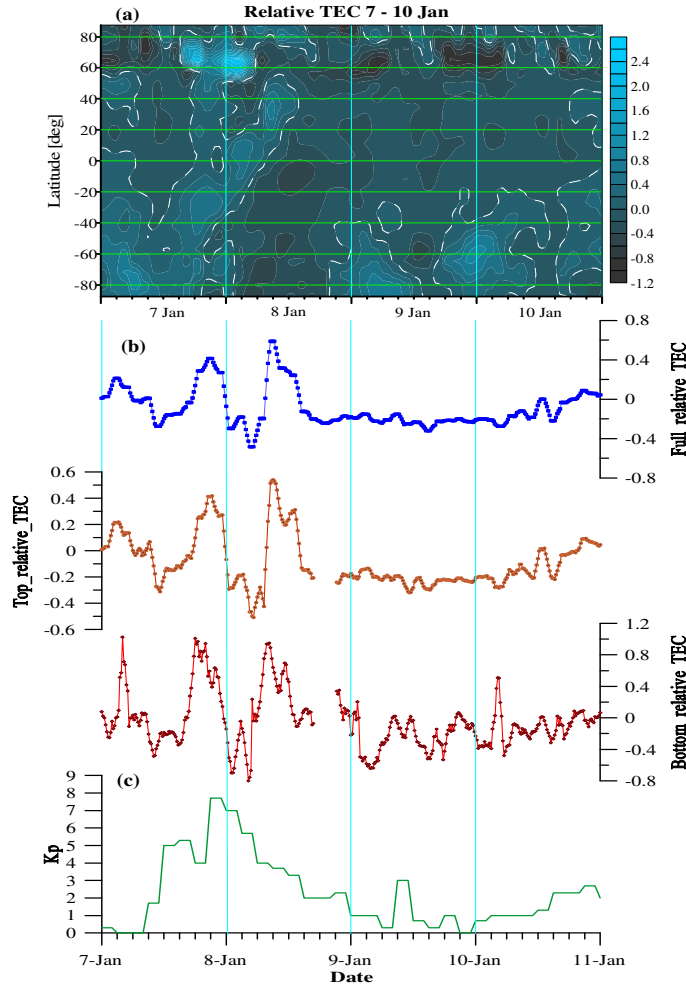


Fig. 1 (a) Global latitude-time cross section of the relative TEC; (b) temporal variability of the relative values of: the full-TEC (upper plot), top-TEC (middle plot), and bottom-TEC (bottom plot), and (c) Kp-index during the period of 7-10 January.

Fig. 2 is the same as Fig. 1 but presents the TEC response to the second geomagnetic storm; the period of 17-20 January is considered. This storm is different from the first one; it is without a sudden commencement and is significantly longer, more than 2 days. Fig. 2a shows the positive responses at latitude of 60°N during the early morning hours on 17 January when the geomagnetic activity, described by the Kp-index, is still lower than 5. Positive anomalies are seen also during the night-time hours of 17/18 and 18/19 January when the Kp-index varies between 6 and 7. It is worth noting that the large values of the night-time relative TEC at high latitudes are a result of the increase of the very low night-time TEC values in conditions close to a polar night. The relative TEC in the SH during the second half of 17 January reveals a positive response however after a midnight a negative response is observed that propagates from the polar latitudes to the equator; this is typical feature for the TEC response to the summer geomagnetic storms. The TEC response in the tropical and middle latitudes of the NH on 17 and 18 January, presented in Fig. 2a, is predominantly positive one.

Two impulses of the negative response are seen during the first half of January 19, however while the first one ranges between 15°N and 50°N the second one is only between 40°N and 50°N. The stable negative response appears during the night hours of 19/20 January ranging at tropical and mid-latitudes. The long duration of this storm accompanied by a significant amount of energy introduced in the Earth's atmosphere together with the increased inertia (Mukhtarov *et al.*, 2013; Mukhtarov *et al.*, 2018) defines a considerable time of the ionosphere recovery. The relative values of the three characteristics: full-, top- and bottom-TEC, shown in Fig. 2b, demonstrates positive anomalies on January 18 as the response is the strongest for the bottom-TEC, ~2.2 above the median one. Further, while the full- and top-TEC show two positive peaks the bottom-TEC reveals three peaks. Similarly to the first storm here also, the temporal variability of the relative bottom-TEC is quite different from those of the full- and top-TEC.

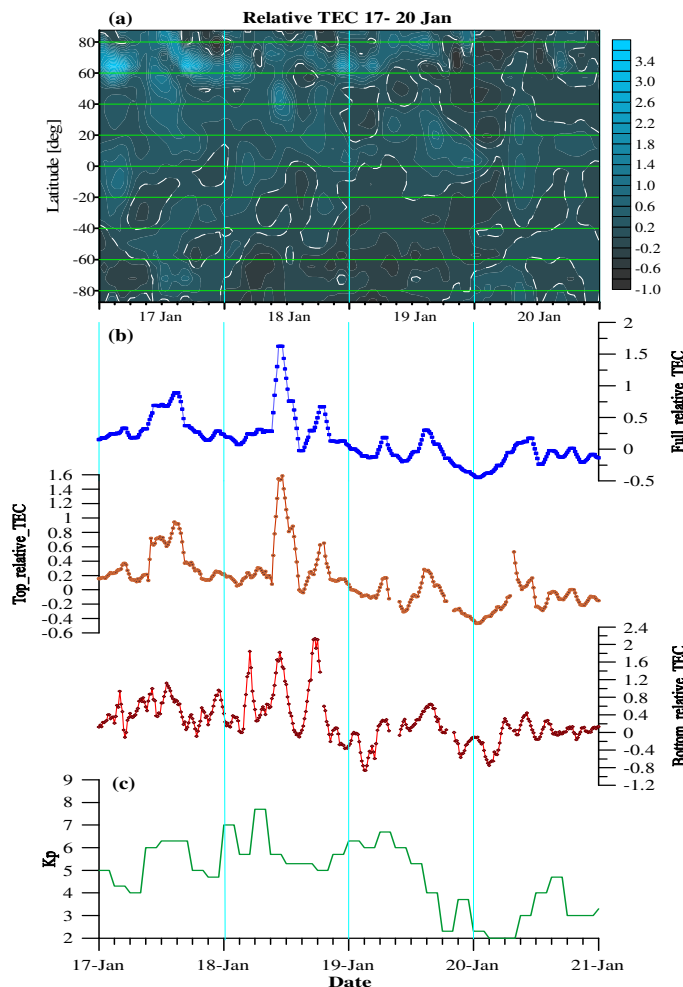


Fig. 2 The same as Fig. 1 but for the period of 17-20 January 2005

Fig. 3 presents the ionospheric response to the third geomagnetic storm that occurs on 21-22 January. This storm has approximately the same intensity as the previous two storms but has a short duration similarly to the first storm, 7-8 January. A short positive response at 60°N (Fig. 3a), coinciding with the onset of the storm, is analogous to the same phenomenon in other storms and is caused by the particle precipitations in the polar oval, i.e. direct ionization. In the SH after the evening hours on January 21 a homogeneous negative response is established. In the NH (Fig. 3a) however the TEC response strongly depends on the latitude. An initial positive response is observed at latitudes lower than 40°N while at high-mid latitudes the response is negative. After midnight all latitudes between the equator and 50°N

demonstrate a negative response; only a short-term positive reaction occurs around noon. The observed complex response, particularly of the mid-latitude ionosphere, is probably related to the incomplete recovery of the previous storm leading to the overlapping of the positive and negative reactions due to different mechanisms acting simultaneously. As a result, this winter-time TEC response appears to be different from the winter-time response of the previous two storms considered in this study, revealing strongly expressed latitudinal dependence of the reaction sign. The relative values of the full-, top- and bottom-TEC for the period of 21-23 January is shown in Fig. 3b. Similarly to the previous two storms here again the bottom-TEC reveals the largest changes (from -0.8 to 0.6) compared to the full- (from -0.5 to 0.2) and top-TEC (from -0.4 to 0.3).

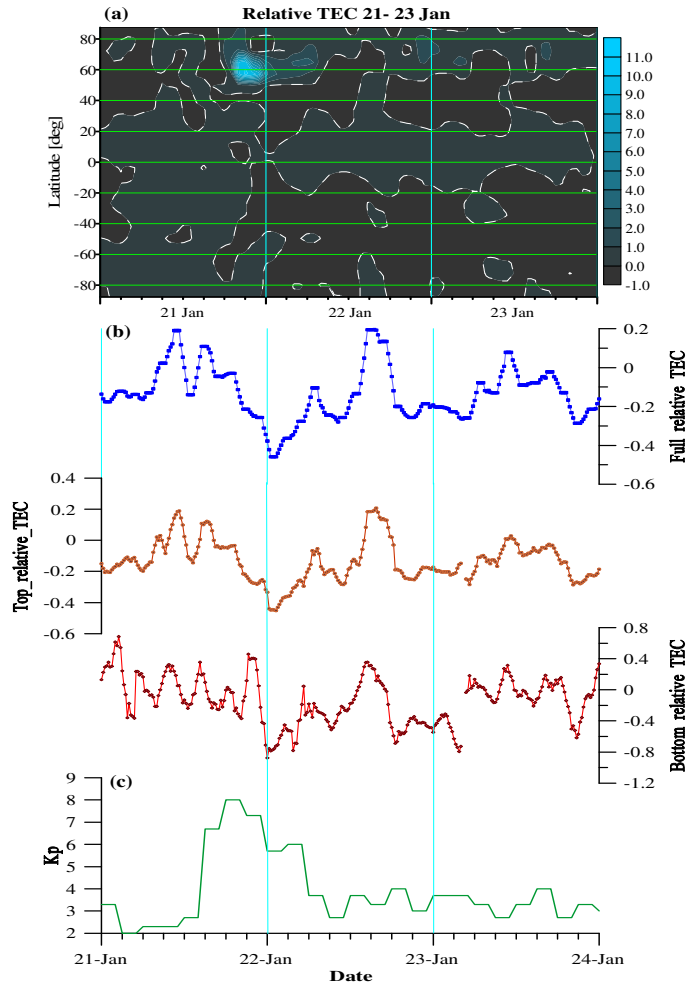


Fig. 3 The same as Fig. 1 but for the period of 21-23 January 2005

Conclusions

In this paper we have presented the global and mid-latitude ionospheric TEC response to three, moderate to intensive, geomagnetic storms occurred in January 2005. The following common pattern of the TEC anomalies is found: (i) there is a positive reaction in the winter during the initial phase of the storm that is most pronounced in day-time; (ii) during the storm with a longer duration (as that in 17-19 January) the positive anomaly continues over two days; (iii) the negative TEC response in the winter is observed during the recovery phase of the storms and after their completion; (iv) the response of the summer TEC is predominantly negative to the considered storms, and (v) the global distribution of the relative TEC during the three storms considered in this work, show the greatest positive response around 60°N.

The comparison between the top- and bottom-TEC over Sofia has been presented also. It has been found that the bottom-TEC response is significantly larger than that of the top-TEC for all three geomagnetic storms. The comparison between the top- and bottom-TEC over Sofia has been presented also. It has been found that the bottom-TEC response is significantly larger than that of the top-TEC for all three geomagnetic storms. The auroral heating during the geomagnetic storms can alter the mean global circulation of the thermosphere. Whereas for quiet conditions there is a general upwelling in the summer hemisphere flow toward the winter one at higher levels, and downwelling in the winter hemisphere, the storm-time heating adds a polar upwelling and equatorward flow in both hemispheres. During the winter the disturbed flow usually reverses the poleward one coming from the summer hemisphere and producing in this way two circulation cells which are situated below the F2-maximum. This process seriously affects mainly the vertical and meridional wind velocities which disturb mainly the ionosphere below the F2-maximum. The increased downwelling at midlatitudes moves the air into regions of increased pressure, and produces compressional heating, i.e. the neutral temperature at midlatitudes changes and affects loss and production rates. During winter downwelling of the poleward wind from the summer hemisphere air with low concentrations of molecular species, i.e. reach of atomic oxygen, is carried downward. This leads to a decrease of the loss rate and an increase of production rate. The temperature and composition effects determine the large positive TEC response seen on 7-8, 17-18 and 22 January 2005. It is worth noting also that usually the molecular-rich air at high latitudes carried by the equatorward circulation cannot reach latitudes lower than 50°N. This is another reason explaining why the ionospheric response over Sofia in the winter is predominantly positive one.

Acknowledgment

This work was partially supported by the Bulgarian Ministry of Education and Science under the National Research Programme “Young scientists and postdoctoral students” approved by DCM # 577 / 17.08.2018 and by FA8655-12-1-57.

References

- G. Roble, R. (1995) Major greenhouse cooling (yes, cooling): The upper atmosphere response to increased CO₂, *Reviews of Geophysics*, 33, 539-546.
- Huba, J. D., Joyce, G., Sazykin, S., Wolf, R., & Spiro, R. (2005) Simulation study of penetration electric field effects on the low-to mid-latitude ionosphere, *Geophysical Research Letters*, 32.
- Mendillo, M. (2006) Storms in the ionosphere: Patterns and processes for total electron content, *Rev. Geophys.*, 44, RG4001.
- Mendillo, M., Rishbeth, H., Roble, R. G., & Wroten, J. (2002) Modelling F2-layer seasonal trends and day-to-day variability driven by coupling with the lower atmosphere, *J. Atmos. Sol.-Terr. Phys.*, 64(18), 1911-1931.
- Mukhtarov, P., Andonov, B., Pancheva, D. (2018) Empirical model of TEC response to geomagnetic and solar forcing over Balkan Peninsula, *J. Atmos. Sol.-Terr. Phys.*, 167, 80–95.
- Mukhtarov, P., B. Andonov, and D. Pancheva (2013a), Global empirical model of TEC response to geomagnetic activity, *J. Geophys. Res. - Space Physics* 118.10, 6666-6685.
- Mukhtarov, P., N. Penov, D. Pancheva (2013b) N(h) profiles derived from ionograms and their application for studying mid-latitude ionospheric response to geomagnetic storms, *Comp. rend. Acad. bulg. Sci.* 66 (9), 1315-1322.
- Mukhtarov, P., R. Bojilova (2017) Influence of Solar and Geomagnetic Activity on the Ionosphere over Bulgaria, *C.R. Acad. Bulg. Sci.*, 70 (9), 1289-1296.
- Pancheva, D, Mukhtarov, P, Andonov, B. (2016) Global structure of ionospheric TEC anomalies driven by geomagnetic storms. *J. Atmos. Sol.-Terr. Phys.*, 145, 10.1016/j.jastp.2016.04.015
- Rishbeth, H. (2006) F-region links with the lower atmosphere? *J. Atmos. Sol.-Terr. Phys.*, 68(3-5), 469-478.
- Schunk, R., & Nagy, A. (2009) *Ionospheres: physics, plasma physics, and chemistry*, Cambridge university press.

Long-term Variations of the Galactic Cosmic Rays Dose Rates

Dachev T.¹, Tomov B.¹, Matviichuk Y.¹, Dimitrov P.¹, Semkova J.¹, Koleva, R.¹
Jordanova M.¹, Bankov N.¹, Shurshakov V.², Benghin, V.²

¹ SRTI-BAS, Sofia, Bulgaria

² IMBP-RAS, Moscow, Russia

E-mail: tdachev59@gmail.com

Abstract

The paper presents the solar modulation of the long-term galactic cosmic rays (GCR) dose rates variations, observed experimentally during 14 space experiments by 10 Bulgarian build Liulin type spectrometers-dosimeters, which worked in the Earth and interplanetary radiation environment between 1991 and 2019. In July 2019, two of the instruments are still operable: Liulin-MO is on the ESA-Roscosmos ExoMars-TGO in 400 km circular orbit around Mars (Semkova et al., 2018) and Liulin-Ten-Koh on the Japanese satellite Ten-Koh at about 620 km circular orbit around the Earth (Okuyama et al., 2019; Fajardo et al. 2019; Dachev et al., 2019 in this issue).

Introduction

There are two sources of primary ionizing radiation in the heliosphere - galactic cosmic rays (GCR) and high fluxes of charged particles emitted during sporadic but intense solar flares and coronal mass ejections (CME) named solar energetic particles (SEP). In low Earth orbit (LEO), energetic electrons and protons trapped in the geomagnetic field that make up the Earth's radiation belts are the third source. In LEO a fourth source, albedo neutrons and protons, is also encountered (Benton and Benton, 2001).

The experimental observations of the solar modulation of cosmic rays in the heliosphere is the main topic of the paper. The existing Liulin type instruments GCR dose rate data, averaged at L values between 4 and 6.2 in LEO and during two flights outside the Earth magnetosphere from 1991 to 2019 are compared with the monthly averaged values of the Oulu Neutron monitor count rate data (<http://cosmicrays.oulu.fi/>).

Material and methods

Liulin instruments description

A Liulin-type spectrometer (LTS) usually contains one semiconductor detector, one charge-sensitive pre-amplifier, a fast 12-channel analogue-to-digital converter (ADC), a discriminator, a real-time clock, two or more microcontrollers and a flash memory (Dachev et al., 2002). Different modifications of the LTS use additional modules such as visual and UV-sensitive photodiodes, temperature sensor, GPS with antenna and receiver, display, multimedia card or SD cards

The microcontrollers through specially developed firmware managed the device. Plug-in links provide the transmission of the data stored on the memory towards the standard personal computer (PC) or towards the telemetry system of the carrier.

A computer program in the PC is used for the full management of the LTS through a standard serial/parallel or USB communication port. The same program stores the full data sets on the satellite telemetry system or PC and visualizes the data for a preliminary analysis.

The different instruments used different power supplies.

Dose rate calculation procedure

A system international (SI) determination of the dose is used to calculate the absorbed dose in the silicon detector. The dose in SI is the energy in Joules deposited in one kilogram of a matter. The following equation relates the dose to energy loss and detector mass:

$$D(Gy) = \sum_{i=1}^{255} N_i E_i MD^{-1} \quad (1)$$

where MD is the mass of the detector in kg, N_i is the number of the pulses registered in channel “i”, E_i is the deposited energy (in Joules, known through the calibration of the detector) corresponding to channel “i”.

Recently, Dachev (2017) published a comprehensive description of the R3DR2 instrument and its calibration. Therefore, we will skip those details. Other LTS are identical to the R3DR2.

Radiation sources selection procedures

The following three primary radiation sources were expected and recognized by the data selection procedures designed for the Liulin spectrometers (Dachev, 2009):

- (i) Globally distributed primary Galactic Cosmic Rays (GCR) particles and their secondary products;
- (ii) Inner radiation belt (IRB) protons in the region of the South-Atlantic anomaly (SAA);
- (iii) Relativistic electrons and/or bremsstrahlung in the high latitudes of the satellite orbits, where the other radiation belt (ORB) is situated.

Dachev et al. (2012) described the first selection procedure based on Heffner’s formulae (Heffner 1971). During the measurements with the R3DR2 instrument, few solar energetic particles (SEP) events were observed. That is why the selection procedure was upgraded (Dachev et al. (2017)). As results, the SEP source was recognized in the International space station (ISS) data. Together with the real SEP particles, a low flux of what were likely to be mostly secondary particles (SP) (protons, neutrons and heavier than H^+ ions), some of them associated with detector interactions, were also found in the data.

Table 1






No	Carrier-name, Experiment-name, Orbit-inclination [Deg], Estimated Shielding [g·cm ⁻²]	Time		Number of meas.; Resolution [sec]; L-value	Average characteristics				External view
		Begin (dd/mm/yyyy), Main Reference	End (dd/mm/yyyy)		Altitude Above Earth [km]	Flux [cm ⁻² ·s ⁻¹]	Dose-rate [μGy·h ⁻¹]	D/F ratio [nGy·cm ⁻² ·part. ⁻¹]	
1	“MIR”-SS, LIULIN, 51.8°, >20	02/01/1991, (Dachev-et-al., 1989)	30/12/1991	52,808; 10; >4<6.2	398	0.69	6.91	2.462	
2.1	ISS, Liulin-E094 (MDU-1), 51.8°, >20	11/05/2001, (Dachev-et-al., 2002)	25/07/2001	6,411; 30; >4<6.2	403	1.56	6.07	1.070	
2.2	ISS, Liulin-E094 (MDU-2), 51.8°, >20	11/05/2001, (Dachev-et-al., 2002)	25/07/2001	6,410; 30; >4<6.2	403	1.84	6.91	1.063	Same as 2.1
2.3	ISS, Liulin-E094 (MDU-3), 51.8°, >20	11/05/2001, (Dachev-et-al., 2002)	25/07/2001	6,755; 30; >4<6.2	403	1.98	6.67	0.967	Same as 2.1
2.4	ISS, Liulin-E094 (MDU-4), 51.8°, >20	11/05/2001, (Dachev-et-al., 2002)	25/07/2001	6,755; 30; >4<6.2	403	1.77	6.56	1.028	Same as 2.1
3	Foton-M2 satellite, R3D-B2, 62°, 1.75	01/06/2005, (Häder-et-al., 2009)	11/06/2005	990; 60; >4<6.2	283	2.34	7.84; 12	0.958	

Table 1 (continued)

4 [□]	Foton-M3, satellite, R3D-B3, 62°, 0.71 [□]	14/09/2007, (Damasso-et-al., 2009) [□]	26/09/2007 [□]	918; 60; 11 >4<6.2 [□]	278 [□]	3.04 [□]	10.70 [□]	1.004 [□]	
5 [□]	Foton-M3, satellite, Liulin-Photo, 62°, >5 [□]	14/09/2007, (Damasso-et-al., 2009) [□]	26/09/2007 [□]	955; 60; 11 >4<6.2 [□]	278 [□]	2.83 [□]	10.82 [□]	1.064 [□]	
6 [□]	HotPay2 rocket, Liulin-R, Apogee at 14.04°E, 70.67°N), ~>20 [□]	31/01/2008	31/01/2008 [□]	1; 30; 4.4 [□]	377 [□]	1.95 [□]	10.18 [□]	1.452 [□]	
7 [□]	ISS, R3DE, 51.8°, 0.3 [□]	22/02/2008 (Dachev-et-al., 2012a) [□]	22/06/2009 [□]	107,900; 10; 11 >4<6.2 [□]	353 [□]	3.23 [□]	11.51 [□]	1.053 [□]	
8 [□]	Chandrayaan-1, satellite, RADOM, Moon encounter, 0.45 [□]	29/10/2008 (Dachev-et-al., 2011) [□]	07/11/2008 [□]	52,688; 10	230,526 [□]	3.08 [□]	12.57 [□]	1.134 [□]	
9 [□]	ISS, R3DR, 51.8°, 0.3 [□]	20/02/2010 (Dachev-et-al., 2015) [□]	20/08/2010 [□]	27,082; 10; 11 >4<6.2 [□]	366 [□]	2.89 [□]	11.38 [□]	1.060 [□]	
10 [□]	BION-M-No.1, satellite, RD3-B3, 65°, >20 [□]	19/04/2013 (Dachev-et-al., 2014) [□]	13/05/2013 [□]	6,442; 60; 11 >4<6.2 [□]	567 [□]	2.83 [□]	9.43 [□]	0.955 [□]	
11 [□]	Foton-M-No.4, satellite, RD3-B3, 65°, >20 [□]	18/07/2014	31/08/2014 [□]	5,997; 60; 11 >4<6.2 [□]	399 [□]	2.19 [□]	7.76 [□]	0.969 [□]	Same-as-10 [□]
12 [□]	ISS, R3DR2, 51.8°, 0.3 [□]	25/10/2014 (Dachev-et-al., 2017) [□]	10/01/2016 [□]	322,709; 10; 11 >4<6.2 [□]	417 [□]	1.9 [□]	7.1 [□]	1.083 [□]	Same-as-9 [□]
13 [□]	ExoMars Trace Gas Orbiter-TGO, Liulin-MO, transit-to-Mars, ~10 [□]	22/04/2016 (Semkova-et-al., 2018) [□]	15/09/2016 (Still-operable-in-Mars-orbit) [□]	2164; 3600	75,880,658 [□]	3.11 [□]	12.08 [□]	1.078 [□]	
14 [□]	Ten-Koh satellite, Liulin-Ten-Koh, 97.8°, ~10 [□]	29/10/2018 (Fajardo-et-al., 2019) [□]	16/01/2019 (Still-operable-in-Earth-orbit) [□]	12; 29.62; >7 [□]	610 [□]	2.71 [□]	12.68 [□]	1.201 [□]	

Dachev (2009) and Dachev (2017) published a comprehensive explanation of the LTS instruments radiation sources selection procedures and associated with them shapes of the deposited energy spectra.

Results for the GCR dose rate distributions

A total of 10 different space instruments were developed, qualified and used in 14 space missions between 1988 and 2019 (Dachev et al. 2015a, 2019; Semkova et al., 2018) by the scientists from the Solar-Terrestrial Physics Section, Space Research and Technology Institute, Bulgarian Academy of Sciences (SRTI-BAS). GCR variations data from 1991 to 2019, observed during 14 experiments in space are used. The last column of Table 1 presented the external view of the 10 LTS used. Table 1 summarizes the information, concerning the different experiments.

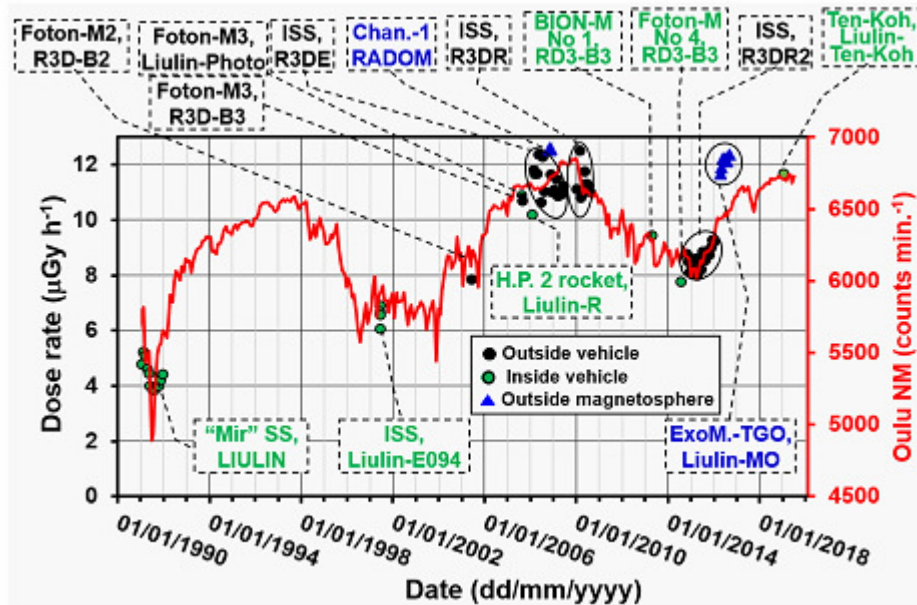


Fig. 1 Long-term variations of the averaged dose rates observed in the L range between 4 and 6.2 (black and dark-green points) or outside the magnetosphere and outside the vehicle (blue triangles) during 14 Liulin-type experiments between 2001 and 2019. The Liulin data are compared with the monthly averaged values of the Oulu Neutron monitor count rate.

Figure 1 presents the long-term variations of the averaged dose rates observed during 12 Liulin type experiments in the L range between 4 and 6.2 outside or inside (black and dark-green points) the vehicle. In addition, the 2 experiments measured outside the magnetosphere are shown by blue triangles. The total of 14 LTS experimental data are compared with the monthly average Oulu neutron monitor (NM) count rate.

First data in Fig. 1 are from LIULIN (Dachev et al., 1989) instrument in 1991. These, are the largest continues amount of LIULIN data, in comparison with more sporadic data obtained in 1989-1990 and 1992-1994. Major finding in the monthly averaged Liulin data in Fig. 1 is the strong decrease of the dose rates in June 1991, connected with the lowest Oulu NM count rates for the whole period.

The LIULIN instrument used voltage to frequency converter (VFC) and the threshold sensitivity was 83 keV. All data from other 13 experiments used Amplitude to digital converters and the threshold sensitivity is 40 keV.

Never the less that different calibrations were performed with LIULIN (Dachev et al., 1998), the final coefficient for the transformation of the pulse rate from the VFC to dose rate was overestimated. To match better the LIULIN data in Fig. 1 with other observations, we modify them by subtraction of $5\text{-}\mu\text{Gy h}^{-1}$ from the values calculated with the overestimated transformation coefficient. No other instrument values in the paper were modified.

Second data set of 4 dark-green points in Fig. 1 is from Liulin-E094 system, which consists of four mobile, battery operated, dosimetry units (MDU) and one control and interface unit (pls. see the picture in road 2.1 of Table 1.). The 4 MDUs worked with 30 sec exposition at different positions inside the American laboratory module and Node-1 of ISS between 11 May and 25 August 2001 (Dachev et al., 2002; Reitz et al., 2005; Nealy et al., 2007; Wilson et al., 2007; Slaba et al., 2011; Badavi, 2014). The MDU position was changed in average once per 5 days. Each of the 4 points in Fig. 1 represent the averaged GCR dose rate value from all data in the interval from 11 May to 25 August 2001.

The R3D-B2 instrument black point presents the averaged GCR dose rates measured inside the ESA BIOPAN-5 facility (<http://www.spaceflight.esa.int/documents/foton/exposure-experiments.pdf>), outside the Russian recoverable Foton-M2 satellite between 1st and 12 of June 2005 (Häder et al., 2009).

R3D-B3 and Liulin-Photo, instruments GCR dose rate point is obtained inside the ESA BIOPAN-6 facility, outside the Russian recoverable Foton-M3 satellite by averaging of all GCR data between 14 and 26 of June, 2007 (Damasso et al., 2009). The Liulin-Photo instrument was situated inside the satellite. The measured GCR dose rates are higher than dose rate in R3D-B2 point in Fig. 1 because the smaller solar activity and respectively higher GCR flux in the heliosphere (Potgieter, 2013).

Next point in Fig. 1 is obtained at the apogee of the HotPay2 rocket (http://www.spaceflight.esa.int/pac-symposium2009/proceedings/papers/s3_26surd.pdf) with Liulin-R instrument. The apogee occurred at 377 km altitude at point with geographical coordinates (14.04°E, 70.67°N) at L=4.4.

R3DE instrument was installed in the ESA EXPOSE-E facility (<http://eea.spaceflight.esa.int/attachments/spacestations/ID50377352548f5.pdf>) outside ESA Columbus module of the ISS. The monthly averaged GCR dose rate data in Fig 1 covered the time interval between 22 February 2008 and 1 September 2009 (Dachev et al., 2012a). Being deeply shielded by the surrounding heavy ISS, Columbus and EXPOSE-E facilities the R3DE instrument GCR dose rate data was contaminant by the secondary radiation, generated in the shielding materials. That is why the R3DE GCR points are spread in relatively broad values range.

The RADOM instrument worked outside the Indian Chandrayaan-1 satellite between October 22 2008 and August 29 2009. The Chandrayaan-1 spacecraft rose to moon rendezvous orbit by five consecutive in-plane perigee maneuvers to achieve the required 386,000 km apogee that placed it in a lunar transfer trajectory. The average dose rate of 12.57 $\mu\text{Gy h}^{-1}$, used in this paper, was obtained between October 29, and November 7, 2008 from more than 52,000 measurements in the altitudinal range between 88,605 and 357,678 km from the Earth and can be considered as free space value (Dachev et al., 2011).

The EXPOSE-R facility, hosted the R3DR instrument (Dachev et al. 2015) in the period from March 11, 2009 to August 20, 2010 outside of the Russian “Zvezda” module. The R3DR instrument data cover 2 periods – from March to June 2009 and from January to August 2010. Only the second period monthly averaged GCR R3DR data points are presented in Fig. 1. The highest monthly averaged point in Fig. 1 by 12.5 $\mu\text{Gy h}^{-1}$ was observed in February 2010, while the highest Oulu NM count rates was found in December 2009.

Next point in Fig. 1 is the averaged GCR dose rate was obtained inside the Russian recoverable “BION- M” No.1 satellite by RD3-B3 battery operated spectrometer between April 19 and May 13, 2013 (Dachev et al., 2014).

The averaged GCR data point obtained with the same RD3-B3 battery operated instrument inside the Russian recoverable “Foton-M” No.4 satellite between July 18 and September 1, 2014 is the next point in Fig. 1.

The monthly averaged GCR dose rate data from R3DR2 instrument, measured in the EXPOSE-R2 platform outside the Russian “Zvezda” module from October 24, 2014 to January 11, 2016 (Dachev et al. 2017a), form the “V” structure of points in Fig. 1, which contain the solar cycle 24 maximum seen with the minimum of the Oulu NM monthly average counts in March 2015. In same month, the R3DR2 GCR dose rate minimum is observed. This is the third solar cycle maximum in Fig. 1 after the first in 1991 and second in 2004. It is remarkable that the measured GCR dose rates on LIULIN, Liulin-E094 and R3DR2 instruments are proportional to the Oulu NM count rate values.

The R3DR2 instrument is the same as the one that flew in the EXPOSE-R facility from 2009-2010. The latter was named R3DR. The instrument in the EXPOSE-R2 platform has the extension R2 to distinguish between the data from the previous mission.

The Liulin-MO dosimetric telescope was launched on ExoMars trace gas orbiter (TGO) (<http://exploration.esa.int/mars/46475-trace-gas-orbiter/>) toward Mars orbit on 16 March 2016. Data obtained during the Mars encounter between 22 April and 15 of September 2016 by the first detector of the dosimetric telescope (Semkova et al., 2018) are used in this study. They are similar to the data from all other instruments data. Liulin-MO data are seen in Fig. 1 as a rising series of points a bit higher than the expected position.

The Liulin-Ten-Koh instrument (Okuyama et al., 2019; Fajardo et al. 2019) is working since October 29, 2018 inside the construction of the Charged Particle Detector (CPD) developed at the Prairie View A&M University, and NASA Johnson's Space Center of Houston, TX, USA. CPD is the primary science instrument of the 22-kilogram mass Japanese satellite Ten-Koh, developed in Kyushu Institute of Technology (Okuyama et al., 2019). The Liulin-Ten-Koh point, obtained in January 2019 is the last one in the Fig. 1.

Conclusions

The paper presents the long-term GCR dose rates variations, observed experimentally during 14 space experiments by 10 Bulgarian build Liulin type spectrometers-dosimeters, which worked in the Earth and interplanetary radiation environment between 1991 and 2019. The main conclusion from the analysis of the data is that they follow relatively very well the variations of the Oulu NM count rate data. This paper can be considered, as a preliminary one of another that will study the long term-variations of the flux and the daily dose rate.

References

- Benton, E. R., & Benton, E. V. (2001), Space radiation dosimetry in low-Earth orbit and beyond. *Nuclear Instruments and Methods in Physics Research B*, 184(1–2), 255–294.
- Badavi, F.F., (2014), Validation of the new trapped environment AE9/AP9/SPM at low Earth orbit. *Adv. Space Res.* 54, 917–928, <http://dx.doi.org/10.1016/j.asr.2014.05.010>.
- Dachev, Ts.P., Matviichuk, Yu., Semkova, J.V., Koleva, R.T., Boichev, B., Baynov, P. Kanchev, N.A., Lakov, P., Ivanov, Ya.J., Tomov, B.T., Petrov, V.M., Redko, V.I., Kojarinov, V.I., Tykva, R., (1989), Space radiation dosimetry with active detections for the scientific program of the second Bulgarian cosmonaut on board the Mir space station, *Adv. Space Res.*, 9, 247-251. [http://dx.doi.org/10.1016/0273-1177\(89\)90445-6](http://dx.doi.org/10.1016/0273-1177(89)90445-6).
- Dachev, Ts., J. Semkova, J., Petrov, V., Redko, V., Benghin, V., Kostereva, T., Miller, J., Heilbronn, L., Zeitlin, C., (1998), Analysis of the pre-flight and post-flight calibration procedures performed on the LIULIN space radiation dosimeter, *Acta Astronautica*, 42, 375-387. [http://dx.doi.org/10.1016/S0094-5765\(98\)00132-5](http://dx.doi.org/10.1016/S0094-5765(98)00132-5).
- Dachev Ts., B. Tomov, Yu. Matviichuk, Pl. Dimitrov, J. Lemaire, Gh. Gregoire, M. Cyamukungu, H. Schmitz, K. Fujitaka, Y. Uchihori, H. Kitamura, G. Reitz, R. Beaujean, V. Petrov, V. Shurshakov, V. Benghin, F. Spurny, (2002), Calibration Results Obtained With Liulin-4 Type Dosimeters. *Adv. Space Res.* V 30, No 4, 917-925. [http://dx.doi.org/10.1016/S0273-1177\(02\)00411-8](http://dx.doi.org/10.1016/S0273-1177(02)00411-8).
- Dachev, Ts.P., (2009), Characterization of near Earth radiation environment by Liulin type instruments, *Adv. Space Res.*, 44, 1441-1449. <http://dx.doi.org/10.1016/j.asr.2009.08.007>
- Dachev, Ts. P., B. T. Tomov, Yu.N. Matviichuk, Pl. G. Dimitrov, Vadawale, S. V., J. N. Goswami, V. Girish, G. de Angelis, (2011), An overview of RADOM results for Earth and Moon Radiation Environment on Chandrayan-1 Satellite, *Adv. Space Res.*, 48, 5, 779-791. <http://dx.doi.org/10.1016/j.asr.2011.05.009>.
- Dachev, Ts., G. Horneck, D.-P. Häder, M. Lebert, P. Richter, M. Schuster, R. Demets, (2012), Time profile of cosmic radiation exposure during the EXPOSE-E mission: the R3D instrument. *Journal of Astrobiology*, 12, 5, 403-411. <http://eea.spaceflight.esa.int/attachments/spacestations/ID501800a9c26c2.pdf>.
- Dachev, Ts., G. Horneck, D.-P. Häder, M. Schuster, and M. Lebert, (2015), EXPOSE-R cosmic radiation time profile, *Journal of Astrobiology*, 14, 17-25. <http://dx.doi.org/10.1017/S1473550414000093>.
- Dachev, T.P., J.V. Semkova, B.T. Tomov, Yu.N. Matviichuk, Pl.G. S. Maltchev, R. Koleva, Pl., Dimitrov, N.G. Bankov, V.V., Shurshakov, V.V., Benghin, E.N., Yarmanova, O.A. Ivanova, D.-P. Häder, M.T. Schuster, G. Reitz, G. Horneck, Y. Uchihori, H. Kitamura, O. Ploc, J. Kubancak, I. Nikolaev, (2015a), Overview of the Liulin type instruments for space radiation measurement and their scientific results, 92–114. <http://dx.doi.org/10.1016/j.lssr.2015.01.005>.

- Dachev, T. P., Bankov, N. G., Tomov, B. T., Matviichuk, Y. N., Dimitrov, P. G., Häder, D.-P. & Horneck, G., (2017), Overview of the ISS radiation environment observed during the ESA EXPOSE-R2 mission in 2014–2016. *Space Weather*, 15, 1475–1489. <https://doi.org/10.1002/2016SW001580>.
- Dachev, T.P., 2018. Relativistic Electron Precipitation Bands in the Outside Radiation Environment of the International Space Station, *Journal of Atmospheric and Solar-Terrestrial Physics*, 177, 247-256. <https://doi.org/10.1016/j.jastp.2017.11.008>
- Dachev, T., P. Dimitrov, B. Tomov, Y. Matviichuk, P. Saganti, S. Holand, K. Okuyama, (2019), Analysis of the first space radiation data, obtained by Liulin Ten-Koh instrument on the Japanize Ten-Koh satellite, Proceedings of the 11th Workshop Solar Influences on the Magnetosphere, Ionosphere and Atmosphere" Primorsko, Bulgaria, June 3-5. (this issue)
- Damasso, M., Dachev Ts., Falzetta G., Giardi M.T., Rea G., Zanini A., (2009), The radiation environment observed by Liulin-Photo and R3D-B3 spectrum-dosimeters inside and outside Foton-M3 spacecraft, *Radiation Measurements*, V. 44, N0 3, 263-272. <http://dx.doi.org/10.1016/j.radmeas.2009.03.007>.
- Fajardo I., A. Lidtke, S.A. Bendoukha, K.-I. Okuyama, D. Faizullin, J.Gonzalez-Llorente, R. Morales, R. Rodríguez, M. Matsuoka, N. Urakami, R. Kwauchi, P. Saganti, D. Holland, T. Dachev, S. Tuttle, R. Dudziak, M. Miyazaki, N. Yamagata, K. Hatanaka, F. Abdullah, (2019), Challenges, development and operation of a small satellite mission to explore the space environment and its effects on spaceborne platforms, *Acta Astronautica*. (in print)
- Heffner, J. W., 1971. *Yadernoe izluchenie i zashchita v kosmose (Nuclear Radiation and Protection in Space)*, pp 115, Atomizdat, Moscow. (book in Russian)
- Häder, D.P., P. Richter, M. Schuster, Ts. Dachev, B. Tomov, Pl. Georgiev, Yu. Matviichuk, (2009), R3D-B2 - Measurement of ionizing and solar radiation in open space in the BIOPAN 5 facility outside the FOTON M2 satellite, *Adv. Space Res.* Volume 43, Issue 8, Pages 1200-1211. <http://dx.doi.org/10.1016/j.asr.2009.01.021>.
- Nealy, J. E., F. A. Cucinotta, J. W. Wilson, F. F. Badavi, N. Zapp, T. Dachev, B.T. Tomov, E. Semones, S. A. Walker, G. de Angelis, S. R. Blattnig, W. Atwell, (2007), Pre-engineering spaceflight validation of environmental models and the 2005 HZETRN simulation code, *Adv. Space Res.*, 40, 11, 1593-1610, <http://dx.doi.org/10.1016/j.asr.2006.12.030>.
- Okuyama, K.-I., Ten-Koh Development Team, P. Saganti, D. Holland, T. Dachev, R. Dudziak, and S. Tuttle, (2019), Observation of Ionospheric Disturbance Near the End of the 24th Solar Cycle Period and Space Deterioration Situation of Advanced Materials Using the Micro-Sat Ten-Koh, 32nd International Symposium on Space Technology and Science, ISTS Japan, June 2019.
- Potgieter, M. S. (2013), Solar modulation of cosmic rays. *Living Reviews in Solar Physics*, 10, 3.
- Reitz, G., Beaujean, R., Benton, E., Burmeister, S., Dachev, T., Deme, S., ... Olko, P. 2005, Space radiation measurements on-board ISS-the DOSMAP experiment. *Radiation Protection Dosimetry*, 116, 374–379. <https://doi.org/10.1093/rpd/nci262>.
- Slaba, T.C., S.R. Blattnig, F.F. Badavi, N.N. Stoffle, R.D. Rutledge, K.T. Lee, E.N. Zappe, T.P. Dachev and B.T. Tomov, (2011), Statistical Validation of HZETRN as a Function of Vertical Cutoff Rigidity using ISS Measurements, *Adv. Space Res.*, 47, 600-610. <http://dx.doi.org/10.1016/j.asr.2010.10.021>
- Wilson, J. W., J. E. Nealy, T. Dachev, B.T. Tomov, F. A. Cucinotta, F. F. Badavi, G. de Angelis, N. Leutke, W. Atwell, (2007), Time serial analysis of the induced LEO environment within the ISS 6A, *Adv. Space Res.*, 40, 11, 1562-1570. <http://dx.doi.org/10.1016/j.asr.2006.12.030>.

Regular Observations of the Power Cosmic Radio Sources on the Radio Telescope URAN-4. Processing Method, Results Keeping System and their Applying in Ionosphere Investigations

Derevyagin V. G., Kravetz R. O., Lytvynenko O. A., Panishko S. K.

Observatory URAN-4, Institute of Radioastronomy NASU

E-mail: spanishko@ukr.net

Abstract.

From 1998 up to present time in monitoring regime the observations of power radio sources were carried out on the radio telescope URAN-4 at the two frequencies 20 and 25 MHz with using radiometers and digital registration of data. The aim of the observation program is to investigate the flux variability of four cosmic radio sources 3C144, 3C274, 3C405, 3C461. In general this variability associated with ionosphere influence on propagating radio waves. Thus our observations are the radio astronomy method of ionosphere sounding. Measurements of the fluxes were consisted in that several passages of each radio source through radio telescope direction pattern for several hour angles were observed near culmination time during one day. During observation interval hundreds of thousands of radio sources records were accumulated. To process such volume of data the procedure was developed and computer program was composed which was allowed to obtain characteristic parameters for each record. In this report information about real observation intervals and quality of the observation material is presented. The procedure of processing of original observations, getting of flux densities and parameters of ionosphere scintillations and the organization of results keeping are discussed. Data applying in ionosphere investigations are cited as an example.

Introduction

Radio telescope (RT) URAN-4 (Figure 1) is the part of the radio interferometer system URAN. Radio interferometer measurements carried out by sessions limited in time therefore for using RT as alone instrument the observation program of power cosmic radio sources was offered with aim to investigate the non-stationarity of their fluxes [Derevyagin V. G. et. al., 2005]. Regular observations of fourth cosmic sources – 3C144, 3C274, 3C405 and 3C461, carried out on RT from 1987 with using radiometers at frequencies 20 and 25 MHz and two polarizations. Influence of ionosphere on propagating from radio source radiation is essential in this range of radio waves. In particular present of compact consistent in angular structure of radio sources caused fluctuations of their fluxes on irregularities of ionosphere plasma, or scintillation effect [Crane R. K., 1977]. In turn the scintillations reflect the state of irregularity structure of ionosphere so in fact they are the component of cosmic weather that induces the interest to investigate this effect.



Fig. 1 Radio telescope URAN-4

Observations: procedure of measurements and processing

Observations on RT URAN-4 were consisted in that several passages of each of 4-th radio sources through RT direction pattern were recorded near the culmination time during day (Figure. 2).

For processing distinct record was separated from day observations. Quality of record was evaluated visually which in general depended from presence of radio interferences and the estimation was assigned in each case:

- 0 – there are many radio interferences on record and it do not processed;
- 1 – very good quality of record;
- 2 – relatively good quality with presence insignificant interferences;
- 3 – radio interferences are essential but record was processed.

Record intensity was reduced to the level of calibration step that measured in the beginning and in the end of daily observations of radio source. Further theoretical function of direction pattern fitted in record obtained from observations by selection of such parameters as amplitude, shift on time, displacement on intensity axe, skew of side lobes, changing of width on zero level of calibration (Figure 3). Besides the part of record of 16 minutes duration separated near amplitude counting and such parameters of ionosphere scintillations as index, period and spectral index calculated on this part of record. Information that obtained was placed to the text files.

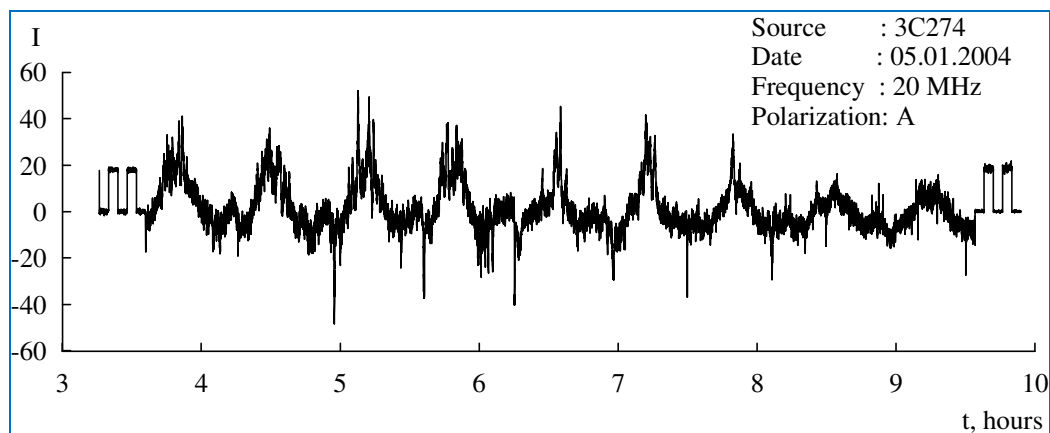


Fig. 2 Sample of the record of radio source 3C274 passages through RT URAN-4 direction pattern on 20 MHz and polarization A during 05.01.2004. The calibration steps are recorded in the beginning and in the end of the graph

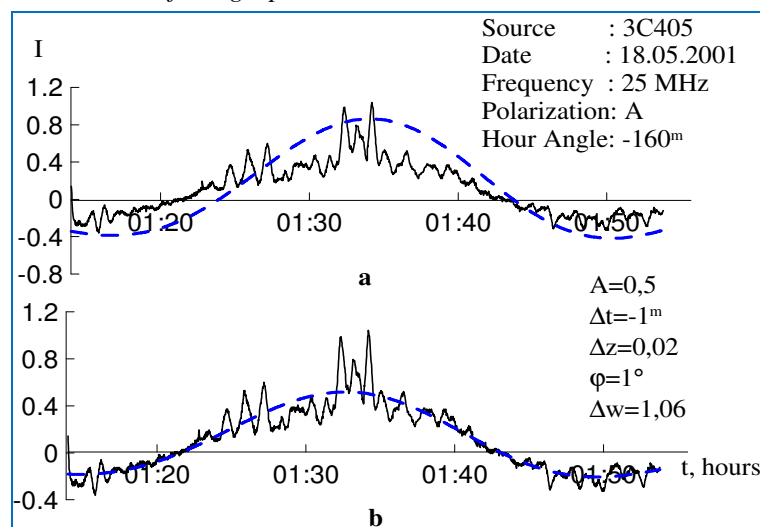


Fig.3 Fitting of the theoretical function of the RT direction pattern (dashed lines) to record obtained from radio source observations (solid lines)

Time intervals of the observations

There are some time intervals in working of RT URAN-4 those characterized of several systems of data registration:

- 1) From 1987-1990 regular observations of fourth radio sources carried out by sessions near 10 days during month. Measurements were written to paper tape of self-recorder. Processing was fulfilled manually with ruler.
- 2) In the 90s first automatical registration was developed that permitted to process of data using computer program but observations carried out very sporadically.
- 3) Regular measurements on RT began from 1998 and continued up to 2001. During this time new system of automatical measurements and digital registration with time interval 1 s was developed. From 2002 the registration system of observations was upgraded – automatical record of calibration step was appeared and time interval became 2 s. Measurements in such format continued up to April 2007. This data processed by computer program.
- 4) From 2007 up to 2010 regular observations on RT URAN-4 did not carried out due to technical occasions and were resumed in 2011. In this time next version of system of automatical measurements and digital registration was developed, time interval 1 s. This format uses in present time and new program of computer processing was created for it.

Data of the numbers of radio sources passages through direction pattern for considered time intervals contained in Table 1. Diagram of record's distribution in dependence of their quality are shown on Figure 4 for all time intervals. As a rule records with estimations 1 and 2 take in account in data analyses that consist of about 46% of all records.

Table 1. Number of the records of the radio sources passages through RT direction pattern for several observations intervals

No	Time interval, years	Number of records
1	1987- 1990	8 703
2	1991-1997	329
3	1998-2007	198 328
4	2011-2018	266 608
Sum	1987-2018	473 968

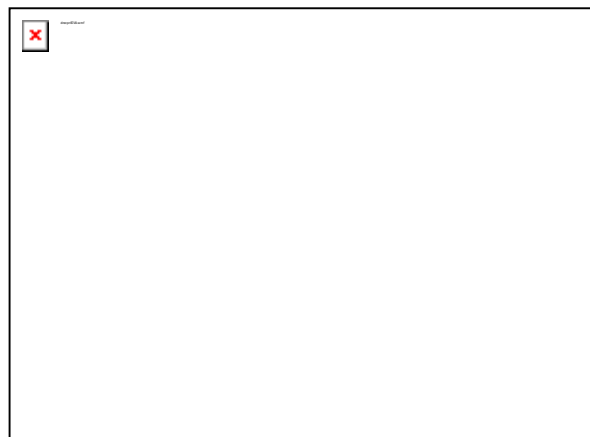


Fig. 4 Distribution of the number of radio source records obtained during 1987-2018 on RT URAN-4 in dependence of its quality: 0 – record did not processed because there are many interferences; 1 – very good quality; 2 – interferences are not essential; 3 – interferences are essential

Organization of keeping of the observations and the processing results

The vast volume of observation material required to develop easy in using system of data keeping both original data and processing results. Original data are stored on laser discs and in computer memory in form binary files and in text files from 2011 for one day and one radio source in directories on years and on months. Results of observation processing for each radio source for one frequency and one polarization placed in text file on years in chronological order. Each string of such file contains parameters of one processing record and also time variables that concerned to this record in different formats from hours to years with fractions for the convenient presentation of data in graphic form for different meaning intervals. Also it contains the references to file with original data if it is needs. Similar system of data organization allows easy enough to find necessary information and to analyze results.

Studying of the scintillation effect

The studying of the ionosphere scintillation effect can consider as an example of applying of radio sources longitude observations in decameter wave range. As mentioned scintillations on irregularities of ionosphere plasma are essential in this wave range. In view of the variability of the ionosphere state the investigation of behavior of ionosphere scintillation parameters requires longitude observation series. Graph of the seasonal-daily dependence on monthly mean values of index, period and spectral index for radio source 3C405 at frequencies 20 and 25 MHz shown on Figure 5. In spite of significant omissions in data seasonal-daily dependence marks clearly enough. You can note that index and spectral index change in a similar way but scintillation period in antiphase to them. More details about investigation of scintillation effect on RT URAN-4 observations can find in [Lytvynenko O. A., Panishko S. K., 2015, Panishko S. K., Lytvynenko O. A., 2019].

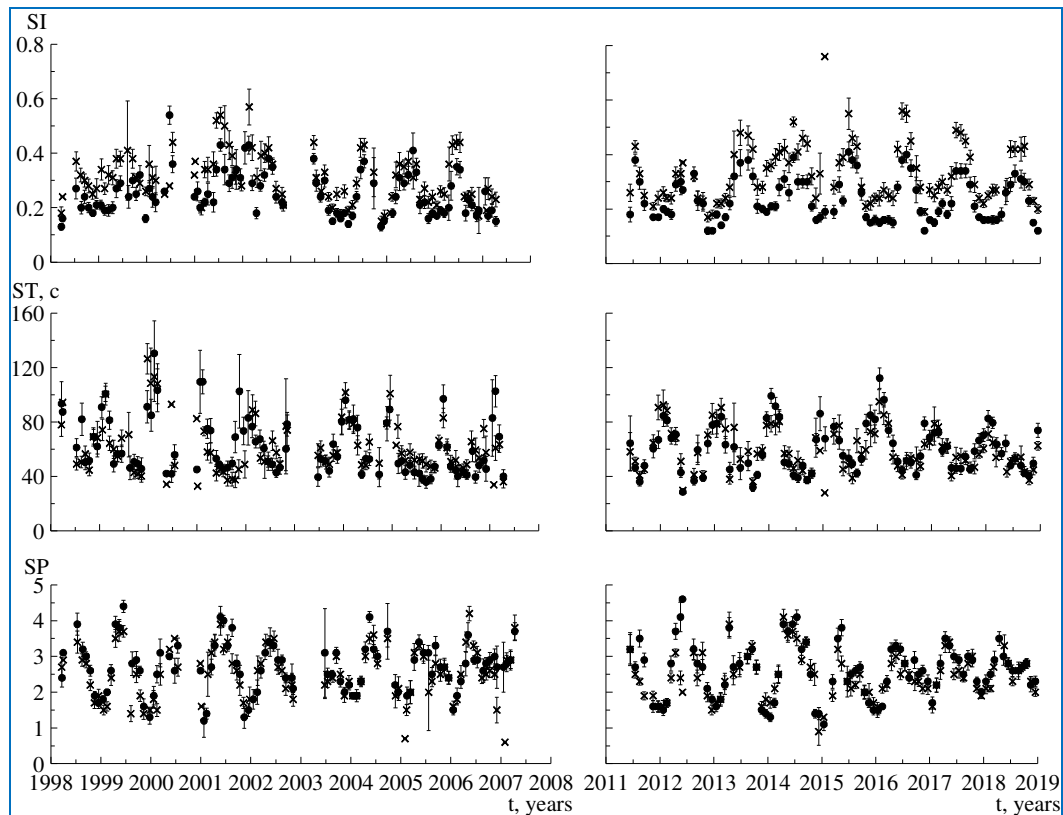


Fig. 5 Variations of the monthly mean values of ionosphere scintillations parameters on frequency 20 MHz (crests) and 25MHz (circles) during 1998-2018: top graph – index; middle – period; bottom – spectral index

Conclusions

1. Using monitoring program longitude series of observations of 4-th power cosmic sources (3C144, 3C274, 3C405, 3C461) were obtained at the frequencies 20 and 25 MHz.
2. Automatical digital registration from 1998 by means of the computer processing was allowed to get the values of relative fluxes and ionosphere scintillation parameters of the sources that observed.
3. Keeping system of data with convenient access to original observations and processing results was designed.
4. Longitude measurements enabled the studying of regularity in the behavior of several values for several time intervals in particular the seasonal-daily dependence of ionosphere scintillation index, period and spectral index was derived which cited as an example for source 3C405.

References

- Crane R. K. (1977). Ionospheric scintillations. *Proceedings of IEEE*, 65, no. 2, 180-199.
- Derevyagin V. G., Isaeva E. A., Kravetz R. O., Lytvynenko O. A., Panishko S. K. (2005). Observations the power cosmic radio sources on the radio telescope URAN-4 during 1998-2004. *Astronomical and Astrophysical Transactions*, 91, no. 5, 421-424.
- Lytvynenko O. A., Panishko S. K. (2015). Seasonal variations of the ionosphere scintillations parameters obtained from the long observations of the power cosmic radio sources at the decameter wave range. *Odessa Astronomical Publications*, 28, 235-237.
- Panishko S. K., Lytvynenko O. A. (2019). Peculiarities in the ionosphere scintillation spectral index behavior on the observations of the cosmic radio sources at the decameter wave range. *Radio Physics and Radio Astronomy*, 24, no. 1, 44-54.

Supersubstorms, High-Latitude Substorms and Space Weather Conditions

*Despirak I.V.*¹, *Lubchich A.A.*¹, *Kleimenova N.G.*²

¹ Polar Geophysical Institute RAS, Apatity, Russia

² Schmidt Institute of the Earth Physics RAS, Moscow, Russia

E-mail: despirak@gmail.com

Abstract.

The aim of our work is to study a possible influence of the solar wind large-scale structure on the substorm appearance. The substorms have been studied basing on the data obtained from SuperMAG and IMAGE networks. Three types of substorms have been considered: two types of the substorms observed at the geomagnetic latitudes higher $\sim 70^\circ$ CGC (“polar” and “expanded” substorms) and the supersubstorms (substorms with SML index < -2500 nT). Different solar wind types were determined by OMNI data base and the catalog of the large-scale solar wind phenomena. Six basic solar wind types were considered: the high speed streams from coronal holes (FAST); the interplanetary manifestations of coronal mass ejections: the magnetic clouds (MC) or EJECTA; the regions of compressed plasma before these streams – CIR and SHEATH; the slow solar wind (SLOW) streams. It is shown that the distribution of these 3 types of substorms on the different solar wind streams is almost opposite. The “Expanded” substorms are observed during FAST streams, in plasma compression regions (CIR and SHEATH) and sometimes during EJECTA observed against the background of FAST streams. The “Polar” substorms are observed during SLOW streams and EJECTA that occur against the background of a slow stream and sometimes at the end or the beginning of a FAST. The Supersubstorms (SSS) were associated with SHEATH, MC, EJECTA and they almost did not observe during FAST and SLOW streams. Thus, the impact of the different solar wind large-scale structure controls the ground-based substorm type appearance.

Introduction

It is known that solar wind is not inhomogeneous, there are different streams and structures [e.g. *Pudovkin M.I.*, 1996]. The complex large-scale structures of the solar wind can be divided into three main types:

- 1) Slow solar wind. It is the slow flux of solar plasma above the coronal streamers, with the velocity ~ 300 -450 km/s.
- 2) Quasistationary high speed streams over coronal holes (velocity ~ 600 -1000 km/s). There are recurrent streams with the period of appearance 27 – days. These streams responsible for recurrent geomagnetic disturbances.
- 3) Interplanetary Coronal mass ejections (CME), which are sources of sporadic high-speed streams and sporadic geomagnetic activity.

These three types of the solar wind vary with their sources on the Sun and interact with each other propagating from the Sun, that result a complex large-scale structure of the solar wind [e.g. *Yermolaev Yu.I.*, et al., 1991]. At the present time different classifications of the solar wind types were developed; one of these is the catalog of large-scale solar wind phenomena [*Yermolaev Yu.I.*, et al. 2009]. It should be noted also that the certain type of the solar wind is characterized by different plasma and field parameters and within certain solar wind type values of these parameters vary only slightly. So, certain solar wind type can be considered as a driver of geomagnetic activity. The purpose of our work is the study of the influence of different types of the solar wind on the geomagnetic disturbances, namely on magnetic substorms.

Data

a) Solar wind types

We defined the solar wind types using the catalog of the large-scale solar wind phenomena (<ftp://ftp.iki.rssi.ru/omni/>) and the OMNI data base. In this catalog there were 3 quasistationary, 5 disturbed types of the solar wind and shock waves are distinguished. The schematic pattern of the solar wind types shown in Figure 1.

In our work we were considered all these types of the solar wind, but HCS was considered not as separated type, it included in the SLOW type.

b) Magnetic substorms determination

Usually two electrojets - the westward and eastward - are observed in the ionosphere, which enhanced in the substorm growth phase. The additional westward electrojet appears in the night side at the substorm onset; it is a part of the substorm current wedge, through its field-aligned currents are closed in the ionosphere. During expansion phase of substorm the westward electrojet propagates poleward, and an expansion of the electrojet follows an auroras expansion [e.g. Despirak I.V., et al., 2008] This poleward expansion often occurs as a series of jumps of the westward electrojet [Wiens R.G. and Rostoker G., 1975]. In some events, the expansion may be continued from the auroral zone up to very high latitudes [e.g. Sergeev V.A., et al., 1979; Nielsen E., et al., 1988]. Note that the westward electrojet may be not inhomogeneous, and the concept of the electrojet “center” (the location of most intense current) was often used for the determination of the latitudinal location of the electrojet. Figure 2 shows the poleward expansion of the polar edge and “center” of the westward electrojet. To study the latitudinal substorm dynamic, we used the magnetic data of the IMAGE meridional chain Nurmijarvi - Ny Alesund, from 57° to 75° of the geomagnetic latitudes.

The substorm intensity is measured usually by AE, AL, AU indices of geomagnetic activity. However, in our work we used the SML index, which calculated by using the data from all SuperMAG system station, because we considered very intense substorms (supersubstorms), which develop in wide area, from lower to high geomagnetic latitudes.

c) Three special types of magnetic substorms

The aim of our work is to consider three special types of substorms, which are only recently identified: extremely intense substorms [Tsurutani B.T., et al., 2015] and substorms observed at very high latitudes [Kleimenova N.G., et al, 2012; Despirak I.V., et al., 2014].

1) First type represents extremely intense substorms (supersubstorms - SSS) which are typically observed at auroral latitudes. There are substorms, when SML or AL indices reach very high negative values (< -2500 nT).

The study of the SSS events was based on the data from magnetic ground-based observations of the SuperMAG network and Scandinavian IMAGE network.

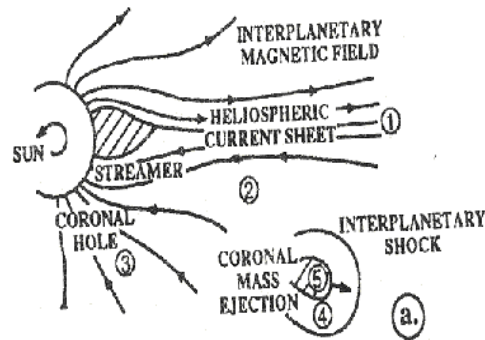


Fig. 1 The pattern of solar wind types:

- 1) heliospheric current sheet (HCS);
- 2) slow plasma flows above streamers (SLOW);
- 3) high speed streams over polar coronal holes (FAST);
- 4) and 5) coronal mass ejections, which consists from body of CME – magnetic cloud (MC) or EJECTA- and the plasma compression region on their front (SHEATH);
- 6) a plasma compression region before the fast stream (CIR).

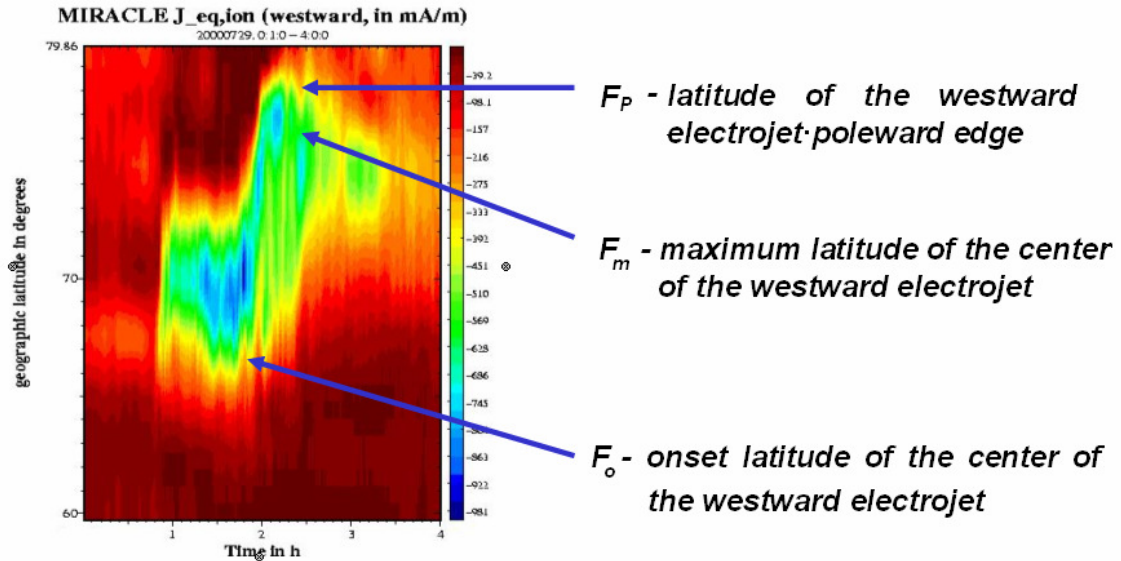


Fig. 2 The westward equivalent current obtained by MIRACLE system during substorm 29.07.2000, 01-04 UT

- 2) The second type represents the “substorms on the contracted oval” or “polar” substorms which were observed under quiet geomagnetic conditions, when the auroral oval is compressed and shifted poleward of the location of those stations from which standard magnetic activity indices are calculated. Figure 3 presents some magnetic stations, which correspond to the location of “contracted”, “extended” and “normal” auroral oval. It is seen that “polar” substorms are substorms, which are registered only at the magnetic latitudes over 70 degrees in the absence of disturbances at the lower latitudes.

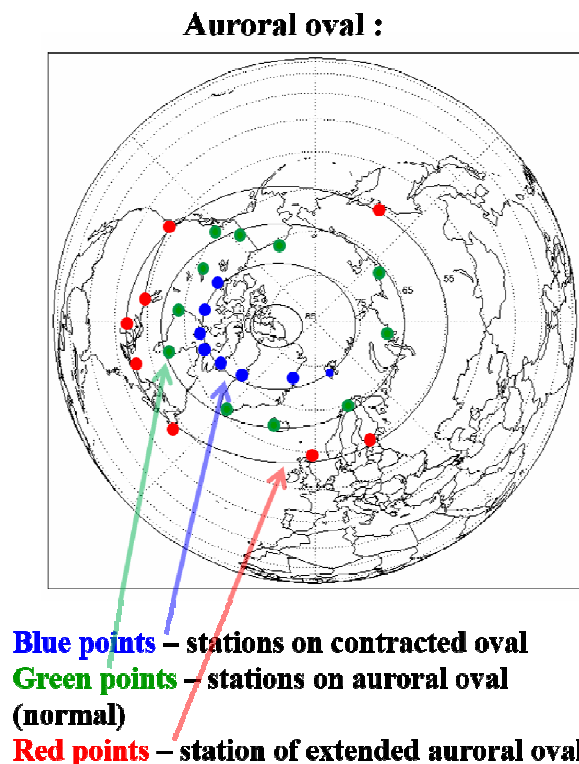


Fig. 3 The map of some magnetic stations, which correspond to the location of “contracted”, “extended” and “normal” auroral oval.

3) The third type represents the “substorms on the extended auroral oval” or “expanded” substorms, which were observed under disturbed geomagnetic conditions. These type of substorm starts at the latitudes of the auroral zone and then moves poleward. Namely, the substorm onset was observed at latitudes from 54 to 66 degrees of geomagnetic latitudes. In the maximal phase of the substorm, the “center” of the westward electrojet is observed at very high geomagnetic latitudes (above 75 degrees), at the LYR or NAL station.

High-latitude magnetic substorms were identified using the data from the IMAGE meridian chains TAR–NAL (Tartu (TAR), CGC lat. = 54.47°; Ny Ålesund (NAL), CGC lat. = 75.25°) for 1995, 1996, 1999, and 2000. For these four year there were over 400 events of high-latitude substorms selected and analyzed.

Results

Some examples of supersubstorms, “polar” and “expanded” substorms collected from SuperMAG and IMAGE stations have been presented in our previous works [Despirak I.V., et al., 2014, 2018]. The objective of this work is to systematize the previously obtained results and to reveal the connection between supersubstorms (SSS), “polar” and “expanded” substorms and the large-scale solar wind structure.

We performed the comparative analysis of the distribution of substorms on the solar wind types. The occurrence of SSS events, “polar” and “expanded” substorms was compared with the simultaneous observations of different types of the solar wind. The comparative histograms of the supersubstorms distribution by the types of the solar wind are shown in Figure 4. The vertical axis presents the number of supersubstorms, the horizontal axis shows the types of the solar wind. The “polar” substorms are marked by the blue color, the “expanded” substorms- by the burgundy color, the “supersubstorms” – by the red color.

It is seen that supersubstorms are observed: (i) mainly during solar wind magnetic clouds and SHEATH region (plasma compression region before MC/Ejecta); (ii) only sometimes they may be observed during Ejecta; (iii) very seldom SSS can be observed during FAST and CIR region (plasma compression region before FAST

The “polar” substorms are observed: (i) mainly during SLOW solar wind streams; (ii) at the end of high-speed streams (FAST); (iii) sometimes during Ejecta. But it was only during Ejecta against to background of the SLOW stream; (iiii) not observed – during Magnetic clouds

It is seen that the “expanded” substorms are observed: (i) mainly during high-speed streams (FAST); (ii) during two regions of plasma compression – CIR and SHEATH; (iii) sometimes during Ejecta. But during these Ejecta which were observed against the background of a high speed stream (FAST); (iiii) only few events are registered during SLOW streams; (iiiii) only few events are registered without certain types of the solar wind.

It is seen that the distributions of these three types of substorms differ sharply, the observation conditions are almost opposite.

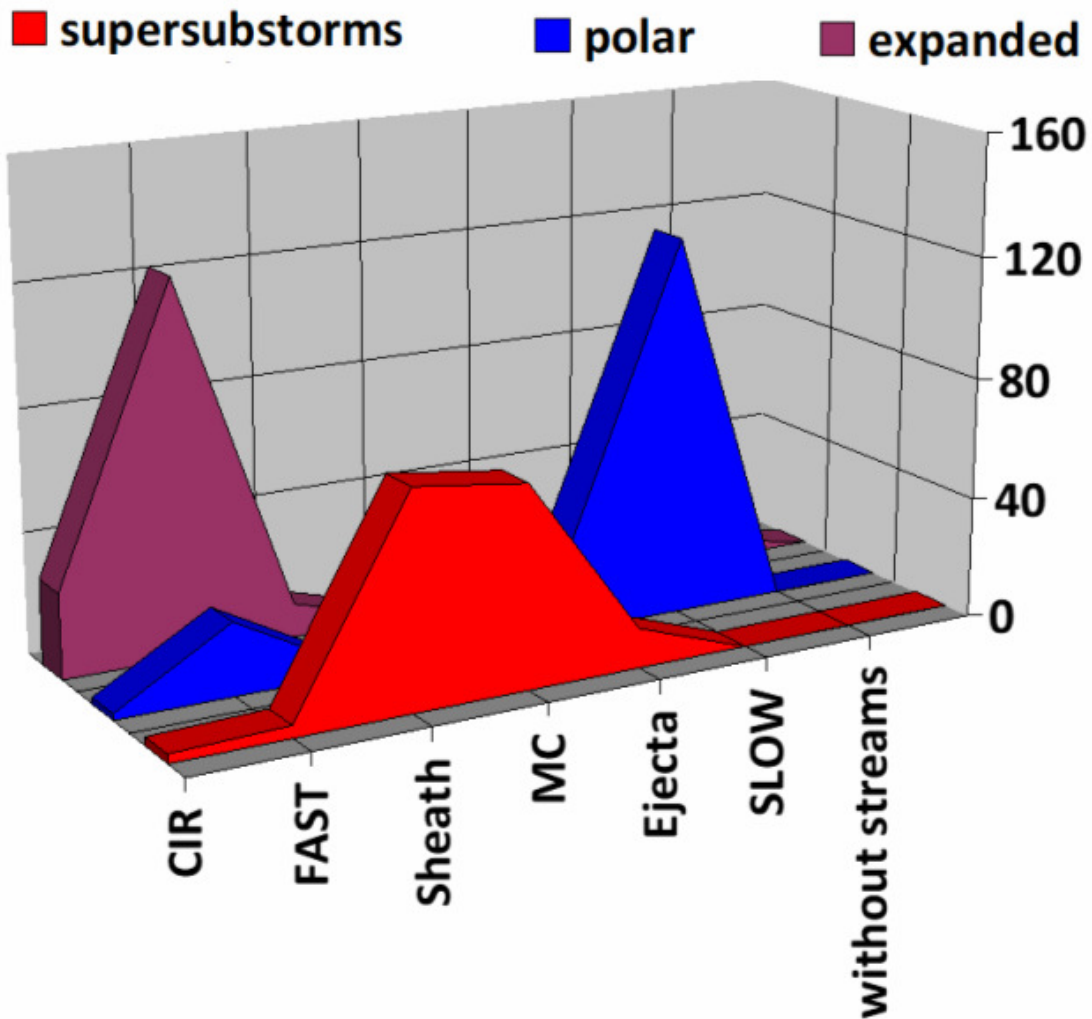


Fig. 4. Histograms of the distribution of “expanded” (burgundy color), “polar” (blue color) and supersubstorms (red color) by solar wind type. The number of events is plotted along the vertical axis.

Conclusions

The comparative analysis shown that under different space weather conditions different types of substorms are observed:

1. The supersubstorms were observed during SHEATH, MC, Ejecta, namely during interplanetary manifestations of coronal mass ejections.
2. The “expanded” substorms were registered during high-speed streams from coronal holes and compressed plasma region (Sheath and CIR)
3. The “polar” substorms were observed during slow streams and Ejecta which were associated with slow stream, also at the end of high speed streams, when solar wind velocity decrease from high to low values.

Thus, 3 types of substorms appear under different solar wind types and we can suppose, that they reflect different sources. But this question is open yet.

Acknowledgment

The IMAGE magnetometers data are available at <http://www.space.fmi.fi/IMAGE>, the SuperMAG magnetometers network data are available at (<http://supermag.jhuapl.edu/>), the IMF data were provided by (<http://omniweb.gsfc.nasa.gov/>)

References

- Pudovkin, M.I. (1996), Solar wind, *Sorovskii Obraz. Zh.*, 12, 87–94.
- Yermolaev, Yu.I. (1991), Large-scale structure of solar wind and its relationship with solar corona: Prognostic observations, *Planet. Space Sci.*, 39, no. 10, 1351–1361.
- Yermolaev, Yu.I., N.S. Nikolaeva, I.G. Lodkina, M.Yu. Yermolaev (2009) Catalog of large-scale solar wind phenomena during 1976–2000, *Cosmic Res.*, 47, no. 2, 81–94.
- Despirak, I.V., A.A. Lyubchich, Kh.K. Birnat, A.G. Yahnin (2008), Poleward expansion of the westward electrojet depending on the solar wind and IMF parameters. *Geomagn. Aeron.*, 48, no. 3, 284–292.
- Wiens, R.G., G. Rostoker (1975) Characteristics of the development of the westward electrojet during the expansive phase of magnetospheric substorms, *J. Geophys. Res.*, 16, 2109–2128.
- Sergeev, V.A., A.G. Yahnin, N.P. Dmitrieva (1979), Substorms in the polar cap: effect of high-velocity solar wind flows. *Geomagn. Aeron.*, 19, no. 6, 1121–1122.
- Nielsen, E., J. Bamber, Z.-S. Chen, A. Brekke, A. Egeland, J.S. Murphree, D. Venkatesan, W.I. Axford (1988) Substorm expansion into the polar cap. *Ann. Geophys.*, 6, 559–572.
- Tsurutani, B.T., R. Hajra, E. Echer, J.W. Gjerloev (2015) Extremely intense ($SML \leq -2500$ nT) substorms: isolated events that are externally triggered? *Ann. Geophys.*, 33, no. 5, 519–524.
- Kleimenova, N.G., E.E. Antonova, O.V. Kozyreva, L.M. Malysheva, T.A. Kornilova, I.A. Kornilov (2012) Wave structure of magnetic substorms at high latitudes, *Geomagn. Aeron.*, 52, no. 6, 746–754.
- Despirak, I.V., A.A. Lyubchich, N.G. Kleimenova (2014) Polar and high latitude substorms and solar wind conditions, *Geomagn. Aeron.*, 54, no. 5, 575–582.
- Despirak, I.V., A.A. Lyubchich, N.G. Kleimenova (2018), High-latitude substorm dependence on space weather conditions in solar cycle 23 and 24 (SC23 and SC24). *J. Atmos. Sol.-Terr. Phys.*, 177, 54–62. doi 10.1016/j.jastp.2017.09.011

Dayside Polar Magnetic Bays under Different Interplanetary Magnetic Field Direction

Gromova L.I.¹, Kleimenova N.G.², Gromov S.V.¹, Malysheva L.M.²

¹ IZMIRAN, Moscow, Russia

² Schmidt Institute Physics of the Earth RAS, Moscow, Russia

E-mail: gromova@izmiran.ru

Abstract

We study magnetic bay-like disturbances occurred in the dayside sector of the high geomagnetic latitudes ($> 70^\circ$ Mlat) under the positive (northward) and negative (southward) IMF Bz. It is known that as a rule, dayside polar magnetic bays are observed under the positive Bz component of IMF in the absence of the night-side auroral activity. In our previous works, we showed that the bay sign is controlled by the IMF By sign. We suppose that these bays could be caused by the enhancement of the so-called NBZ–system of the Field Aligned Currents. However, unlikely to that, we found that the dayside polar magnetic bays should be observed during the negative IMF Bz as well. In this case, the dayside bays occur simultaneously with strong night-side substorms. The IMF By sign does not control the sign of these bays. We suppose that this non-typical phenomenon was caused by the development of the global complicated system of the substorm ionospheric currents when the westward electrojet expands into the dayside sector. As the examples, we present several events from the ground–based Scandinavian IMAGE magnetometer chain, Intermagnet and SuperMAG data collections.

Introduction

As a rule, dayside polar magnetic bays are observed under the *positive* Bz component of IMF [Kleimenova, et al. 2015, Levitin, et al., 2015, Gromova et al., 2016]. In these papers we showed that under such IMF conditions the bay sign is controlled by the IMF By sign. It was supposed that these bays could be associated with the high-latitude ionospheric electric currents, so-called the polar electrojet – PE. The PE current direction is determined by the IMF By sign [Friis-Christensen and Wilhelm, 1975, Feldstein et al., 2006, Gromova et al., 2018]. The Field-Aligned Currents (FACs) observed under positive Bz in the polar region termed NBZ FACs. They are located in the dayside sector of the high latitudes and are more intensive in summer season. We assumed that the studied dayside high-latitude bays could be caused by an enhancement of the NBZ FACs [Gromova, 2019]. It was also noticed that there is no night-side auroral activity simultaneously with such dayside magnetic bays.

Moreover, we found that the dayside polar magnetic bays could be occurred under the *negative* IMF Bz as well, and observed simultaneously with strong night-side substorms. The IMF By sign does not control the sign of these bays.

The aim of this paper is to analyze the dayside magnetic bays observed under different IMF conditions: when the IMF Bz was strong and positive or negative (i.e. the IMF Bz dominated over the IMF By) and when the IMF Bz was weak and unstable (i.e. IMF By dominated over the IMF Bz). We present the result of case study of the high-latitude daytime magnetic bays on 30 May 2003, 23 June 2015, 22 June 2015 and 7 September 2017.

Observations and Discussion

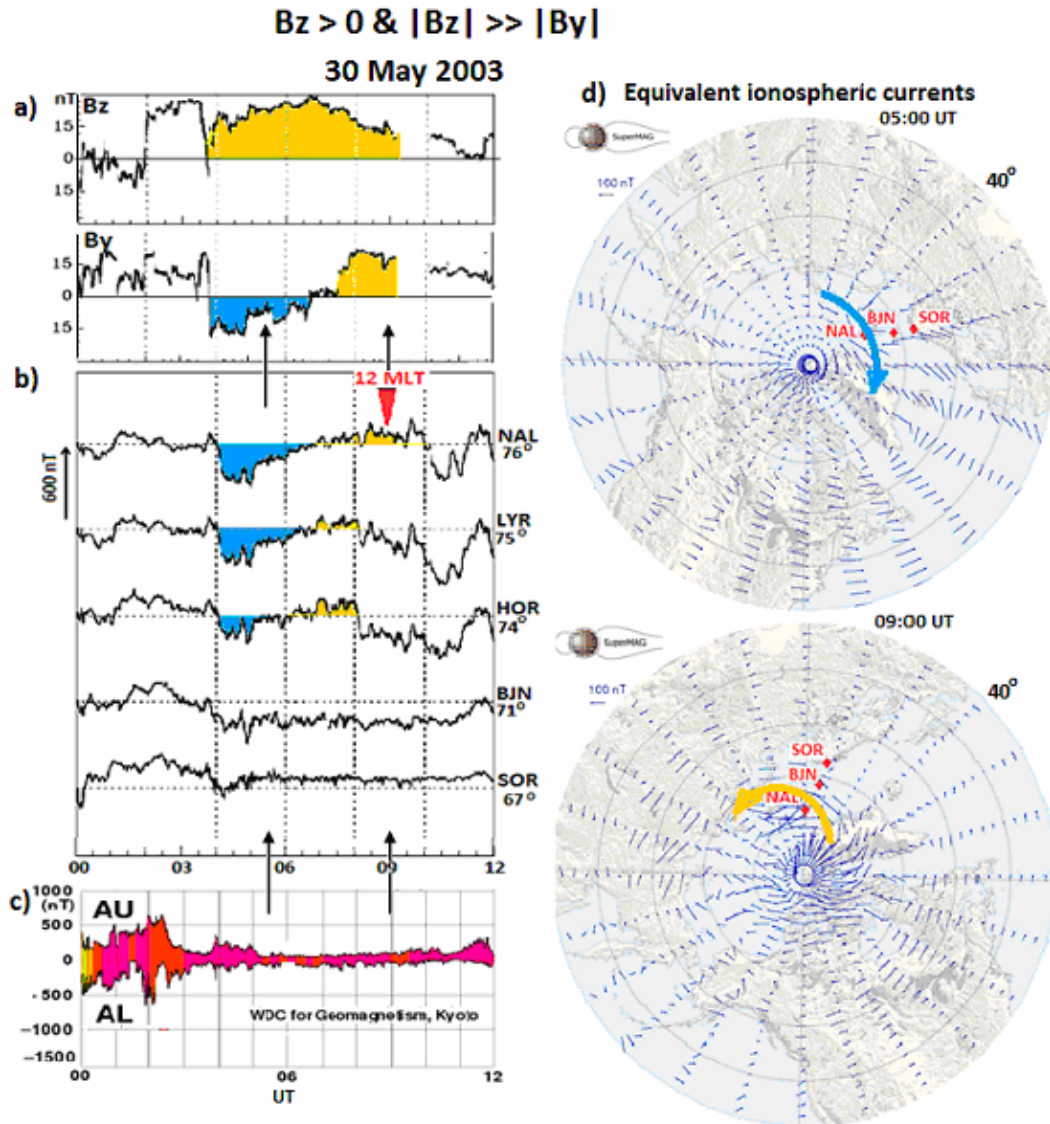


Fig.1. 30 May 2003. Left: (a) Variations of the IMF B_z and B_y , (b) difference magnetograms of the polar IMAGE stations. The local geomagnetic noon is shown by the triangle. The considered dayside magnetic bays are marked by orange/blue according to the IMF B_y and B_z signs; (c) AU/AL indexes of the substorm activity. Right: (d) distribution of the equivalent ionospheric currents at 05 UT and 09 UT related with considered bays; blue/orange arrows on the maps indicate the ionospheric current direction; location of the polar dayside stations is shown by red circles. Arrows on the UT-time axis of (a), (b), (c) point the map moments.

Dayside polar magnetic bays under the strong positive IMF B_z

Some features of the event on 30 May 2003 under *stable strong positive* IMF B_z are shown in Fig.1. The negative and positive dayside magnetic bays were observed at the polar latitudes (Fig 1b). The sign of the dayside polar magnetic bays were controlled by the IMF B_y sign (Fig 1a, b). The distribution of the ionospheric currents (Fig. 1d) shows the development of the westward polar electrojets (PE) (the negative bay about 05 UT) and the eastward one (the positive bay at 09 UT). We suppose that these magnetic bays could be caused by the enhancement of the so-called *NBZ FACs* system. According to AU/AL indices (Fig. 1c) and the maps of the ionospheric electric field vectors (Fig.1d), there was no geomagnetic activity in the auroral zone.

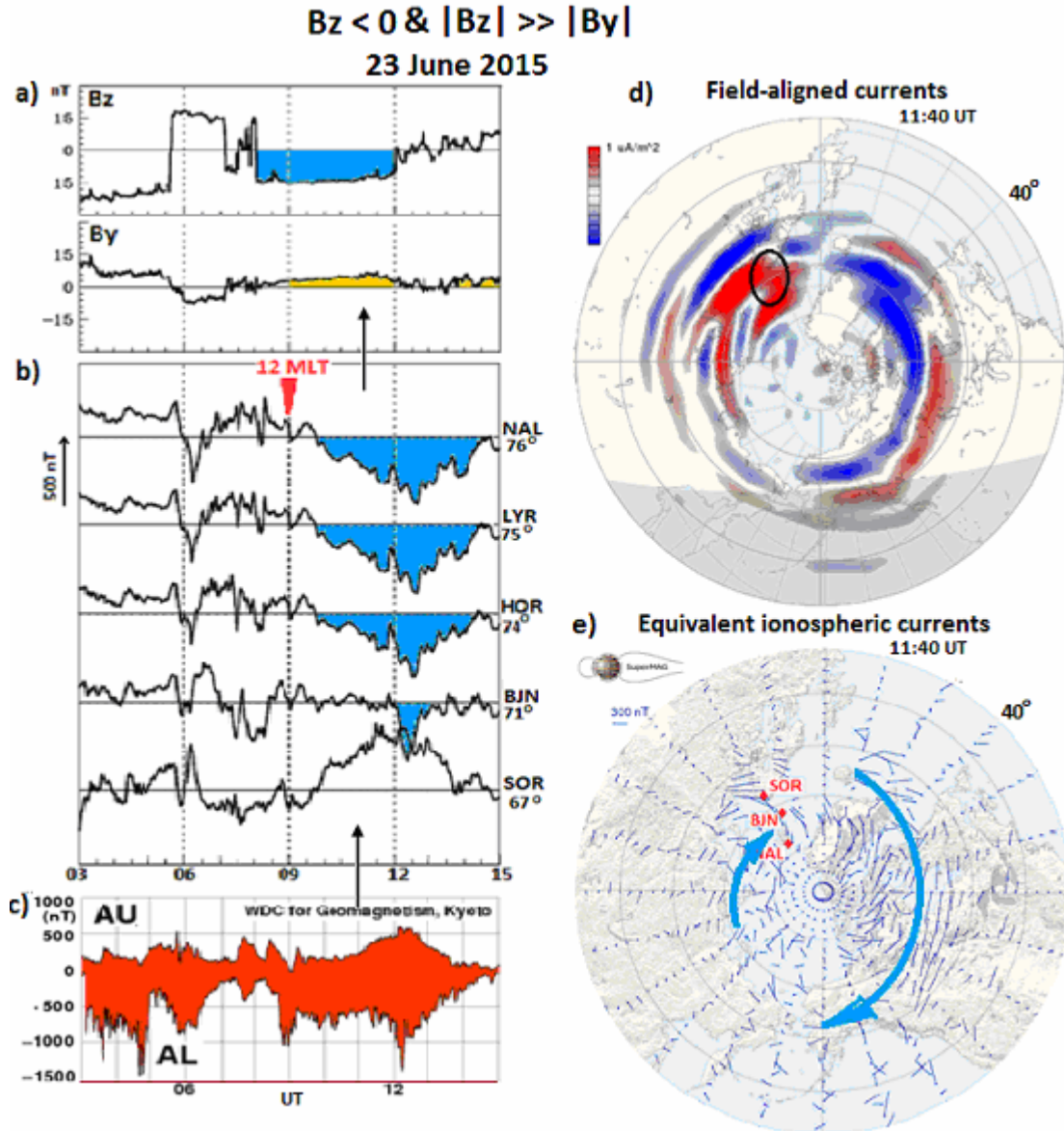


Fig.2. 23 June 2015. Left: (a) (b) (c) are the same as in Fig. 1 Right: (d) the AMPERE spatial distribution of FACS at 11.40 UT, upward currents are shown by red and downward ones in blue; the circle shows the location of the IMAGE polar stations; (e) distribution of the equivalent ionospheric currents related with the considered dayside negative bays. Arrows on the UT-time axis of (a),(b),(c) point the map moment; blue arrows on the maps indicate the ionospheric current direction, location of the dayside stations are shown by red circles.

Dayside polar magnetic bays under the strong negative IMF B_z

Polar magnetic bays could be recorded under the negative IMF B_z as well.

The dayside magnetic bay on 23 June 2015 occurred under the *strong stable negative* IMF B_z (Fig 2a). The *negative* dayside magnetic bay was observed at the IMAGE polar stations when the IMF B_y was *positive*, i.e., IMF B_y sign did not control the sign of the bay (Fig.2a,b).

This magnetic bay was accompanied by the simultaneous enhancement of the night-side substorm activity (Fig. 2c). Field Aligned Currents (FACs) increased in the night sector of the auroral latitudes (Fig. 2d) and caused an expansion (Fig. 2e) of the enhanced auroral westward electrojet into the polar region [Feldstein *et al.*, 2006] and, thus, development of the dayside polar magnetic bay.

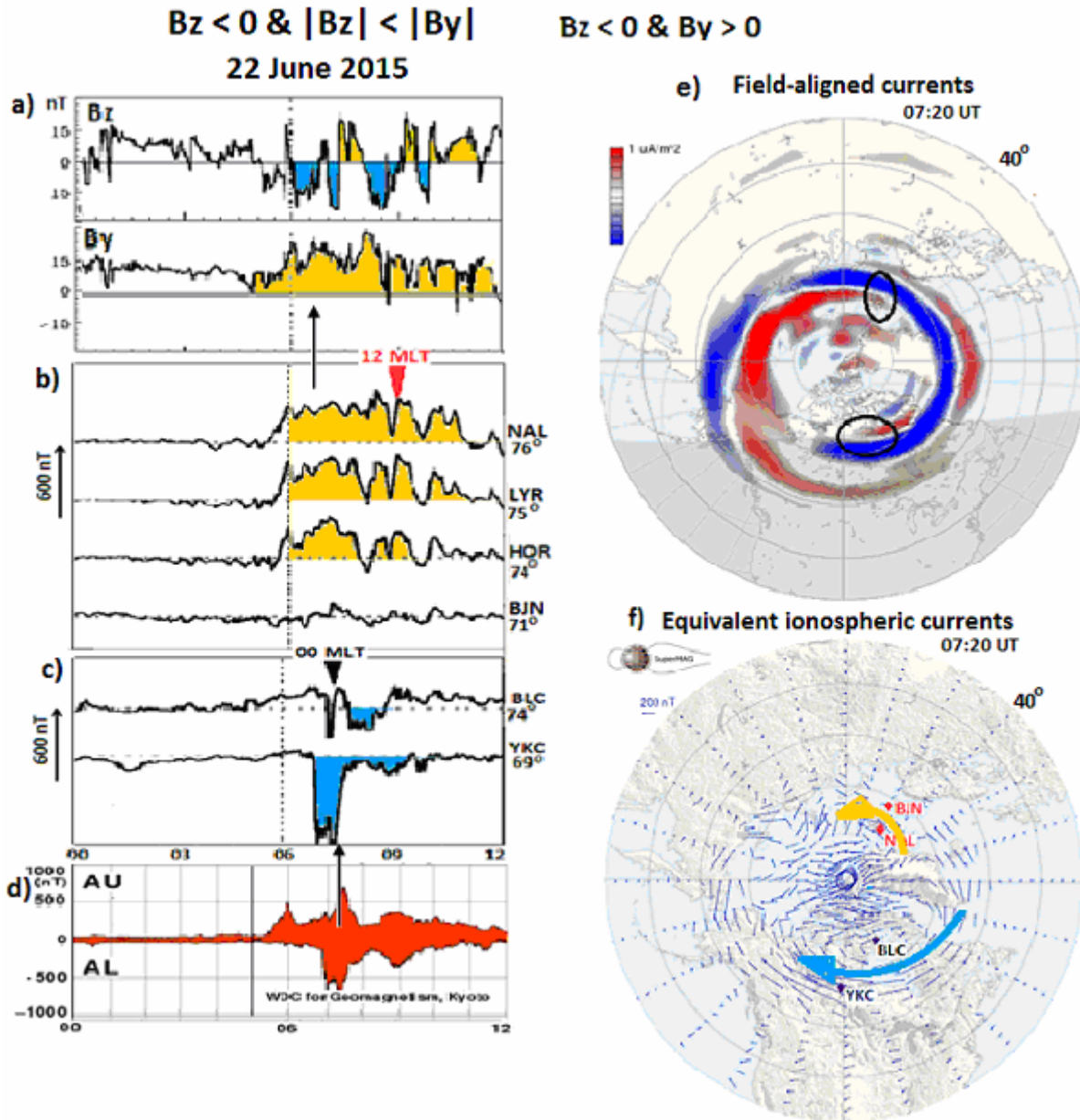


Fig.3. 22 June 2015. Left: (a), (b), (d) are the same as in Fig. 1; (c) different magnetograms of the Northern American stations in the night-side. Right: (e) the AMPERE spatial distribution of FACs as in Fig. 2 (f) distribution of the equivalent ionospheric currents at 07.20 UT related with the considered dayside positive bay, Arrows on the UT-time axis of (a),(b),(c) point the map moment; blue and orange arrows on the maps indicate the ionospheric current direction, location of the dayside/night stations are shown by red/black circles.

Dayside polar magnetic bays under weak and unstable negative IMF B_z

The dayside magnetic bays on 22 June 2015 and 7 September 2017 occurred under the weak and unstable mainly negative IMF (Fig.3a, b and Fig 4a,b). The negative and positive bays were observed at the polar latitudes, their signs were controlled by the IMF B_y sign due to dominating of the IMF B_y over the IMF B_z . But in Fig 3c,d, and Fig. 4c,d, one can see the short intervals of the non-typical enhancement of night side substorm activity as well. Development of the complicated global ionospheric currents system with the westward electrojet expanding into the dayside sector should be caused by sharp FACs increasing under abrupt burst of the negative IMF B_z (Fig. 3 e,f and Fig. 4e,f).

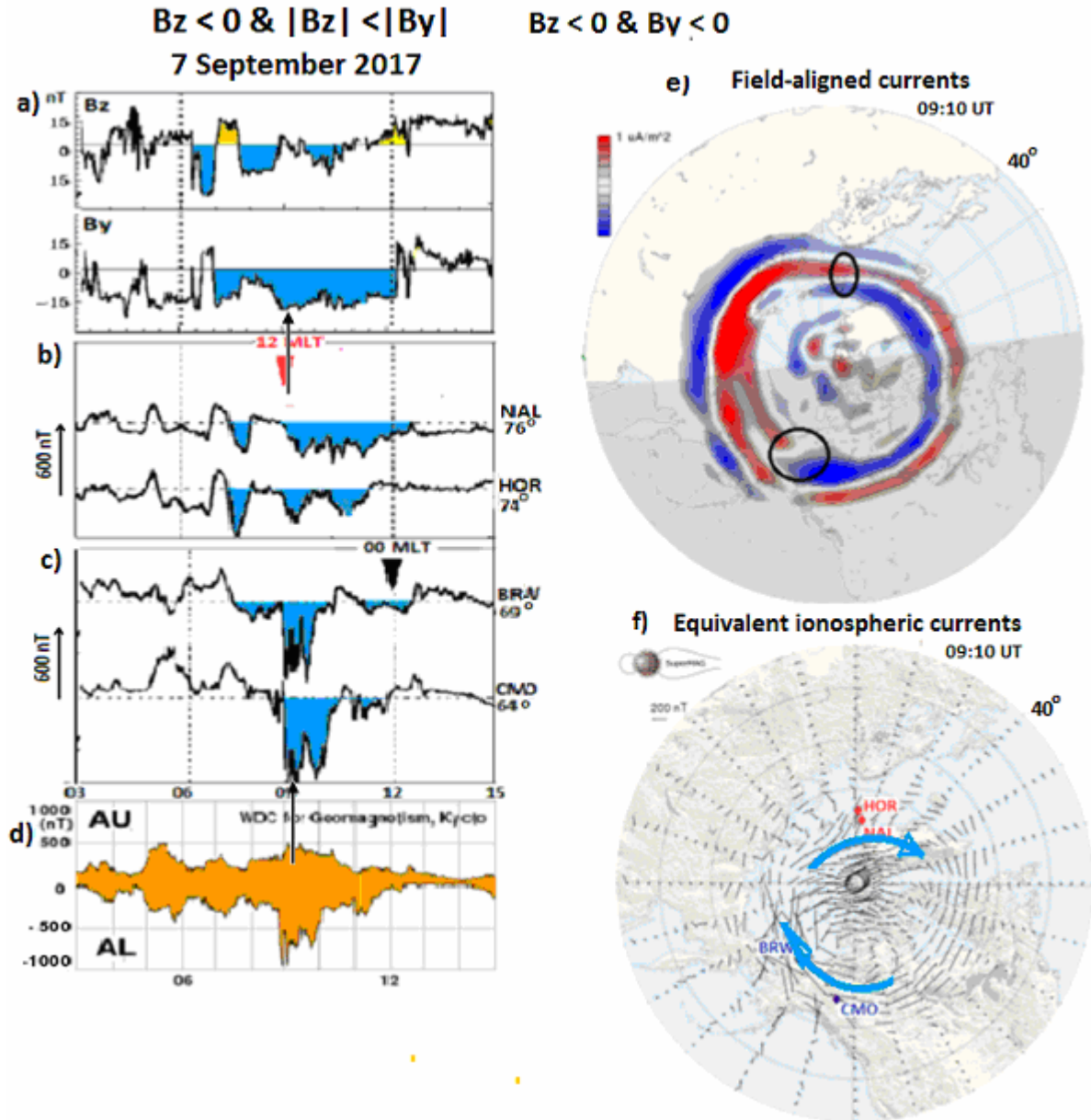


Fig.4. 7 September 2017. The same as in Fig. 3

Conclusion

The case study of the relationship of the dayside high-latitude magnetic bays with different IMF conditions showed:

- the dayside polar magnetic bays observed under the *strong positive* IMF B_z could be caused by an enhancement of the polar NBZ-system of the Field-Aligned Currents (FACs) that leads to PE increasing;
- the FAC intensification in the polar latitudes could produce dayside negative magnetic bays when the *negative* IMF B_z was dominated above the IMF B_y ;
- the non-typical dayside polar magnetic bays were observed under the *weak unstable negative* IMF B_z and could be associated with the development of the global complicated system of the ionospheric currents with an expansion of the westward electrojet into the dayside sector. Both, the dayside polar bays and night-side auroral latitude substorms were accompanied by the enhancement of the FACs.

Data

In our study we used

- (i) the ground-based IMAGE magnetometer data (<http://space.fmi.fi/image>) and database of the global network of observatories, monitoring the Earth's magnetic field (<http://www.intermagnet.org/>);
- (ii) the AL index of the geomagnetic activity (<http://wdc.kugi.kyoto-u.ac.jp/>);
- (iii) the IMF data sets of the 1-min resolution OMNI database (<http://omniweb.gsfc.nasa.gov>);
- (iv) the global distribution of the equivalent ionospheric currents provided by SuperMAG system service (<http://supermag.jhuapl.edu/>);
- (v) the AMPERE data, based on the magnetic measurements on 66 low-altitude globally distributed Iridium communication satellites (<http://ampere.jhuapl.edu/products>).

Acknowledgment

The work of N.K. and L.M. was partly supported by the Program no.12 of the Russian Academy of Sciences (RAS).

References

- Feldstein, Y.I., V.A Popov, J.A Cumnock., A. Prigancova, L.G Blomberg, J.U. Kozyra, B.T. Tsurutani, L.I. Gromova, and A.E. Levitin (2006), Auroral electrojets and boundaries of plasma domains in the magnetosphere during magnetically disturbed intervals, *Ann. Geophys.*, 24, 2243-2276.
- Friis-Christensen, E. and Wilhelm, J.(1975), Polar currents for different directions of the interplanetary magnetic field in the Y-Z plane, *J. Geophys. Res.*, 80, 1248–1260.
- Gromova, L.I., Kleimenova, N.G., Levitin, A.E., Gromov, S.V., Dremukhina, L.A., and Zelinsky, N.R. (2016), Daytime geomagnetic disturbances at high latitudes during a strong magnetic storm of June 21–23, 2015: The storm initial phase, *Geomagn. Aeron. (Engl. Transl.)*, 56(3), 281–292, doi: [10.1134/S0016793216030051](https://doi.org/10.1134/S0016793216030051)
- Gromova, L. I., Förster, M., Feldstein, Y. I., and Ritter, P. (2018), Characteristics of the electrojet during intense magnetic disturbances, *Ann. Geophys.*, 36, 1361-1391, <https://doi.org/10.5194/angeo-36-1361-2018>
- Gromova L.I., Gromov S.V., Kleimenova N.G., Dremukhina L.A. (2019), Response of the High-latitude Daytime Magnetic Bays to the IMF By: Case study, *Sun and Geosphere*, 14(1), 25-30, doi: [10.31401/SunGeo.2019.01.04](https://doi.org/10.31401/SunGeo.2019.01.04)
- Kleimenova, N.G., Gromova, L.I., Dremukhina, L.A., Levitin, A.E., Zelinskii, N.R., and Gromov, S.V. (2015) High-latitude geomagnetic effects of the main phase of the geomagnetic storm of November 24, 2001 with the northern direction of IMF, 2015, *Geomagn. Aeron. (Engl. Transl.)*, 55(2), 174–184.
- Levitin A.E., Kleimenova N.G., Gromova L.I., Antonova E.E., Dremukhina L.A., Zelinsky N.R, Gromov S.V., and Malysheva L.M. (2015), Geomagnetic disturbances and pulsations as a high-latitude response to considerable alternating IMF variations during the magnetic storm recovery phase (Case Study: May 30, 2003), *Geomagn. Aeron. (Engl. Transl)*, 55(6), 755–768.

Anomalous TEC Disturbances of the South American Ionosphere before and after the Main Shocks of Some Powerful Chilean Earthquakes

Ishkova L.M., Ruzhin Yu.Ya., Bershadskaya I.N.

Pushkov Institute of Terrestrial Magnetism, Ionosphere and Radio Wave Propagation RAS,
Moscow, Troitsk, Russia
E-mail: ishkova@izmiran.ru

Abstract

The analysis results of the large-scale space-time disturbances of the total electron content (TEC) of the South American ionosphere before and after the powerful Chilean earthquakes on February 27, 2010 (M=8.8), April 1, 2014 (M=8.2) and after the main shock of the Chilean earthquake on September 16, 2015 (M=8.3), according to GPS network station data, are presented.

It is studied the development in the quiet geomagnetic conditions of the anomalous in the daily courses of TEC values during the periods 18-27.02.2010 and 28.02-09.03.2010; 25.03÷01.04.2014 and 02.04-09.04.2014; 17-26.09.2015, characterized by foreshock and high aftershock activities, with respect to the median levels during these periods (values of δTEC , %, the time interval is 2 hours) in the longitudes $45^\circ\div 105^\circ\text{W}$ ($\Delta\lambda=15^\circ$) and in the latitudes $0^\circ\div 60^\circ\text{S}$ ($\Delta\phi=5^\circ$).

Estimates of the characteristics of TEC disturbances (δTEC , %, spatial dimensions of ionosphere regions with anomalous TEC disturbances, duration of the disturbances in daily TEC courses) for the periods considered are presented. It is shown that the anomalous disturbances of TEC ($|\delta\text{TEC}| \geq 30\%$) in the extended regions of the ionosphere took place both before the main shocks of these Chilean earthquakes and after them independently.

Introduction

The results of experimental studies show that there is coupling between the Earth's lithosphere processes and electromagnetic and plasma disturbances in the ionosphere. The use of the Global Positioning System (GPS) are provided new opportunities in studying the space-time characteristics of the ionosphere modification before earthquakes [Ruzhin *et al.*, 2000; Ruzhin *et al.*, 2002; Liu *et al.*, 2004; Zakharenkova *et al.*, 2006; Ruzhin *et al.*, 2016].

The analysis of GPS observations showed that variations of the ionosphere total electron content (TEC) are very sensitive to changes in the F2-layer electron concentration. The correlation coefficient between TEC and foF2 reaches a value of 0.9. Since the electron concentration at the F2-layer maximum is one of the ionosphere parameters most sensitive to seismic activity, we can use TEC data to estimate spatial scales and temporal dynamics of seismo-ionospheric effects practically in any seismic active region of the world [Ruzhin *et al.*, 2000; Ishkova *et al.*, 2017; Ishkova *et al.*, 2018].

The present paper deals with this area of research. In the paper are presented the analysis results of the large-scale space-time variations of TEC before and after the main shocks of the three powerful Chilean earthquakes.

Data

It was studied the development for the quiet helio-geomagnetic conditions of the anomalous in the daily courses of TEC values during the periods 18÷27.02.2010 and 28.02÷09.03.2010; 25.03÷01.04.2014 and 02.04÷09.04.2014; 17-26.09.2015, characterized by foreshock and high aftershock activity, with respect to the median levels during these periods.

Estimates of the characteristics of TEC disturbances ($\delta\text{TEC},\%$, spatial scales of ionosphere regions with anomalous TEC disturbances, duration of the disturbances in daily TEC courses) for the periods considered are made.

The nature study of the TEC variations relative to the median level in the period 7-16.09.2015, before the main shock of the Chilean earthquake on 16.09.2015, was not conducted due to the disturbed state of the geomagnetic field in the first half of this period.

The period 17-26.09.2015, after the main shock 16.09.2015, was characterized by a calm state of the geomagnetic field, except on September 20, when a moderate magnetic storm took place for a period of 15 hours (class G3, $A_p = 44$).

The information on the parameters of some major seismic events in the Chilean zone of earthquakes during considered periods is given in Tables 1-3.

Table 1. The Andes seismic activity on February-March, 2010

Date	UTC	$\varphi,^\circ$	$\lambda,^\circ$	M	Date	UTC	$\varphi,^\circ$	$\lambda,^\circ$	M
03.02.2010	07:26	-31.6	-66.3	4.7	27.02.2010	15:45	-24.8	-65.6	6.3★
03.02.2010	18:30	-24.2	-67.1	4.6	28.02.2010	11:25	-34.9	-71.6	6.2
07.02.2010	17:09	-23.2	-66.5	5.6	01.03.2010	02:44	-35.0	-72.4	5.7
12.02.2010	12:03	-33.6	-68.7	5.8	03.03.2010	17:44	-36.6	-73.3	6.1
18.02.2010	20:56	-23.0	-68.5	5.2	04.03.2010	22:39	-22.2	-68.3	6.3
20.02.2010	09:55	-39.5	-75.0	4.9	05.03.2010	11:47	-36.6	-73.3	6.6
23.02.2010	00:06	-22.8	-66.6	4.7	07.03.2010	15:59	-37.9	-73.3	5.9
27.02.2010	06:34	-36.1	-72.9	8.8★	08.03.2010	17:03	-25.7	-66.6	5.8
27.02.2010	08:01	-37.7	-75.0	7.4	11.03.2010	14:55	-34.3	-71.7	7.0

Table 2. The Andes seismic activity on March-April, 2014

Date	UTC	$\varphi,^\circ$	$\lambda,^\circ$	M	Date	UTC	$\varphi,^\circ$	$\lambda,^\circ$	M
20.03.2014	18:41	-24.0	-69.0	5.1	03.04.2014	02:43	-20.5	-70.4	7.7
22.03.2014	12:59	-19.7	-70.8	6.2	04.04.2014	01:37	-20.6	-70.6	6.3
23.03.2014	18:20	-19.6	-70.8	6.3	04.04.2014	09:52	-31.5	-70.2	5.4
24.03.2014	11:26	-19.8	-70.7	5.7	05.04.2014	02:22	-32.8	-71.5	5.6★
27.03.2014	23:50	-29.1	-68.7	5.7	05.04.2014	05:44	-20.1	-70.5	5.2
28.03.2014	00:10	-29.1	-68.8	5.2	06.04.2014	14:06	-20.4	-71.0	5.2
31.03.2014	12:53	-19.5	-69.1	5.6	07.04.2014	13:43	-20.1	-70.8	5.7
31.03.2014	14:58	-34.7	-71.6	4.8	08.04.2014	10:14	-20.5	-70.9	5.6
01.04.2014	23:46	-19.6	-70.7	8.2★	09.04.2014	11:14	-20.6	-70.8	5.2
02.04.2014	04:46	-20.0	-70.8	5.5	11.04.2014	00:01	-20.6	-70.6	6.2
03.04.2014	01:58	-20.3	-70.5	6.5	11.04.2014	01:08	-33.3	-72.0	5.0

Table 3. The Andes seismic activity on September, 2015

Date	UTC	$\varphi,^\circ$	$\lambda,^\circ$	M	Date	UTC	$\varphi,^\circ$	$\lambda,^\circ$	M
1.09.2015	15:28	-19.7	-69.2	5.4	18.09.2015	09:10	-32.3	-72.2	6.2
5.09.2015	10:17	-37.9	-73.6	5.1	19.09.2015	12:52	-32.3	-72.0	6.2
5.09.2015	22:13	-25.7	-64.6	5.2	21.09.2015	17:40	-31.7	-71.3	6.6
12.09.2015	08:13	-31.6	-68.3	5.0	22.09.2015	07:13	-31.4	-71.2	6.0
15.09.2015	21:21	-20.0	-70.8	5.0	23.09.2015	11:32	-31.6	-71.9	5.0
16.09.2015	22:54	-31.5	-71.6	8.3★	24.09.2015	16:13	-30.7	-71.3	5.2
16.09.2015	23:18	-31.5	-71.4	7.0	26.09.2015	02:51	-30.8	-71.3	6.3
17.09.2015	04:10	-31.5	-71.8	6.7	27.09.2015	21:04	-31.6	-71.7	5.4

Results

In [Ishkova et al., 2017] the analysis results of the character of TEC daily variations in the South American region with respect to ten-day median levels during periods February 17-27, 2010 and March 25-April 03, 2014 were reported. The conclusion was made about a similar pronounced character of the South American ionosphere reaction to seismic processes before these powerful Chilean earthquakes. In [Ishkova et al., 2018] it was shown that TEC anomalous disturbances took place both before the main shock of the powerful Chilean earthquake of 2014 and after it.

The results of previous studies and the newly obtained results of the analysis of TEC variations in the periods after the main shocks of the powerful Chilean earthquakes of 2010 and 2015 allowed us to conclude that TEC anomalous disturbances (from 30 to 50-60% and higher relative to the median level) in extended regions (up to several thousand kilometers) of the South American ionosphere took place both before the main shocks of the powerful Chilean earthquakes and after them.

The Tables below illustrate the characteristic features of the large-scale space-time variations of TEC before and after the main shocks of the considered powerful Chilean earthquakes.

Tables 4-5 are presented the spatial distributions of the maximum daily δTEC values during the periods before and after the Chilean earthquake main shock of 2010. Tables 6-7 represent similar data for the maximum daily δTEC values before and after the Chilean earthquake main shock of 2014. In Table 8 the spatial distributions of the maximum daily δTEC values after the main shock of the Chilean earthquake 2015 are presented.

An analysis of the data showed that the duration of TEC anomalous disturbances in the diurnal course of TEC at given geographical point may reached 2 or more hours. The duration of such disturbances are indicated in the Tables (for example: 2h, 4h, 6h).

The spatial scales of the ionosphere regions with anomalous TEC disturbances could reach several thousand kilometers at latitude and longitude directions at a single moment of UT. The estimates of the spatial scales of TEC anomalous disturbances at the UT moments (DUT) are provided in the Tables (for example, 27.03.2014 D7UT=3200km and D9UT=4800km at $\varphi = -30^\circ$).

Table 4. Maximum δTEC , % on February 22 and 26, 2010 (before the main shock 27.02.2010)

φ° λ°	The seismic events, DUT	22.02.2010					The seismic events, DUT	26.02.2010				
		-105	-90	-75	-60	-45		-105	-90	-75	-60	-45
0	D3UT=1665km D21UT=1665km	30.6	31.1	31.7	37.5	54.7	D7UT=6660km	-21.6	-20.7	-17.8	-12.5	17.1
-5		15.0	17.4	20.3	37.3	49.3		-20.9	-14.4	-20.7	-12.2	-10.9
-10		19.5	14.0	8.7	14.1	30.6		-24.6	-20.1	-31.5	-24.5	-14.2
-15		18.7	12.2	5.0	17.1	20.2		-20.6	-22.5	-25.3	-25.8	-13.5
-20		20.1	18.1	21.1	33.6	45.5		-23.9	-22.3	27.5	-15.7	-8.1
-25	27.02 6.3 -24.8 -65.6 D1UT=1500km	24.8	21.2	32.8	41.4	47.8	27.02 6.3 -24.8 -65.6	-23.0	-22.5	37.2	17.1	-9.7
-30	D1UT=1440 km	25.3	22.1	30.1	42.1 2h	38.0		-24.5	-26.5	-21.3	11.5	13.5
-35	27.02 8.8 -36.1 -72.9	23.3	26.8	32.9	35.7	23.1	27.02 8.8 -36.1 -72.9	-23.3	-27.6	-21.9	-16.3	-18.4
-40	D21UT=2550km	34.6	36.1	31.1	38.7	15.2		-19.8	-20.0	-15.4	-14.4	22.8
-45	D21UT=2350km	31.7	36.7 2h	43.5	36.0	16.1		-15.0	-15.4	-17.8	-17.2	30.7
-50		22.6	29.2	31.8	18.9	10.5		-13.2	-10.5	15.0	11.2	29.6
-55		19.6	21.0	22.8	15.6	20.1		-17.1	-15.1	14.2	-6.7	21.1
-60		23.8	23.8	25.1	21.0	21.8		-18.6	-20.1	-14.0	8.6	11.6

Table 5. Maximum $\delta\text{TEC},\%$ on February 28 and March 4, 2010 (after the main shock 27.02.2010)

φ° λ°	The seismic events, DUT	28.02.2010					The seismic events, DUT	4.03.2010				
		-105	-90	-75	-60	-45		-105	-90	-75	-60	-45
0	28.02. 5.2 -1.1 -80.3 D3UT=1665km D21UT=1665km	-34.6	-36.2	41.3	-37.2	-16.3	D7UT=6660km	33.6	48.3	34.0	31.3	34.7
-5		-23.9	-22.9	-16.6	-18.8	-12.6	D7UT=3310km	47.7	47.9	31.1	27.3	41.5
-10		-15.2	-19.6	9.0	11.8	21.4	D7UT=1640km	46.0	39.2 2h	24.6	15.4	32.3
-15		-14.5	-15.4	7.5	15.8	28.9		29.4	30.0	19.0	19.7	27.3
-20		-17.3	-29.5	-17.7	-18.9	50.4	D3UT=1560km	20.1	23.3	28.4	59.8 2h	36.1 2h
-25	27.02 6.3 -24.8 -65.6	-23.4	-31.2	-29.4	-37.7 6h	43.4	4.03 6.3 -22.3 -68.3 D3UT=3010km	16.4	28.1	32.6	48.1 2h	33.3 2h
-30	D1UT=1440km D19UT=1440km	-32.2	-34.2	-32.2	-37.9	-18.3	4.03 5.4 -31.1 -72.0 D1UT=2880km	17.0	37.9	31.6	38.7 2h	27.7
-35	28.02 6.2 -34.9 -71.6	-32.8	-36.4 2h	-29.6	-20.0	21.2	5.03 6.6 -36.6 -73.3 D1UT=1360km	-19.6	28.9	33.0	45.0	36.9
-40		-24.4	-28.0	-26.2	22.3	-17.3	D7UT=1270km	16.8	18.6	12.1	35.5 2h	33.3
-45		-19.0	-23.7	-17.4	-24.1	26.8	D5UT=1170km	16.3	27.0	26.6	40.6	36.0 2h
-50		-22.5	-23.2	-16.9	-20.1	-22.6		-11.9	18.5	24.1	26.9	31.9 2h
-55	D9UT=950km	-26.1	-30.2	-31.7	-24.5	-22.8		-12.0	-12.2	15.0	21.8	25.7
-60		-21.0	-26.5	-26.8	-21.1	-10.0		-7.6	-7.5	-5.8	12.8	18.8

Table 6. Maximum $\delta\text{TEC},\%$ on March 27 and 30, 2014 (before the main shock 01.04.2014)

φ° λ°	The seismic events, DUT	27.03.2014					The seismic events, DUT	30.03.2014				
		-105	-90	-75	-60	-45		-105	-90	-75	-60	-45
0	D7UT=3330 km	11.6	-15.1	37.3	38.7	46.6		-10.3	-10.2	-21.1	-12.9	20.6
-5	D5UT=1650 km D7UT=1650 km	12.1	14.1	30.7	37.9	45.7- -41.4		-6.7	9.5	-14.2	-10.1	19.0
-10	D7UT=1630 km	25.0	15.7	24.0	40.6	35.4 -30.8		-14.1	-22.0	-13.4	-18.4	-26.1
-15	D7UT=4820 km D9UT=1600 km	45.7 2h	37.0 2h	47.5	52.4	30.0		-16.0	-18.3	-22.9	-34.0	-29.2
-20	1.04 8.2 -19.6 -70.7 D7UT=4690km D9UT=3120km D11UT=1560km	60.9 4h	69.5 4h	73.2 2h	74.1 2h	39.5	31.03 5.6 -19.5 -69.1 1.04 8.2 -19.6 -70.7 D5UT=1560km	-21.8	-27.4	-33.8	-36.3	-39.4
-25	D7UT=4520km D9UT=3010km D11UT=1500km	60.8 2h	89.2 6h	68.3 4h	70.5	45.4	D5UT=1500km D7UT=1500km	-19.4	-25.7	-34.6	-38.5 2h	-40.2
-30	27.03 5.7 -29.1 -68.7 D7UT=2880km D9UT=4320km D11UT=1440km	52.4 2h	69.2 2h	77.1 2h	55.1- 2h	49.3	D5UT=1440km	-11.4	-15.9	-23.5	-30.3	-32.5
-35	D9UT=2720km D11UT=1360km	52.7 2h	43.6 2h	66.9	50.7 2h	40.0		-7.7	-12.1	-14.8	-24.8	-22.3
-40	D9UT=2550km D11UT=1270km D13UT=1270km	57.4 2h	46.4 4h	46.8	60.8	26.2		-11.8	-11.3	-12.6	-18.3	-24.5
-45	D9UT=1170km D11UT=2350km	52.4 2h	52.0 2h	55.5 2h	53.0	22.7		-21.2	-30.9	-29.2	-28.2	-24.0
-50	D11UT=1070km	38.5 2h	38.4	37.0	25.4	15.6		-24.0	-33.0	-28.0	-24.7	-15.2
-55		28.6	26.0	18.2	-13.8	18.5		-21.3	-32.5	-30.0	-28.5	-21.2
-60		18.1	-17.7	-17.7	-15.8	-25.0		-15.2	-21.8	-18.8	-30.0	-28.5

Table 7. Maximum δTEC , % on April 2 and 5, 2014 (after the main shock 01.04.2014)

φ° λ°	The seismic events, DUT	2.04.2014					The seismic events, DUT	5.04.2014				
		-105	-90	-75	-60	-45		-105	-90	-75	-60	-45
0		-25.5	-14.4	-17.1	10.7	-16.3		11.0	14.5	15.0	20.8	41.6
-5		-22.9	-19.7	-13.1	-11.3	-25.8		26.2	18.8	19.7	14.7	-29.0
-10		-20.7	-24.7	-17.3	-12.7	-26.1		16.6	11.7	19.3	-13.4	-34.0
-15		-15.5	-15.0	-15.8	-17.6	-18.8		13.8	-16.8	26.8	-17.3	-27.7
-20	01.04. 8.2 -19.6 -70.7	-13.6	-15.5	-15.5	-30.2	-22.9	05.04 5.2 -20.1 -70.5	11.1	-22.8	-22.8	-18.4	-32.5
-25		-13.6	-16.0	-25.8	-31.2	22.9		11.5	-20.6	-17.6	20.0	24.9
-30		24.2	16.2	20.5	27.9	39.5	D21UT=1440km	-12.2	17.7	20.0	42.7	65.9
-35		14.7	19.3	21.5	32.5	21.5	5.04 5.6 -32.8 -71.5 D21UT=2720km	20.6	23.1	31.4	67.4	121.5
-40		12.6	17.1	24.8	21.5	16.4	D21UT=3820km	32.7	35.7	37.5	53.6	68.1
-45		10.5	21.3	21.7	15.8	18.3		29.6	30.1	29.0	26.3	52.2
-50		20.9	16.7	16.2	14.0	15.9	D19UT=4280km D21UT=2140km	44.3 2h	39.3 2h	37.9 2h	38.1	39.4 2h
-55		21.9	18.8	26.0	19.3	34.0	D17UT=2860km D19UT=3820km D21UT=3820km	44.6 2h	54.1 4h	55.7 4h	59.1 4h	54.8 4h
-60		17.4	17.1	24.0	14.9	26.5	D17UT=2490km D19UT=3330km D21UT=3330km	41.4 2h	64.3 4h	67.3 4h	72.4 4h	61.2 4h

Table 8. Maximum δTEC , % on September 17 and 20, 2015 (after the main shock 16.09.2015)

φ° λ°	The seismic events, DUT	17.09.2015					The seismic events, DUT	20.09.2015				
		-105	-90	-75	-60	-45		-105	-90	-75	-60	-45
0	D5UT=1665km D7UT=1665km	-20.5	-14.2	-20.5	-45.6	-43.2	D1UT=1665km	33.5	20.1	29.0	35.3	38.1
-5	D7UT=1650km	-18.3	-19.4	-19.2	-37.3	-33.3	D1UT=4970km	23.6	34.2	39.3	45.0	31.6
-10		-23.1	-27.8	-17.5	-24.2	-38.9	D1UT=1640km	19.0	29.4	59.8 2h	36.5	-23.6
-15		-25.9	-20.8	-18.2	-18.3	-45.7	D3UT=1600km	32.7 2h	28.4	-33.7 36.8 2h	31.4	-22.0
-20	17.09 5.1 -18.5 -69.1	-24.5	-28.9	-22.6	-19.4	-40.5 2h	D19UT=3120km	52.1 2h	44.7	-35.0 4h	25.6	22.3
-25		-29.1	-50.2	-31.5	-25.1	-36.6 2h	D19UT=3020km	-31.2 48.3 2h	51.8	-35.0 4h	28.5	26.3
-30	17.09 6.7 -31.5 -71.8 D19UT=1440km	-33.7	-28.0	-28.9	-30.3	-36.1	19.09 6.2 -32.3 -72.0 D15UT=1440km D17UT=4320km D19UT=2880km	-31.0 42.3 4h	44.1 4h	-32.1 44.8 4h	32.6	27.2
-35	D1UT=1360km D19UT=1360km	-34.6	-35.4	-35.1	-30.9	-30.9	D15UT=1360km D17UT=4090km	44.0 2h	46.7 2h	54.0 4h	34.6	33.9
-40	D1UT=1270km	-35.5	-35.4	-27.7	-25.3	-30.7	D15UT=2550km D17UT=3820km D19UT=1270km	49.5 2h	51.4 4h	57.7 2h	41.6 2h	29.4
-45		-28.6	-25.1	-20.6	-19.7	-30.6	D15UT=2350km D17UT=4700km	46.8 4h	59.2 4h	61.4 2h	48.9 2h	35.4
-50		-23.8	-19.8	-18.1	-17.9	-24.8	D15UT=1070km D17UT=4280km	46.7 2h	60.5 4h	58.4 2h	49.7	41.4
-55		-18.9	-18.8	-18.4	-19.3	-18.4	D17UT=3820km	44.4T	53.7	47.7	46.1	39.3
-60		-20.2	-17.9	-21.8	-22.7	-18.0	D17UT=1660km	28.0	34.5	31.2	36.8	27.5

The extent of the ionosphere regions with anomalous TEC-perturbations along the meridians could also reached several thousand kilometers at a single moment UT. For example, 27.03.2014 D7UT = 3885km at $\lambda = -60^\circ$, D7UT = 3330km at $\lambda = -75^\circ$ and D11UT = 3885km at $\lambda = -105^\circ$. 09.20.2015 D17UT = 3330km at $\lambda = -60^\circ$ and $\lambda = -75^\circ$.

The characteristic features of anomalous TEC disturbances before these Chilean events were the development in the quiet helio-geomagnetic conditions of positive TEC perturbations relative to the median level (from 30 to 50-60% and higher) at distances up to several thousand kilometers at a single moment UT a few days before the main shocks and in change of positive phase by negative phase for 3-4 days before the main shocks.

After the main shocks, within 2-3 days, predominantly negative δTEC values occurred, close to or exceeding background (28.02.2010 and 17.09.2015) or background positive and negative δTEC values (2.04.2014).

Later 4-5 days after the main shocks of these earthquakes, a positive phase of TEC disturbances began, with a gradual transition to TEC variations close to the background.

The main characteristics of the positive TEC disturbances after the main shocks of the considered earthquakes (δTEC values, spatial scales, duration of disturbances in the TEC daily courses) were comparable with similar characteristics before the main shocks.

The maximum characteristics of positive disturbances significantly exceed similar characteristics of negative TEC disturbances.

Conclusions

1. The use of GPS data with sufficient space-time resolution made it possible to investigate the space-time dynamics of the development of TEC anomalous disturbances (from 30 to 50-60% and higher relative to the median level) for the quiet helio-geomagnetic conditions in extended regions (up to several thousand kilometers) of the South American ionosphere.
2. The space-time scales of TEC anomalous disturbances are different on different days, at different latitudes and longitudes. In general, the maximum characteristics of positive perturbations (δTEC values, their durations in daily courses and spatial scales) are higher than similar characteristics of negative TEC disturbances.
3. The TEC anomalous disturbances for the quiet geomagnetic conditions took place both before the main shocks of the powerful Chilean earthquakes and after them.
4. The main characteristics of the positive TEC disturbances after the main shocks of the earthquakes considered were comparable with similar characteristics before the main shocks.

References

- Ruzhin Yu.Ya., Oraevsky V.N., Shagimuratov I.I. (2000). Anomalies of Ionospheric TEC above the Turkey before two strong Earthquakes at 1999. Proc. 15th Wroclaw EMC Symposium, 508–512.
- Ruzhin, Yu.Ya., Oraevsky V.N., Shagimuratov I.I. and Sinelnikov V.M. (2002). Ionospheric precursors of earthquakes revealed from GPS data and their connection with “sea-land” boundary. Proc. 16th Wroclaw EMC Symposium, 723-726.
- Liu J.Y., Chuo Y.J., Shan S.J., Tsai Y.B., Chen Y.I., Pulnits S.A., Yu S.B. (2004). Pre-earthquake ionospheric anomalies registered by continuous GPS TEC measurement. *Annales Geophysicae*, 22, 1585-1593.
- Zakharenkova I.E., Shagimuratov I.I., Krankowski A. et al. (2006). Ionospheric precursors observed during the Mediterranean region earthquakes. Proc. 18th International Wroclaw Symposium and Exhibition on Electromagnetic Compatibility, 85–90.
- Ruzhin Yu.Ya., Smirnov V.M. (2016). Pulsed TEC during 20 minutes before the Chilean earthquake. Handbook: The 2nd International Workshop of CSES Mission. Beijing, Chin, 26-30.
- Ishkova L., Ruzhin Yu., Bershadskaya I. (2017). The Large-Scale Ionosphere TEC Disturbances before Two Power Chilean Earthquakes. Proceedings of Ninth Workshop «Solar Influences on the Magnetosphere, Ionosphere and Atmosphere». Sunny Beach, Bulgaria, May 30-June 3, 2017, 97-102.
- Ishkova L.M., Yu.Ya. Ruzhin, I.N. Bershadskaya. (2018). TEC perturbations of the South American ionosphere before and after the main shock of the powerful Chilean earthquake of 2014. Proceedings of Tenth Workshop «Solar Influences on the Magnetosphere, Ionosphere and Atmosphere». Primorsko, Bulgaria, June 4-8, 2018., 84-89.

Strong Magnetic Storm on 25-26 August 2018 with Reference to the Solar Cycle 24 Declining

Kleimenova N.G.¹, Gromova L.I.², Gromov S.V.², Malysheva L.M.¹

¹ Schmidt Institute Physics of the Earth RAS, Moscow, Russia

² IZMIRAN, Moscow, Russia

e-mail: kleimen@ifz.ru

Abstract

It is well known that the CIR (Corotating Interaction Region) driven magnetic storms are typical ones for a solar cycle declining but the CME (Coronal Mass Ejection) driven storms mostly appear during the solar cycle maximum. The CMEs rare occur during the solar cycle declining because they are associated with flares or filament eruptions, both of which are relatively rare in the low part of the cycle. However, in the Sun's downward cycle 24, all strong magnetic storms (e.g., in March, June and December 2015, May and September 2017) were caused by CMEs. The strong magnetic storm on 25-26 August 2018 (Dst = -171 nT) was the last storm of this series. In this case, the CME was associated with a filament eruption on 20 August under the very low solar wind speed. The comparison of two last sever magnetic storms (Sep2017 and Aug2018) showed that there is no linear relationship between the storm intensity (Dst index) and planetary geomagnetic activity (Ap index). So, the planetary geomagnetic disturbances in the Sep2017 storm were stronger than in the Aug2018 storm despite the fact that the Dst values in the first storm were smaller than in the second one. The solar cycle 24 continues to produce surprises. The cycle has not yet reached a minimum. Will be new magnetic storms or not?

Introduction

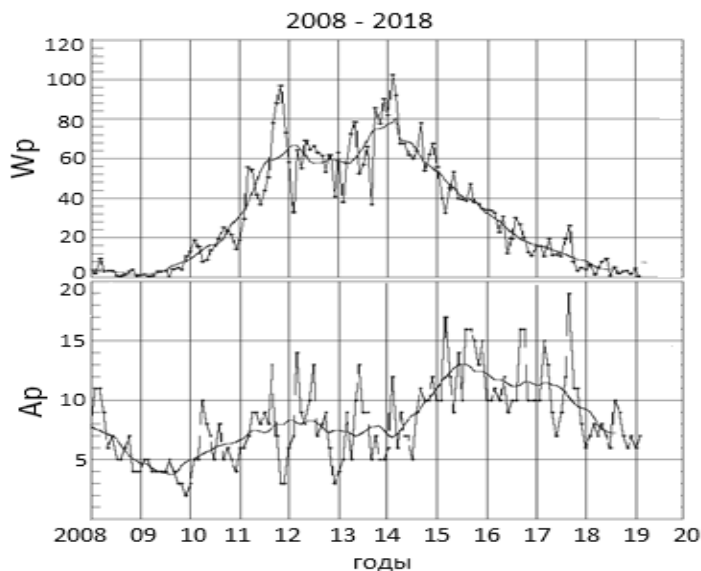


Fig. 1. Solar (Wp) and magnetic (Ap) activity in the solar cycle 24.

Several strong magnetic storms occurred in the beginning of the solar cycle 24 (SC-24) declining phase in 2015÷2017: 17÷18 March 2015 (Dst = -223 nT), 22÷23 June 2015 (Dst = -204 nT), 20÷21 December 2015 (Dst = -155 nT), 27-28 May 2017 (Dst = -125 nT), 7÷8 September 2017 (Dst = -124 nT).

All of these magnetic storms have been caused by the Coronal Mass Ejections (CME). However, it is well known that such magnetic storms are dominated in the solar cycle maximum [e.g., Tsurutani and Gonzalez, 1997; Richardson et al., 2001; Denton et al., 2006; Borovsky and

Denton, 2006]. The CMEs seldom occur during the solar cycle declining because they are associated with flares or filament eruptions, both of which are relatively rare in this phase of the cycle.

Figure 1 demonstrates the solar (Wp index) and geomagnetic (Ap index) activity progress in the solar cycle 24. It is seen that the strongest geomagnetic disturbances have been

observed as the Sep2017 storm, however, the value of the Dst index (a proxy of the storm intensity) does allow to attribute this storm to the very strong one. Thus, there was no relationship between the storm intensity (Dst index) and planetary geomagnetic activity (Ap index).

One year after the Sep2017 storm, the new strong magnetic storm occurred on August 2018. The aim of this paper is to compare the high-latitude geomagnetic effects of these two storms.

Solar wind and IMF conditions during the Sep2017 and Aug2018 magnetic storms

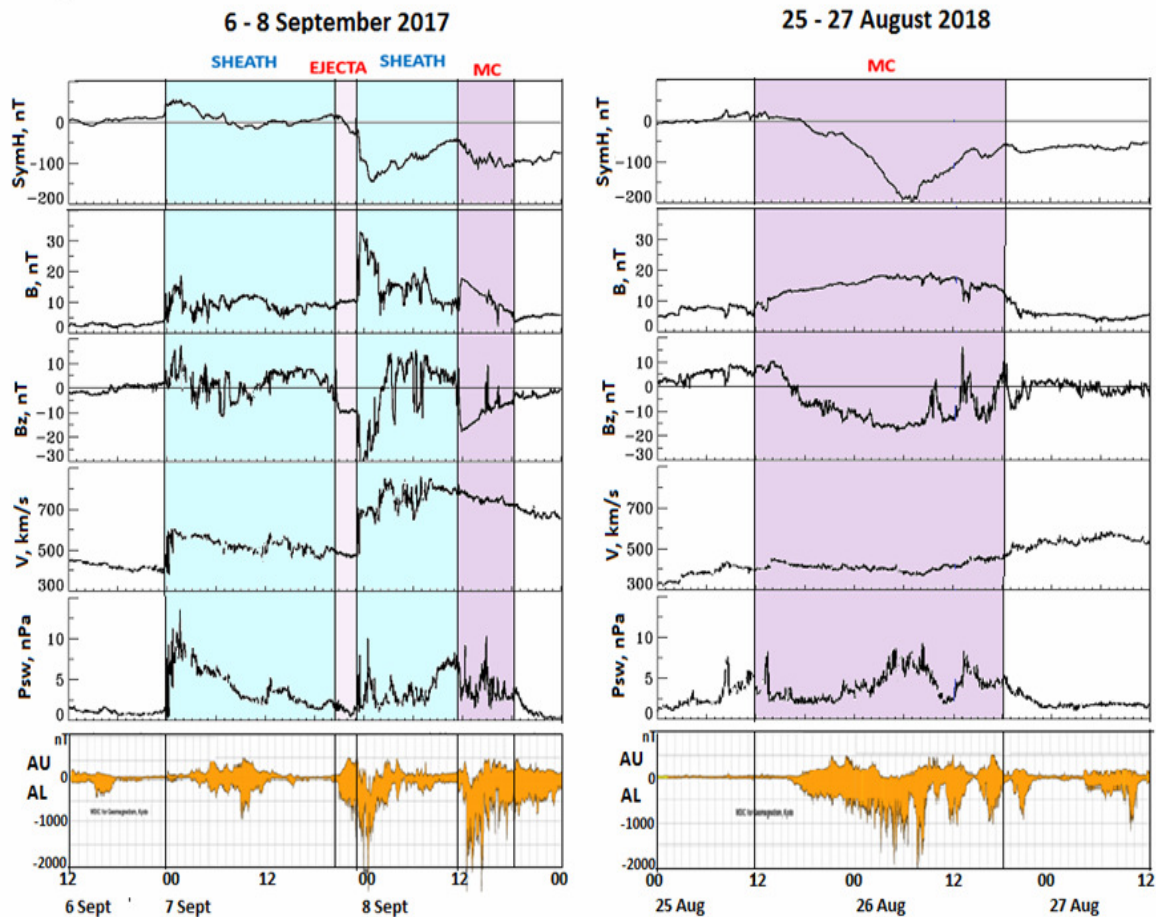


Fig. 2. Solar wind and IMF data during the Sep2017 and Aug2018 magnetic storms.

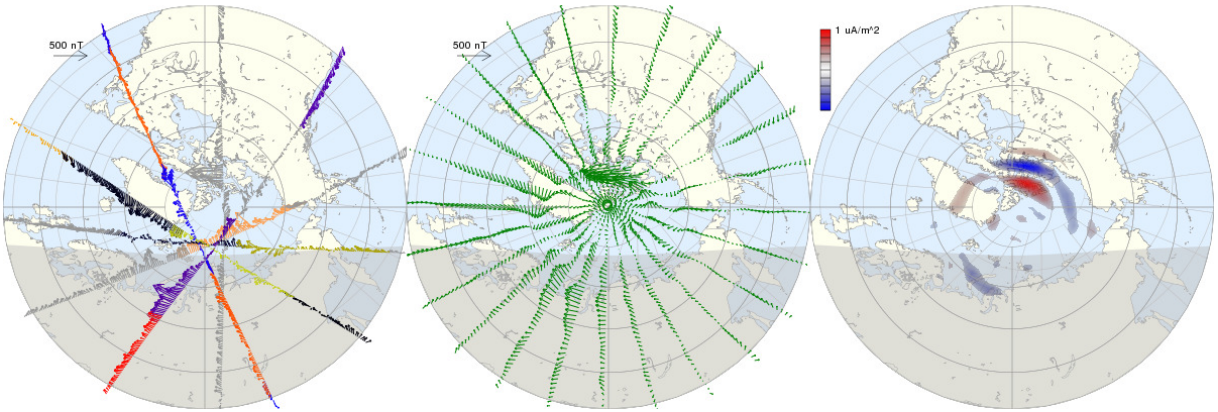
As it was mentioned above, the Sep2017 magnetic storm was not the strongest in terms of the Dst index, but produced significant geomagnetic disturbances (see Ap index in Fig. 1). The variations of the solar wind IMF parameters (Fig. 2) were classified according to the catalog of large-scale solar wind phenomena (<ftp://ftp.iki.rssi.ru/omni/>) as sheath, magnetic clouds (MC) and ejecta.

The interplanetary conditions in the Sep2017 storm (in terms of IMF Bz and Vsw) were stronger than in Aug2018 storm, however, the Dst values in the first event were smaller than in the second case, probably, due to shorter duration of the negative IMF Bz values.

Field Aligned Currents (FACs) during the Sep2017 magnetic storm

The high-latitude FACs distributions in time of the magnetic storm on 7 September have been studied by using the data from the AMPERE facilities (Active Magnetosphere and Planetary Electrodynamics Response Experiment) which consist of 66 commercial satellites at the 780 km polar circular orbits distributing over 6 orbital planes. Unfortunately, there were no AMPERE data for the Aug2018 storm.

07 Sep 2017 18:00:00 - 18:10:00 UT



07 Sep 2017 23:48:00 - 23:58:00 UT

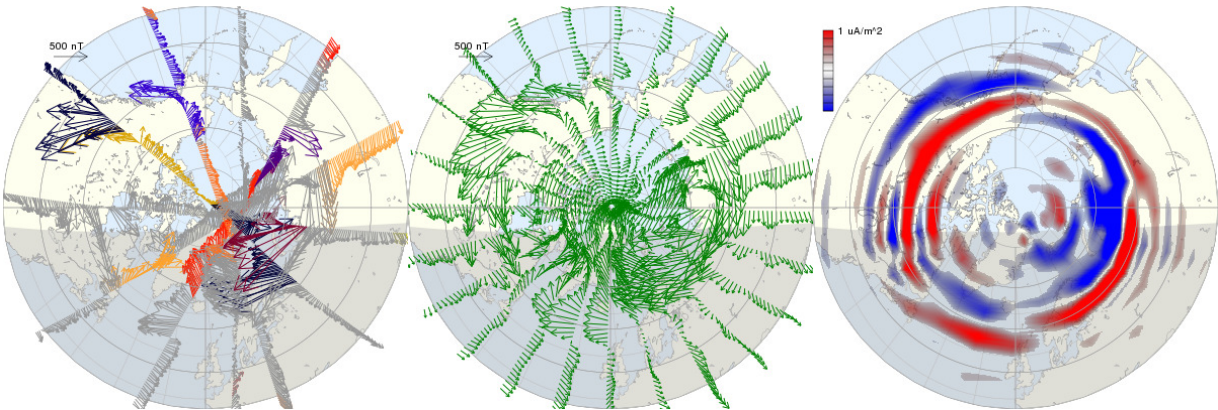


Fig. 3. AMPERE data (orbital plans, magnetometer data, calculated FAC maps) for the Sep2017 storm (upper plots - before storm, bottom plots – during the beginning of the storm main phase), red – upward FACs, blue – downward.

It is seen that before this magnetic storm (upper plots in Fig. 3) under the positive values of the IMF Bz (Fig. 2), the magnetic disturbances as well as FACs were recorded only at dayside polar latitudes. However, in the beginning of the main phase of these magnetic storms (bottom plots in Fig.3), they were globally observed everywhere at the auroral and subauroral latitudes. The FAC distribution exhibited a typical feature of a strong magnetic storm: the pancake structure of the upward and downward currents.

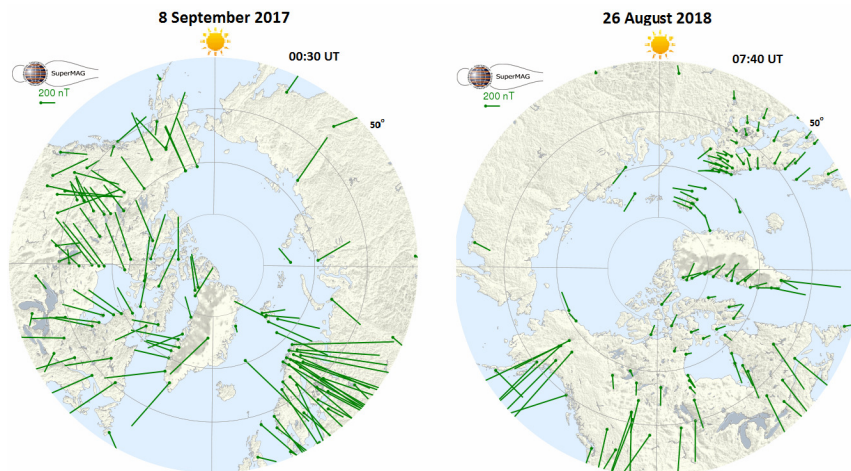


Fig. 4. The maps of the magnetic vectors from the ground stations after the SuperMAG data

Storm main phase

To compare the geomagnetic activity during the considered storms, we used the magnetic data from the global SuperMag network of the more than 300 ground-based magnetometer stations [<http://supermag.jhuapl.edu/>]. The detailed description of the SuperMag project is given in [Newell and Gjerloev, 2011; Gjerloev, 2012].

It was found that the planetary geomagnetic disturbances in the main phase of the Sep2017 storm were stronger than in the Aug2018 storm despite the fact that the Dst values in the first storm were smaller than in the second event. It is seen in Fig. 4.

Storm recovery phase

In the storm recovery phase of the both storms, there were observed strong fluctuations in the IMF Bz with different quasi-periods (Fig. 2) which were accompanied by simultaneous ground-based magnetic fluctuations at 06-08 UT on 8 September 2017 (Fig. 5) and at 10-20 UT on 26 August 2018 (Fig. 6).

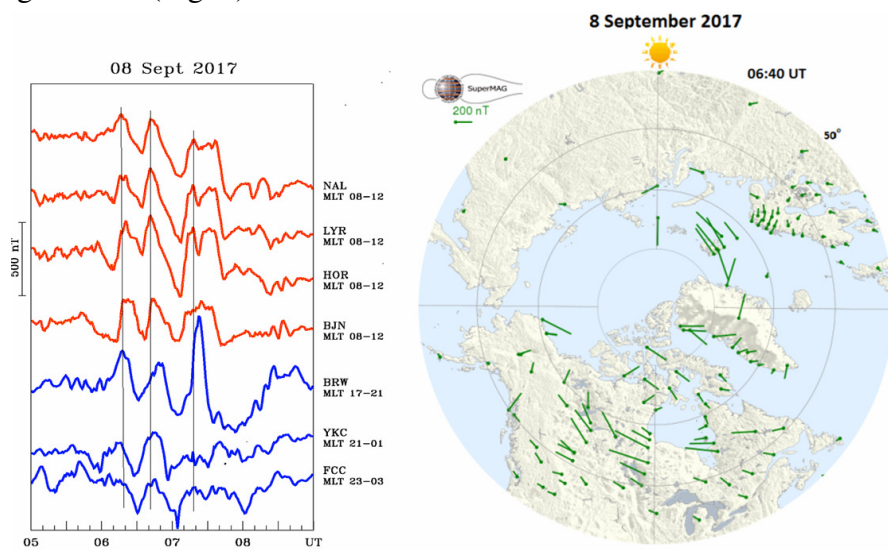


Fig. 5. Magnetic fluctuations at the dayside (red) and nightside (blue) stations and the SuperMag map of the magnetic vectors of these data on 8 September 2017

Figure 5 shows the strong 15-30 min magnetic fluctuations occurred simultaneously at the dayside and nightside stations (marked by red and blue color) on 8 September 2017. The SuperMag map of the magnetic vectors supports the existence of global disturbances. Note, there were no stations located between 09-18 MLT.

In the recovery phase of the Aug2018 storm, there were observed the strong quasiperiodic bay-like excursions of the negative IMF Bz values causing the similar deviations in the AU and AL indexes of the geomagnetic activity at auroral latitudes (see Fig. 6). We found that near 12 UT, one of the relevant substorms has been observed not only after the local midnight (BRW and YKC stations), but simultaneously at the local afternoon at the high-latitude IMAGE stations (HOP-NAL) as well. The SuperMag map demonstrates the magnetic disturbances in the vast area of the Earth surface. Unfortunately, there were no ground-based stations located in the evening (~16-24 MLT).

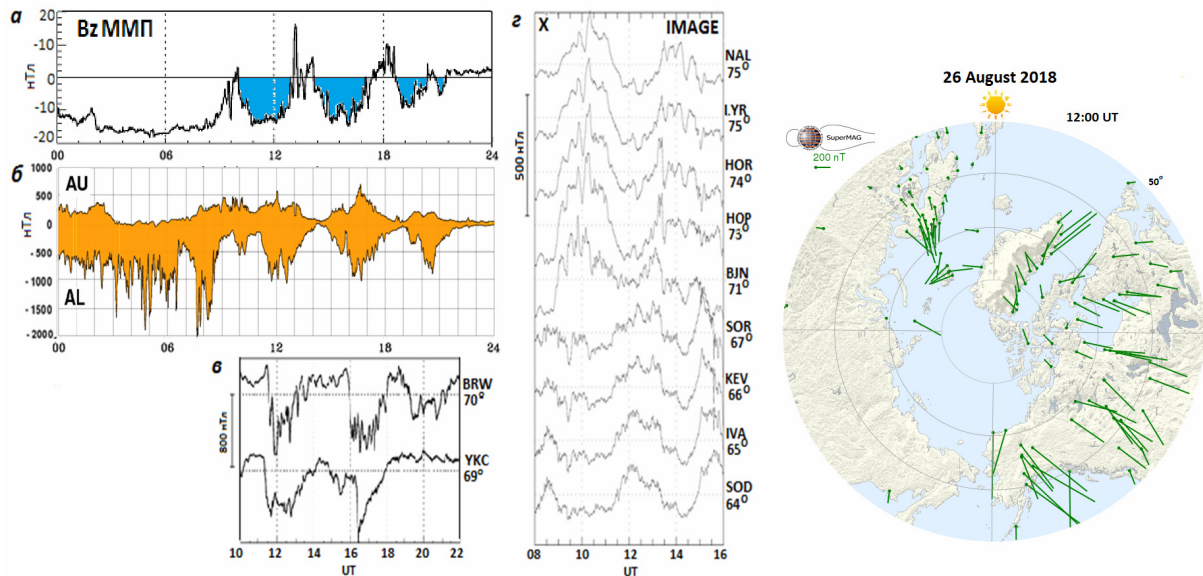


Fig. 6. Magnetic fluctuations in IMF Bz and AU-AL indexes (left panels), the high-latitude dayside IMAGE (middle panel) and nightside (BRW, YKC) magnetograms, and the SuperMag map of these data on 26 August 2018.

Discussion

It is well known that magnetic storms in the declining phase of the solar cycle tend to be CIR (Corotating Interaction Region) driven [Tsurutani and Gonzalez, 1997; Richardson et al., 2001] associated with high-speed streams emanated from coronal holes [Burlaga et al., 1978]. However, the strong magnetic storms in the declining phase of the solar cycle 24 (SC24) were CME driven. Moreover, the intense geomagnetic storm occurrence rate during the SC-24 was reduced nearly by a factor of 4 of that in the SC-23 [Rawat et al., 2018].

The Sep2017 storm was caused by the CME which was associated with the 6 September X-9 flare. The Aug 2018 storm was caused by the Aug25 CME which was thought to be associated with a filament eruption on 20 August. There were no flares and 5 days later. The CME itself was too weak to be automatically detected by satellites. After additional manual analysis, the CME was estimated to have only minor Earth-directed parts, but the geomagnetic effects of this storm were not minor. The Aug2018 storm raises the question: why so rather small disturbances on the Sun under the low-speed solar wind resulted the sever (in terms of Dst-index) magnetic storm?

Summary

1. The comparison of two last sever magnetic storms (Sep2017 and Aug2018) showed that there is no linear relationship between the storm intensity (Dst index) and planetary geomagnetic activity (Ap index). So, the planetary geomagnetic disturbances in the Sep2017 storm were stronger than in the Aug2018 storm despite the fact that the Dst values in the first storm were smaller than in the second one.
2. The interplanetary conditions in the Sep2017 storm were stronger (higher solar wind speed, IMF B and negative IMF Bz) than in Aug2018 storm, however, the in the first event, the Dst values and the storm main phase duration were smaller than in the second case, probably, due to shorter time of the negative IMF Bz values.
3. During the recovery phase of both storms, there were strong IMF Bz variations. The high-latitude geomagnetic disturbances, caused by these IMF Bz variations, have been observed in the global scale, i.e., simultaneously at the day and night sides.

Final remark

The solar cycle 24 is not yet reached a minimum and overall the sun activity can still continue, thus, some new additional events may occur.

Acknowledgements

The ground-based IMAGE magnetometer data were taken from <http://space.fmi.fi/image>; the IMF and solar wind data of the 1-min resolution were taken from the OMNI database (<http://omniweb.gsfc.nasa.gov>); the AMPERE data are available at <http://ampere.jhuapl.edu>; the AL, AU and Dst indexes of the geomagnetic activity are available at <http://wdc.kugi.kyoto-u.ac.jp/>; the global maps of the geomagnetic disturbances were provided by SuperMAG system service (<http://supermag.jhuapl.edu/>), The work of N.K. and L.M. was partly supported by the Program no.12 of the Russian Academy of Sciences (RAS).

References

- Borovsky, J. E. & M. H. Denton (2006). Differences between CME-driven storms and CIR-driven storms, *J. Geophys. Res.* 111. A07S08. doi:10.1029/2005JA011447.
- Burlaga, L. F., K. W. Behannon, S. F. Hansen, G. W. Pneuman, and W. C. Feldman (1978), Sources of magnetic fields in recurrent interplanetary streams, *J. Geophys. Res.*, 83, 4177 – 4185, doi:10.1029/JA083iA09p04177.
- Denton, M. H., J. E. Borovsky, R. M. Skoug, M. F. et al. (2006). Geomagnetic storms driven by ICME- and CIR-dominated solar wind, *J. Geophys. Res.* 111. A07S07. doi:10.1029/2005JA011436.
- Gjerloev J.W. (2012). The SuperMAG data processing technique. *J. Geophys. Res.*, 117. A09213, doi:10.1029/2012JA017683. 6
- Newell P.T., J.W. Gjerloev (2011) Substorm and magnetosphere characteristic scales inferred from SuperMAG auroral electrojet indices. *J. Geophys. Res.*, 116, A12232. doi:10.1029/2011JA016936.
- Rawat, R., Echer, E., & Gonzalez, W. D. (2018). How different are the solar wind-interplanetary conditions and the consequent geomagnetic activity during the ascending and early descending phases of the solar cycles 23 and 24. *J. Geophys. Res. Space Physics*, 123, 6621–6638, doi.org/10.1029/2018JA025683
- Richardson, I. G., Cliver E. W., & Cane H. V. (2001). Sources of geomagnetic storms for solar minimum and maximum conditions during 1972–2000 // *Geophys. Res. Lett.* 28. 2569.
- Tsurutani, B. T., & Gonzalez, W. D. (1997). The interplanetary causes of magnetic storms: A review. In B. T. Tsurutani (Ed.), *Magnetic storms, geophysics monograph series* (Vol. 98, pp. 77). Washington, DC: AGU. <https://doi.org/10.1029/GM098p0077>.

Auroral VLF Hiss as a Signature of the Growth Phase of the Magnetic Substorm

Manninen J.¹, Kleimenova N.G.², Gromova L.I.³, Turunen T.¹

¹ Sodankylä Geophysical Observatory, Finland,

² IFZ RAS, 3 IZMIRAN, Russia

E-Mail: kleimen@ifz.ru

Abstract

Auroral hiss is a well-known evening-nighttime natural VLF emission with a noise-like structure and the strongest intensity at the frequencies of 8-11 kHz. These VLF emissions are generated by the Cherenkov radiation above the ionosphere. The analysis of auroral hiss observed at Kannuslehto (KAN, MLAT = 64.2°) in Finland has been performed. The VLF receiver is located in the equatorial area of the auroral oval. During the 11 winter months (334 days) in 2015-2018, there were found 207 days with the auroral hiss bursts, the majority (82%) of them was observed in association with magnetic substorms. We have selected 106 events of isolated clearly defined substorms recorded within the typical time of the auroral hiss occurrence and found that in 97 events, auroral hiss was observed in the substorm growth phase. When weather conditions allowed, the auroral hiss bursts were found to be accompanied by the equatorward movement of the auroral arcs recorded poleward of KAN. The auroral breakup (substorm onset) abruptly suppressed auroral hiss. We found that the auroral hiss occurrence is controlled by the dynamics of the Field Aligned Currents (FACs) estimated from the AMPERE facility consisted of the 66 globally distributed telecommunication satellites carrying engineering magnetometers. It was revealed that auroral hiss at the equatorial area of the auroral oval exhibits a typical signature of the substorm growth phase.

Introduction

Auroral hiss is one of prominent natural whistler-mode VLF emissions [Helliwell, 1965] which have a noise-like structure and are commonly recorded both by the ground-based instruments and onboard satellites with the strongest intensity at the frequencies of ~8-11 kHz [e.g., reviews by Makita, 1979; Sazhin et al., 1993; LaBelle and Treumann, 2002]. Auroral hiss is generated by Cherenkov radiation of precipitating soft electrons above the ionosphere and typically occurs in the evening-night time at the auroral zone latitudes with the maximum of occurrence in the winter season. On the ground, auroral hiss is observed as separated bursts lasting from several tens of seconds to several minutes and associated with visible auroras. The aim of this paper is to focus on the relationship of ground-based auroral hiss, observed at the equatorial part of the auroral oval, with the magnetic substorms.

Data

In this study, we have been analyzing the VLF observations (up to 39 kHz) in Northern Finland at Kannuslehto (KAN) station (MLAT= 64.2°N) during the 11 winter months in 2015-2018.

The majority of the previous ground-based studies of the auroral hiss have been based on the VLF observations at high geomagnetic latitudes [e.g., Makita, 1979; Nishino et al., 1982], at the Antarctic station Syowa (MLAT ~70°S) located in the poleward part of the auroral oval. However, our station KAN is located at the equatorial part of the auroral oval (see Fig. 1). Note, the VLF observations at Syowa have been based on the chart records of several narrow bands from 4 to 128 kHz with the different scales and different receiver threshold level at different frequencies [Makita, 1979]. Contrary to that, we used the continuous digital VLF registration with the high temporal and frequency resolution [Manninen, 2005].

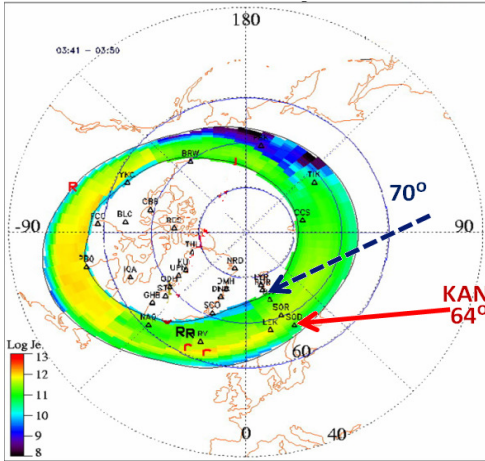


Fig. 1. The typical auroral oval and KAN and Syowa location

The VLF recordings at KAN latitude are badly hampered by sferics (originated from lightning) which hid almost all VLF emissions above ~4 kHz (Fig. 2, upper plots).

To study auroral hiss, the special method of filtering out the impulsive sferics was applied. The method has been briefly described in *Manninen et al.* (2016). The auroral hiss bursts become visible only after filtering out the sferics as it is seen in Fig. 2 (bottom plots). The filtered VLF KAN data are available at http://www.sgo.fi/pub_vlf/ as the power spectrograms in 24-h, 1-h and 1-min intervals for all campaigns 2006-2019.

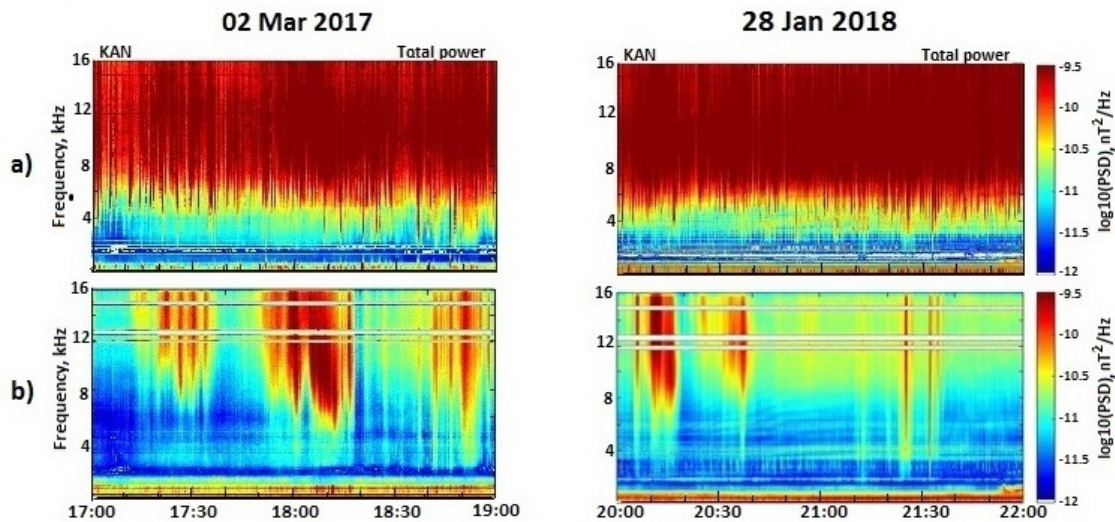


Fig. 2. The upper plots show non-filtered VLF spectrograms, bottom plots – the same intervals after sferics filtering.

During the 11 winter months in 2015-2018, the auroral hiss bursts at KAN were recorded in 207 days (total number of campaign days was 334). There were no auroral hiss under very quiet conditions with $K_p \leq 1$ (93 days) or very disturbed ones with $K_p > 3-4$ (34 days). The auroral hiss emissions at KAN were typically observed at 17-21 UT (i.e., before the local midnight).

We considered the visible auroras in the time of the auroral hiss occurrence at KAN using the auroral keograms (zenith angles of aurora versus time) at Sodankylä station (SOD, MLAT= 64.1°N, located ~ 45 km from KAN) or at Abisko station (ABK, MLAT= 65.4°N, located ~300 km to North-West from KAN) depending of where the weather allowed the aurora observation. We found that the auroral hiss events at KAN were accompanied by the auroral arcs whenever the optical observations were possible, the arcs were located poleward from KAN.

Two examples of auroral keograms at ABK are shown in Fig. 3 (middle panels). The auroral hiss at KAN was accompanied by auroral arc poleward of ABK. These hiss bursts suddenly disappeared by the time of the auroral breakup (around at 20:30 UT on 22 Jan 2016 and around at 21:30 UT on 28 January 2018).

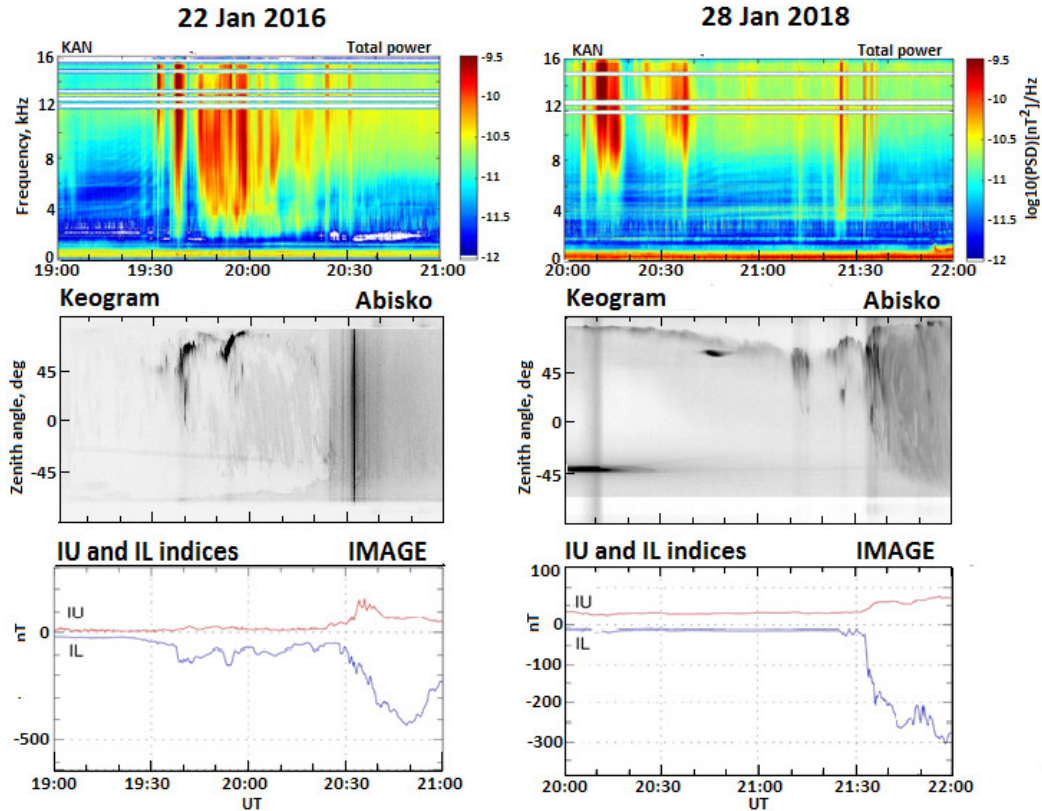


Fig. 3. The upper panels: spectrograms of auroral hiss, the middle panels: aurora keograms, the bottom panels – IL and IU indexes of the magnetic activity at this meridian (IMAGE magnetometer chain)

The auroral breakup is an indicator of the sudden onset of the magnetospheric substorm [e.g., Rostoker *et al.*, 1980]. Bad weather conditions often make impossible observations of visible auroras, and to the substorm definition, the planetary AL geomagnetic index is commonly used, its sharp decrease of at least 100 nT within 10-15 min indicates the substorm onset.

Here for highlighting the substorm, we used the magnetic observations at Scandinavian IMAGE magnetometer chain and correspondingly the IMAGE electrojet indicators IL and IU which are simply estimated the total eastward and westward currents crossing the magnetometer network [Tanskanen, 2009]. The definition of these indicators is quite similar to that of the standard AL and AU indices. The bottom panels in Fig. 3 show the development of the substorm according to the IL and IU indexes. It is seen that the abrupt substorm onset suppresses the auroral hiss.

One more typical auroral hiss event (on 23 December 2016) is presented in Fig. 4. In this event, the optical auroras were observed at ABK and SOD. Both keograms showed the same auroral arc poleward from these stations until ~17:45 UT. Then the arc began to move equatorward, and the auroral breakup was observed at ~18:10 UT that completely stopped the auroral hiss.

Since it is generally accepted that the auroral hiss is caused by Cherenkov radiation of the low-energetic precipitating electrons, we considered the spatial features of the Field Aligned Currents (FACs) that is the system of the upward and downward soft electron flows above the ionosphere. The upward FACs correspond to the low-energetic electron precipitation. Here we use the FAC data from AMPERE facility (Active Magnetosphere and Planetary Electrodynamics Response Experiment) which consists of the 66 globally distributed telecommunication satellites at 780 km altitude [Anderson *et al.*, 2014].

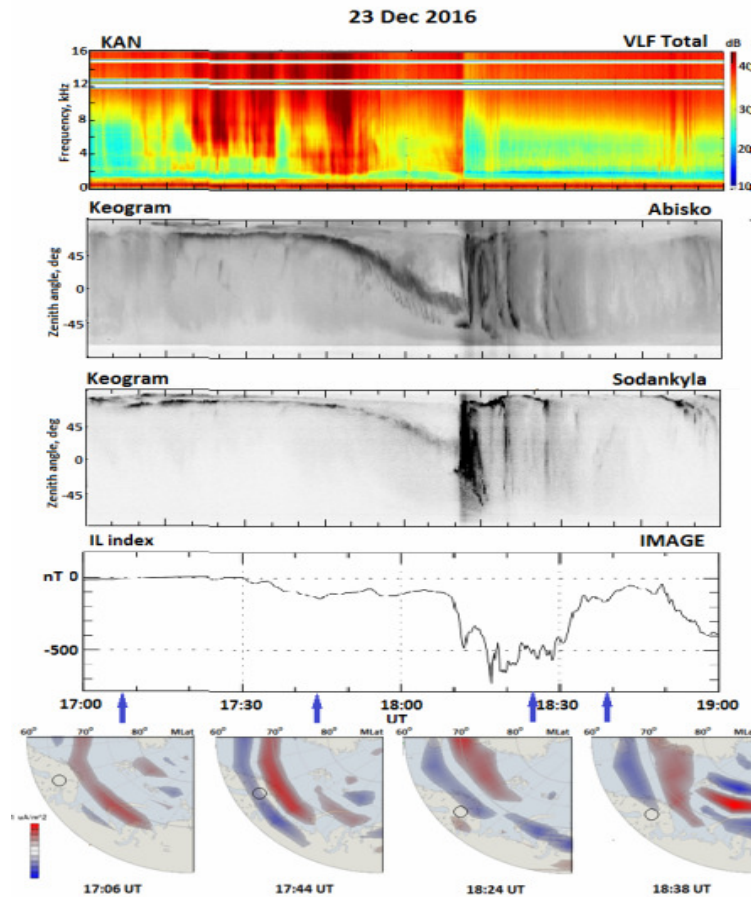


Fig. 4. The example of the auroral hiss disappearance with the substorm onset and auroral breakup, the bottom panel - the FAC according to AMPERE data (red - the upward FACs, blue - downward FACs). Circle shows the location of KAN.

Near 17:00 UT, under the absence of strong auroral hiss at KAN and well before the substorm onset, the upward FACs were spaced far poleward from KAN. Together with moving auroral arc, the FACs started to move to the lower latitudes, and KAN became in the vicinity of the upward FAC location. In the substorm expansion phase, after 18:10 UT, auroral oval significantly expanded, and the substorm westward traveling surge (WTS) expanded also poleward as it is typical for substorms [e.g., Hones, 1985]. At this time, the upward FACs were observed around MLAT $\sim 70^\circ$, poleward from KAN. The Antarctic Syowa Station is located at the similar MLAT ($\sim 70^\circ$ S), so, it was logical that there the auroral hiss has been observed mainly during the substorm expansion phase [Makita, 1979].

Discussion

We found that within 207 auroral hiss days, altogether 170 events (82%) were associated with magnetic bay-like disturbances recorded at IMAGE magnetometer chain. It was found that the bursts of auroral hiss were mainly observed *before* substorm onsets. Then, in the time interval correspondent to the typical daily variation of auroral hiss occurrence (17-21 UT), we selected the 100 well developed magnetic substorms which signature of the IL indicator was associated with a typical substorm feature [e.g., Rostoker et al, 1980]: the abrupt drop of the IL indicator was more than 200 nT within 10-15 min, the magnetic bay lasted less than 3 hours, before this bay there were no magnetic disturbances higher than 200 nT. To study the In the 88 isolated substorm events, there were auroral hiss bursts observed *before* substorm onsets, and only 12 substorms did not accompanied by auroral hiss.

Thus, we found that the majority of the auroral hiss bursts recorded at KAN occurred prior to substorm onset and accompanied by the equatorward movement of the pre-breakup auroral arcs which were originally located far poleward from KAN. Such auroral arc dynamics are typical for the substorm *growth* phase (e.g., *Sergeev et al., 2011*).

The concept of an existence of a *growth* phase prior to the magnetic substorm onset was previously discussed by several authors (e.g., *Pudovkin et al., 1968; McPherron, 1970; Sergeev et al., 2011*). They demonstrated some magnetospheric phenomena at this time, such as temporal activation of the pre-breakup quiet auroral arcs and their gradual equatorward shift, Pi2 geomagnetic pulsations, and soft electron precipitation enhancement. The substorm growth phase lasts from several minutes up to 2-3 hours.

We suppose that in the equatorward area of the auroral oval, the auroral hiss bursts exhibit a typical ground-based signature of the substorm *growth* phase. This is contrary to the previous results (e.g., *Makita, 1979; LaBelle and Treumann, 2002*) obtained in the poleward region of the auroral oval, at Syowa Station (MLAT ~70°S), which showed that there the impulses of the auroral hiss could be observed in any phase of the substorm, but mainly in the substorm *expansion* phase. We found that at lower latitudes (KAN, MLAT= 64.2°N), i.e., in the equatorward part of the auroral oval, the auroral hiss bursts typically appear *prior* to substorm onset, i.e., in the substorm *growth* phase, and the sudden substorm onset suppresses the auroral hiss appearance.

This apparent contradiction may be the result of the spatial-temporal dynamics of the localized upward FACs that correspond to the precipitation of the low-energetic electrons during the substorm cycle: in the substorm growth phase, all these processes develop in the equatorward area of the auroral oval, while in the substorm expansion phase they move to much higher latitudes as well [e.g., *Hones, 1985, Sergeev et al., 2011*].

The global maps of FAC distribution, obtained by AMPERE data during the substorm cycle, demonstrated an excellent agreement with the paradigm of the polar cap expansion in the substorm growth phase. The ground-based feature of the auroral hiss at different latitudes is controlled by the spatial-temporal dynamics of the substorm progress.

Conclusion

The analysis of the observations of the 11 winter months (2015-2018) of the auroral hiss at Kannuslehto (KAN, MLAT = 64.2°) in Northern Finland has been performed. This station is located in the equatorial area of the auroral oval.

The analysis of the 100 events of the “classical” substorms recorded within the local time of the typical auroral hiss occurrence (17-21 UT) showed that in the 88 events, the substorm *growth* phase was accompanied by the auroral hiss bursts. This is different from the previous results obtained at the Antarctic Syowa Station (MLAT ~70°S), i.e., in the poleward part of the auroral oval, where the auroral hiss impulses were found to be typical for the substorm *expansion* phase.

We suppose that this apparent contradiction is caused by the spatial-temporal dynamics of the Field Aligned Currents (FACs) in the substorm progress: in the substorm growth phase, the FACs are located at lower latitudes, and in the substorm expansion phase they shift poleward.

Acknowledgements

The IMAGE magnetometers and IL indicator data are available at <http://www.space.fmi.fi/IMAGE>. The auroral keograms were taken from http://www.space.fmi.fi/All_sky_cameras_of_MIRACLE. The AMPERE data are available at <http://ampere.jhuapl.edu>. The research by N.K. and L.G. was supported by the Academy of Finland (grant no.308501). The work of N.K. and Yu.F. was partly supported by the Program no.12 of the Russian Academy of Sciences (RAS).

References

- Anderson, B.J., Korth, H., Waters, C.L., Green, D.L., Merkin, V.G., Barnes, R.J., & Dyrud, L.P. (2014). Development of large-scale Birkeland currents determined from the Active Magnetosphere and Planetary Electrodynamics Response Experiment. *Geophys. Res. Lett.*, 41(9), 3017–3025.
- Helliwell, R.A. (1965) Whistler and related ionospheric phenomena. Stanford. Stanford Univ. Press. 349 p.
- Hones, E.W. (1985). The poleward leap of the auroral electrojet as seen in auroral images *J. Geophys. Res.*, 90, 5333–5337.
- LaBelle, J., & Treumann, R. (2002). Auroral Radio Emissions, 1. Hisses, Roars, and Bursts, *Space Sci. Rev.*, 101(3), 295–440.
- Makita, K. (1979). VLF/LF hiss emissions associated with aurora. *Memories of National Institute of Polar Research. Ser. A*, 16, 1–126.
- Manninen, J. (2005). Some aspects of ELF-VLF emissions in geophysical research, *Sodankylä, Geophysical Observatory Publication*, 98, Oulu University Press, Sodankylä, Finland, 177p.
- Manninen, J., Turunen, T., Kleimenova, N., Rycroft, M., Gromova, L., & Sirviö, I. (2016). Unusually high frequency natural VLF radio emissions observed during daytime in Northern Finland, *Environmental Research Letters*, 11, 124006. doi.org/10.1088/1748-9326/11/12/124006.
- McPherron, R.L. (1970). Growth phase of magnetospheric substorms. *J. Geophys. Res.*, 75 (28), 5592–5599.
- Nishino, M., Tanaka, Y., Iwai, A., & Kamada, T. (1982). Comparison between the arrival direction of auroral hiss and the location of aurora observed at Syowa station. *Memories of National Institute of Polar Research*, 22, 35–45.
- Pudovkin, M.I., Shumilov, O.I., & Zaytseva, S.A. (1968). Dynamics of the zone of corpuscular precipitation. *Planetary and Space Science*, 16(6), 881–890.
- Rostoker, G., Kawasaki, K., Akasofu, S.-I. et al. (1980). Magnetospheric substorms - definition and signatures. *J. Geophys. Res.*, 85(A4), 1663–1668.
- Sazhin, S.S., Bullough, K., & Hayakawa, M., (1993). Auroral hiss: a review. *Planet and Space Sci*, 41, 153–166.
- Sergeev, V., Angelopoulos, V., Kubyshkina M., Donovan, E., Zhou, X.-Z., Runov, A., Singer, H., McFadden, J., & Nakamura, R. (2011). Substorm growth and expansion onset as observed with ideal ground-spacecraft THEMIS coverage. *J. Geophys. Res.* 116, A00I26.
- Tanskanen, E.I. (2009): A comprehensive high-throughput analysis of substorms observed by IMAGE magnetometer network: Years 1993–2003 examined. *J. Geophys. Res.*, 114, A05204, doi:10.1029/2008JA013682.

Ground-Based Auroral Hiss: Wave Direction Finding

Nikitenko A.S.¹, Lebed O.M.¹, Fedorenko Yu.V.¹, Manninen J.², Kleimenova N.G.³,
Gromova L.I.⁴, Turunen T.²

¹ Polar Geophysical Institute RAS, Apatity, Russia

² Sodankylä Geophysical Observatory, Sodankylä, Finland

³ Institute of the Earth Physics of RAS, Moscow, Russia

⁴ IZMIRAN, Moscow, Troitsk, Russia

E-mail: alex.nikitenko91@gmail.com

Abstract.

The auroral hiss emission is generated at altitudes of about 10000 - 25000 km as a result of the Cherenkov radiation of precipitating soft electrons. Electromagnetic waves propagate from the generation region to the ground at frequencies between the lower hybrid resonance frequency and the electron gyro-frequency. Ground-based observations of the auroral hiss are typically accompanied by a visible aurora. The ground-based observations of the auroral hiss at two points, namely Kannuslehto (Finland) and Lovozero (Russia) located at about the same high geomagnetic latitudes and spaced in longitude by ~400 km have been made simultaneously. We proposed and used a new approach to estimate the arrival angles of the auroral hiss observed at the ground. It is shown that the ionospheric exit region of auroral hiss is located southward of the visible aurora. To explain the experimental results, we applied a model of the auroral hiss propagation from the generation region through the ionosphere to the ground. The results of modeling are consistent with the observations.

Introduction

It is known that auroral hiss emission is generated at the altitudes of about 10000 - 25000 km as a result of the Cherenkov radiation of precipitating soft electrons. Electromagnetic waves propagate from the generation region to the ground at frequencies between the lower hybrid resonance frequency and the electron gyro-frequency. Ground-based observations of the auroral hiss are typically accompanied by a visible aurora. We consider the auroral hiss registered at two points located close each other at high geomagnetic latitudes and spaced in longitude by 400 km: Kannuslehto (KAN, Finland) and Lovozero (LOZ, Russia). The map of the observation sites is presented in figure 1.

The aim of our paper is to study the relationship between the auroral hiss exit region location and the associated visible aurora.

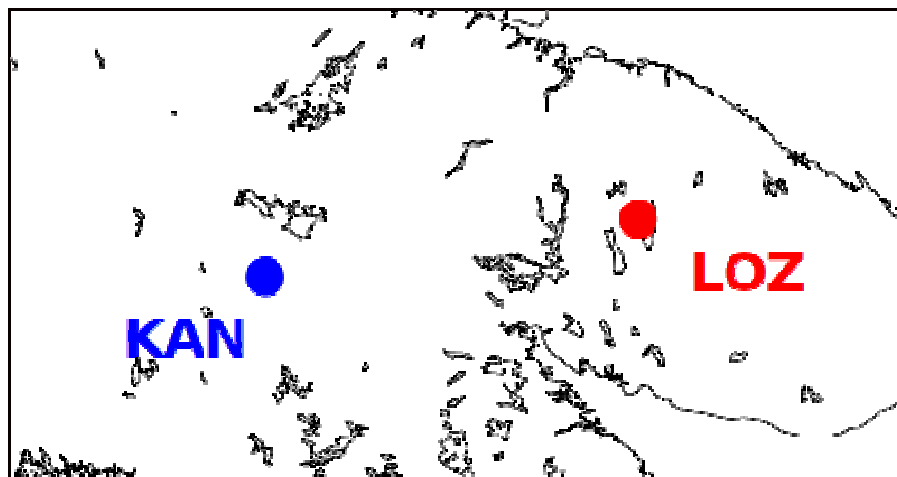


Fig. 1. The map of the observation sites. Kannuslehto, Finland (KAN) and Lovozero, Russia (LOZ).

Equipment

Both stations are equipped with similar VLF receivers. The sensors consist of two orthogonal magnetic loop antennas and one vertical electric dipole antenna. Two orthogonal magnetic loop antennas measure horizontal components of the magnetic field H_x , H_y while a vertical dipole antenna measures the vertical component of the electric field E_z in the Cartesian coordinate system with the X-axis directed to the North, Y – to the East and Z directed downwards. Because of the large ground conductivity, E_x , E_y and H_z components are small and not recorded. Measurements of three components allow finding the arrival angle φ_s of electromagnetic waves without ambiguity of $\pm 180^\circ$. We define this angle as the angle between the inverted Poynting vector and the northward direction.

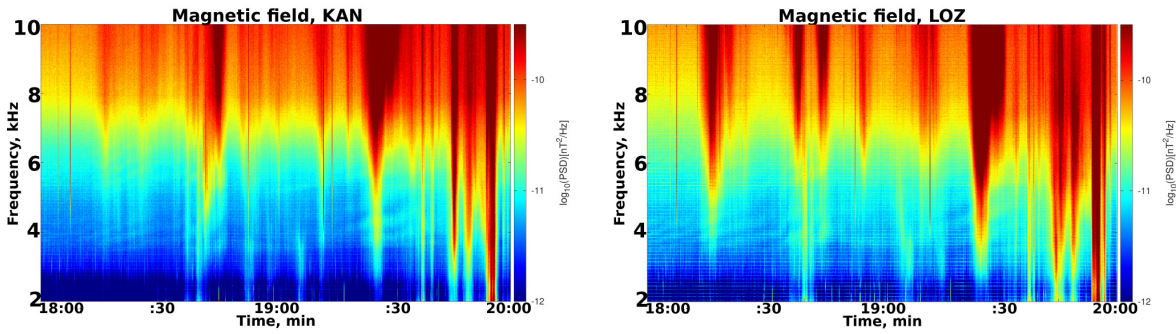


Fig. 2. Spectrograms of the auroral hiss registered in KAN and LOZ between 18:00 and 20:00 UT on 20 Dec 2018.

Direction finding method

Ground-based observations of VLF auroral hiss exhibit random changes of the arrival angle. Representation of this angle by its probability density function provides valuable information about the propagation and generation properties of VLF emissions. In this work we estimate the location of the exit region of VLF auroral hisses using a distribution of Poynting vector magnitude over the arrival angle.

The magnitude and the direction of a Poynting vector are defined by the formula below:

$$\vec{S} = \frac{1}{2} \text{Re}(\vec{E} \times \vec{H}) = \frac{1}{2} \left(-\text{Re}(\dot{E}_z \dot{H}_y^*) \hat{e}_x + \text{Re}(\dot{E}_z \dot{H}_x^*) \hat{e}_y \right)$$

Here \dot{H}_x , \dot{H}_y , and \dot{E}_z are H_x , H_y , and E_z components after the Hilbert transform, the asterisk denotes the complex conjugate, symbol Re stands for real part of a value.

To estimate the distribution of φ_s we choose a time interval of 120 seconds in the vicinity of the auroral hiss intensity maxima. For every data sample, we calculate Poynting vector components and average them in the time interval of 0.1 seconds. When estimating the distribution of Poynting vector magnitudes over the arrival angles the range of possible angles was divided by equal sectors. Then we calculate mean value of the magnitude of \vec{S} in every sector, thus obtaining the distribution of the magnitudes over the arrival angles.

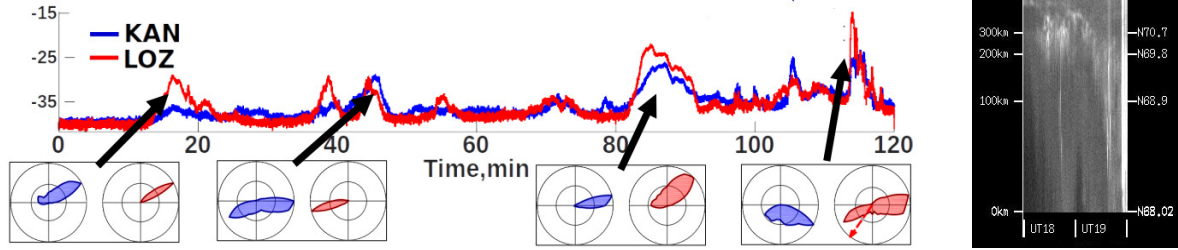


Fig. 3. The envelope of the magnetic horizontal components and the Poynting vector distributions 20 Dec 2018 in the time interval 18:00 - 20:00 UT (left); Abisko (ABK) keogram, demonstrating the aurora location far northward (right).

Observation of the auroral hiss

We analyzed the auroral hiss registered in KAN and LOZ at 18:00 - 20:00 UT on 20 Dec 2018. The spectrograms of the auroral hiss are shown in Fig. 2. To analyze propagation properties of the auroral hiss we filtered the components using a bandpass filter with center frequency $f_c = 8500$ Hz and bandwidth $f_{bw} = 1000$ Hz. Assuming that the filtered signal is stationary and ergodic we calculated the distribution of Poynting vector magnitudes over the arrival angles. The results of our calculations are presented in Fig. 3 (left). It is clearly seen that the location of the wave exit region changed with time. Initially, the wave exit region located north-east of both stations and moved to the position between the stations later. Then the situation repeated and wave exit region again located north-east of the stations moving finally to the previous position. The registered emissions are accompanied by visible aurora. The all-sky camera data at Abisko station located ~300 km to North-West from KAN showed the aurora occurrence far northward (these data do not show here).

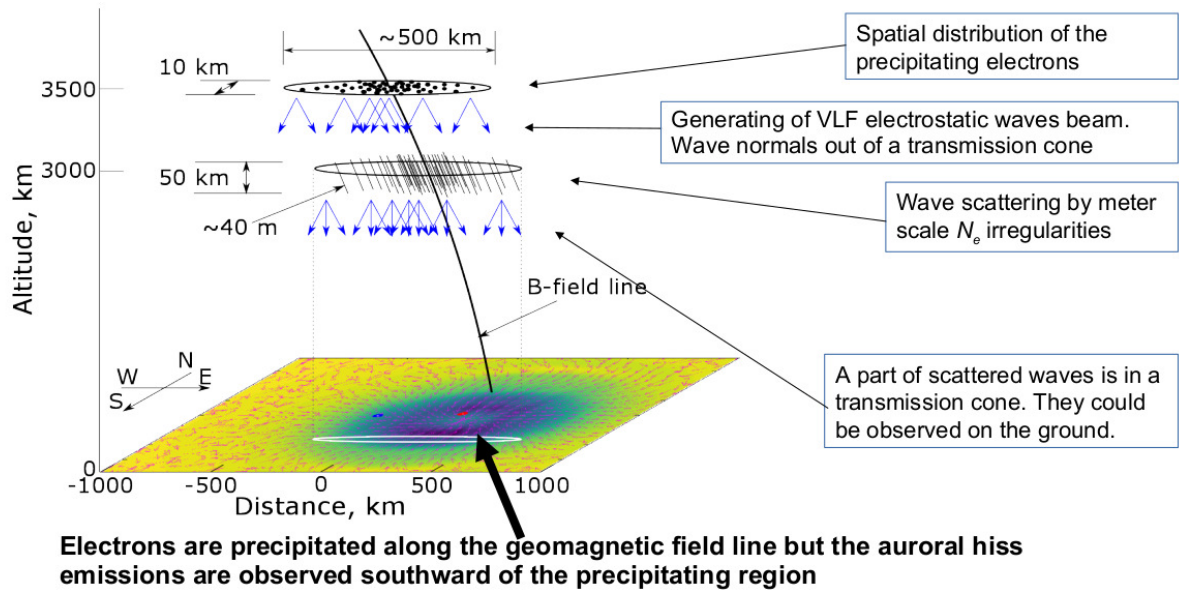


Fig. 4. Auroral hiss generation and propagation model.

Auroral hiss generation and propagation model

To explain the observed results, we simulated the auroral hiss propagation from the generation region to the ground through the plane-stratified ionosphere according to the methods described in the paper [Lebed et al., 2018]. A sketch of the model is shown in Fig. 4.

Auroral hiss is generated via Cherenkov resonance at altitudes of about $10000 \div 20000$ km with $k/k_0 \gg 1$, k is the wave vector magnitude, $k_0 = \omega/c$, ω is wave angular frequency, c - speed of light in free space. It propagates at electrostatic whistler mode to lower altitudes (about 3000 km) where waves with $k/k_0 \gg 1$ are scattered by meter-scale irregularities to the propagation cone $-1 < k/k_0 < 1$. Only a small part of the scattered waves propagates to the ground.

The auroral electrons are precipitated along the geomagnetic field line, however, the results of simulation show that the auroral hiss is observed southward of the precipitating region due to deviation of the waves in the propagation cone from the magnetic field line to the vertical.

Discussion and conclusions

The analysis of the 20Dec2018 event showed that the first and third bursts of auroral hiss arrived to KAN and LOZ from North-East, and the correspondent aurora was observed far to the North as well. We may assume that the precipitating electron generating hiss were located much far northward from KAN and LOZ, thus exit area of the considered auroral hiss may locate at much higher geomagnetic latitudes. It matches with the described above model of these wave propagation from the wave generation region to the ground [Lebed et al., 2018].

Thus, we proposed a new approach to estimate the arrival angles of the auroral hiss observed on the ground and applied it to VLF auroral hiss observations at KAN and LOZ. The proposed model shows that the ionospheric exit region of the auroral hiss is located southward of the visible aurora and soft electron precipitation. The results of modeling are consistent with the observation results.

Acknowledgment

The research was partly supported by the Academy of Finland (grant no.308501 and no.315716). The filtered VLF KAN data are available at <http://www.sgo.fi/pub/vlf/> as the power spectrograms in 24-h, 1-h and 1-min intervals for all campaigns 2006-2019.

References

Lebed O.M., Fedorenko Yu. V., Nikitenko A.S., Kleimenova N.G. (2018), Model of auroral hiss propagation from source region to the ground. Transactions of the kola science centre, heliogeophysics, 5-4, 97-107. doi: 10.25702/KSC.2307-5252.2018.9.5.97-107 (in russian)

TEC Response to the Solar Flare on 6 September 2017

*Shagimuratov I.I.*¹, *Chernouss S.A.*², *Despirak I.V.*², *Tepenitsyna N.Yu.*¹,
*Filatov M.V.*², *Efishov I.I.*¹, *Yakimova G.A.*¹

¹ WD IZMIRAN, Kaliningrad, Russia

² Polar Geophysical Institute, Apatity, Russia

E-mail: shagimuratov@mail.ru

Abstract.

The series of the solar flares took place in September 2017. In this work we presented the TEC response on the intense solar flare (X9.3) that occurred on 6 September 2017. According to GOES satellite, this flare started at 11:53 UT and had the peak of intensity at 12:02 UT. Solar flare effects in TEC for sun light ionosphere were carried out using IGS and EPN GPS network. Stations are grouped around latitude of 50°N and ranging from ~85°W ° to ~ 100°E longitudes. Direct response of TEC on the solar flare was be connected with the TEC variations along the satellite passes over individual stations. The maximal TEC enhancement was ~ 2.5-2.7 TECU during the local noon time. We found out the significant linear correlation between the TEC enhancement and the solar zenith angle. We examine the spatial and temporal changes of TEC during the solar flare using TEC maps over Europe. The maximal time resolution of these maps was 5 min. The maps demonstrated the sudden TEC enhancement after 12 UT over whole Europe. Differential maps between 5 and 6 September 2017 were also formed. The five-minute resolution maps of TEC shown the essential TEC dynamics during the solar flare.

Introduction

The investigation of the solar flares is of interest for an ionospheric researches, the space weather application [Yamauchi M. et al., 2018] and also the GPS/GLONASS navigation [Berdermann J, et al., 2017], [Yasyukevich Y. et al., 2018].

A solar flare is associated with the significant enhancements of the solar irradiation fluxes, from X-ray to EUV radiations.

During solar flares, the sudden increase in the X-ray and EUV causes the increase ionization of the Earth's ionosphere. It is generally accepted that the X-rays penetrate deep into the ionosphere and could cause the enhanced D region ionization during solar flares, the EUV flux increases the ionization in the E and F regions of the ionosphere. For the intensive solar flare of 7 September 2005 [Bo X. et al., 2011] shown that the average percentage enhancements of the electron density during the flare are more than 200 % near the E region peak height but only about 10% near the F region peak height. A poor correlation was observed between the X-ray fluxes and the EUV fluxes during solar flares (only 0.66 was the correlation coefficient) [Mahajan K. et al., 2010] while after the correction to the central meridian distance (CMD) the correlation coefficient between $\Delta X\text{-ray} \cdot \cos(\text{CMD})$ and ΔEUV reaches 0.90 [Le H. et al., 2013]. But the X-ray flux could use as the indicator of the solar flare intensity.

The GPS TEC data were widely used now to describe the ionospheric response to the solar flares. Dual-frequency observations of the GPS signals provide the TEC measurement with the higher spatial and temporal resolution. Methods of the detection of solar flares using the GPS/TEC measurements were presented by [Afraimovich E. et al., 2000; Hernandez-Pajares M. et al., 2004; Liu J.Y. et al., 2004; Hazarika et al., 2016]. Several scientific investigations have been carried out to the study of the global response of the ionospheric total electron content (TEC) to many intense solar flares in the recent years.

The ionospheric effect depends on the solar flare location on the solar disk. Flares with the same X-ray level produce a stronger ionospheric response if they have a smaller central

meridian distance (CMD) [Le H. et al., 2013; Leonovich L.A. et al., 2010]. The TEC enhancement reduces with the increase of the zenith angle of the solar flare.

This result was in contrasting to the earlier study by Mendillo M. et al. (1974), in which was found that no exists the correlation between the TEC enhancement and the solar zenith angle. At the same time the correlation between the TEC enhancement and the solar zenith angle was shown by Garsia-Rigo M. et al. (2007). So, the ionospheric effects were differed for different flares. However, due to the complexity and variety of ionospheric response to the solar flares, still further studies are needed, and these studies remain relevant to this day. In this work we presented the detail analyses of the TEC response to the strong flare (X9.3) of 6 September 2017.

Method and data

The dual-frequencies phase of the GPS observations was used to extract the solar flare effects in the GPS/TEC measurements. An absolute TEC values were obtained using the procedure which was presented by Shagimuratov I. et al. (2013). The TEC variations along the individual satellite passes were used as the initial data of the sores. The enhancement of the TEC was evaluated by the subtracting of the background TEC values before the solar flare, similar method was outlined by Hazarika et al. (2016). The peak of the enhancement (Δ TEC) was used to describe the TEC responses to the solar flare. In Table 1 some parameters discussed X9.3 class flare are presented.

Table 1. Time parameters of the flare on September 06, 2017

Class	Data	UT		
		start	maximum	end
X9.3	2017/09/06	11:53	12:02	12:10

Figure 1 shows the variations of the X- ray fluxes observed by the geosynchronous satellite GOES- 13 (www.spaceweatherlive.com) and the map of the active regions of the Sun provided by the Mees Solar Observatory for the event on 6 September 2017.

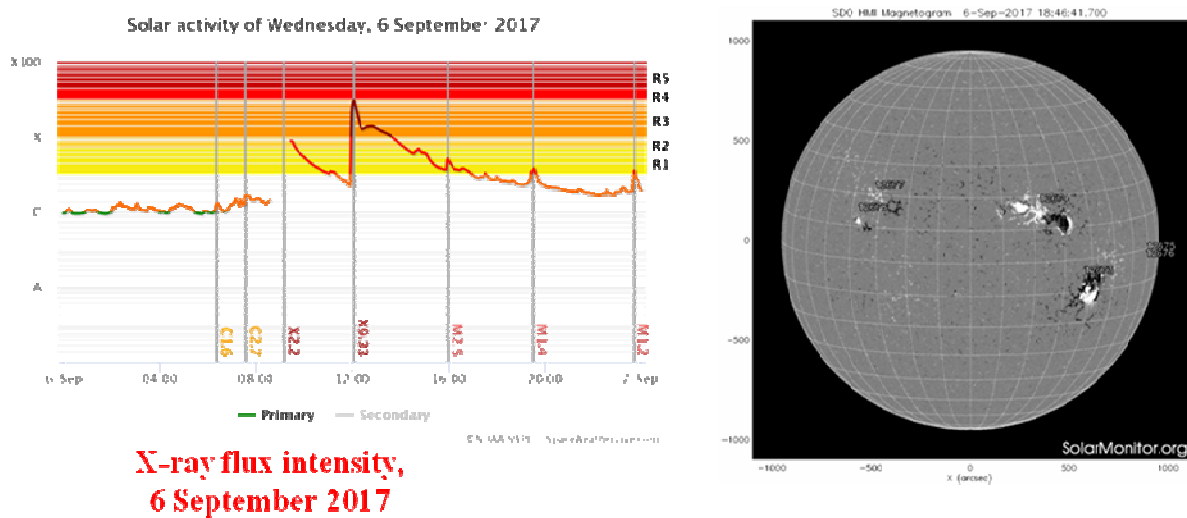


Fig.1 Variations of the X-ray intensity and the active regions maps of the Sun for the solar flare (X9.3) on 6 September 2017.

The positions of the active regions are given in the both heliographic and heliocentric coordinates: S27W38 (519", -476").

Results

a) occurrence of the solar flares at different longitudes

The detail occurrence of the solar flares was analyzed using the temporal variations of the TEC along the satellite passes as well as in the time derivative of the TEC, $d\text{TEC}/dt$ ($dt=1$ min). The TEC enhancement is clearly seen over all stations located on the sunlight region (Fig. 2). The unit of the TEC is TECU ($1 \text{ TECU} = 10^{16} \text{ electron/m}^2$). The over ionization is clearly seen for the different stations at almost the same UT time.

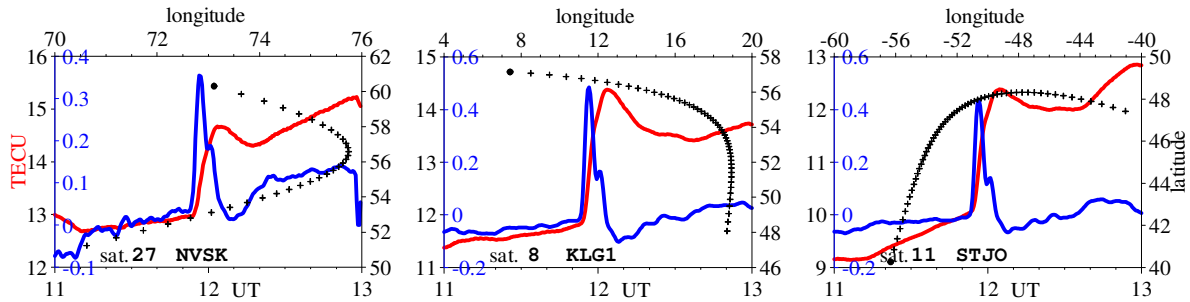


Fig. 2. The variations of the TEC along satellite passes over stations NVSK (54.7°N; 83.2°E), KLG1 (54.5°N; 20.5°E), STJO (47.4°N; 52.7°W). Red lines market the TEC, blue lines — $d\text{TEC}/dt$, black lines indicated the satellite trajectory.

b) dependence of the TEC enhancement on the solar zenith angle

The solar zenith angle is an important parameter for the study of the solar ionization of the Earth atmosphere. The solar irradiance increase during the solar flare, and, as a consequence, it evokes to the TEC enhancement.

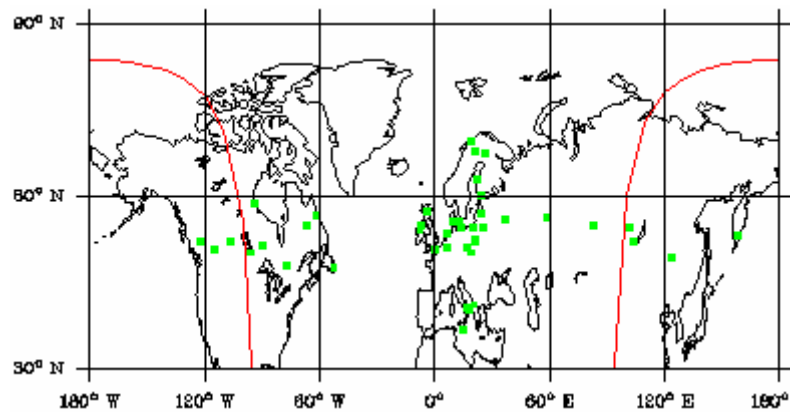


Fig.3 The spatial locations of the stations (green dots) were used for the analysis the dependence of the ΔTEC vs the solar zenith angle. Red lines are the lines of the solar terminator.

Figure 3 shows the worldwide locations of the GPS stations which were used to evaluate the TEC enhancement in depending on the solar zenith angle. To reduce the latitudinal influence of the TEC response, the stations are grouped around the latitude of 50°N. A longitudinal distribution of the GPS stations ranging from the sunrise to the sunset. Our observations shown that the closer location was to the subsolar point, the larger TEC enhancement was observed. As it was presented previously [Krakowski A. et al. 2003; Garcira-Rigo M. et al., 2007] the TEC enhancement depend on the solar zenith angle.

The longitudinal and latitudinal views of the dependence of the ΔTEC on the solar zenith angle is plotted in Fig. 4 for the stations presented in the Figure 3. An analysis shows that the

values of the TEC enhancement were some differ for the different satellite passes observed by each stations. We averaged the ΔTEC values over all satellites visibly by the stations. From the figure it is, seen the significant dependence of the ΔTEC on the solar zenith angle: the value of ΔTEC increases with the decreasing of the solar zenith angle. The solid lines in Figure 4 are the corresponding linear regressions. A linear regression equation to estimate the ionospheric TEC responses to a solar flare is as follows:

$\Delta\text{TEC} = -0.03 \times \chi + 3.97$. The correlation coefficient was $R = 0.853$. It is the latitudinal view. ΔTEC was obtained as the mean values using of the TEC measurements over stations located near the longitude of 25°E .

$\Delta\text{TEC} = -0.04 \times \chi + 4.39$. The correlation coefficient was $R = 0.939$. It is the longitudinal view. ΔTEC was obtained as mean values using of the TEC measurements over stations located around the latitudes of 50°N .

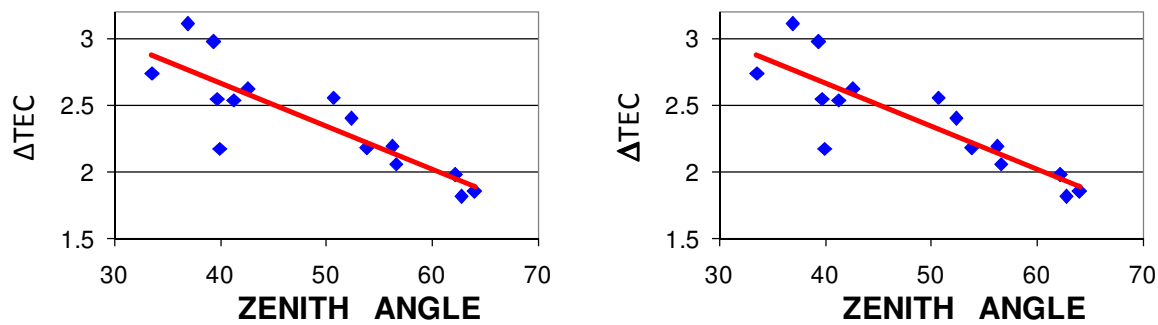


Fig. 4. Scatter plots of the observed ΔTEC vs. zenith angle (χ), the longitudinal (left) and the latitudinal (right) views.

Figure 5 illustrates the TEC maps over Europe on the time interval 08 - 19 UT. It can be seen clearly that the TEC enhancement took place after 12 UT. Maximal effect was occurred at the southern stations.

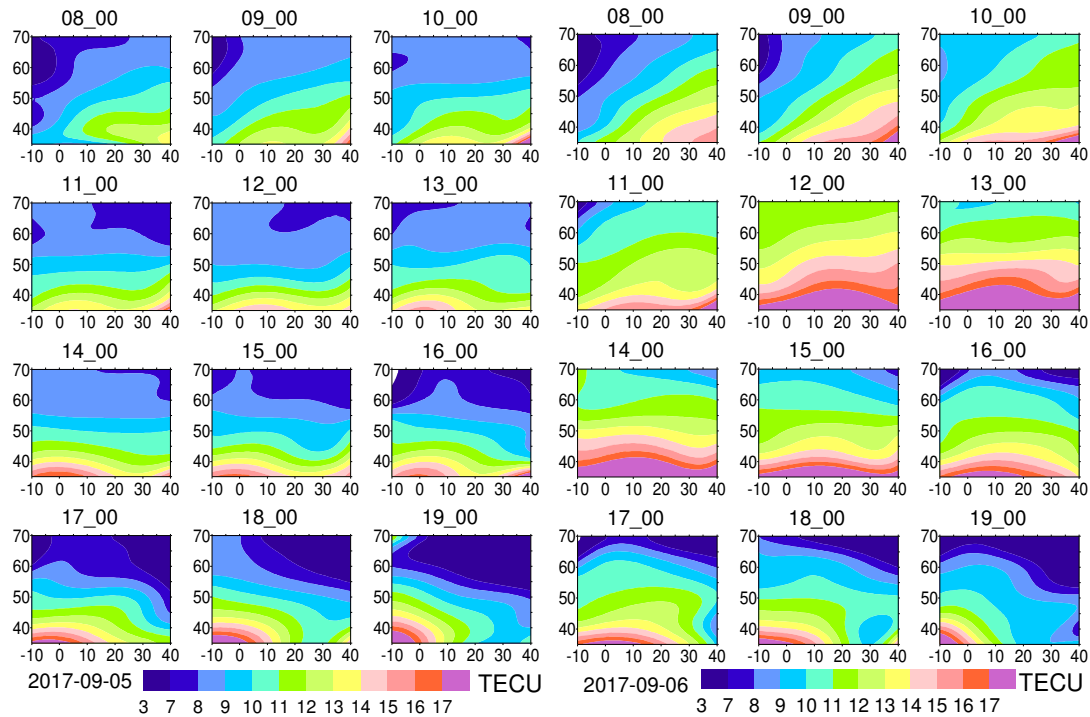


Fig.5. The 1-hour resolution maps of the TEC over Europe for 5 and 6 September 2017.

c) spatial occurrence the solar flare

For the analysis of the spatial distribution of the TEC during the solar flare, TEC maps over Europe were produced. We used the GPS measurements collected by the 150÷180 GPS stations. In the multi-site algorithm, simultaneous GPS measurements at all stations used to obtain the spatial pattern of the solar flare. The distinct European GPS network provides the high spatial resolution and the TEC accuracy. The description of a technique forming of the TEC maps was presented by Shagimuratov et al. (2013).

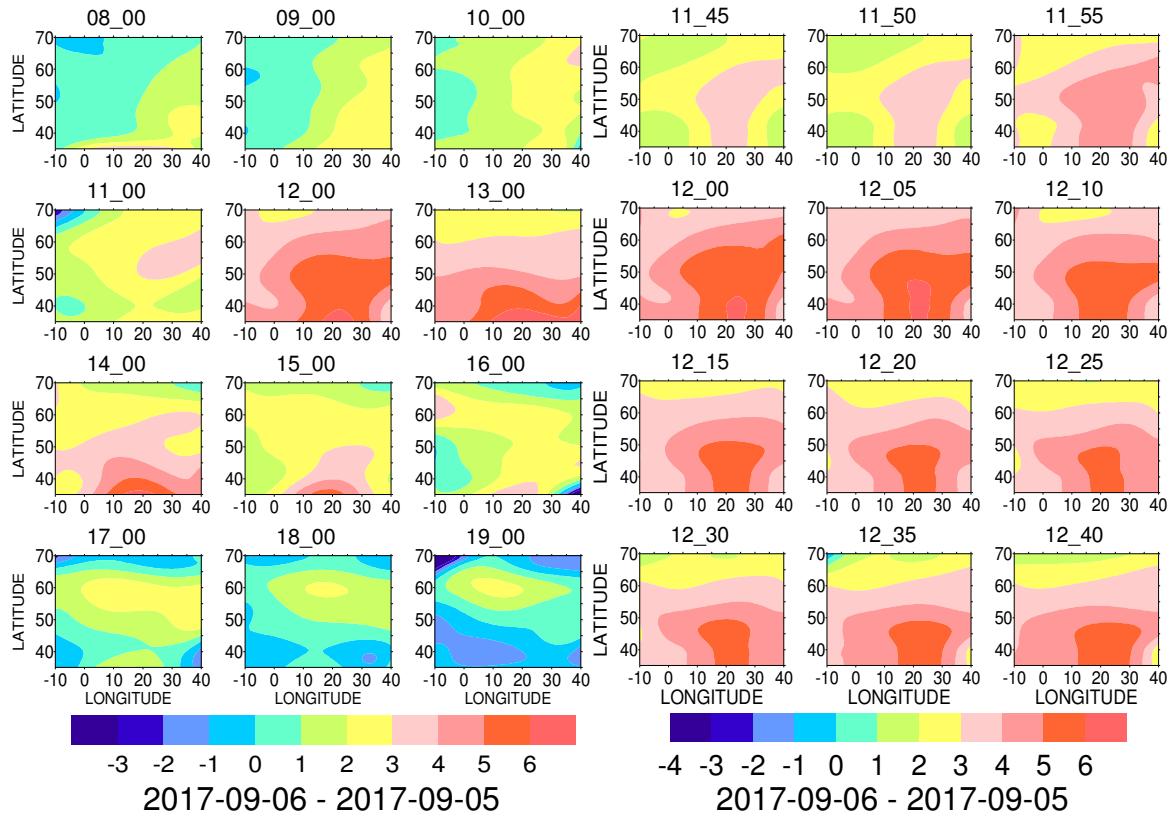


Fig.6. Difference of the TEC between events on 5 and 6 September 2017 (left), TEC maps with 5 min. interval for the time when the maximal effect of the solar flare took place (right).

Figure 6 shows the differential TEC maps with 1-hour interval between 5 and 6 September 2017 for the period 08-19 UT. The positive effect after 12 UT is clearly observed. Five-minute maps of the TEC shown the essential dynamics of the response of the TEC to the solar flare.

Conclusions

The flare caused a sudden increase of the TEC over whole sunlight ionosphere. The response of the TEC to the flare was evaluated by the diurnal variation of the TEC and the ROT over the selected stations. More detailed information on the TEC dynamics during the flare can be derived from the TEC variations along the satellite passes over individual stations. We found a significant linear correlation between the TEC enhancement and the solar zenith angle. The latitudinal behavior of the TEC response to the flare demonstrates also a linear dependency with the latitude. The peak of the TEC enhancements is delayed about only 2-3 min relative to the peak X-ray intensity. The maximal effect of ~3.0 TECU was reached at the solar zenith. A percentage of the TEC enhancement was about 20. To estimate the spatial and the temporal changes of the TEC during that solar flare, we examine the high resolution of the TEC maps over Europe. The temporal resolution of these maps was 5 min. The maps

demonstrate a sudden TEC enhancement after 12 UT over whole Europe. The larger enhancement took place at the lower latitudes. The recovery stage lasted more than 1-2 hours. We analyzed also the differential TEC maps in the period between 5 and 6 September 2017. The 5-min differential TEC maps shown an essential dynamics of the TEC response to the solar flare.

Acknowledgment

This investigation was supported by RFBR Grant № 19-05-00570.

References

- Afraimovich E.L., A.T. Altynsev, E.A. Kosogorov, N.S. Larina and L.A. Leonovich (2001). Ionospheric effects of the solar flares of September 23, 1998 and July 29, 1999 as deduced from global GPS network data, *J. Atmos. Sol. Terr. Phys.*, 63, 1841–1849, doi:10.1016/S1364-6826(01)00060-8.
- Berdermann J., M. Kriegel, D. Banyrs, et al. (2017). Ionospheric response to the X9.3 Flare on 6 September 2017 and its implication for navigation services over Europe. *Space Weather*, 16, 1604–1615. <https://doi.org/10.1029/2018SW001933>.
- Bo Xiong, Weixing Wan, Libo Liu et al. (2011). Ionospheric response to the X-class solar flare on 7 September 2005. *J Geophys Res*, 116, doi:10.1029/2011JA016961.
- Garcia-Rigo M. Hernandez-Pajares, J.M. Juan, J. Sanz (2007). Solar flare detection system based on global positioning system data: First results. *Advances in Space Research*, 39, 889–895.
- Hazarika R., Kalita B.R., Bhuyan P.K. (2016). Ionospheric response to X-class solar flares in the ascending half of the subdued solar cycle 24. *J. Earth Syst. Sci.*, 125, N 6, 1235–1244, doi: 10.1007/S12040-016-0726-6.
- Hernandez-Pajares, M., J. M. Juan, and J. Sanz (1997). High resolution TEC monitoring method using permanent ground GPS receivers, *Geophys. Res. Lett.*, 24, 1643.
- Krankowski A., I.I. Shagimuratov, L.W. Baran, et al. (2003). Response of the ionosphere to the great solar flare on October 28, 2003. Poster in: European Geosciences Union, General Assembly, 2003.
- Le H., L. Liu, Y. Chen, W. Wan (2013). Statistical analysis of ionospheric responses to solar flares in the solar cycle 23, *J. Geophys. Res. Space Physics*, 118, 576–582, doi:10.1029/2012JA017934.
- Leonovich L.A., E.L. Afraimovich, E.B. Romanova, A.V. Tashchilin (2002). Estimating the contribution from different ionospheric regions to the TEC response to the solar flares using data from the international GPS network, *Ann. Geophys.*, 20, 1935–1941, doi:10.5194/angeo-20-1935-2002.
- Leonovich L.A., A.V. Tashchilin, O.Yu. Portnyagina (2010). Dependence of the ionospheric response on the solar flare parameters based on the theoretical modeling and GPS data, *Geomagn. Aeronomy*, 50 (2), 201–210, doi: 10.1134/S0016793210020076.
- Liu J.Y., C.H. Lin, H.F. Tsai, Y.A. Liou (2004). Ionospheric solar flare effects monitored by the ground-based GPS receivers: Theory and observation, *J. Geophys. Res.*, 109, A01307, doi:10.1029/2003JA009931
- Liu J.Y., C.H. Lin, Y.I. Chen, Y.C. Lin et al. (2006) Solar flare signatures of the ionospheric GPS total electron content, *J. Geophys. Res.*, 111, A05308, doi:10.1029/2005JA011306.
- Mahajan K.K., N.K. Lodhi, A.K. Upadhyaya (2010). Observations of X-ray and EUV fluxes during X-class solar flares and response of upper ionosphere, *J. Geophys. Res.*, 115, A12330, doi:10.1029/2010JA015576.
- Mendillo M. et al. (1974). Behavior of the ionospheric F region during the great solar flare of August 7, 1972. *J. Geophys. Res.*, 79, 665-672, DOI: 10.1029/JA079i004p00665.
- Shagimuratov I.I., Yu.V. Chernyak, I.E. Zakharenkova, G.A. Yakimova (2013). Use of Total Electron Content Maps for Analysis of Spatial–Temporal Structures of the Ionosphere, *Russian Journal of Physical Chemistry B*, 7 (5), 656–662.
- Yamauchi, M., T. Sergienko, C.-F. Enell, et al. (2018). Ionospheric response observed by EISCAT during the 6–8 September 2017 space weather event: Overview. *Space Weather*, 16, 1437–1450. <https://doi.org/10.1029/2018SW001937>.
- Yasyukevich Y., E. Astafyeva, A. Padokhin et al. (2018). The 6 September 2017 X-class solar flares and their impacts on the ionosphere, GNSS, and HF radio wave propagation. *Space Weather*, 16, 1013–1027. <https://doi.org/10.1029/2018SW001932>.

The Nitric Oxide Density in the Polar Region from Ground-Based Photometer Data

Dashkevich Zh.V., Ivanov V.E.

Polar Geophysical Institute, Apatity, Russia

E-mail: zhanna@pgia.ru

Abstract.

The effect of the nitric oxide NO on the 5577Å emission intensity during electron polar aurora is studied. It is shown that the reaction $O_2^+ + NO$ is a significant channel of the 5577Å intensity suppression. This reaction reduces the contribution of O_2^+ dissociative recombination in the $O(^1S)$ excitation. The approach of evaluation of nitric oxygen density in the polar region using the ground based photometer data of intensity of 4278Å, 5577Å and 6300Å emissions, is suggested based on the research. The NO density is determined using the photometer emission intensity data obtained Polar Geophysical Institute observatories. This NO density is between $1 - 3.3 \cdot 10^8 \text{ sm}^{-3}$. It is noticed that the obtained estimations indicate the absence of correlation between the 4278 Å intensity and the NO density.

Introduction

Being a small component of the atmosphere, nitric oxide plays an important role in physicochemical processes taking place during auroral electron precipitations. Nitric oxide is produced in the polar ionosphere when charged particles are precipitating in the earth's atmosphere. Due to its long lifetime, nitric oxide is accumulating in the atmosphere. Therefore the NO concentration generally depends on the duration and the intensity of auroral activity preceding the event studied.

The direct mass-spectrometer measurements of the NO density, which were made in the aurora, are absent. The evaluations of the NO density in aurora were made using the rocket measurements of the atmosphere ion composition and intensity of the NO₂ continuum emission at 5200Å [Swider and Narcisi, 1977, Sharp, 1978], as well as the NO density obtained from satellite measurements of the NO (1-0) band intensity [Siskind et al., 1989]. Estimates show that the NO density in the altitude profile maximum varies by a factor of 10^2 .

In this connection, the search is actual for the possibilities of diagnosing the NO density by the data of optical observations of the particular aurora shapes, which are made from both the earth's surface and on board the space apparatuses.

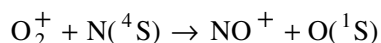
The nitric oxygen effect on the 5577 Å emission

Consider a possibility of diagnostics of the "instantaneous" NO density in the aurora, using the measured intensities of atomic oxygen emissions at 5577Å and 6300 Å and the N₂⁺ First negative system emission at 4278 Å, because these emissions are often observed by ground-based photometer during aurora.

How does the nitric oxide concentration affect on the emissions intensities, first of all, the green line intensity because this emission is related to nitric oxide through chemical reactions. Some of the channels of the production of the atomic oxygen ¹S state which is the source of auroral 5577Å emission, are:

a) a dissociative recombination of the molecular oxygen ion: $O_2^+ + e \rightarrow O(^1S) + O(^1D)$

b) a collisional reaction between molecular oxygen ion and excited nitrogen:



In turn, the molecular oxygen ion interacts with nitric oxide: $O_2^+ + NO \rightarrow NO^+ + O_2$

Besides, nitric oxide suppresses the excited oxygen $O(^1S)$: $O(^1S) + NO \rightarrow O + NO$.

The various reactions contribution to the $O(^1S)$ production for different NO densities has been calculated by the physicochemical model of auroral ionosphere, characterized in detail in [Dashkevich et al., 2017]. The model is constructed on the basis of the data available in scientific literature and comprises 56 physicochemical reactions, of which 23 reactions take place with the participation of odd nitrogen NO, N(4S), N(2D). The input parameters of the model are the neutral atmosphere model and the precipitating electrons flux parameters. The MSIS-90 has been taken as a neutral atmosphere model. The energy spectrum of the precipitating electrons flux was specified as the Maxwellian distribution: $N(E) = N_0 E \exp(-E/E_0)/E_0^2$, where N_0 and E_0 are the initial particles flux and the characteristic energy, respectively.

The nitric oxide density in the altitude profile maximum $[NO]_{\max}$ was varied between 10^7 and 10^9 cm^{-3} , the characteristic energy E_0 was varied within the interval of 1-10 keV. This interval corresponds to the average energy of the precipitating electrons inducing arc- and band-shaped aurora.

Figure 1 shows the calculated relative contributions of physicochemical reactions to the $O(^1S)$ production in the aurora, depending on the $[NO]_{\max}$ value. The figure shows that the contribution of dissociative recombination being one of the basic channels of 1S excitation, greatly depends on the NO density, and this contribution increasing with the increase of the average energy of the precipitating electrons flux.

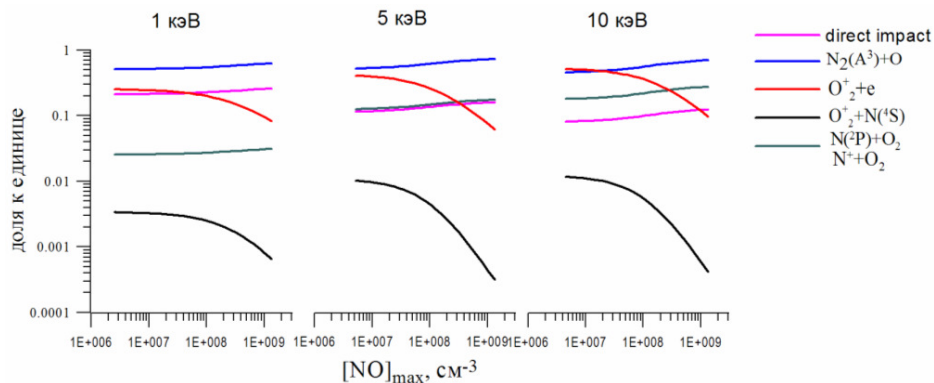


Fig.1. The contribution of various reactions to the formation of excited atomic oxygen $O(^1S)$

Thus, the NO density value may be expected to influence the green line intensity. Presented in the figure 2 are the dependencies of the 5577 Å intensity on the $[NO]_{\max}$ value, which are calculated at the energy flux of $1 \text{ erg cm}^{-2} \text{ s}^{-1}$. It is seen that with the increase of the $[NO]_{\max}$ value by a factor of 10^3 , the green line intensity decreases by 30-70% within the range E_0 between 1 to 10 keV.

The NO diagnostics in the aurora.

As the green line intensity is sensitive to the nitric oxide density, consider a possibility to carry out estimations of the nitric oxide density using the measured intensities of emissions at 4278 Å, 5577 Å and 6300 Å.

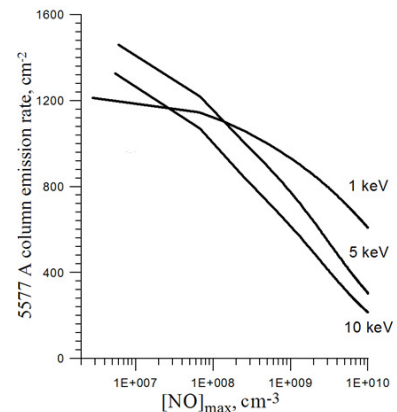


Fig.2. Dependencies of the 5577 Å column emission rate on the nitric oxide density in the altitude profile maximum $[NO]_{\max}$ value

The auroral emissions intensities depend on the average energy and energy flux of precipitating electrons. But the I_{5577}/I_{4278} and I_{6300}/I_{4278} volume emission rate ratios slightly depend on the precipitating electrons energy flux, Figure 3 shows that. The calculation was made by physicochemical model of auroral ionosphere [Dashkevich et al., 2017]. Hence, the I_{5577}/I_{4278} ratio is mainly determined by the values of E_0 and NO density. Figure 4a shows the dependence of the I_{5577}/I_{4278} ratio on $[\text{NO}]_{\text{max}}$ for E_0 in the range of 1 to 10 keV.

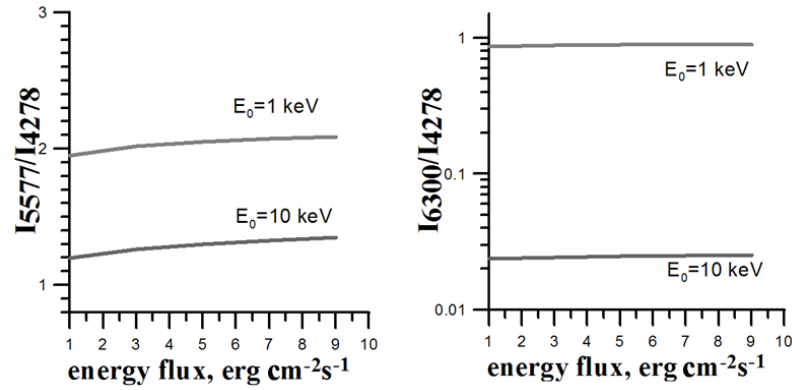


Fig.3. Dependencies of I_{5577}/I_{4278} and I_{6300}/I_{4278} value from the energy flux of precipitating electrons

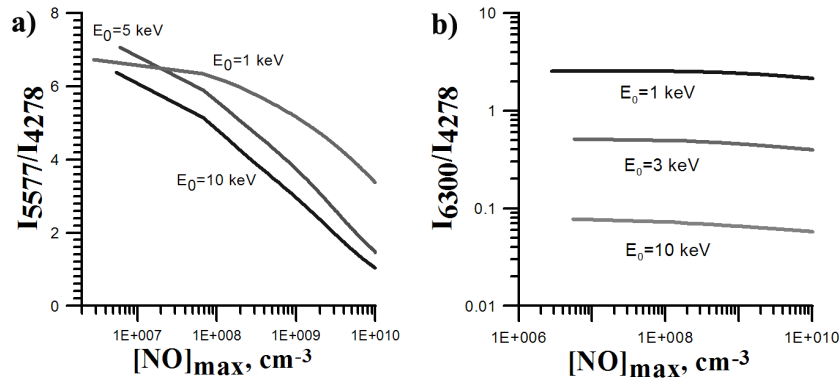


Fig.4. Dependencies of I_{5577}/I_{4278} and I_{6300}/I_{4278} value on the nitric oxide density in the altitude profile maximum $[\text{NO}]_{\text{max}}$

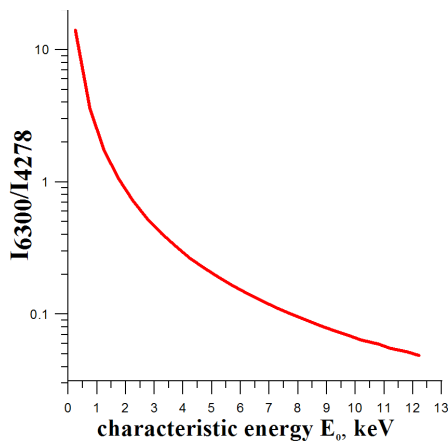


Fig.5. The dependence of the I_{6300}/I_{4278} value from characteristic energy E_0 .

Among the channels of excitation of ^1D state atomic oxygen which is the source of emission at 6300 Å, there are two channels subject to the process of nitric oxide deactivation. These are a dissociative recombination $\text{O}^+ + \text{NO} \rightarrow \text{O} + \text{NO}^+$ and a radiative transition $\text{O}(^1\text{S}) \rightarrow \text{O}(^1\text{D}) + h\nu$. However, calculations showed that the I_{6300}/I_{4278} ratio demonstrates slight dependence on $[\text{NO}]_{\text{max}}$ value. This is shown in the picture 4b.

As shown by [Rees and Luckey, 1974], it is possible to estimate E_0 from the I_{6300}/I_{4278} ratio. Shown in Figure 5 are the calculated dependence of the I_{6300}/I_{4278} volume emission rate ratio on E_0 for a $[\text{NO}]_{\text{max}}$ lying within the range of $10^7 \div 10^{10} \text{ cm}^{-3}$.

Thus, we can determine the nitric oxide density by the following algorithm:

- 1) based on the measured I_{6300}/I_{4278} ratio, we gain an estimation of characteristic energy E_0 of the precipitating electron flux (Figure 5)
- 2) based on the dependence of the I_{5577}/I_{4278} ratio on $[\text{NO}]_{\text{max}}$ for the E_0 found, we determine the nitric oxide density in the altitude profile maximum (Figure 4a)
- 3) based on $[\text{NO}]_{\text{max}}$ gained, we reconstruct the nitric oxide altitude profile using the physicochemical model of the auroral ionosphere [Dashkevich et al., 2017]

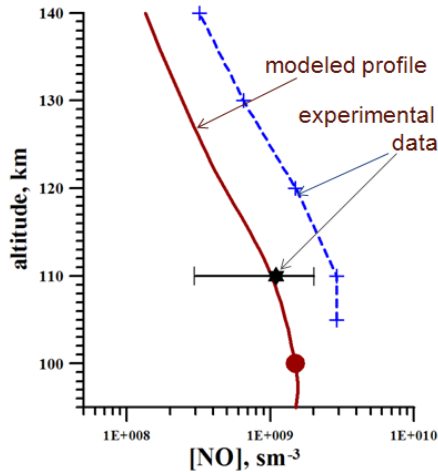


Fig.6. The estimated of $[\text{no}]_{\text{max}}$ (ball), modeled altitude profile of the no density (solid line) and the no density estimations obtained in [sharp,1978] (dashed line)

Approbate the proposed technique of estimating $[\text{NO}]_{\text{max}}$ in aurora using the data obtained into coordinated rocket-satellite experiment. Presented in [Rees et al, 1977, Sharp, 1978, Sharp et al, 1979] are the results of these measurements of OI 5577Å and 6300 Å intensities and 1NG N_2^+ 3914 Å intensity. Also given are the estimates of the NO density in aurora. Using the results of emission intensities measurements presented in these studies, and the technique presented above, we determined the characteristic energy E_0 of the precipitating electrons flux and estimated the nitric oxide density $[\text{NO}]_{\text{max}}$. The value of $[\text{NO}]_{\text{max}}$ is shown in Figure 6 together with the altitude profile of the NO density, normalized on this maximum and modeled within the disturbed ionosphere model [Dashkevich, et al., 2017]. Also presented here are the NO density estimations obtained in [Sharp,1978] using both the intensity of the NO_2

continuum emission at 5520 Å and the measured $[\text{NO}^+]/[\text{O}_2^+]$ ratio. The figure shows good consistence of the NO estimation obtained by technique proposed above with the experimental obtained values.

Experimental result

The nitric oxide density has been assessed using the data of photometer observations at the 4278Å, 5577Å and 6300 Å emissions, made in Polar Geophysical Institute observatories. The experimental data include 1335 measurements in 8 midnight series at the observatory Lovozero ($\Phi' = 64.17^\circ\text{N}$) and 1200 measurements at the observatory Tumanny ($\Phi' = 65.24^\circ\text{N}$). The 4278 Å emission intensity is in the range between 1-2 kR. The data have been grouped in 100 R ranges of 4278 Å emission intensity and averaged on two stations.[Dashkevich et al.,2006]

At the first stage were determined the parameters precipitating electrons flux, namely:

Table 1. Results of the $[\text{NO}]$ diagnostic

$I_{427.8}, \text{R}_{\text{exp}}$	$I_{557.7}/I_{427.8}$ exp	$I_{630.0}/I_{427.8}$ exp	E_0, eV calc	$[\text{NO}]_{\text{max}},$ 10^8 cm^{-3}
150	5.21±0.55	1.63±0.14	1039	1.6
250	5.31±0.43	1.46±0.28	1116	1.6
350	5.35±0.44	1.17±0.22	1291	1.8
450	5.49±0.43	1.07±0.18	1370	1.7
550	5.38±0.5	0.90±0.24	1541	2.3
650	5.48±0.32	0.84±0.16	1607	2.2
750	5.52±0.44	0.88±0.21	1559	2.2
850	5.82±0.38	0.72±0.17	1780	1.5
950	5.87±0.62	0.61±0.13	1987	1.4
1100	6.12±0.66	0.68±0.29	1858	1.0
1350	5.84±0.77	0.56±0.17	2102	1.7
1700	5.46±0.12	0.44±0.12	2465	3.3

the characteristic energy E_0 and the particle flux N_0 . The values of characteristic energy E_0 were estimated from the I_{6300}/I_{4278} ratio measured in the observations. The values of the particle flux N_0 were determined from measured 4278 Å intensities.

The second stage included the evaluation of the nitric oxide density in the altitude profile maximum and simulation of the altitude distributions of the NO density. The absolute NO density values for each particular case were determined based on reaching the best consistency between the calculated values of the I_{6300}/I_{4278} volume emission rate ratio and measured one. The experimental data, estimated average energy E_0 and evaluated values of the NO density in the altitude profile maximum $[\text{NO}]_{\text{max}}$ are presented in Table 1.

It is necessary to note that the results resaved at this research evidence that the absence of direct correlation between the NO density and the 4278 Å emission intensity, and, hence, the auroral brightness. The absence of such correlation may be explained by a greater period of the lifetime of the nitric oxide, which can accumulate in the ionosphere. So the NO density amount in aurora in each particular case may be determined not only by the precipitating electrons flux intensity but also by the duration and the intensity of the auroral activity prior to the event studied.

Conclusions

1. The effect of the nitric oxide on the 5577 Å emission in aurora induced by electrons precipitation, has been studied. It is shown that the reaction of $\text{O}_2^+ + \text{NO} \rightarrow \text{NO}^+ + \text{O}_2$ is a channel of the 5577 Å emission suppression. This reaction diminishes the contribution of the dissociative recombination into the production of the atomic oxygen ^1S state.
2. It is shown, the nitric oxide does any effect on the intensities ratio I_{6300}/I_{4278} . This ratio mainly depends on the precipitating electrons energy. In turn, the I_{5577}/I_{4278} intensities ratio depends on both the nitric oxide density and the electrons energy. Based on this fact, the technique of NO density estimation in the aurora by the data of photometer measurements at 4278 Å, 5577 Å and 6300 Å is suggested in this study.
3. Also presented are the estimations of the nitric oxide content in aurora. The model calculations are made based on ground-based photometer measurements of the 4278 Å, 5577 Å and 6300 Å intensities in the midnight sector of the auroral oval. It is shown that the NO density in the maximum of altitude profile $[\text{NO}]_{\text{max}}$ is within the interval of $1 \div 3.3 \cdot 10^8 \text{ cm}^{-3}$ for aurora with the 4278 Å intensity within the interval from 0.1 to 2 kR. No direct correlation has been found of the amount of the nitric oxide with auroral brightness.

References

- Dashkevich Zh.V., V.L. Zverev, V.E. Ivanov (2006). Ratios of $I_{630.0}/I_{427.8}$ and $I_{557.7}/I_{427.8}$ emission intensities in auroras. *Geomagnetism and Aeronomy*, 46, 366–370.
- Dashkevich Zh.V., V.E. Ivanov, T.I. Sergienko, B.V. Kozelov (2017). Physicochemical model of the auroral ionosphere. *Cosmic Res.*, 55, 88–100.
- Rees M.H., D. Luckey (1974). Auroral electron energy derived from ratio of spectroscopic emissions. 1. Model computations. *J. Geophys. Res.*, 79, 5181–5186.
- Rees M.H., A.I. Stewart, W.E. Sharp, P.B. Hays, R.A. Hoffman, L.H. Brace, J.P. Doering, W.K. Peterson (1977). Coordinated rocket and satellite measurements of an auroral event, 1, Satellite observation and analysis. *J. Geophys. Res.*, 82, 2250–2261.
- Sharp W.E. (1978) NO_2 continuum in aurora. *J. Geophys. Res.*, 83, 4373–4376.
- Sharp W.E., M.H. Rees, A.I. Stewart (1979). Co-ordinated rocket and satellite measurements of an auroral events 2. The rocket observations and analysis. *J. Geophys. Res.*, 84, 1977–1985.
- Siskind D.E., C.A. Barth, D.S. Evans, R.G. Roble (1989). The response of the thermospheric nitric oxide to an auroral storm. 2. Auroral latitudes. *J. Geophys. Res.*, 94, 16899–16911.
- Swider W., R.S. Narcisi (1977). Auroral E-region: Ion composition and nitric oxide. *Planet. Space Sci.*, 25, 103–116.

The Efficiencies of O(¹S) and O(¹D) Excitation Mechanisms in Aurora

Dashkevich Zh.V., Ivanov V.E.

Polar Geophysical Institute, Apatity, Russia

E-mail: zhanna@pgia.ru

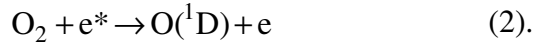
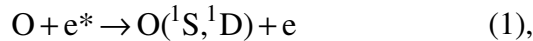
Abstract.

Efficiencies of six O(¹S) excitation mechanisms and seven O(¹D) excitation mechanisms in aurora were studied using a numerical modeling with the novel time-dependent physico-chemical model of auroral atmosphere. It is shown that in interval 90-200 km the main mechanism of the ¹D state excitation is electron impact on atomic and molecular oxygen. The ¹S state excitation occurs mainly by electron impact on atomic oxygen and energy transfer from N₂(A³).

Introduction

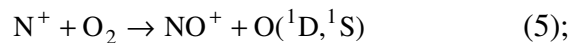
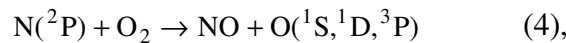
In the polar aurora, the sources of the green line emission 5577Å and the red line emission 6300Å are the excited oxygen atoms in the ¹S and ¹D states, respectively. As these lines are among the strong ones in the polar aurora, being induced by electron precipitation, it is very important to understand the mechanisms of the excited oxygen atoms production and quenching. In the electron aurora, O(¹D) and O(¹S) atoms are formed as a result of direct energetic electrons impact on atomic and molecular oxygen, as well as in the course of different physicochemical reactions taking place in electron precipitations.

The direct electrons impacts are:

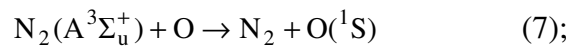
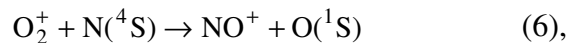


The different physicochemical reactions are:

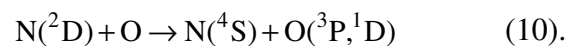
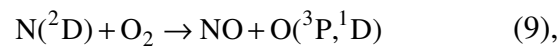
a) reactions in which both of the considered atoms are formed:



b) reactions in which only the atom O(¹S) is formed:



c) reactions in which only the atom O(¹D) is formed:



The efficiencies of individual excitation channels of ¹S and ¹D states of atomic oxygen in aurora has been repeatedly considered in papers [Solomon et al., 1988, Cattinger et al., 1985, Rees, 1984, McDade et al., 1985]. The purpose of this work is to study the complete set of known excitation channels of ¹S and ¹D states using a single physicochemical model of the polar ionosphere, which defines the electron flux energy dissipation processes [Dashkevich et al., 2017].

The calculation method

A comparison of the different excitation mechanisms of the atoms under consideration was made using the physicochemical model of the polar ionosphere [Dashkevich et al, 2017]. The model allows the calculation of: the altitude concentration profiles for the following ionosphere components: N_2^+ , O_2^+ , $O^+(^4S)$, $O^+(^2D)$, $O^+(^2P)$, $O(^1D)$, $O(^1S)$, $N(^4S)$, $N(^2D)$, $N(^2P)$, NO , NO^+ , N^+ , $N_2(A^3\Sigma_u^+)$, $N_2(B^3\Pi_g)$, $N_2(W^3\Delta_u)$, $N_2(B^3\Sigma_u^-)$, $N_2(C^3\Pi_u)$ and for the electrons in the auroral ionosphere; the temporal dynamics of the ionosphere components concentrations; the altitude profiles of the basic auroral emissions intensities, including 4278 Å, 5577 Å, 6300 Å. The input parameters for the numerical model are the atmosphere neutral components concentrations and the electron flux parameters.

The calculations were made in the neutral atmosphere model MSIS-90 for the electron fluxes with the initial energy spectrum $N(E) = N_0 E \exp(-E/E_0)/E_0^2$, where N_0 and E_0 are the initial particle flux and the characteristic energy, respectively. The characteristic energy varied within 1-5 keV. This range of characteristic energies corresponds to the mean energies of the typical auroral precipitations forming the polar aurora arcs and bands. All the calculations made are normalized to a single energy flux of $1 \text{ erg cm}^{-2} \text{ s}^{-1}$.

The green line intensity is sufficiently dependent of the nitric oxide concentration in the atmosphere. So, in numerical modeling, the nitric oxide concentration maximum is $2 \cdot 10^8 \text{ cm}^{-3}$, which corresponds to the experimental estimation of the NO-concentration in the polar aurora. [Dashkevich, Ivanov, 2019]

Results

Figure 1 shows the altitude profiles of the concentration of the atomic oxygen in the 1S state, calculated for electron fluxes with characteristic energies E_0 equal to 1, 3, and 5 keV. From the figures one can see that at the altitude range of 90-200 km, the dominating contribution into the $O(^1S)$ excitation is made by the direct impact $O + e^* \rightarrow O(^1S) + e$ and by the reaction $N_2(A^3\Sigma_u^+) + O \rightarrow N_2 + O(^1S)$. A distinctive feature of the channel for dissociative molecular oxygen ion recombination $O_2^+ + e \rightarrow O(^1S) + O(^1D)$ is pronounced decrease of its contribution into the range of the altitude profile $O(^1S)$ maximum height. This decrease is due to the reaction of molecular oxygen ion quenching by the nitric oxide NO, which reduces the role of O_2^+ into the excitation of the 1S -state of atomic oxygen in the altitude profile maximum.

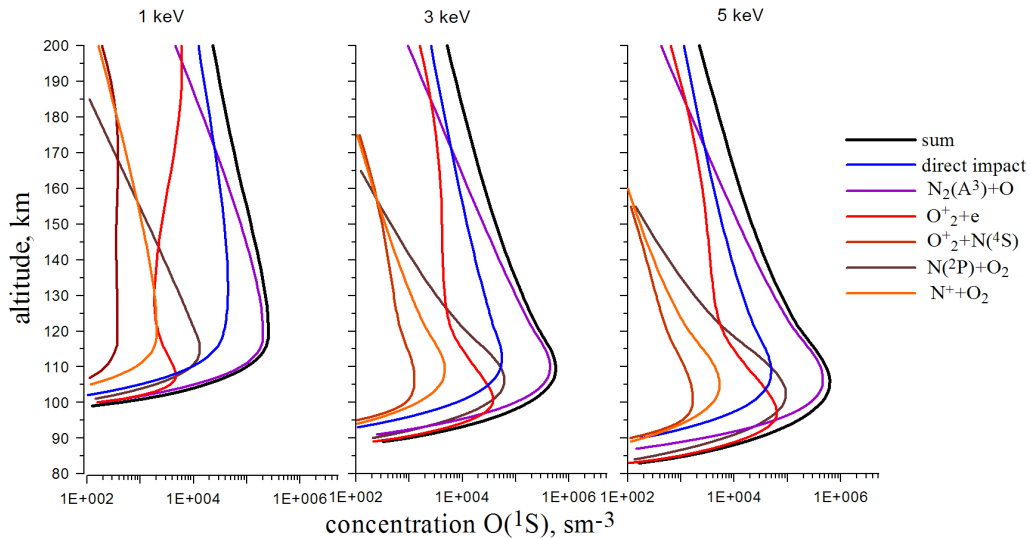


Fig.1. Altitude profiles as a result of different physicochemical reactions contribution into the production of the $1S$ state for the characteristic energies of 1, 3 and 5 keV

Figure 2 presents the height variations of the contributions of the considered reactions to the O(¹S) excitation for various characteristic energies. The total contribution of direct impact and of the reaction $N_2(A^3\Sigma_u^+) + O \rightarrow N_2 + O(^1S)$ in the region of the altitude profile maximum of the O(¹S) concentration makes up 80-95% and decreases to 70% at altitude of 200km. It should be noted that the altitude dependences of these reactions contributions are of opposite nature. The contribution of dissociative recombination $O_2^+ + e \rightarrow O(^1S) + O(^1D)$ makes up 30-10% and 10-28% at altitudes of 150-200 km. It is characteristic of the excitation channel $N(^2P) + O_2 \rightarrow NO + O(^1S)$ to sharply reduce its contribution with altitude. The contribution of this reaction becomes marked in the region of the altitude profile O(¹S) maximum, making up 4-9%. The contributions of reactions $O_2^+ + N(^4S) \rightarrow NO^+ + O(^1S)$ and $N^+ + O_2 \rightarrow NO^+ + O(^1D, ^1S)$ made up less than 1%.

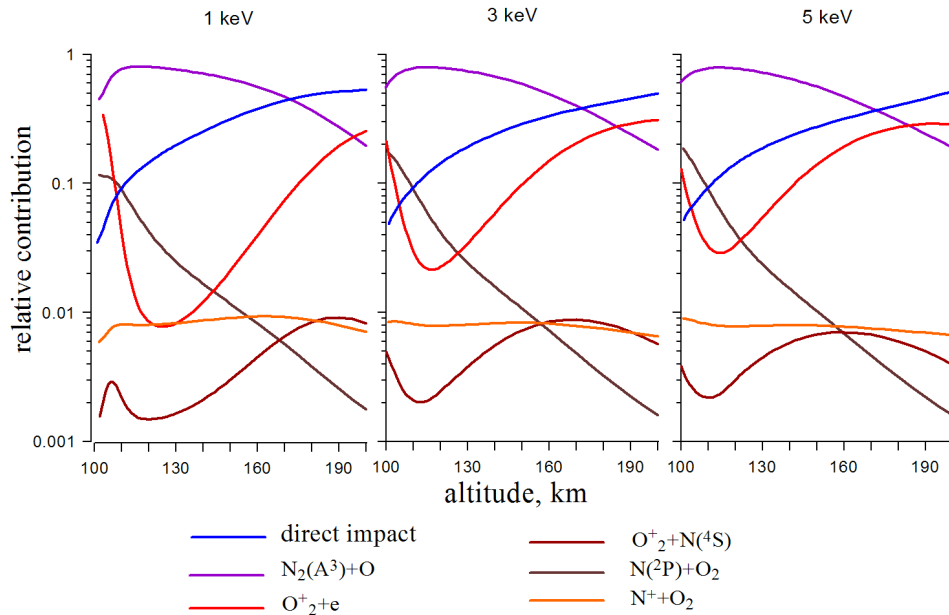


Fig.2. Height dependents of contributions of different physicochemical processes into excitation of the ¹S state for the characteristic energies of 1, 3 and 5 keV

Figure 3 presents the altitude profiles of the concentration of the atomic oxygen in the ¹D state, calculated for electron fluxes with characteristic energies E_0 equal to 1, 3, and 5 keV. Within the altitudes of 90-200 km, the dominating contribution into the O(¹D) state excitation is produced by direct impacts: $O + e^* \rightarrow O(^1D) + e$ and $O_2 + e^* \rightarrow O(^1D) + e$. The excitation channels corresponding to the reactions $N(^2D) + O_2 \rightarrow NO + O(^1D)$, $O(^1S) \rightarrow O(^1D) + h\nu$ and $N^+ + O_2 \rightarrow NO^+ + O(^1D)$ make the comparable contributions into the excitation O(¹D).

Figure 4 shows the height variations of the contributions of the considered reactions to the excitation of O(¹D) atoms for various characteristic energies. The contribution of direct impact in the excitation accounts for 60%, 50% and 45% for the characteristic energies 1, 3 and 5 keV, respectively. The total contribution of the reactions (5), (8,), (9) in the region of the altitude profile maximum of the O(¹D) concentration makes up 34-45%. With an increase in height, the total contribution of these processes drops to 15% and 21% percent, respectively. The contribution of the reaction $N(^2P) + O_2 \rightarrow NO + O(^1D)$ is insignificant at any altitudes and is less than 3% for the considered range of characteristic energies.

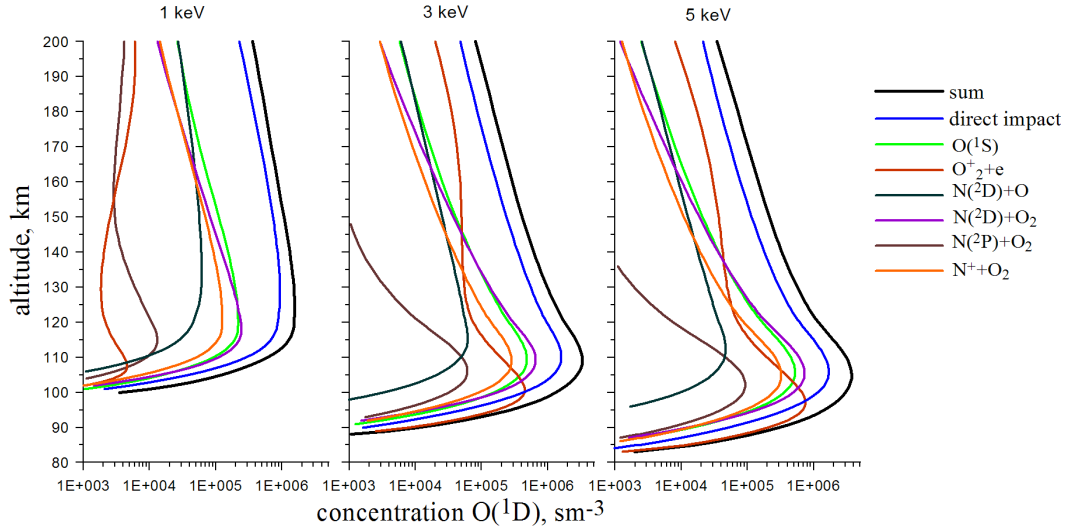


Fig.3. Altitude profiles as a result of different physicochemical reactions contribution into the production of the 1D state for the characteristic energies of 1, 3 and 5 keV

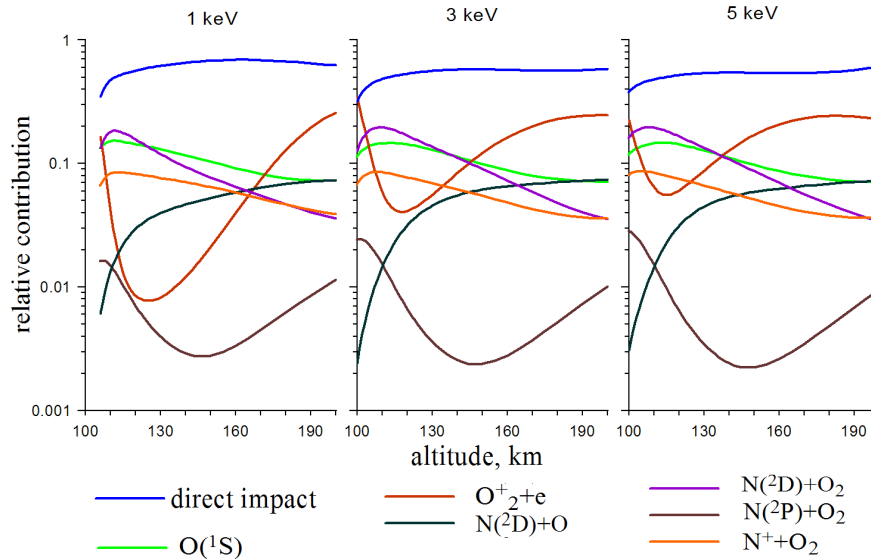


Fig.4. Dependents of contributions of different physicochemical processes into excitation of the 1D state for the characteristic energies of 1, 3 and 5 keV

Conclusions

Efficiencies of six $O(^1S)$ excitation mechanisms and seven $O(^1D)$ excitation mechanisms in the polar aurora were studied using numeric modelling, with a new time-dependent physico-chemical model of the auroral atmosphere.

The main contribution into the atom $O(^1D)$ excitation is made by the sum of direct precipitating electrons impact on atomic and molecular oxygen. The atoms $O(^1S)$ excitation in the polar aurora is mainly produced by direct electrons impact on atomic oxygen, as well as by the reaction of interaction between the excited molecular nitrogen $N_2(A^3)$ and atomic oxygen. In spite of the fact that the contribution of the dissociative recombination of the molecular oxygen ion is negligible in the region of the maximum of emission altitude profile, at altitudes of 150-200 km the excitation of the atom $O(^1S)$ in the reaction of the dissociative recombination makes up 10-30%.

References

- Dashkevich Zh.D., V.E. Ivanov, T.I. Sergienko, B.V. Kozelov (2017). Physicochemical model of the auroral ionosphere. *Cosmic Research*, 55, 88-100.
- Dashkevich Zh.V., V.E. Ivanov (2019). Estimated nitric oxiden density in auroras from ground-based photometerric data. *Solar-Terrestrial Physics.*, 5, 58–61.
- Gattinger R.L., F.R. Harris, Jones A.Vallance (1985). The height, spectrum and mechanism of type-B red aurora and its bearing on the excitation of $O(^1S)$ in aurora. *Planet. Space Sci.*, 33, 207-221.
- McDade I.C., E.J. Llewellyn, B.H. Solheim (1985). A rocket measurement of $O(^1S)$ and N_2^+ emissions in a pulsating aurora. *Can.J.Phys.*, 63, 983-987.
- Rees M.H. (1984). Excitation of $O(^1S)$ and emission of 5577 Å radiation in aurora. *Planet.Space.Sci.*, 32., 373-378.
- Solomon S. C., P. B. Hays, V. J. Abreu (1985). The auroral 6300Å emission: observations and modeling. *J.Geophys. Res.*, 93, 9867-9882.

The Calculation of the Intensity of the Mg I Spectral Lines in Solar Prominences Using the Cloudy code Model

Kupryakov Yu.A.^{1,2}, Dodin A.V.², Schwartz P.³, Kashapova L.K.⁴

¹ Astronomical Institute CAS, Ondřejov, Czech Republic

² Sternberg Astronomical Institute, Moscow, Russia

³ Astronomical Institute SAS, Tatranská Lomnica, Slovak Republic

⁴ Institute of Solar-Terrestrial Physics, Irkutsk, Russia

E-mail: kupry@asu.cas.cz

Abstract.

Spectroscopical observations of several prominences in the MgI lines were carried out from 2014 to 2017. These lines from visible part of the solar spectrum play an important diagnostic role, complementing the UV Mg II resonance lines regularly observed by the IRIS satellite. We found that a rather weak Mg I emission, e.g., in the 5172.6 Å line correlates well with the presence of extended bright areas on the solar disk observed in the 1600 Å SDO/AIA band. However, in many cases the radiation in the 5172.6 Å line is very low, even not detectable, although a bright prominence above the limb or flare on the solar disc were observed. To explain this phenomenon, we have calculated spectra of optically thin plasma using Cloudy code and found that observed ratio of optical lines and UV continuum is possible and the presence of heel processes stimulates luminescence in Mg I and 1600 Å lines.

Observations

The following observations were chosen for measurements: 2015-04-21, 13:21:11 UT and 2016-05-22, 12:14:48; 12:21:04 UT, which were obtained on a multichannel flare spectrograph (MFS http://www.asu.cas.cz/~sos/archive_mfs.html). In fig. 1c shows an example of well-observed radiation in Mg I lines. In fig. 2 we note the position of flares in the "legs" of the prominence and the glow of the prominence and the chromosphere in lines 304 Å, 1600 Å. In the second case, the emission does not occur in 2016-05-22 12:14:48 UT (Figs. 3.4). As noted in [Heinzel P., et al., 2016], we also do not observe glows in the 1600 Å line. The absolute radiation intensity in H α , MgI 5183 Å (MFS) and 1600 Å (SDO/AIA) was determined from observations. The results of calculations of the intensity ratio for 2015-04-21 13:21:11 correspond to (H α / 1600 = 0.352; Mg I / 1600 = 0.130; H α / Mg I = 2.70).

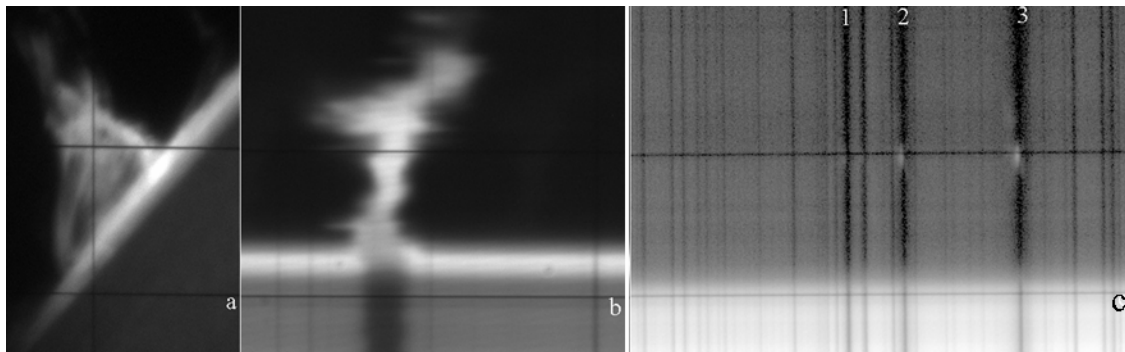


Fig. 1 2015-04-21, 13: 21: 11 UT a)slit-jaw image (the vertical line corresponds to the position of the spectrograph slit), lines b) H α , c) MgI 5167.3Å (1), 5172.6 Å (2), 5183.6 Å (3), [MFS].

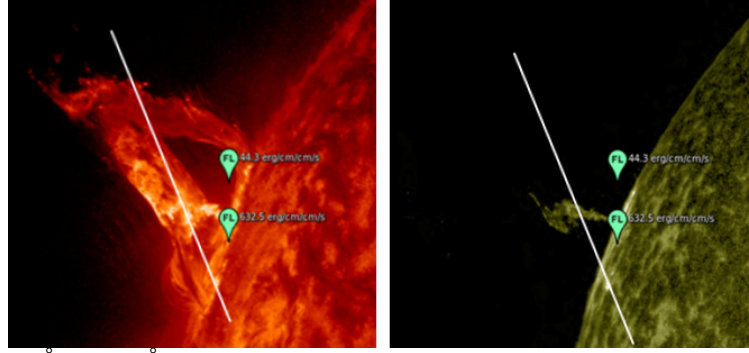


Fig. 2 SDO/AIA 304 Å, 1600 Å 2015-04-21, 13: 21: 11 UT for the observed position flares (white line - corresponds to the position of the spectrograph slit).

In the second case, 2016-05-22 12:14:48 UT (Figs. 3.4), even during a weak flare at 12:21:04 UT (Figs. 5, 6), we do not observe emission in the Mg I line, although it is present in the 1600 Å line.

Spectra simulation

A realistic calculation of the observed spectrum requires a time-dependent radiative hydrodynamic modeling. Here we restrict ourself to study parameter space of solar plasma, at which the observed line ratios can be obtained. To do this, we will apply simplified model of a steady-state optically thin plasma, calculated with the Cloudy code [Ferland G. J., et al., 2017] solve a set of statistical equilibrium equations for populations of atomic levels, taking into account collisional and radiative transitions for lines and continua. The joint solution of the and radiative transfer equations was carried out in an approximate way by means of escape probability technique, but in our case of optically thin plasma limitations of this method are unimportant. Note that at high density of plasma the accuracy of the Cloudy's results decreases due to the increasing role of unaccounted or approximately accounted collisional processes, in the particular three-body recombination, the cross section of which for most ions is poorly known.

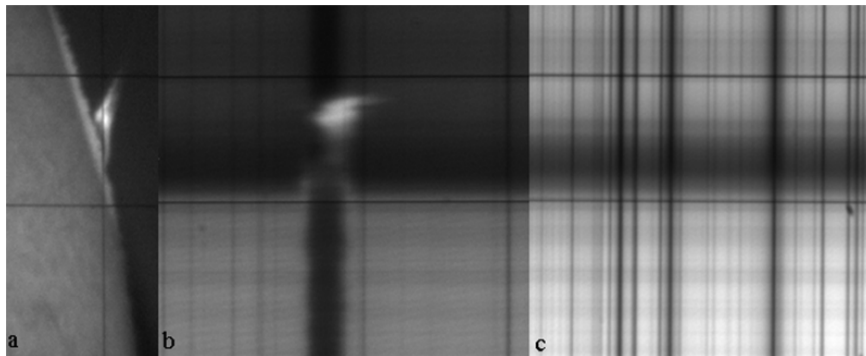


Fig. 3 2016-05-22 12:14:48 UT a) slit-jaw image, lines b) H α , c) MgI 5172 Å, [MFS].

To simulate the physical conditions in the prominence, we examined a plane-parallel optically thin layer of gas, placed in a blackbody radiation field with $T = 6000$ K and a dilution of 0.5 (that is, near the surface of the Sun). The number density and temperature of the gas layer are constant and varied in ranges of $N = 10^8 - 10^{14} \text{ cm}^{-3}$, $T = 5 - 24\,000$ K. We used the default solar chemical composition, distributed in Cloudy v.17 (in particular, for magnesium $(\text{Mg} / \text{H}) = -4.46$, see Cloudy documentation for other elements). An UV radiation

is important factor in simulations of spectra, because it produces significant departures from LTE by shifting ionisation balance to ions with higher ionization energies.

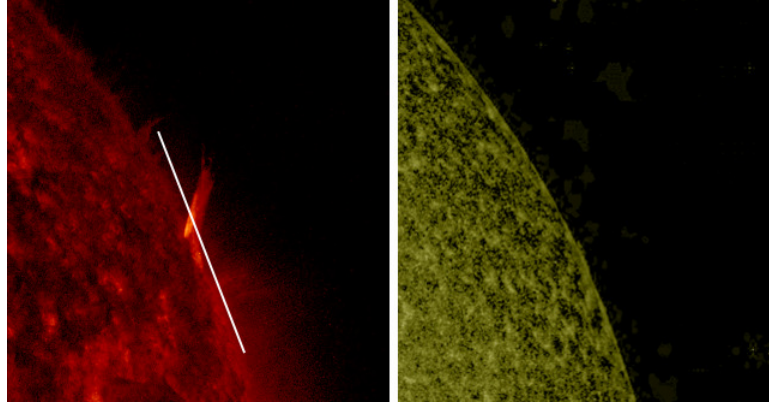


Fig. 4 SDO 304 Å, 1600 Å 2016-05-22 12:14:48 UT.

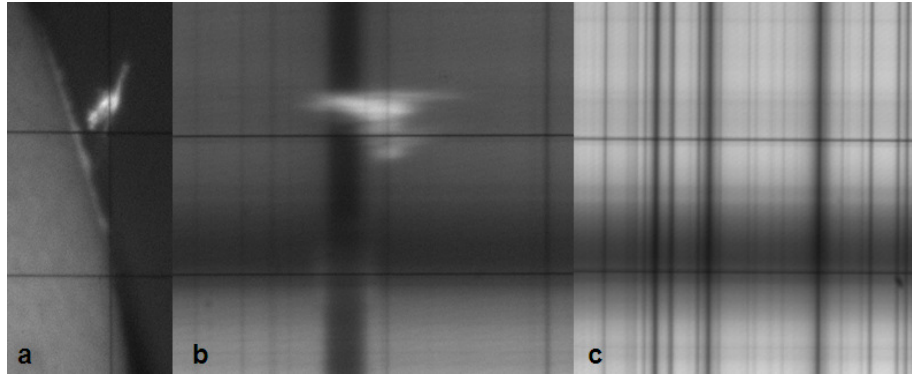


Fig. 5 2016-05-22 12:21:04 UT a) slit-jaw image, lines: b) H α , c) MgI 5172 Å, [MFS].

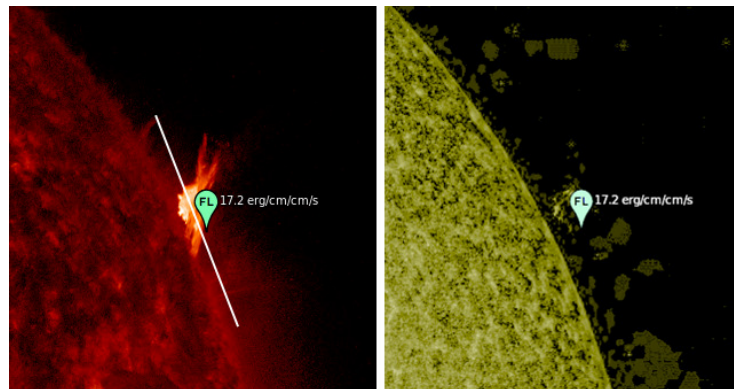


Fig. 6 SDO/AIA 304 Å, 1600 Å 2016-05-22 12:21:04 UT.

About the local UV radiation field in the particular active region, we considered it as a blackbody radiation with $T = 100\,000\text{ K}$ with a dilution factor from 0 to 10^{-8} . We calculated emergent fluxes for Mg I and H α lines and total contribution of lines and continuum in the 1500 – 1600 Å band using a grid of about 4000 models. Interpolating over this grid, we find parameters of the gas, at which the observed relations between fluxes in Mg I, H α and the

band 1500 – 1600 Å are achieved. The spectral width of the SDO / AIA 1600 Å filter was taken from the work [Simões P. J. A. et al., 2019]. This parameters are shown in the T - logN diagramm in Fig. 7, where various dilution factors are shown in different colors. The intersection of the curves of the same color gives the parameters, at which all the relations between the lines are fulfilled. There are several such points and all of them show a presence of a moderate UV background, corresponding to the dilution factor of 10^{-11} - 10^{-9} for the assumed blackbody radiation. We conclude therefore that observed ratio of the lines and the UV continuum is possible and the presence of heel processes stimulates luminescence in the Mg I and 1600 Å lines. However to derive more reliable gas parameters, a more realistic model should be considered.

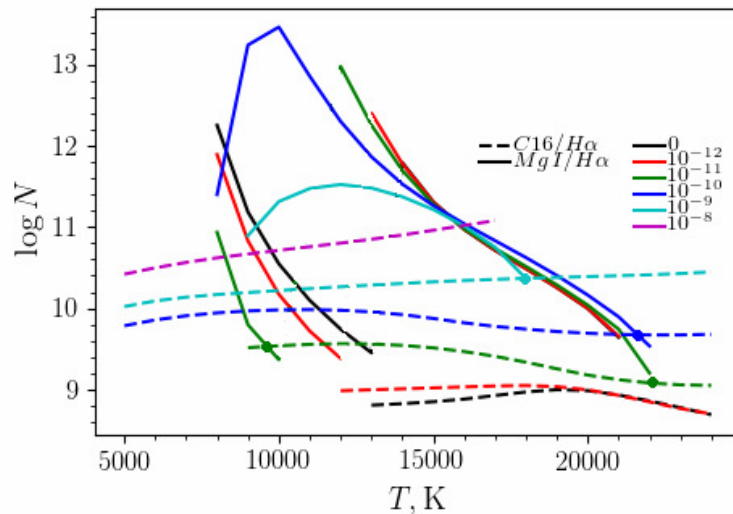


Fig. 7 Results of calculations for 2015-04-21 13:21:11 UT ($H\alpha/1600 = 0.352$; $MgI/1600 = 0.130$; $H\alpha/MgI = 2.70$). Various colors are for various dilution factors of blackbody radiation with $T=100\,000$ K.

Results

It follows from our observations and modelling that:

- luminescence in the Mg I lines was observed during the flare processes in the lower region of the prominences with a radiation flux in the range of $44\div630 \text{ erg cm}^{-2} \text{ s}^{-1}$ (observation 2015-04-21);
- during observation 2016-05-22 12:21:04 UT, when a flare with a low energy of $17 \text{ erg cm}^{-2} \text{ s}^{-1}$ occurred at the top of the prominence, emission in optical Mg I lines was absent, although it was observed in the 1600 Å line;
- observed relationship between the lines H α , Mg I and the continuum UV can be reproduced in the models;
- the presence of heel processes stimulate luminescence in the Mg I and 1600 Å lines.

Acknowledgment

The authors thank the SDO/AIA, SDO/HMI, GOES teams for a possibility to freely use the data from those instruments.

References

- Heinzel P., Kupryakov Yu., Schwartz P. (2016), Lines of MgI Detected in Solar Prominences. Central European Astrophysical Bulletin, vol.40, pp. 81-87
- Ferland G. J., Chatzikos M., Guzmán F. et al. (2017), The 2017 Release Cloudy. Revista Mexicana de Astronomía y Astrofísica Vol. 53, p. 385-438
- Simões P. J. A., Reid H. A. S. et al. (2019), The spectral content of SDO/AIA 1600 and 1700 Å filters from are and plage observations. The Astrophysical Journal, Vol. 870, 2, p. 114

State Space Reconstruction for Sunspot Area Time Series

Sarp V.¹, Kilcik A.¹

¹ Akdeniz University, Faculty of Science, Space Science and Technologies Department,
Antalya/Turkey
E-mail: volkansarp@akdeniz.edu.tr

Abstract.

We analyzed the sunspot area time series by means of state space reconstruction for the time period between 1875 and 2015. Two different local neighborhood models, namely Simplex Projection and S-Map are employed to project state space reconstructions. Various classification schemes in the literature are then tested in these models to compare the predictive ability of multivariate and univariate time series. According to our results, multivariate time series represent the true dynamics of sunspot areas better than univariate time series, which implies more accurate predictions, can be obtained if proper classification schemes of sunspot area time series are employed and each class is predicted separately.

Introduction

Studies on understanding and forecasting solar activity comprises sunspot recognition, classification and analysis. Sunspot observations have a long temporal expansion (~400 years) and since the beginning of their recognition on the solar disk, various attempts have been performed to investigate their dynamics, distribution and periodicities. The earliest results demonstrated a statistical causality of powerful solar eruptions with the large and complex sunspots (Giovanelli R.G., 1939). This discovery led the earlier studies on classifying sunspots to be more systematically and detailed. After several modifications on the earlier classification schemes, the most widely used system up to now, “McIntosh Classification” which is also known as “Modified Zurich Classification” (McIntosh P.S., 1990) is introduced.

On the other hand, it has been long known that, sunspots display different temporal variations on different solar hemispheres. This phenomenon is known as “Hemispheric Asymmetry” or “North-South Asymmetry”. Also some other studies regarding sunspot classification is performed by various authors based on the sizes or complexities of sunspot groups (e.g. Kilcik A. et al., 2011; Javaraiah J., 2016; Gao P.X. et al. 2017). Here, we performed multivariate prediction methods on four different classification schemes and calculated their prediction performance to compare with each other.

Classification Schemes

i) Empirical Classification

Sunspot observations in the Debrecen and Greenwich photoheliographic data are empirically classified from the last (complexity) parameter of Zurich Classification Scheme (c, o, i and x parameters). Each groups average areas are taken from the NOAA Space Weather Prediction Center (SWPC) and upper/lower bounds for each empirical group are calculated by means of these averages. Determined ranges are extrapolated to the historical measurements.

ii) Ratio Classification

This classification scheme is introduced by Gao P.X. et al. (2017) as the ratio of the total sunspot area to its umbra. The authors stated that if this ratio is less or equal to 4.5, corresponding sunspot group is simple. They call a sunspot complex, if the ratio is greater than 6.2. The frequencies of simple and complex sunspots after the Solar Cycle 12 can be seen in Figure 1. It should be noted that these authors did not take into account the values between 4.5 and 6.2, showed with black bar in Figure 1. Both possibilities are tested in this

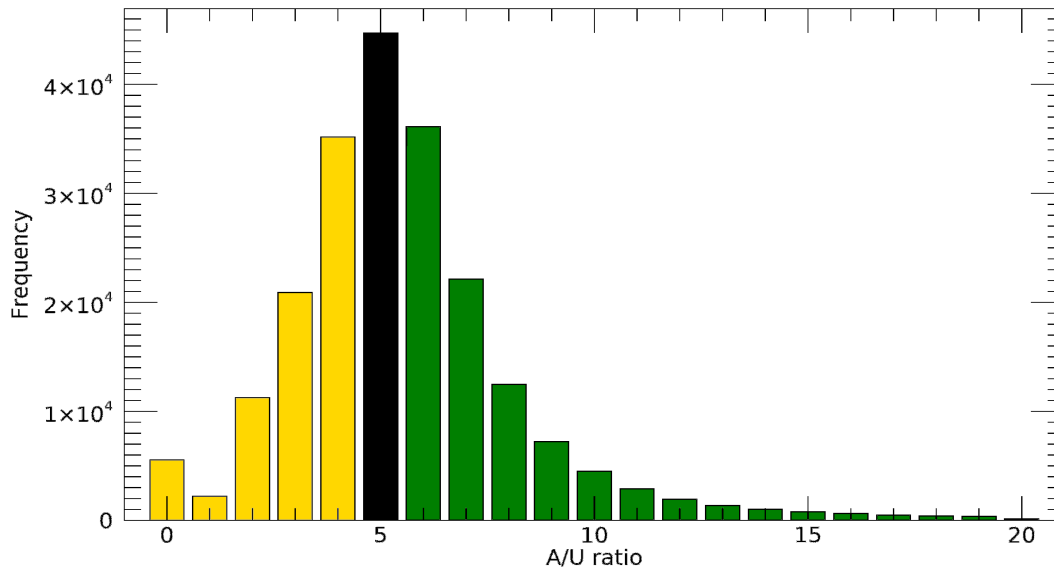


Figure 1 – Simple (yellow) and complex (green) sunspots frequencies for the last 13 cycles based on the ratio of total area and umbral area. (Adapted from Gao P.X. et al. 2017).

study by first considering only simple and complex sunspots, and also considering simple, middle and complex sunspots.

iii) Small & Large Classification

This classification scheme is introduced by Kilcik A. et al. (2011) as using the first parameter of modified Zurich classification. A sunspot group is called as small if their Zurich class is A, B, C, H, or J classes and called as large if their Zurich class is D, E, F, or G classes. Here, NOAA SWPC data are used as reference again to extrapolate this classification to the historical measurements of Debrecen and Greenwich photoheliographic data. Averages of the reference data for both classes and their mean ranges used for extrapolating can be seen in Table 1.

Table 1 – Mean values of small & large sunspots for the last 2 cycles and their extrapolated ranges for the last 13 cycles. Adapted from Kilcik et al. (2011).

	Large	Small
Means from reference [MSH]	233.28	51.72
Range for Extrapolation	large ≥ 142.5	142.5 > small

iv) North-South Hemispheric Classification

It has been long known that, sunspots display different temporal variations on different solar hemispheres and there is a so called “Hemispheric Asymmetry” of sunspots (Roy J.R. 1977). This classification scheme is both used as a distinct separation and also combined with other three classification schemes that are mentioned above

Methods

All components of each classification scheme are taken into account as a separate dimension of the target time series which is the total sunspot area in a method called Multiview Embedding. The main idea of that method is that multidimensional time series can be used to reconstruct target time series from multiple viewpoints, and these viewpoints can be combined into a single model (Ye H. and Sugihara G. 2016). Although this method is proposed in the field of ecosystems, it is also possible to apply on various complex systems. Multiple state spaces from components of the time series which are classes of each scheme

are reconstructed and a single nearest neighbor is selected from each of them to produce final predictions. These reconstructions are then tested according to their prediction performance by comparing and calculating their correlation coefficient with the observed values. Combining information from multiple state space reconstructions is expected to improve the performance with increasing dimensionality

Results

As a first step of our analysis, we calculated the prediction performance of total sunspot areas without any components, which can be seen in Figure 2. Here, the optimal embedding dimension is found as 4 and the decay of prediction performance, which is an indicator of chaotic dynamics, can also be seen. We selected 12-month prediction performance, which has a correlation coefficient of 0.67 with the observed values to compare with other classification schemes.

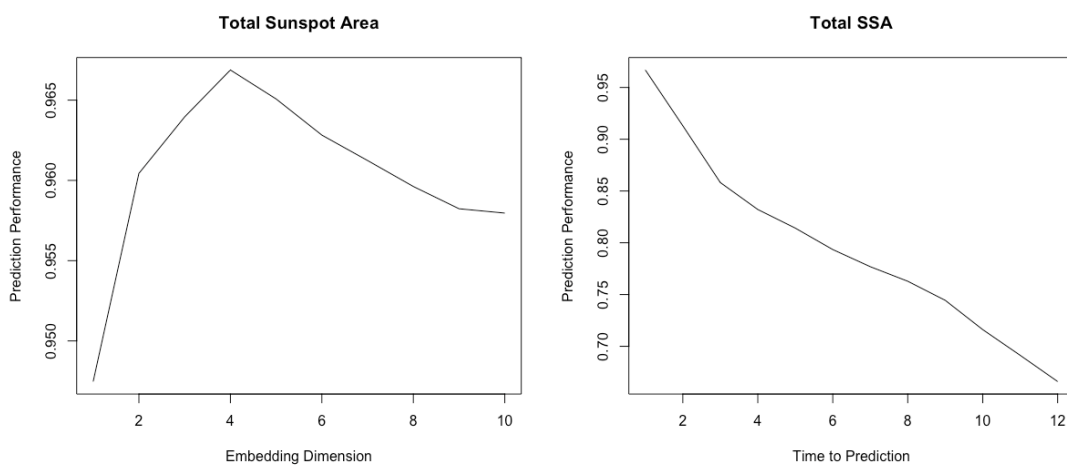


Figure 2 – Optimal embedding dimension and reference prediction performance for total SSA

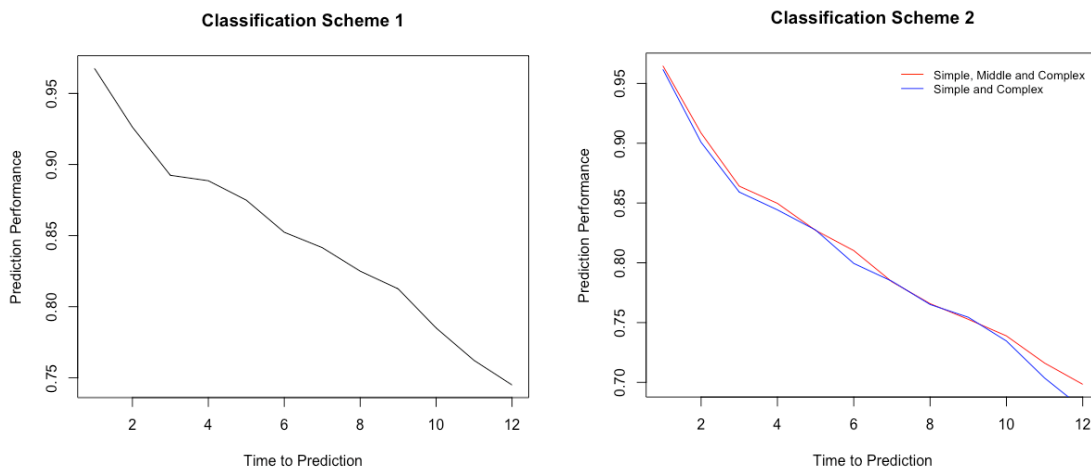


Figure 3 – Multiview Embedding prediction performance of Empirical and Ratio Classification Schemes

Then we applied the Multiview Embedding with the same parameters to the first two classification schemes. They both slightly improved the 12-month prediction performance as can be seen in Figure 3. It should be noted that, in the second classification scheme (ratio classification), Gao P.X. et al. (2017) did not consider the middle group. Here we performed the analysis in both ways and show that taking the middle group into account, has improved the performance of the predictions after 10 months.

We also analyzed remaining two classification schemes (Small & Large and North & South) but they both decreased the prediction performance (Figure 4). In order to overcome this problem, these two classification schemes are combined as Small-North, Small-South, Large-North, and Large-South. This combination is greatly increased the Multiview Embedding prediction performance as can be seen at Figure 4.

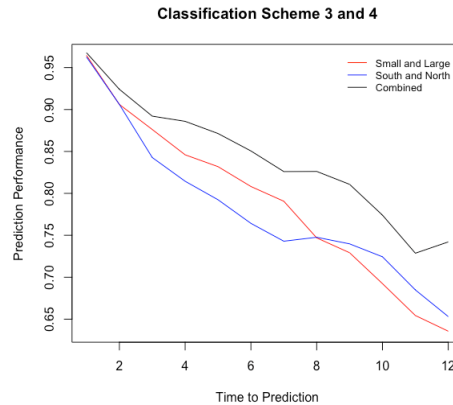


Figure 4 – Multiview Embedding prediction performance of Small & Large (red curve) and North & South (blue curve) classification schemes and their combinations (black curve).

Conclusions

1. Empirical Classification (complexity parameter of Zurich class) gives the highest increase in prediction performance (Table 2).
2. North – South Classification can be combined with other classification schemes.
3. Separating SSA time series to constituents increases the prediction performance

Table 2 – Results of Multiview embedding prediction performances of each classification scheme (first row) and combining them with the North & South asymmetry (last row)

Empirical	A/U ratio	Small & Large	C North & South
0.75	0.70	0.64	0.65
0.79	0.78	0.74	<- Combined

Acknowledgment

This Study was supported by Scientific and Technological Research Council of Turkey (TÜBİTAK) Project No: 117F145

References

- Giovanelli R.G. (1939) The Relations Between Eruptions and Sunspots. ApJ. 89, p. 555
- Gao, P.X., Li, K.J. & Li, F.Y. (2017) Variations and Regularities in the Hemispheric Distributions in Sunspot Groups of Various Classes. Sol Phys. 293:79
- Javaraiah J. (2016) North-south asymmetry in small and large sunspot group activity and violation of even-odd solar cycle rule. Astrophysics and Space Science. 361:208
- McIntosh P.S. (1989) The Classification of Sunspot Groups. Sol Phys, 125, p.251-267.
- Roy J.R., (1977) The north-south distribution of major solar flare events, sunspot magnetic classes and sunspot areas (1955–1974). Sol Phys, 52, p.53-61
- Kilcik A., Yurchyshyn V.B., Abramenko V., Goode P.R., Ozguc A., Rozelot J.P., and Cao, W. (2011) Time Distributions of Large and Small Sunspot Groups over four Solar Cycles. ApJ 731, 1
- Ye H. and Sugihara G. (2016). Information leverage in interconnected ecosystems: Overcoming the curse of dimensionality. Science 353:922–925

Scheme to Forecast the Local UV-index over Bulgaria

Werner R.¹, Petkov B.², Valev D.¹, Guinevav V.¹, Atanasov A.¹, Kirillov A.³

¹ Space Research and Technology Institute (SRTI), BAS, Stara Zagora Department,
Stara Zagora, Bulgaria

² Institute of Atmospheric Sciences and Climate (ISAC), CNR, Bologna Branch,
Bologna, Italy

³ Polar Geophysical Institute (PGI), Kola Science Centre, Murmansk, Apatity Division,
Apatity, Russia

E-mail: rwerner@space.bas.bg

Abstract

The UV-index is a measure of the erythemally effective solar radiation reaching the Earth surface. It was introduced to alert people about the need of sun protection. Therefore the UV-index has to be determined with adequate accuracy. To minimize the risk of too high levels of sunburn the UV-index is determined usually for clear sky conditions. To alert people in time the UV-index forecast is essential. Here the schemes of UV-index forecast for one day in advance are presented. Because the UV-index under clear sky conditions depends on the total ozone column over a given geographic location the UV-index forecast (cloud free and aerosol free) implicates the forecast of the total ozone column. The scheme of ozone forecast is based on satellite data. For the determination of the UV-index, model calculations using the radiation transfer model TUV of Madronich are implemented. The land snow cover is taken into account.

Introduction

Ultraviolet (UV) irradiance reaching the Earth surface has an impact on the human's health. The UV-B irradiance stimulates the production of vitamin D, important for good being. However the overexposure to solar ultraviolet evokes erythema and over long time it represents a risk of DNA damage and of skin cancer [Blumthaler M., 2018]. Sun related eye diseases and in acute cases snow blindness are well established. To alert people about the need of sun protection the UV-index (UVI) was introduced as a measure of the erythemally effective solar radiation reaching the Earth surface. At a given moment t it is defined as scaled integral over the wavelength given in nm of the solar irradiance at the Earth surface $F_t(\lambda)$ measured in $\text{mW}/(\text{m}^2\text{nm})$ weighted by the erythema action spectrum $A_e(\lambda)$, where $1/25 \text{ mW}/\text{m}^2$ is used as scaling factor [WHO, 2020]. By the scaling the UVI is a dimensionless quantity and ranges between 8 and 10 at midlatitudes at noon under cloudless conditions when the risk of harmful sunburn is the highest. The UVI can be determined by highly precise spectrometric measurements, by multichannel filter instruments and by UV photometers of the solar irradiance [Dahlback A., 1996, Fioletov V.E., et al., 2003].

In many countries, UV monitoring networks were established. In Canada there are 13 spectral UV stations. In Austria the network involves 12 stations at different locations, equipped with broadband UVB radiometers [Schmalwieser A. and Schauburger G., 2001]. In Europe currently 160 stations in 25 countries deliver online values to the public *via* the Internet [Schmalwieser, A. et al., 2017]. In Bulgaria a comparable net of automatically working stations does not exist.

Under clear weather conditions the UVI depends strongly on the total ozone column (TOC). The UVI varies with the surface albedo and with the sun elevation change.

The UV-index forecast (cloud free and aerosol free) implicates the forecast of the total ozone column for a given geographic location. Statistical models of ozone based on monthly means and are not suitable for daily forecasts. Allaart et al. (2004) has developed a simple empiric model to predict the UV-index based on solar zenith angles and daily total ozone data

and proposed to use satellite ozone data for ozone forecast. Here a scheme of UV-index forecast for Bulgaria for one day in advance is presented. In the forecast models based on TOC ground based observations a persistence of TOC up to 2 days is assumed, which guarantees a quality that is convenient with the requirements of UV Index forecast procedures. [Schmalwieser A., et al., 2003]. Here a UV forecast scheme is proposed where the ozone forecast is based on satellite data. For the determination of the UV, model calculations using the radiation transfer model TUV of Madronich are implemented. The land snow cover is taken into account.

Ozone forecast and downscaling

Starting point of the UV-forecast is the ozone forecast. It is based on global ozone field. To provide the near-real time data and forecast for the next five days the ozone field observations by GOME-2 are input in a data assimilated program (<http://www.temis.nl/protocols/O3forecast.html>) considering chemical ozone production and loss as well as dynamical processes. The total ozone column field data are gridded by 0.25° by 0.25° . Bulgaria is extended over the geographic region between about 22° and 29° longitude and 41° up to 45° latitude. Thus the ozone field over Bulgaria is determined by a matrix of 24 by 12 values. The forecast system gives also the mean altitude h of the land surface in the grid cell. This allows to recalculate the total ozone column to sea level high by

$$TOC(h = 0) = TOC(h)_{obs} / (1 - c_{elev.} * h/1000) \quad (\text{with } h \text{ in } m)$$

where the value of $c_{elev.} = 0.01$ per 1000 m results from the assumption that the tropospheric ozone content is about 10% of the TOC and the mean tropopause is at about 10 km height [Krzyscin J.W., 2000]. Schmalwieser (2003) found altitude dependences of 1.13% per 1000 m based on UV measurements at the Austrian Sonnenblick high mountain station in comparison with EP TOM satellite observations. Additionally it was presumed that the stratospheric ozone is nearly constant in the grid cell. Then the TOC values can be interpolated to a new topographic grid with higher resolution of about 1km and the TOC values can be recalculated using the mean elevations of surface of the new topographic grid.

Topography for elevation corrections

The Shuttle Radar Topography Mission (SRTM) provided global elevation data up to 1arcsec (terrain.org/Elevation/SRTM/). Here we have used the 3 arcsec data set to retrieve the elevation map for the described above geographic region where Bulgaria is located. (The map data were downloaded from the web site <https://gdex.cr.usgs.gov/gdex/>.) The elevation map was smoothed by 11x11 points and the map originally comprising 8400 by 4800 pixels was reduced to 763 by 436 pixels corresponding to a resolution of approximately 1km.

UVI forecast and downscaling

Allaart (2004) has developed an empirical model for the UVI dependence from TOC and sun elevation. Here we have used the radiation transfer model TUV of Madronich (1993) to calculate look up tables describing the UVI relation to TOC and the sun elevation. The TUV model uses a mean ozone profile of the U.S. Standard Atmosphere1976. In cases for low ozone events caused by transport of low ozone polar or tropical air to Bulgaria typical polar or tropical ozone profiles could be used in the TUV model [Kazantzidis A., et al., 2005; Petkov B., et al., 2006, Vitale V., et al., 20011]. For the surface around the location where the spectral measurements are provided, the back scattered UV radiation is to be calculated in order to obtain the incident radiation depending on the surface albedo.

Feister and Grewe (1995) have been measured an albedo in the UVA region of 0.02 for vegetation, of 0.05 up to 0.08 for bare soils and from 0.14 (for a wavelength at 300nm) to 0.24 (for a wavelength at 400 nm) for dry (beach) sands. Webb et al. (2000) have found a

grassland albedo of 0.01. For asphalt, concrete, red bricks and metallic roofs the albedos are higher. Here we have used an effective albedo of 0.03 for the calculation of the look up table (see Fig. 1).

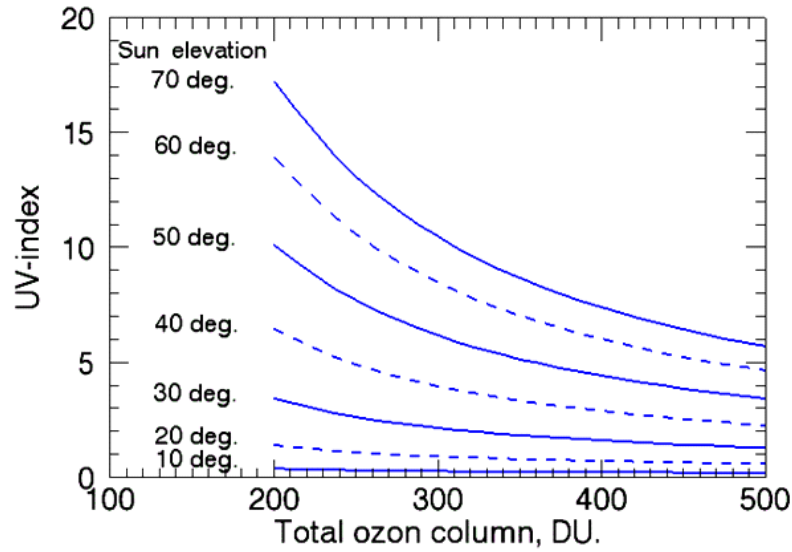


Fig. 1. Calculated look up table for the determination of the UVI for given TOC and sun elevation for an albedo of 0.03.

The resulting sea level UVI has to be multiplied by the factor $(R/R_0)^2$ to consider the solar irradiance change caused by the Earth – Sun distance variation during the year.

In the next step the UVI has to be downscaled to a new topographic grid with higher resolution and recalculated to the mean elevation of the new grid cells. Using the TUV model it was found that the UVI elevation correction depends only weakly from the sun elevation and from the sea level TOC. We found an UVI of 0.06% per 1000 m which is in very good agreement to the values of 6% to 8% per 1000 m given by Vanicek et al. (1999) and Dahlback et al. (2007). Other authors were reported higher altitude corrections, e.g. Diffey (1977) has established 16% per 1000 m (for more details see Schmalwieser, 2000, and the citations herein).

$$UVI(h) = UVI(h=0) * c_{alb.} * (1 + c_{elev.} * h/1000) \quad (\text{with } h \text{ in } m)$$

$$c_{elev.} = 0.06$$

In winter, when the surface is snow covered the albedo is substantially higher than the overall mean of 0.03 and the albedo correction has to be introduced. For the snow and beach sand albedo correction we use the UVI ratio

$$c_{alb.} = \frac{UVI(albedo)}{UVI(reference\ albedo)}$$

$$c_{alb.} = \begin{cases} 1.25 & \text{for snow (albedo = 0.6)} \\ 1.07 & \text{for beach and sand (albedo = 0.20)} \\ 1.0 & \text{for soil and vegetation (albedo = 0.03)} \end{cases}$$

Feister and Grewe (1995) found an albedo of 0.62 to 0.76 for a surface fully covered by polluted snow. McKenzie et al. (1998) established an enhancement in the UVA region of 22% and in the UVB of 28% by snow, corresponding to an albedo of 0.62 ± 0.08 . For Tibet in high altitudes mountains (over 5000 m) UV measurements show an increase of the UVI by snow

cover by 35% in comparison with snow free surface (Dahlback A., et al., 2007). It has established a stronger UV irradiance enhancement for fresh snow and a decrease when the snow pollution increases and the snow is more packed. Whereas the effective albedo of soils and vegetation is about 0.03, during the winter, the albedo over snow covered surfaces is about 0.6. The snow coverage is provided by the National Ice Center's Interactive Multisensor Snow and Ice Mapping System (IMS). The maps are given in polar coordinates and have to be transformed in other map projections, and the resolution has to be scaled to the used topographic grid (<https://nsidc.org/data/g02156>).

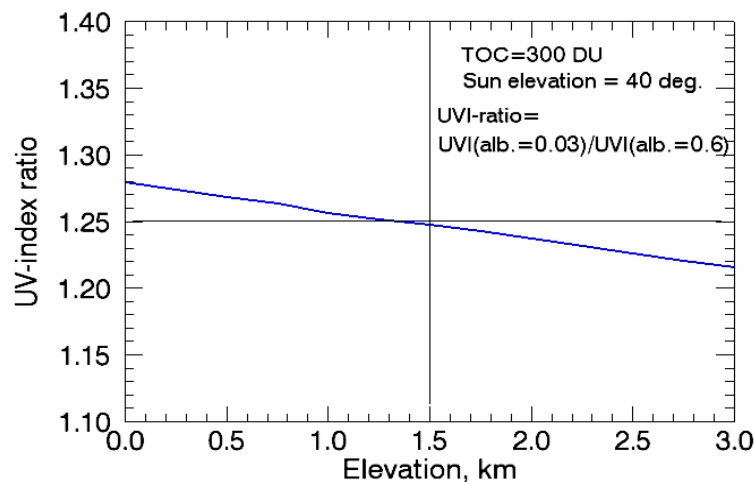


Fig. 2. Albedo correction obtained as UVI ratio for a snow covered surface with an albedo of 0.6 related to a reference snow free surface covered by vegetation and soil with a mean albedo of 0.03 in dependence on the surface elevation. The UVI ratio shows a weak dependence from the surface elevation (blue line).

The UVI ratios calculated by TUV model depend only very weakly on the TOC. A weak dependence from the elevation was found out and the albedo correction factor 1.25 for the approximately mean Bulgarian mountain height (about 1.5 km), above which the land is almost snow covered during the winter/spring season, is to be used (FIG. 2). For the beach line a correction for a mean albedo of 0.20 is used. To describe the influence of neighbour pixels with different albedos a Gaussian filter process is foreseen.

Summary

A forecast scheme for the TOC and the UVI was worked out based on downscaling of satellite data to a grid with higher resolution. It is foreseen to correct the ozone and UVI values for surface elevations and albedos for snow, soil and vegetation and beach sand by parametrization. The correction factors were determined using the radiation transfer model TUV of Madronich.

References:

- Allaart M., M. Van Weele, P. Fortuin, H. Kelder (2004). An empirical model to predict the UV-index based on solar zenith angles and total ozone, *Meteorol. Appl.*, 11, 59-65.
- Blumthaler M. (2018). UV Monitoring for Public Health. *Int. J. Environ. Res. Public Health*, 15, 1723.
- WHO (2002). Global Solar UV Index, A practical guide. Fact Sheet 271, <http://www.who.int/mediacentre/factsheet/who271/en/index.html>.
- Dahlback A. (1996). Measurements of biological effective UV doses, total ozone abundances, and cloud effects with multichannel, moderate bandwidth filter, *Appl. Opt.*, 30, 33, 6514-6521.
- Dahlback A., N. Gelsor, J.J. Stamnes, Y. Gjessing (2007) UV measurements in the 3000–5000 m altitude region in Tibet. *J. Geophys. Res.*, 112, D09.
- Diffey B.L. (1977). The calculation of the spectral distribution of natural ultraviolet radiation under clear day conditions, *Phys. Med. Biol.* 22, 309-316.
- Feister U., R. Grewe (1995). Spectral albedo measurements in the UV and visible region over different types of surfaces. *Photochemical & Photobiological Sciences*, 62, 4, 7736-744.
- Fioletov V.E., J.B. Kerr, L.J.B. McArthur, D.I. Wardle, T.W. Mathews (2003). Estimating UV Index Climatology over Canada, *Journ. Appl. Meteorol.*, 42, 417-433.
- Fioletov V., J.B. Kerr, A. Fergusson (2010) The UV Index, Definition, Distribution and Factors Affecting It., *Canadian J. Public Health*, 101, 4, I-5 – I-9.
- Kazantzidis A, A.F. Bais, D.S. Balis, E. Kosmidis, C.S. Zerefos (2005). Sensitivity of solar UV radiation to ozone and temperature profiles at Thessaloniki (40.5°N, 23°E), Greece. *J. Atmos. Solar-Terr. Phys.*, 67, 14, 1321-1330.
- Krzyscin, J. W. (2000). Impact of the ozone profile on the surface UV radiation: Analysis of the Umkehr and UV measurements at Belsk (52°N, 21°E), Poland, *J. Geophys. Res.*, 105, 5009–5015.
- Madronich S. (1993). UV radiation in the natural and perturbed atmosphere, in *Environmental Effects of UV (Ultraviolet) Radiation*, M. Tevini, ed. (Lewis, Boca Raton, 1993), pp. 17– 69.
- McKenzie R.L., K.J. Paulin, S. Madronich (1998) Effects of snow cover on UV irradiance and surface albedo: A case study. *J. Geophys. Res.*, 103, D22, 28785-28792.
- Petkov B., Vitale, V., Tomasi, C., Bonafé, U., Scaglione, S., Flori, D., Santaguida, R., Gausa, M., Hansen, G., and Colombo, T (2006). Narrowband filter radiometer for ground-based measurements of global ultraviolet solar irradiance and total ozone, *Appl. Optics*, 45, 18, 4383.
- Schmalwieser A.W., G. Schauburger (2000). Validation of the Austrian forecast model for solar, biologically effective UV radiation □ UV index for Vienna, *J. Geophys. Res.*, 105, D21, 26,661-26,667.
- Schmalwieser A.W., G. Schauburger (2001). A monitoring network for erythemally-effective solar ultraviolet radiation in Austria: determination of the measuring sites and visualisation of the spatial distribution. *Theor. Appl. Climatol.* 69, 221–229.
- Schmalwieser A.W., G. Schauburger, P. Weihs, R. Stubi, M. Janouch, G.J.R. Coetzee, S. Simic (2003). Preprocessing of total ozone content as an input parameter to UV Index forecast calculations. *Journ. Geophys. Res.*, 108, D6, 4176.
- Schmalwieser A., J. Gröbner, M. Blumthaler, B. Klotz, H. de Backer, D. Bolsee, R. Werner, B. Petkov, et al. (2017). UV Index monitoring in Europe. *Photochemical & Photobiological Science*, 16, 1349-1370.
- Stamnes, K., J. Slusser, M. Bowen (1991). Derivation of total ozone abundance and cloud effects from spectral irradiance measurements, *Appl. Opt.*, 30, 30, 4418-4426.
- Vanicek K., T. Frei, Z. Litynska, A. Schmalwieser (1999). UV-Index for Public, A guide for publication and interpretation of solar UV Index forecasts for the public, prepared by the Working Group 4 of the COST-713 Action “UVB Forecasting”, Brüssel.
- Vitale V, B. Petkov, F. Goutail, C. Lanconelli, A. Lupi, M. Mazzola, M. Busetto, A. Pazmino, R. Schioppo, L. Genoni, C. Toamsi (2011). Variations of UV irradiance at Antarctic station Concordia during the springs of 2008 and 2009, *Antarctic Science* 23, 4, 389–398.
- Webb A.R., I.M. Stromberg, H. Li, L.M. Bartlett (2000). Spectral reflectivities at ultraviolet wavelengths (290–500 nm) measured from airborne platform. *J. Geophys. Res.* 105, D4, 4945-4948.

ENSO Variations Driven by Solar Cycles, Expressed by N-S Solar Asymmetry

Ya. Chapanov

Climate, Atmosphere and Water Research Institute, BAS

E-mail: yavor.chapanov@gmail.com

Abstract.

The solar activity cycles affect all surface geosystems, including weather and climate indices, winds, rains, snow covers, mean sea level, river streamflows and other hydrological cycles. These processes are due mainly to the Total Solar Irradiance (TSI) variations, followed by weather and climate changes. Recently a new mechanism of climate modulation, based on cosmic ray variations, has been discovered. This mechanism explains chain processes arising from cosmic ray (CR) modulation by the heliosphere and geomagnetic field, followed by ozone production in near tropopause and water content change. The atmospheric water is the most powerful greenhouse gas and its changes produce significant variations of the temperature. The CR modulation by heliosphere depends on solar wind and solar magnetic field variations, represent by North-South (N-S) solar asymmetry. The shapes of decadal and centennial solar cycles are rather different from sinusoidal form, and this is the reason to generate a lot of interannual and decadal harmonics. These harmonics are visible as common cycles with periods 1-9, 12-19 and 23-33 years in various time series of Earth phenomena like mean sea level, climate and etc. The decadal and interannual cycles of N-S solar asymmetry strongly affect corresponding cycles of El Nino/Southern Oscillation ENSO. It is remarkable that the solar indices have good agreement with the ENSO oscillations with periods from band 2-7 years.

Introduction

The solar activity affects terrestrial systems by means of direct radiation over Earth surface, influences charged particles of the solar wind, and the solar magnetic field. The solar wind directly affects Earth magnetic field, ionosphere and atmosphere. The variations of solar magnetic field modulate solar wind and cosmic rays in the frame of the solar system. The cosmic rays near Earth are modulated by Earth magnetic field variations, too. Recently, a new mechanism of climate variations, due to cosmic rays was proposed [Kilifarska N. and Haight G.D., 2005; Kilifarska N., 2008, 2011, 2015; Kilifarska N. and Bojilova R., 2019; Velinov P.I.Y. et al., 2005]. According to the new models, the cosmic rays produce an ionization of the atmosphere, changes of atmospheric conductivity, and lightning, and an increase of ozone concentration. This mechanism is based on chain processes near tropopause by ozone production, temperature variations, followed by vertical winds and water content change. The last step of this chain affects strongly surface temperature, because the atmospheric water is one of the most powerful greenhouse gas. This model provides an explanation for the cascade processes in which cosmic rays, whose total energy is relatively small, cause climatic effects with much more energy. The solar activity cycles modulate the cosmic rays directly by the heliosphere and indirectly by the geomagnetic field changes, whose effect is visible mainly at high latitudes and regions with strong geomagnetic anomalies.

Now it is well known that the solar activity affects ENSO variations [Lanscheidt T., 2000; Kirov B. and Georgieva K., 2002; Asenovski S. et al, 2015; Zhai Q., 2017; Maruyama F., 2018]. Most of authors point out that ENSO variations are stronger during solar minima, or they have negative correlation with the sunspot numbers for some periods. The temperature anomaly, represented by ENSO data should be affected by the TSI variations, but the above

results are clear signature that TSI have minor effects on ENSO and we have to find other appropriate explanation of solar influence on ENSO events.

Data and methods

The ENSO, N-S solar asymmetry and TSI data are presented in Fig.1. The ENSO monthly data since 1817 are available at the WEB page of the Joint Institute for the Study of the Atmosphere and Ocean <http://research.jisao.washington.edu/data/globalstsenso/>. The North-South solar asymmetry is determined from the relation $(S_n - S_s)/(S_n + S_s)$, where the S_n and S_s are monthly sunspot area on the Northern and Southern solar hemispheres, respectively (in units of millionths of a hemisphere). The data since 1874 are observed by the Royal Greenwich Observatory and merged after 1976 with the US Air Force (USAF) and the US National Oceanic and Atmospheric Administration (NOAA) data by D. Hathaway (<https://solarscience.msfc.nasa.gov/greenwch.shtml>). The last version of estimated solar irradiances for the last 400 years is based on the NRLTSI2 historical TSI reconstruction model by J. Lean [Kopp G. et al., 2016; Lean J., 2000, 2010; Coddington O. et al., 2015].

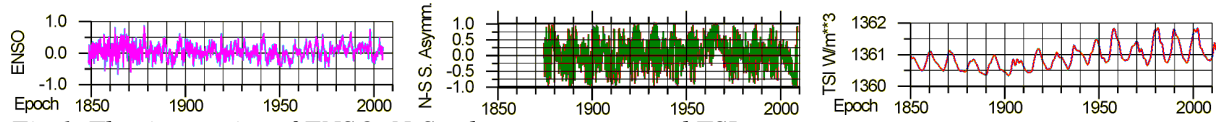


Fig.1. The time series of ENSO, N-S solar asymmetry and TSI.

The periodical variations are derived from the data by means of partial Fourier approximation based on the Least-Squares (LS) estimation of Fourier coefficients. The Partial Fourier approximation $F(t)$ of discrete data is given by

$$F(t) = f_0 + f_1(t - t_0) + \sum_{k=1}^n a_k \sin k \frac{2\pi}{P_0}(t - t_0) + b_k \cos k \frac{2\pi}{P_0}(t - t_0), \quad (1)$$

where P_0 is the period of the first harmonic, t_0 - the mean epoch of observations, f_0, f_1, a_k and b_k are unknown coefficients and n is the number of harmonics of the partial sum, which covers all oscillations with periods between P_0/n and P_0 . The application of the LS estimation of Fourier coefficients needs at least $2n+2$ observations, so the number of harmonics n is chosen significantly smaller than the number N of sampled data f_i . The small number of harmonics n yields to LS estimation of the coefficient errors. This estimation is the first essential difference with the classical Fourier approximation. The second difference is the arbitrary choice of the period of first harmonic P_0 , instead of the observational time span, so the estimated frequencies may cover the desired set of real oscillations. This method allows a flexible and easy separation of harmonic oscillations into different frequency bands by the formula

$$B(t) = \sum_{k=m_1}^{m_2} a_k \sin k \frac{2\pi}{P_0}(t - t_0) + b_k \cos k \frac{2\pi}{P_0}(t - t_0), \quad (2)$$

where the desired frequencies ω_k are limited by the bandwidth

$$\frac{2\pi m_1}{P_0} \leq \omega_k \leq \frac{2\pi m_2}{P_0}, \quad (3)$$

After estimating the Fourier coefficients, it is possible to identify a narrow frequency zone presenting significant amplitude, and defining a given cycle. Then this cycle can be reconstructed in time domain as the partial sum limited to the corresponding frequency bandwidth. Doing this for terrestrial and solar time series, we shall identify their respective cycles, isolate and compare the common ones.

The used time series cover 125-year overlapped time interval for the period 1875.0 – 2000.0. Each time series consist of 1500 monthly data points. The PFA performs estimation of 150 harmonics with the accuracy better than 0.01 for ENSO; 0.02 for N-S solar asymmetry and 0.5mW/m^2 for TSI.

Time series spectra

The time series spectra are determined by the Fast Fourier Transform (FFT). The common spectral peaks of ENSO and N-S solar asymmetry are with periods 1-3yr; 4-6yr, 8-10yr 15-28yr. The TSI and ENSO have common spectral peaks with periods 17-25yr, so significant common influence of TSI and N-S solar asymmetry on Enso variations are expected in decadal periods between 17 and 25yr.

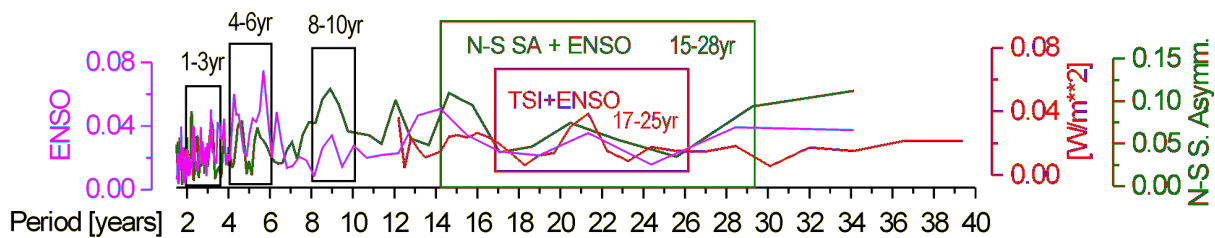


Fig.2. Time series spectra of ENSO, N-S solar asymmetry and TSI.

TSI influence on ENSO variations

The Enso event is connected with the surface temperature anomalies, so they should be affected by the TSI variations with significant positive correlation (Figs 3 and 4). Actually in some time intervals the TSI – ENSO connection is positively correlated, e.g. in 1870-1910 and 1960-2000 for the oscillations with periods 17-19yr (Fig.3); and in 1930-1960 for the oscillations with periods 2-7yr (Fig.4). In other time intervals the TSI – ENSO connection is negatively correlated – in 1910-1960 (Fig.3) and in 1890-1920; 1975-200 (Fig.4).

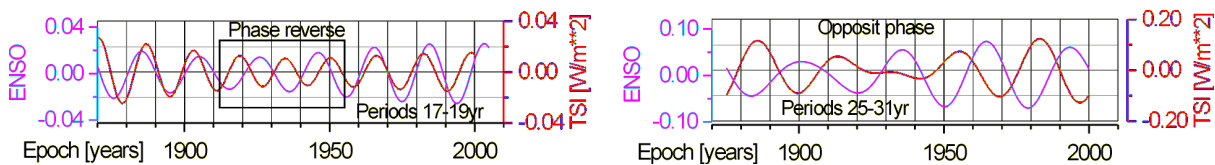


Fig.3. TSI influence on ENSO oscillations with periods between 17-19 and 25-31 years.

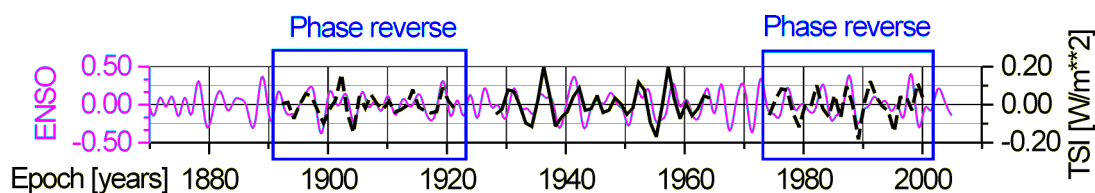


Fig.4. TSI influence on ENSO oscillations with periods between 2 and 7 years. The dashed lines represent TSI variations, taken by negative sign.

The TSI oscillations with periods 25-31yr have opposite phase with ENSO oscillations (Fig.3), so the solar activity has significant cooling mechanism, affecting ENSO event in these cases. The probable cooling mechanism is provided by the cosmic rays influence on the ozone and water content. The cosmic rays have opposite phase with solar wind, sunspot and TSI variations. Kilifarska N. [2008, 2011, 2015] suggests a model of cosmic rays influence on climate over high latitudes, where the cosmic rays produce cooling effect by ozone variations and water content decrease. According to Kilifarska's model, the cosmic rays and TSI have synchronous phases of warm/cool cycles in high latitudes, while the opposite phases between ENSO and TSI variations needs a new model of warm cycles during the cosmic rays maxima.

The water content decrease and vertical winds are essential in this model and they produce significant dry effect, so the dry atmosphere leads to less clouds. In case of cosmic rays over equatorial region this means more solar irradiance on the ocean surface and increasing the temperature anomaly during sunspot and TSI minima.

N-S solar asymmetry influence on decadal and interannual ENSO variations

The cosmic rays may excite ENSO variations, if they reach equatorial region: They are high energy galactic cosmic rays or solar energetic particles; the low energy cosmic rays may reach equator in 1900-2000, when the magnetic axe tilt is 10° - 20° (Fig.10). Other possibility of cosmic rays influence on equatorial regions are geomagnetic anomalies [Kilifarska N. and Bojilova R., 2019]. The N-S solar asymmetry influence variations of solar magnetic field and heliosphere. These variations modulate the cosmic rays intensity.

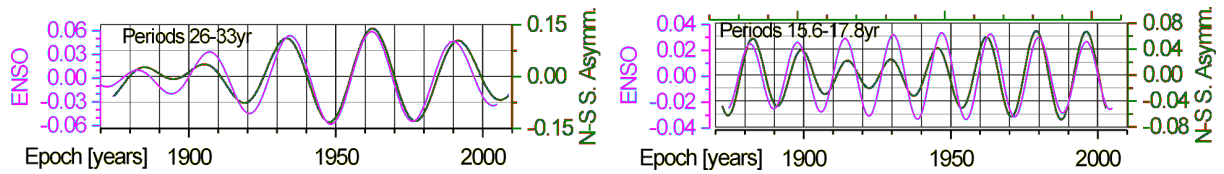


Fig.5. N-S solar asymmetry influence on decadal ENSO oscillations with periods 15.6-17.8yr and 26-33yr.

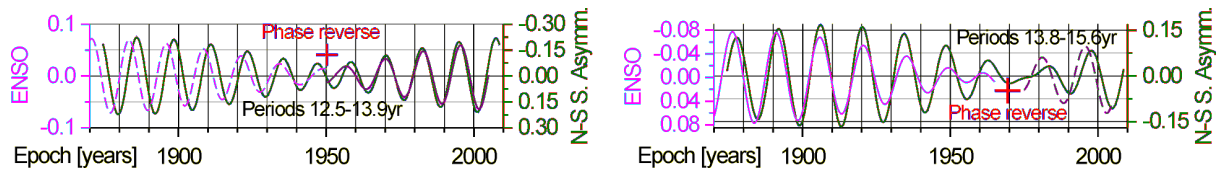


Fig.6. N-S solar asymmetry influence on decadal ENSO oscillations with periods 12.5-13.9yr and 13.9-15.6yr.

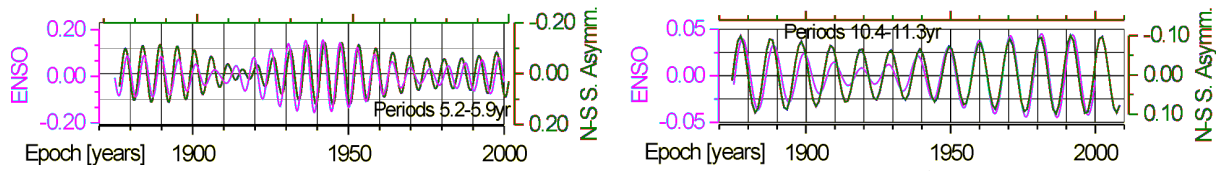


Fig.7. N-S solar asymmetry influence on ENSO oscillations with periods 5.2-6.9yr and 10.4-11.3yr.

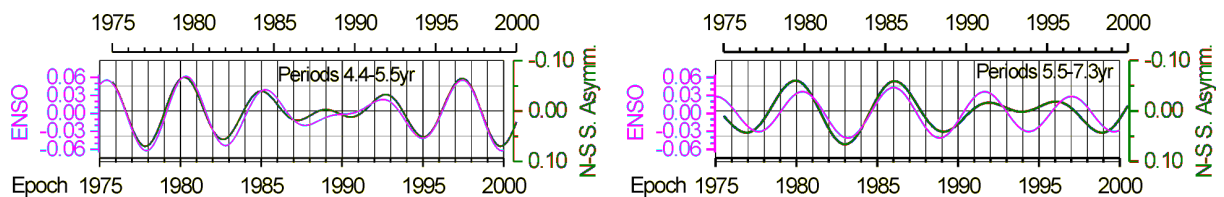


Fig.8. 22-year model: N-S solar asymmetry influence on interannual ENSO oscillations with periods 4.4-5.5yr and 5.5-7.3yr.

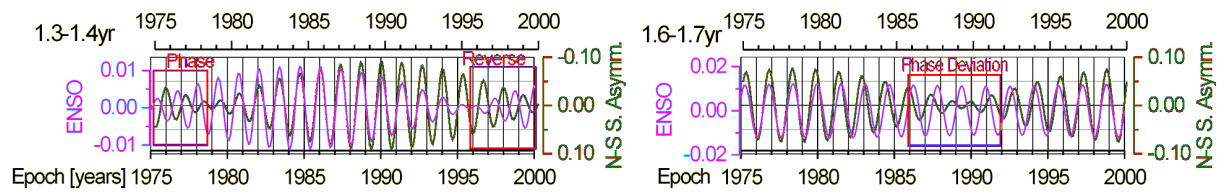


Fig.9. 22-year model: N-S solar asymmetry influence on interannual ENSO oscillations with periods 1.3-1.4r and 1.6-1.7yr.

The N-S solar asymmetry affect Enso variations in large frequency bands, whose periods are decadal and interannual (Figs. 5-9). The 11-year and interannual ENSO oscillations are positively correlated with the South solar hemisphere domination (Figs. 7-9). The decadal variations of ENSO with periods 15.6-17.8yr and 26-33yr are connected with the North solar hemisphere domination (Fig.5). The ENSO oscillations with periods 12.5-13.9yr and 13.9-15.6yr depend on N-S solar asymmetry with sudden phase reverse in 1950 and 1970 (Fig.6).

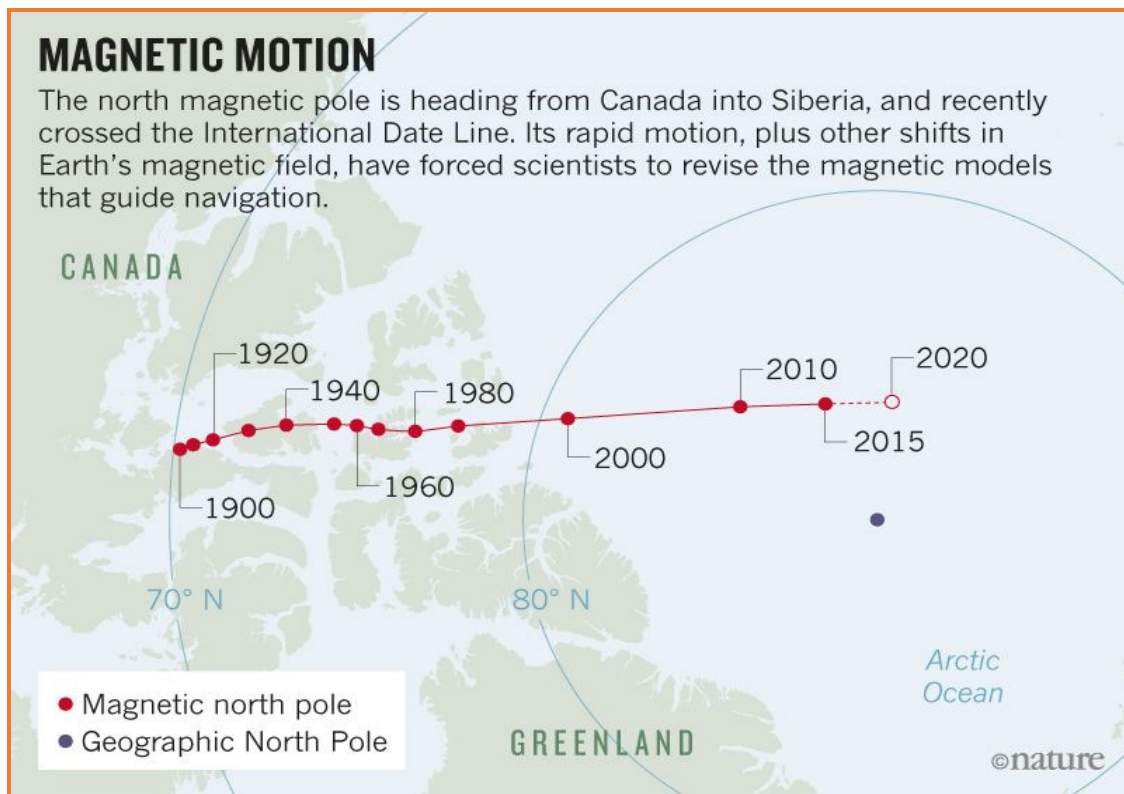


Fig.10. The north magnetic pole motion after 1900.

Discussion and conclusions

Haam E, and Tung K.K. [2012] conclude that El Nino and La Nina are independent from 11-year solar cycle, but they didn't take into account that the 11-year solar signals are weak and hidden inside the time series noise. Roi I. and Haigh J.D. [2012] find no consistent ENSO-like variation in tropical SSTs following peak years of the 11-year sunspot cycle. Actually the 11-year sunspot and TSI signals are not important to the ENSO response, because the ENSO frequencies are composed by the response to solar harmonics with periods 2-7yr.

Misos S. and Schmidt H. [2012] suppose that the coupled atmosphere-ocean interactions may amplify 11-yr solar cycle signals in a way that they resemble El Nino or La Nina. Meehl G. A. et al. [2009] suppose two mechanisms to explain 11-year solar influence on the magnitude of observed climate signals in the tropical Pacific: the top-down stratospheric response of ozone to fluctuations of shortwave solar forcing and the bottom-up coupled ocean-atmosphere surface response. These mechanisms decrease the sea surface temperatures during peaks in the 11-year solar cycle, and reduce low-latitude clouds to amplify the solar forcing at the surface. They are close to the ideas used here of N-S solar asymmetry influence on ENSO variations.

Presented results of high correlation between interannual and decadal harmonics of N-S solar asymmetry and ENSO events may resolve the question of the existence of solar influence on Pacific temperature anomalies. The N-S solar asymmetry is connected with solar magnetic field disturbances, followed by temporal variations of solar wind and corresponding changes of the heliosphere and these processes produce modulation of cosmic rays. Possible reason of influence of N-S solar asymmetry on ENSO are modulated cosmic rays, dropped over equatorial regions of the Earth, so the solar cycles may drive Enso variations by modulation of cosmic rays over the Pacific Ocean.

References

- Asenovski, S. Kirov B., Asenovska Ya., 2015, Solar activity correlation with NAO and ENSO , Meeting of the ISSI team “Effects of Interplanetary Disturbances on the Earth’s Atmosphere and Climate Bern, Sutzterland 24-28, March 2014 http://www.issibern.ch/teams/interplanetarydisturb/wp-content/uploads/2015/01/Asikainen_03_2014.pdf
- Coddington, O., Lean, J.L., Pilewskie, P., Snow, M. and Lindholm, D.: 2015, A solar irradiance climate data record, Bull. American Meteorological Soc. doi: 10.1175/BAMS-D-14-00265.1
- Haam E., Tung K.K., . 2012, Statistics of Solar Cycle–La Nina Connection: Correlation of Two Autocorrelated Time Series, Journal of the atmospheric sciences, Vol. 69, 2934-2939.
- Kilifarska, N.A.: 2015. Bi-decadal solar influence on climate, mediated by near tropopause ozone. Journal of Atmospheric and Solar-Terrestrial Physics, SI:Vertical Coupling 136, 216–230. <https://doi.org/10.1016/j.jastp.2015.08.005>
- Kilifarska N., Bojilova R.: 2019, Geomagnetic focusing of cosmic rays in the lower atmosphere –evidence and mechanism, Compt. rend. Acad. bulg. Sci., 72(2), 365-374.
- Kilifarska, N.A. and Haight, J.D.: 2005, The impact of solar variability on the middle atmosphere in present day and pre-industrial atmospheres. J. Atmos. Solar Terr. Phys., 67, 3, 241-249. DOI: 10.1016/j.jastp.2004.10.003
- Kilifarska, N.A., Tassev, Y.K. and Tomova, D.Y.: 2008, Cosmic ray showers and their relation to the stratospheric sudden warmings. Sun and Geosphere, 3, 1, 10-17.
- Kilifarska, N.A.: 2011, Long –term variations in the stratospheric winter time ozone variability – 22 year cycle. Comptes rendus de l’Académie bulgare des Sciences, 64, 6, 867-874.
- Kirov B., Georgieva K., 2002, Long-term variations and interrelations of ENSO, NAO and solar activity, Phys. and Chem. of the Earth, Parts A/B/C, V. 27, Iss. 6–8, 441-448, DOI:doi.org/10.1016/S1474-7065(02)00024-4
- Kopp, G., Krivova, N., Lean, J., and Wu, C.J.: 2016, The Impact of the Revised Sunspot Record on Solar Irradiance Reconstructions, Solar Physics. doi: 10.1007/s11207-016-0853-x
- Lanscheidt, T., 2000, Solar Forcing Of El Niño and La Niña, in Wilson A. (Edit.), The Solar Cycle and Terrestrial Climate-2000, Proc. 1st Solar & Space Weather Euroconf., Tenerife, Spain, 25–29 Sept. 2000, ESA SP-463, pp. 135–140
- Lean, J.: 2000, Evolution of the Sun's spectral irradiance since the Maunder Minimum. Geophysical Research Letters, 27, 16, 2425-2428. DOI: 10.1029/2000GL000043
- Lean, J.L.: 2010, Cycles and Trends in Solar Irradiance and Climate, Wiley Interdisciplinary Reviews, Climate Change 1. doi: 10.1002/wcc.018
- Maruyama, F., 2018, The Relation among the Solar Activity, the Total Ozone, QBO, NAO, and ENSO by Wavelet-Based Multifractal Analysis. J. of Appl. Math. and Phys., 6, 1301-1314. doi: 10.4236/jamp.2018.66109.
- Meehl G. A., Arblaste J.M., Matthes K., Sassi F., van Loon H., 2009, Amplifying the Pacific Climate System Response to a Small 11-Year Solar Cycle Forcing, Science Vol. 325, Iss. 5944, 1114-1118, DOI: 10.1126/science.1172872
- Misios S., Schmidt H., 2012, Mechanisms Involved in the Amplification of the 11-yr Solar Cycle Signal in the Tropical Pacific Ocean, J. of Climate, Vol.25, 5102-5118.
- Roy I. and Haigh J.D., 2012, Solar cycle signals in the pacific and the issue of timings, J. of Atm. Sci., Vol.69, 1446-1451
- Velinov, P.I.Y., Mateev L. and Kilifarska N.A.: 2005, 3-D model for cosmic ray planetary ionisation in the middle atmosphere. Ann. Geophys., 23, 9, 3043-3046. DOI: 10.5194/angeo-23-3043-2005
- Zhai, Q., 2017, Evidence for the effect of sunspot activity on the El Niño/Southern Oscillation, New Astronomy, 52, ISSN1384-1076, 1-7

Water Transport and Earth Rotation Variations Due to Solar Cycles

Ya. Chapanov

Climate, Atmosphere and Water Research Institute, BAS

E-mail: yavor.chapanov@gmail.com

Abstract.

The solar activity affects wide range of surface processes over Earth, including weather and climate indices, winds, rains, snow covers, and mean sea level. These processes are due mainly to the Total Solar Irradiance TSI variations, followed by weather and climate changes. The ocean surface absorbs more thermal energy during solar maxima. This increases evaporation processes, atmospheric water content, clouds and rains. Some part atmospheric water is transported globally from ocean to polar regions by circulation in Hadley, Ferrel, and polar atmospheric cells. The water transfer to polar regions leads to polar ice thickness increase, synchronously with the solar cycles. This, together with the Mean Sea Level MSL decrease, changes the Earth shape and the corresponding principal moments of inertia. As the consequence, the Earth rotation is faster during the solar maxima, according to the law of angular momentum conservation. The model of Universal Time UT1 oscillations due to TSI and MSL variations is created. Common UT1, LOD, TSI, Wolf's numbers W_n and MSL cycles from selected frequency bands with interannual and decadal periodicity are presented.

Introduction

The global hydrologic cycles are widely affected by climatic variations, which are mostly driven by solar-terrestrial influences. The decadal climatic signals are associated with the solar activity cycles with periods of 11, 22, 45 and more years. The solar effects on climate and environment are synchronous oscillations of the water content, mean sea level and polar ice thickness and volume, due to global water redistribution between ocean and continental polar ice. The polar ice thickness increases and the mean sea level decreases during the solar maxima, followed by the decrease of the mean Earth radius and the principle momentum of inertia relative to the rotational axes. Any change of the principle momentum of inertia leads to significant variations of the Earth rotation, due to the conservation of the Earth angular momentum. The synchronous cycles of solar indices, mean sea level, ice thickness accumulation, LOD and UT1 are analyzed.

Time series data

The observational data consist of UT1 variations for the period 1623.5-2005.5 [Stephenson F.R. and Morrison L.V., 1984] (Fig.1); the Wolf's numbers W_n combined by annual values for the period 1700-1748 and monthly values since 1748 (Fig.2, a); TSI since 1610 (Fig.3, a); the North-South solar asymmetry $S_a = (S_n - S_s) / (S_n + S_s)$, where the S_n and S_s are monthly sunspot area on the Northern and Southern solar hemispheres, respectively (in units of millionths of a hemisphere) (Fig.3, b); the detrended mean sea level at Stockholm for the period 1800-2002 (Fig.4, a); and the Greenland ice thickness accumulation data from the Agassiz Ice Cap (Fig.4, b). The longest observational series of the temporal variations of the sea level at a fixed point is completing by Ekman M. [2003] for station Stockholm and cover observational span from 1774.04 to 2001.0 with two short data gaps in the beginning (Fig.4, a).

The long-periodical part of UT1 variations (Fig.1, b), determined by parabolic trend remove, are used to extract the decadal cycles of the Earth rotation. The LOD time series are determined by derivation of UT1 time series. The solar magnetic cycles are represented by the extended time series of 22-year Wolf's numbers (Fig.2, b), determined by sign alternation of the even 11-year Schwabe cycles.

The S_n and S_y data since 1874 are observed by the Royal Greenwich Observatory and merged after 1976 with the US Air Force (USAF) and the US National Oceanic and Atmospheric Administration (NOAA) data by D. Hathaway (<https://solarscience.msfc.nasa.gov/greenwch.shtml>). The last version of estimated solar irradiances for the last 400 years is based on the NRLTSI2 historical TSI reconstruction model by J. Lean [Kopp G. et al., 2016; Lean J., 2000, 2010; Coddington O. et al., 2015].

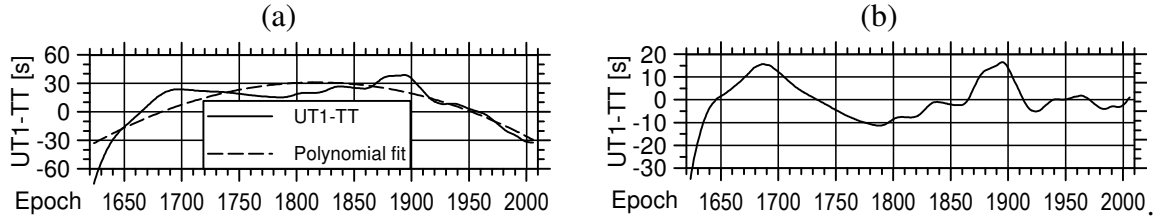


Fig. 1. UT1 data for the period 1623.5-2005.5 (a) and periodical part of UT1 variations (b)

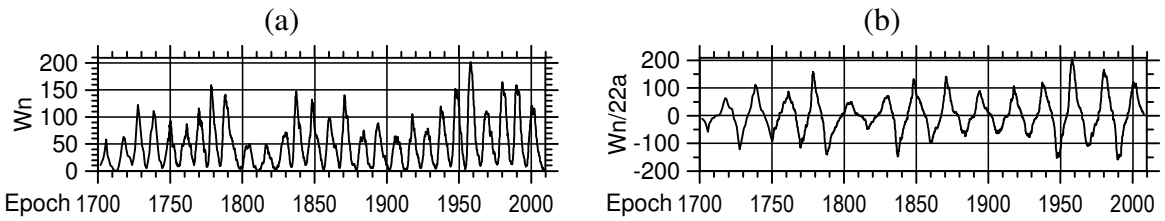


Fig. 2. Wolf's numbers W_n represented by annual (1700-1748) and monthly values (a). Extended time series of 22-year cycles of the wolf numbers $W_{n/22a}$ (b).

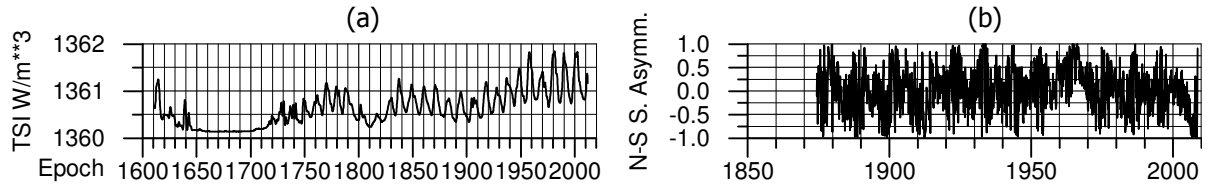


Fig. 3. TSI variations (a). N-S solar asymmetry (b).

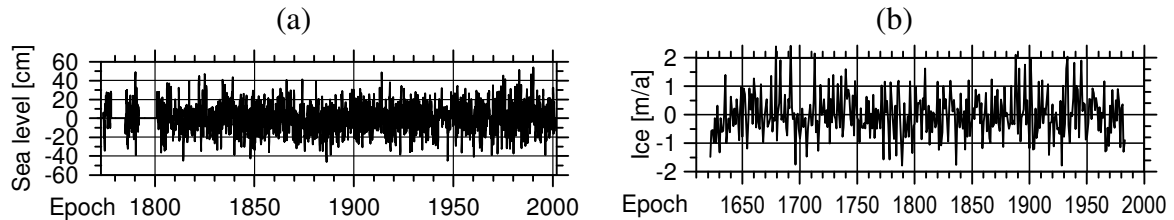


Fig. 4. Sea level data from Stockholm mareograph station, after the linear trend remove (a). Greenland ice thickness accumulation data from the Agassiz Ice Cap (b).

Global water transport and LOD variations

The Length of Day is the difference between the astronomically determined duration of the day and 86400 SI seconds. The relationship of the angular velocity of the Earth with LOD is (<http://www.iers.org/IIERS/EN/Science/EarthRotation/UT1LOD.html>)

$$\omega = \omega_0 - \omega_1 L_{OD},$$

$$\omega_0 = 72921151.467064, \quad (1)$$

$$\omega_1 = 0.843994809,$$

where ω is the Earth angular velocity, L_{OD} – the Length of Day in milliseconds, ω , ω_0 and ω_1 , are in picoradians/s. According (1), the variations of LOD depend on the variations of the Earth angular velocity by the formula

$$L_{OD} = -\frac{\Delta\omega}{\omega_1} \quad (2)$$

Let consider a homogeneous sphere with radius $R=6371\text{km}$, density 5.519g/cm^3 [Neff R.F. and Zitewitz P.W., 1995], inertial moment C , mean angular velocity ω_0 and constant mass M . From the conservation of angular momentum, the small changes of the inertial moment ΔC , due to variations of the radius ΔR , are connected with a corresponding change of angular velocity $\Delta\omega$ by the expressions

$$\begin{aligned} \Delta C\omega_0 + C\Delta\omega &= 0, \\ C + \Delta C &= \frac{2}{5}M(R^2 + 2R\Delta R + \Delta R^2). \end{aligned} \quad (3)$$

The relationship of the variations of the radius and angular velocity is

$$\Delta\omega = -\frac{2\Delta R\omega_0}{R} \quad (4)$$

From (2) and (4) the relationship of L_{OD} and ΔR is

$$\Delta L_{OD} = \frac{2\Delta R\omega_0}{\omega_1 R} \quad (5)$$

The transfer from homogeneous elastic sphere to the real Earth need to replace the variations of radius ΔR by equivalent changes of the mean sea level ΔM_{SL} . It is necessary to determine transfer coefficient k between the homogeneous elastic sphere and the real Earth, which value represent the ratio between ΔM_{SL} and ΔR

$$k = \frac{\Delta M_{SL}}{\Delta R} \quad (6)$$

Involving coefficient q of ice sheets influence on the moment of inertia, we obtain from (5) and (6)

$$L_{OD} = \frac{2\omega_0(1-q)}{k\omega_1 R} \Delta M_{SL}, \quad (7)$$

The value of the coefficient k depends on the mean density of sea water at the ocean surface, total ocean surface and the moment of inertia of the thin ellipsoidal shell over the ocean with thickness equal to ΔM_{SL} . In case of small MSL variations (significantly less than 1m), the water lost occurs from all Earth surface, more intensive from the free water surfaces and less intensive from the ground. The coefficient k is approximately equal to 6 in this case [Chapanov Ya. and Gambis D., 2010]. The MSL changes are more than 100m during the glaciations, so the level of the water lost from the ground is neglectful and the coefficient k is

$$k = \frac{D_E S_E I_{ES}}{D_O S_O I_{OS}}, \quad (8)$$

where D_E is the mean Earth density, D_O – the mean sea water density at the ocean surface, S_E – the total Earth surface, S_O – the global ocean surface, I_{ES} - the moment of inertia of the thin ellipsoidal shell over the Earth, I_{OS} - the moment of inertia of the thin ellipsoidal shell over the ocean. The mean sea surface water density is 1.025g/cm^3 , or the ratio D_E/D_O is equal to 5.38. The total Earth surface is $510 \times 10^6 \text{ km}^2$, the global ocean surface - $361 \times 10^6 \text{ km}^2$, and their ratio – 1.414. The proper calculation of the LOD need also knowledge of the surfaces covered by ice and their axial moments of inertia. The MSL decrease leads to decreasing of the Earth axial moment of inertia, while the redistributed water over the ice sheets and corresponding increase of the ice thickness leads to some increase of the axial moment of inertia. The relative effect of the ice sheets on the I_{OS} is

$$q = \frac{S_O I_{Ice}}{S_{Ice} I_{OS}}, \quad (9)$$

where S_{Ice} is the total ice surface and I_{Ice} - the total moment of inertia of thin ellipsoidal shell over the continental ice sheets. The sea ice does not affect the moment of inertia changes, due to its hydrostatical equilibrium with the ocean water.

Let the surface data is represented over a grid with size $\alpha \times \alpha$ degrees and the geocentric coordinates of the center of the n -th grid element are geocentric distance r_n , longitude λ_n and latitude θ_n . If a and b denote Earth equatorial and polar radii ($a=6478.137\text{km}$, $b=6356.572\text{km}$), then the geocentric distance r_n is

$$r_n = \sqrt{\frac{a^2 b^2}{a^2 \sin^2 \theta_n + b^2 \cos^2 \theta_n}}. \quad (10)$$

The distance h_n from the center of the n -th grid element to the Earth axis of rotation is

$$h_n = r_n \cos \theta_n. \quad (11)$$

The surface s_n of the n -th grid element is approximately

$$s_n = 4\pi^2 \left(\frac{\alpha}{360} \right)^2 r_n h_n. \quad (12)$$

The surface S of a given Earth area is the sum of its grid elements surfaces

$$S = \sum_n s_n. \quad (13)$$

The axial moment of inertia I of thin ellipsoidal shell with unit density and thickness over this area is

$$I = \sum_n s_n h_n^2. \quad (14)$$

The axial moment of inertia of ellipsoidal shell with unit density and thickness over the Earth is $1.38 \times 10^{14} \text{ km}^4$ and over the ocean - $1.0 \times 10^{14} \text{ km}^4$. Their ratio is 1.38, and according (8) the value of the transfer coefficient k between the homogeneous elastic sphere and the real Earth is $k=10.5$.

The ratio between the total ocean surface S_O and total ice surface S_{Ice} is 12.45. The ratio between I_{Ice} and I_{OS} , calculated by formula (10-14) is 0.0019, so the value of q is 0.024, or the influence of polar ice caps on the moment of inertia is 2.3%. Note that the value of coefficient q depends non-linearly on MSL variations and its value is significantly higher during the glacial maxima. Finally, the dependence between LOD and MSL variations is

$$\text{LOD} = 2.526 \Delta \text{MSL}, \quad (15)$$

where MSL variations are in meters and LOD – in milliseconds.

The 11-year solar activity cycles strongly affect earth climatic variations by the variations of the total solar irradiance with maximal amplitudes between 0.5 W/m^2 . These variations provide additional amount of energy $\sim 2 \times 10^{16} \text{ MJ}$ for the whole Earth and 160 MJ per square meter on the equator during these cycles. This energy is capable to evaporate 65l of water from 1 square meter equatorial ocean surface and 30l of water from the north latitudes. The periodical LOD and UT1 variations due to solar cycles are provided by additional water evaporation and global mean sea level oscillations, synchronized with the global water redistribution and corresponding change of the ice thickness at the polar caps. These events cause periodical change of the Earth axial moment of inertia and periodical oscillations of the Earth rotation, according the law of angular momentum conservation. The excitation of the

observed oscillations of the Earth rotation needs less than 7mm of MSL variations during the solar cycles.

Common solar and terrestrial cycles

The decadal cycles of Earth rotation for the period 1623.5-2005.5 are extracted by means of Fourier approximation of the UT1-TT variations with use of 100 harmonics, which includes oscillations with periods above 3.8a and accuracy of the amplitudes about 11ms. Common solar and terrestrial cycles exist in various decadal and interannual frequency bands. Presented oscillations in Figs. 5-10 show good agreement between the solar indices, Earth rotation, MSL and polar ice accumulation rate. The W_n and TSI variations correlate with UT1 and ice thickness accumulation rate. Anticorrelation exist between solar indices, MSL and LOD variations. The variations of the polar ice accumulation with periods 11a and 22a are due to the total solar irradiance changes during the solar cycles and corresponding additional water evaporation. When the evaporated water is redistributed over the continental polar ice it leads to arising of the continental polar ice during the solar maxima, so the TSI variations are the reasons of the observed polar ice thickness oscillations with the decadal solar frequencies.

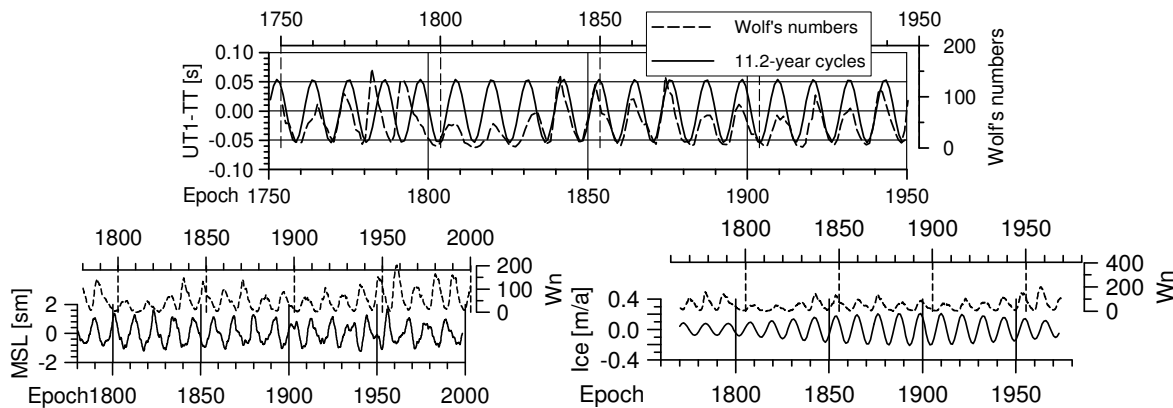


Fig. 5. Comparison of 11-year cycles of W_n (dashed line), UT1, MSL and ice accumulation (bold line).

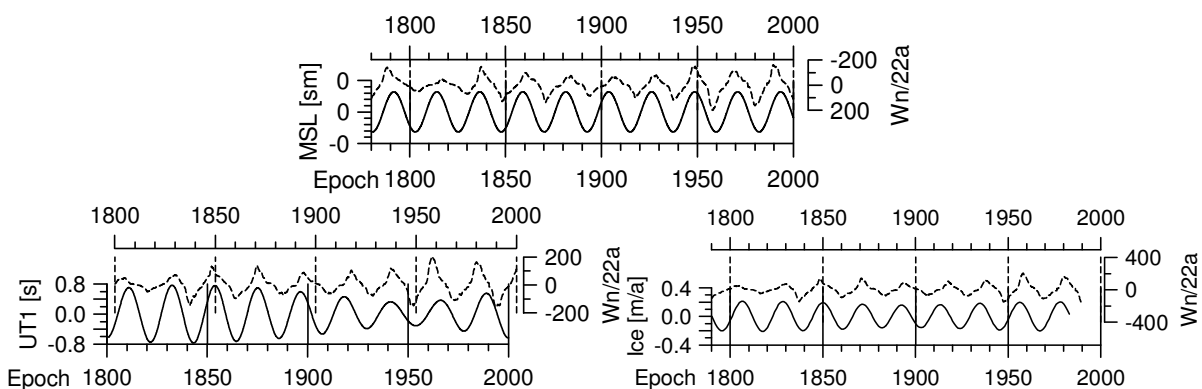


Fig. 6. Comparison of 22-year cycles of extended Wolf's numbers $W_n/22a$ (dashed line), MSL, UT1 and ice accumulation (bold line).

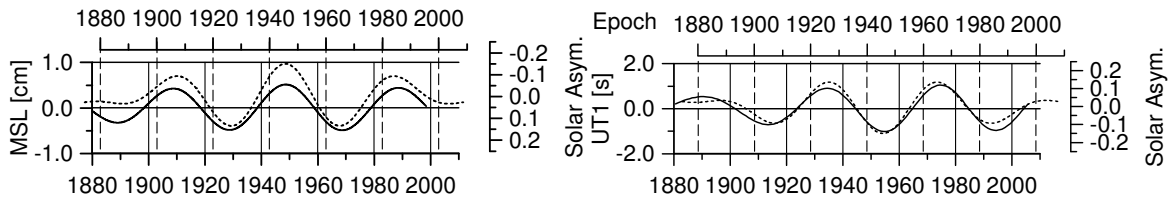


Fig. 7. Comparison of 45-year cycles of N-S solar asymmetry (dashed line), MSL, and UT1 (bold line).

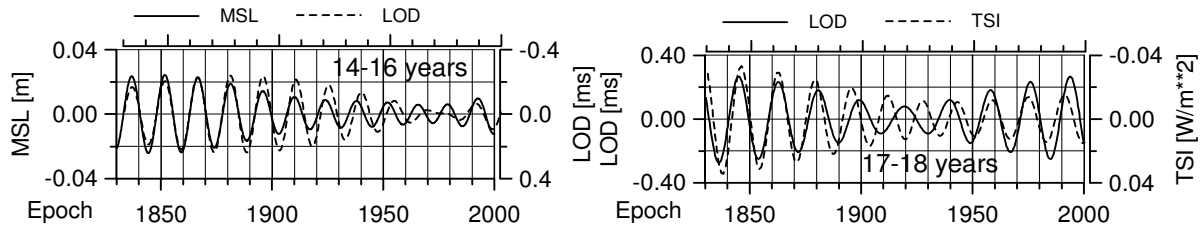


Fig. 8. Comparison of MSL, LOD and TSI cycles with periods 14-16yr and 17-18yr.

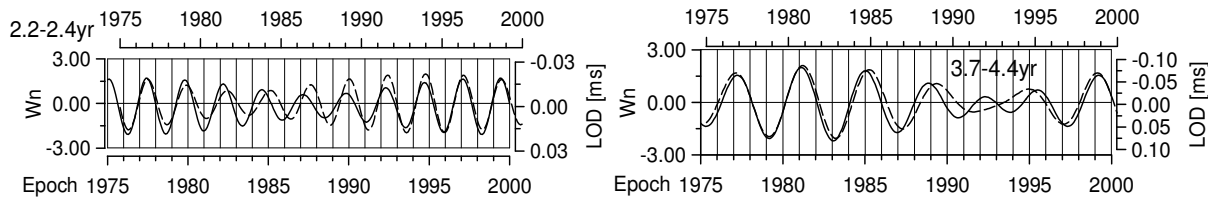


Fig. 9. Common cycles of W_n (dashed line) and LOD (bold line) with periods 2.2-2.4yr and 3.7-4.4yr.

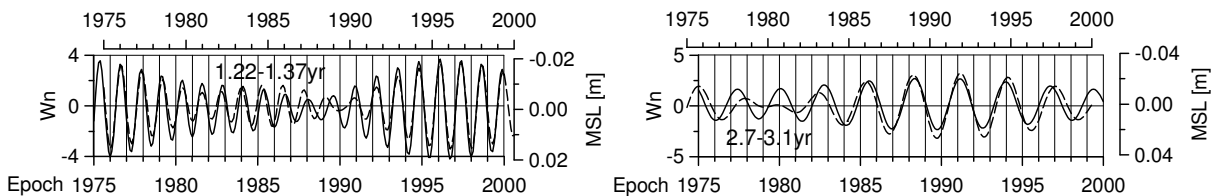


Fig. 10. Common cycles of W_n (dashed line) and MSL (bold line) with periods 1.22÷1.37yr and 2.7÷3.1yr

Conclusions

The main source of excitation of the decadal and interannual variations of Earth rotation are climatic variations due to the solar activity and connected with them oscillations of the mean sea level and continental polar ice. The solar activity cycles affect climate by variations of the total solar irradiance with amplitude 0.5W/m^2 . These variations provide additional amount of energy, which is capable to evaporate 30-65 liters of water from 1 square meter of ocean surface. The changes of MSL, due to total solar irradiance variations and additional evaporation, followed by global water redistribution and ice thickness variations over the polar caps, lead to corresponding oscillations of the axial Earth moment of inertia, and according to the law of angular momentum conservation – to changes of Earth rotation velocity.

The proposed model of global water redistribution determines the relationships between the observed periodical oscillations at the solar activity frequencies of the Earth rotation, mean sea level and ice thickness accumulation rate over the polar continental ice sheets. It is possible to reconstruct the periodical behavior of the global hydrological cycles by means of available astronomical data, or to reconstruct Earth rotation data by means of available mean sea level changes.

References

- Chapanov, Ya., D. Gambis Solar-terrestrial energy transfer during sunspot cycles and mechanism of Earth rotation excitation, Proc. of the IAU, Vol.5, Symp. S264 (Solar and Stellar Variability: Impact on Earth and Planets), Cambridge University Press, 2010, pp 404-406 doi:10.1017/S1743921309992997, journals.cambridge.org/article_S1743921309992997
- Coddington, O., Lean, J.L., Pilewskie, P., Snow, M. and Lindholm, D.: 2015, A solar irradiance climate data record, Bull. American Meteorological Soc. doi: 10.1175/BAMS-D-14-00265.1
- Ekman, M, 2003, The world's longest sea level series and a winter oscillation index for northern Europe 1774 – 2000, Small Publications in Historical Geophysics, 12, 31 pp
- Kopp, G., Krivova, N., Lean, J., and Wu, C.J.: 2016, The Impact of the Revised Sunspot Record on Solar Irradiance Reconstructions, Solar Physics. doi: 10.1007/s11207-016-0853-x
- Lean, J.: 2000, Evolution of the Sun's spectral irradiance since the Maunder Minimum. Geophysical Research Letters, 27, 16, 2425-2428. DOI: 10.1029/2000GL000043
- Lean, J.L.: 2010, Cycles and Trends in Solar Irradiance and Climate, Wiley Interdisciplinary Reviews, Climate Change 1. doi: 10.1002/wcc.018
- Neff, R. F. and P. W. Zitewitz, 1995, Physics, Principles and Problems. New York: Glencoe, 159 pp.
- Stephenson, F. R., Morrison, L. V., 1984, Long-Term Changes in the Rotation of the Earth: 700 BC to AD 1980, Philosophical Transactions of the Royal Society of London, Ser. A, pp. 47--70.

Observations Supporting Hypothesis for Global Electrical Circuit as Mediator between Solar Events and Weather

Tonev P.T.

Space Research and Technology Institute BAS, Sofia, Bulgaria

E-mail: ptonev@bas.bg

Abstract.

Some of the few available experimental studies are discussed which demonstrate peculiarities of the local response of the global atmospheric electrical circuit (GEC) to major solar proton events (SPE), concerning conductivity, the fair-weather electric current J_z from ionosphere to ground, and the related field E_z . For more representative picture, these experiments include auroral and lower latitudes, as well as different altitudes: the ground level, stratosphere and mesosphere. The experimental data show typical peculiarities: although these are not fully understood yet, they can give a key to the global response of GEC to SPE. It is concluded that a relevant 3D dc model of GEC is necessary to determine factors and physical conditions which would lead to the locally observed characteristics.

Introduction

The aim of this work is to demonstrate the specific peculiar response of the global atmospheric electrical circuit (GEC) during major solar proton events (SPEs) seen from the available experimental studies performed in different atmospheric locations. These comprise measurements of the main electrical characteristics (conductivity σ , electrical field \mathbf{E} and current density \mathbf{J}) within several groups: a) at high and middle latitudes - balloon experiments at altitudes between 26 km and 31 km, as well as rocket measurements in stratosphere and mesosphere; b) ground-based measurements at high and low latitude. All these experimental studies demonstrate peculiar and large variations which cannot be predicted theoretically [Farrell and Desch, 2002]. Some factors are formulated in this work which can be responsible for the demonstrated peculiar behavior, together with their further analysis. The main future goal is to clarify the global-scale behavior of GEC during SPEs. Recent studies demonstrate that SEP can affect weather [Veretenenko, 2017], with GEC as hypothetical mediator between solar drivers and weather formation. According to the hypothesis [Tinsley, 2000] weather formation is affected by variations of the electric current J_z of few pA/m² which flows in GEC from the ionosphere to the surface in fair-weather regions where J_z influences creation of cloud and the atmospheric circulation.

Peculiarities demonstrated from experimental results in stratosphere

a) Measurements in Antarctic stratosphere during SPE'69 (GLE) on 20 January 2005

Fig.1 demonstrates data from GOES-10 for the solar proton flux during SPE'69 on 20.01.2005 (the upper-left panel), together with the simultaneously obtained balloon-borne data for the conductivity σ (the lower-left panel), the vertical electric field E_z (the upper-right panel), and the related current density J_z (the lower-right panel) in Antarctic stratosphere at coordinates between (70.9°S, 10.9°W) and (71.4°S, 21.5°W), and at altitude 30.9 - 33.2 km [Kokorowsky et al., 2006; 2012]. Some of the peculiarities of the observed characteristics (not satisfactorily explained yet) are discussed by us here. Before the SPE onset at 06:51 UT σ , E_z , and J_z have typical values: σ is few $\times 10^{-10}$ S/m; the electric current J_z is downward, with mean value ~ 2 pA/m², however E_z and J_z are unusually dispersed. After SPE onset, till 13:48 UT: i) the conductivity σ increases due to ionization by protons with energies ~ 100 MeV - initially ~ 20 times or more; ii) E_z initially suddenly drops almost to zero, then E_z increases to its usual values; iii) J_z shows large variations to values about 5 times larger than usually. In

the period 13:48-5:58 UT conductivity exceeds 5-10 times its usual values, and E_z , as well as J_z remain close to zero. After 15:58 UT E_z and J_z suddenly change their direction from downward to upward for at least 5 hours, yet J_z exceeds more than twice its typical value. This occurred together with the sudden increase of protons with energies <5 MeV which do not reach stratosphere. Also, a geomagnetic storm (12:00-18:00 UT; $K_p=4$, 5-), and a strong sub-storm from $\sim 15:00$ till $\sim 18:00$ UT (with $AE \sim 1200$ nT) occurred. The current J_z remained reversed to upward for hours, yet exceeds more than twice its typical value (these last features are hard to explain). Although SPE'69 causes dramatic modification of conductivity σ in the middle atmosphere at high latitudes due to strong ionization, as demonstrated in Fig.2 [Usoskin *et al.*, 2014], the model results by the well-known oversimplified 1D model presentation of GEC by an equivalent circuit predicts that changes of J_z are $< \sim 5\%$; thus, this model does not predict the large and long-time variations in Fig.1.

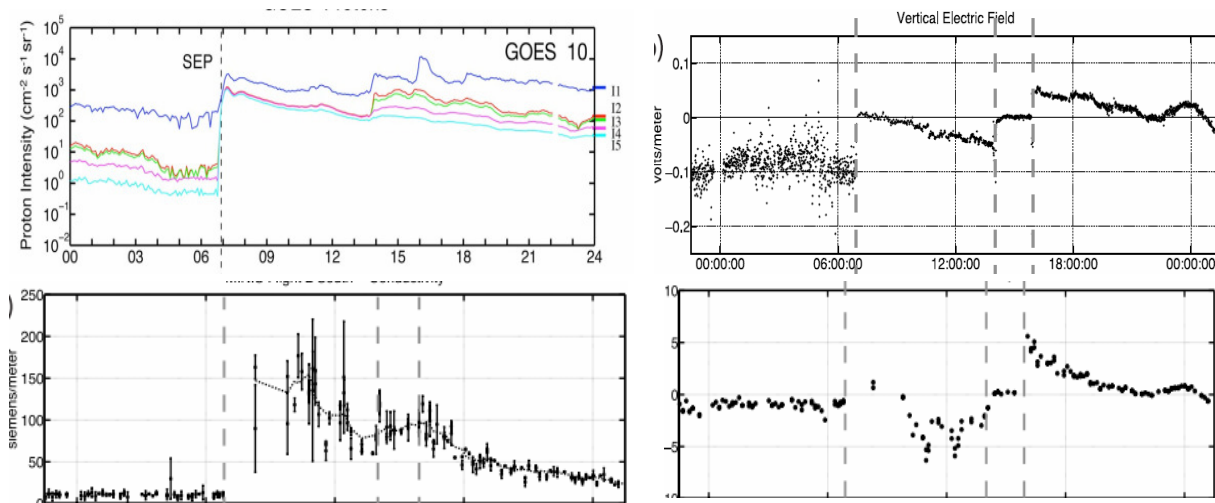


Fig.1. Data from GOES-10 for the integral proton intensity energies for channels > 1 , 10, 30, and 50 MeV (the upper-left panel); simultaneous measurements of conductivity \square (the lower-left panel); vertical electric field E_z (the upper-right panel); and the vertical current density J_z (the lower-right panel) computed from \square and E_z [Kokorowski *et al.*, 2006; 2012].

Similar model estimations are obtained also by [Farrell and Desh, 2002], in contradiction with experimental data for E_z and J_z .

b) Measurements in stratosphere at middle latitudes during SPE on 16 February 1984

During SPE (with GLE) on 16 Feb.1984 the electric characteristics σ , E_z , and J_z were obtained on a balloon payload EMA-8 with coordinates (44.6°S, 142.7°E), $\Lambda = -56.3^\circ$ [Hozlworth *et al.*, 1987]. Data obtained are presented in Fig.2. This SPE occurred in short time period (\sim one hour). Simultaneously was obtained data from identical payload EMA-7 located on lower latitude ($\Lambda = -48.8^\circ$) which indicated no effect of SPE on σ , E_z , and J_z . Both σ and E_z increased initially (σ enhanced more than twice); J_z also increased (2.2 times). Peculiarities of perturbations of σ , J_z , and E_z , though smaller and in shorter time, resemble those demonstrated in Fig.1. These perturbations are also in contradiction with modeling [Farrell and Desch, 2002], and are even more striking than in the former case, since they take place at latitude with much higher cutoff rigidity (> 1 GV).

Features of vertical electric fields in mesosphere and stratosphere

In a series of rocket experiments above Heiss Island (80°37'N, 58°03'E) and above southern Indian Ocean [Zadorozhny *et al.*, 1998] found unusually large (~ 1 V/m) vertical electric field E_z in the mesosphere which still remain unexplained. Fig.3 demonstrates profiles of E_z in three cases above Indian Ocean. On 21.10.1989 19:31 UT, at (58.5°S, 51.1°E), $\Lambda=62.7^\circ$ S the electric field E_z (presented by thick solid line) reached much larger peak in mesosphere (12.2 V/m) than in all other cases (the second largest peak E_z was for 12.10.1989 shown in Fig.3 by dashed line). The first case on 21.10 coincided with both strong solar proton event and major geomagnetic storm (with $K_p=8$) which cause the enhancement of E_z .

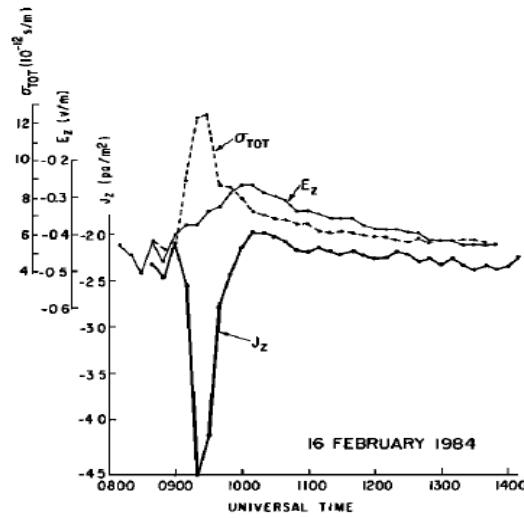


Fig.2. Conductivity σ_{TOT} , vertical electric field E_z and current density $J_z = \sigma E_z$ during SPE on 16 Feb.1984 from balloon-borne measurements at 26 km altitude, at (44.6°S, 142.7°E), $\Lambda = -56.3^\circ$.

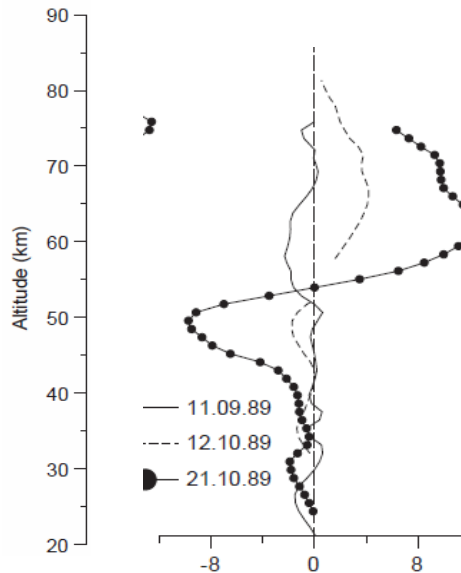


Fig.3. Vertical electric fields E_z measured in Southern Indian Ocean in 1989 on: 11 September 20:15 UT at (52.4°S, 41.07°E) (thin solid line); 12 Oct. 18:30 UT at (57.1°S, 45.0°E) (dashed line); 21 Oct., 19:31 UT at (58.5°S, 51.1°E) (thick solid line). First two cases are during quite geomagnetic conditions. The last case is during a major geomagnetic storm ($K_p=8$) and GLE.

The following peculiarities are observed: *i*) Paradoxically large and still unexplained electric fields E_z are observed in mesosphere and stratosphere in large number of cases; in Southern hemisphere E_z peaks are often much bigger than those in Heiss Island (80.6°N); *ii*) usually, direction of the vertical electric field E_z changes at ~50 km, but while on 11.09 E_z points to downward above 50 km and to upward below, in the other two cases it is upward above 50 km and downward below. The positive and the negative E_z peaks have comparable values. The source of the large electric fields in mesosphere is under debate. [Zadorozhny *et al.*, 1998], etc. suggested as hypothetical factors effects of charged aerosol particles and decreased conductivity.

Behavior of potential difference E_z at surface during SPEs

a) High latitudes (Kola Peninsula) during two major SPEs in 2001

Measurements of air-earth current (AEC) J_z and the potential difference (PD) E_z at ground level at high latitudes have been realized in very few places and for limited periods of time. Fig.4 demonstrates observed variations of E_z in Apatity (Kola Peninsula, Russia) at geomagnetic latitude 63.3° during two major SPE (with GLE) in 2001: SPE-1 on 18 April, and SPE-2 on 4 November [Kasatkina *et al.*, 2009]. In both cases CMEs took place. The following features are valid: 1) Variations of E_z strongly enhance after the beginning of SPE; (E_z can enhance up to ~1 kV/m); 2) For both SPEs the behavior of E_z in the first and the second phase of a SPE is quite different: in the first phase E_z varies strongly, yet remains positive; in the second phase E_z becomes sometimes negative; its negative peaks can be as large as positive ones.

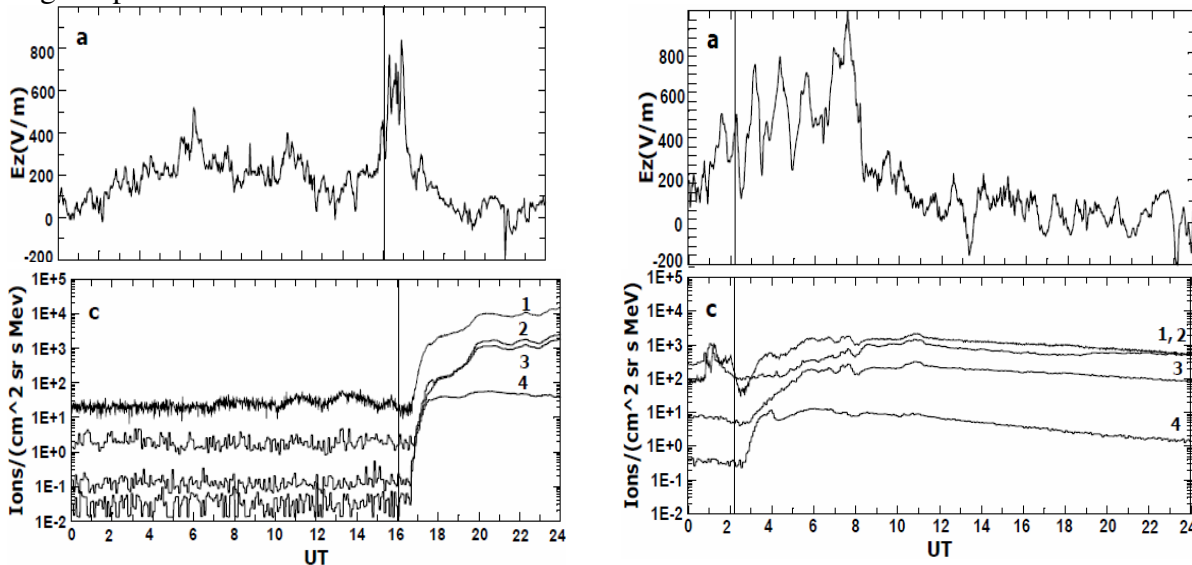


Fig.4. Potential difference E_z at surface in Apatity during SPE-1 on 18.04.2001 (left upper panel) and SPE-2 on 04.11.2001 (right upper panel). The two lower panels show the integral proton intensity energies for channels > 1, 10, 30, and 50 MeV (marked by numbers from 1 to 4 for SPE-1 and SPE-2, respectively). The vertical line marks the flare onset.

b) Low latitudes

Fig.5 demonstrates ground-level variations of the potential difference E_z , (denoted here as atmospheric electric field, AEF) at low latitudes: in CASLEO, Argentina (31.8°S, 69.3°W) at 2552 m altitude during SPE (GLE) on 17.05.2012 [Tacza *et al.*, 2017]. Data for E_z in the upper and the lower panels shown by black lines are obtained respectively from measurements at two stations, CAS1 and CAS2. The red lines in both panels show the average electric field E_{za} . Data show significant and typical deviations for a period of ~10 hours from the SPE onset at 0 UT. During the first phase (for 3.5 – 4 h) E_z is well smaller than E_{za} ; then, for the next 5–6 hours, E_z becomes well larger than E_{za} , as indicated by arrows.

Similar features take place also for a group of 8 solar proton events: during the first phase of SPE the measured electric field E_z is lower than its average value for few hours, and the relation is opposite in the second (somewhat longer) phase of SPE. This pattern of E_z during SPE at low latitudes is ‘reversed’ compared to that high latitudes (although the last is stronger expressed). This indicates that the global-scale reaction of GEC to SPE is of interest.

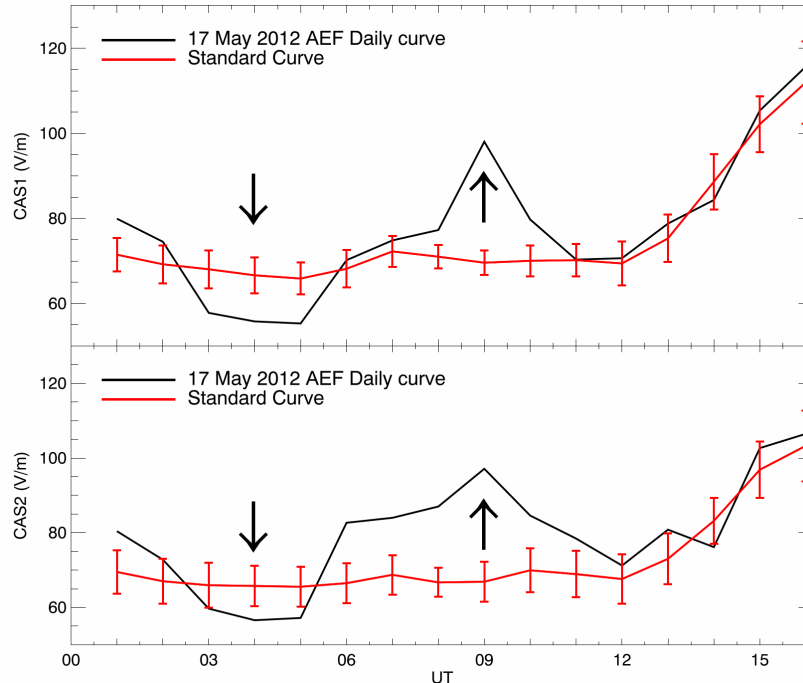


Fig.5. Atmospheric electric field (AEF) measured at CASLEO, Argentina (31.798°S, 69.295°W) at 2552 m altitude, during GLE on 17 May 2012 [Tacza et al., 2017].

Factors hypothetically possible to enforce effects of SPE on GEC

All considered here results in Figures 1-5 demonstrate that the response of GEC to a SPE is much stronger and specific than predicted by modeling [Farrell and Desch, 2002]. For a possible explanation, four factors are considered in this work as hypothetically responsible for the specificity of the considered measurements.

Factor 1. Increase of conductivity \square in middle atmosphere at high latitudes by enhanced ionization by solar proton flux.

Factor 2. More effective electrical coupling of auroral ionosphere with GEC during SPE due to enhanced conductivity in middle atmosphere at high latitudes. Even penetration of a tiny part J_{IS} of FAC (say, $\sim 10^{-6}$) into the middle atmosphere (due to larger conductivity during SPE) could be significant as superposed current in GEC. The total ionosphere-to-ground current J_z would be then $J_z = J_{TS} + J_{IS}$ where J_{TS} is the current from tropospheric sources [Tonev, 2018]. The relation between the geomagnetic activity and the current density J_z in auroral stratosphere has been first supported experimentally by balloon-borne data series [D’Angelo et al., 1982].

Factor 3. A series of studies demonstrate that SPE can produce aerosol particles in the stratosphere [Mironova et al., 2014] and thus can cause decrease of the conductivity.

Factor 4. Penetrating energetic solar protons during SPE could create regions with charged particles, leading to formation of electric fields.

In order to take into account the possible effects of these factors on the electric characteristics new more adequate models of GEC (2D and 3D, as well as steady-state and quasi-statistic) have to be developed as future tasks.

Conclusions

1. Peculiar variations of the vertical electric field E_z and related current density J_z are observed during major SPEs at different altitudes and latitudes which are not explained in terms of equivalent electrical circuit. The responsible mechanisms should be searched.
2. Four factors are formulated which can play role in creation of the observed specific and large local variations in GEC during SPE.
3. Development is needed of 2D and/or 3D model of GEC with account to Factors 1-4.

References

- Farrell, W.M., Desch, M.D. (2002). Solar proton events and the fair weather electric field at ground, *Geophys. Res. Lett.*, 29, no.9, 1323, 10.1029/2001GL013908, 2002.
- Hozworth, R.H. Norville, K.W., Williamson, P.R. (1987). Solar flare perturbations in stratospheric current systems, *Geophys. Res. Lett.*, 14, 8, 52-855, 1987.
- Kasatkina E.A., Shumilov O.I., Rycroft M.J., Marcz F., Frank-Kamenetsky A. V. (2009). Atmospheric electric field anomalies associated with solar flare/coronal mass ejection events and solar energetic charged particle “Ground Level Events” *Atmos. Chem. Phys. Discuss.*, 9, 21941-21958, 2009.
- Kokorowski, M., Sample, J.G., et al. (2006). Rapid fluctuations of stratospheric electric field following a solar energetic particle event, *Geophys. Res. Lett.*, 33, L20105.
- Kokorowski, M., Seppälä, A., et al. (2012). Atmosphere-ionosphere conductivity enhancements during a hard solar energetic particle event, *J. Geophys. Res.*, 117, A05319.
- Tacza J.C., Raulin, J.-P, and De Juli. M.C. (2017). Solar effects on the Global Atmospheric Electric Circuit, *32nd URSI GASS, Montreal, 19-26 August 2017*
- Tinsley B.A.. (2000). Influence of solar wind on the global electric circuit, and inferred effects on cloud microphysics, temperature and dynamics in the troposphere. *Space Sci. Rev.*, 94, 231-258.
- Tonev, P. (2018). Electrical coupling of auroral ionosphere with lower atmospheric regions during SEP, *Proc. 10-th Workshop “Solar Influences on the Magnetosphere, Ionosphere and Atmosphere”*, Bulgaria, June 4-8, 2018.
- Usoskin, I.G., Kovaltsov, G.A. (2011). Ionization effect of solar particle GLE events in low and middle atmosphere. *Atmos. Chem. Phys.*, 11, 1979-1988.
- Veretenenko, S.V. (2017) Особенности пространственно-временной структуры эффектов солнечной активности и вариаций космических лучей в циркуляции нижней атмосферы, DSc.Thesis, Saint Petersburg University, 2017, 327 p.
- Zadorozhny, A.M., A.A. Tyutin (1998). Effects of geomagnetic activity on the mesospheric electric fields, *Ann. Geophysicae* 16, 1544–1551, 1998.

Analysis of the First Space Radiation Data, Obtained by Liulin Ten-Koh Instrument on the Japanize Ten-Koh Satellite

*Dachev T.*¹, *Dimitrov P.*¹, *Tomov B.*¹, *Matviichuk Y.*¹, *Saganti P.*²,
*Holland D.*³, *Okuyama K.-I.*⁴, *Fajardo I.*⁴

¹ SRTI-BAS, Sofia, Bulgaria

² Radiation Institute for Science and Engineering Prairie View A&M University, TX, USA

³ Holland-Space LLC, Houston, TX, USA

⁴ Kyushu Institute of Technology, Graduate School of Engineering, Kyushu, Japan
E-mail: tdachev59@gmail.com

Abstract

On 29 October 2018 was successfully launched, at about 623 km altitude and at 98° inclination, the 23.5-kilogram mass satellite Ten-Koh, developed in Kyushu Institute of Technology by Prof. K. Okuyama. Ten-Koh's primary science instrument is the Charged Particle Detector (CPD) developed at the Prairie View A&M University, and NASA Johnson's Space Center of Houston, TX, USA. The Liulin Ten-Koh instrument is mounted on the top of the CPD. The following three primary radiation sources were expected and recognized in the data obtained with the Liulin Ten-Koh instrument: (i) globally distributed primary GCR particles and their secondary products, (ii) energetic protons in the South Atlantic Anomaly (SAA) region of the inner radiation belt (IRB); (iii) relativistic electrons and/or bremsstrahlung in the high latitudes of the Ten-Koh orbit where the outer radiation belt (ORB) is situated. The obtained data is compared with data from other Liulin type instruments. The aim of the paper is to confirm the presence of these radiation sources in the first space radiation data obtained by the satellite.

Introduction

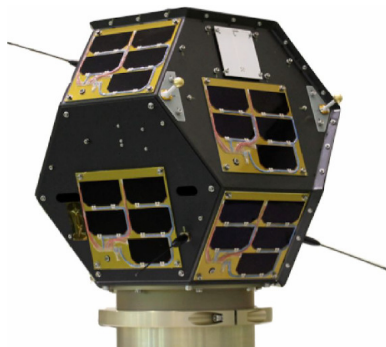


Fig. 1. The “Ten-Koh” satellite.

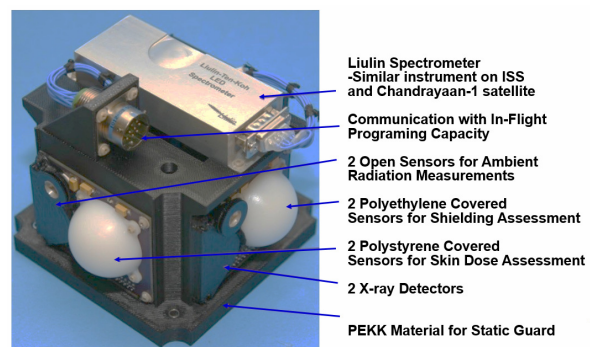


Fig. 2. CPD with mounted “Liulin Ten-instrument.

The Ten-Koh satellite shape is quasi-spherical (Fig. 1), which diameter is about 500 mm and surrounded by solar cells. This satellite is constituted of structure, thermal control, attitude control, telecommunication, bus power system and payload power system. The size is: H465×W500×D500 mm and the mass is about 23.5 kg (Okuyama et al., 2019)

The first purpose of the Ten-Koh satellite missions is the observation of LEO environment. The “Ten-Koh are going to measure various LEO environment parameters and unveil the data via internet initially. The second purpose of the Ten-Koh satellite is to measure the degradation of advanced material, which has potential to use in the future. Involving students in satellite development, manufacture testing and operations is an important part of their curriculum and enhances their education (Fajardo et al., 2019).

The Charged Particle Detector (CPD) and the “Ten-Koch” satellite

The “Liulin Ten-Koh” (LTK) instrument is mounted on the top (Fig. 2) of the Charged Particle Detector (CPD) developed at the Prairie View A&M University, and NASA Johnson's Space Center of Houston, TX, USA. Principal Scientist of this payload is Prof. P. Saganti (<https://www.pvamu.edu/raise/space-payload/charged-particle-detector-2018/>). Principal Engineer of the CPD project is S. D. Holland (formerly with NASA-JSC and currently with Holland-Space LLC, Houston, TX, USA (www.holland-space.com)).

The CPD manage the measurements with the following sensors: Liulin Spectrometer, 2 Open Sensors for Ambient Radiation Measurements, 2 Polyethylene Covered Sensors for Shielding Assessment, 2 Polyethylene Covered Sensors for Skin Dose Assessment, 2 X-ray Detectors. CPD also communicate with In-Flight programming capacity with “Ten-Koch” satellite.

Description of the “Liulin Ten-Koh” instrument

The LTK instrument is a Liulin-type deposited energy spectrometer DES instrument, which was successfully flown: (1) in the US Laboratory module of the ISS in May–August 1991 (Dachev et al., 2002, Wilson et al. 2007, Nealy et al., 2007, Slaba et al. 2011, Badavi, 2014); (2) inside ESA Biopan-5/6 facilities on Foton M2/M3 satellites in 2005 and 2007 (Häder et al., 2009, Damasso et al., 2009; (3) Indian Chandrayaan-1 satellite (Dachev et al., 2011), and (4) in-side the ESA EXPOSE-E/R/R2 facilities outside the Columbus/Zvezda modules of the ISS in 2008–2016 (Dachev et al., 2012, 2015 and 2017).

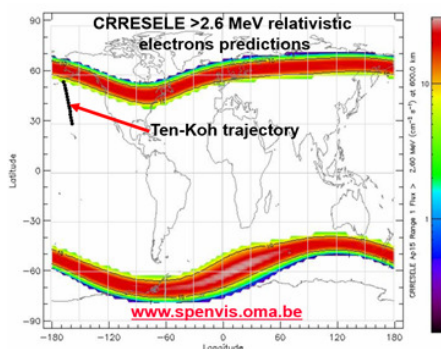


Fig. 3. The Ten-Koh satellite trajectory for 17 January 2019 is plotted over the CRRESELE>2 MeV at 630 km relativistic electrons (>2.6 MeV) predicting global map, obtained online from (www.spenvis.oma.be).

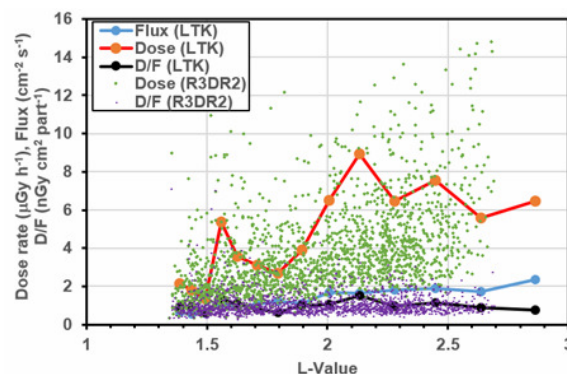


Fig. 4. The L-value profiles of the flux, dose and dose to flux rate, obtained by the “Liulin Ten-Koh Saganti” spectrometer on 17 January 2019.

Fig. 2 shows the external view of the LTK instrument (pls. look the box at the top of the CPD) with the size of 122x40x20 mm and 0.092 kilograms mass. The power consumption is about 17 mA from 12 V DC. After switching on, the LTK spectrometer performs internal test and wait to obtain external command. On a receipt of command, it starts to accumulate in 256 channels the deposited energy spectrum used further to estimate the predominant radiation source and to calculate the dose and the flux of particles in the silicon detector. The exposition time of one spectrum depends on the frequency of issue of the external command to measure and can be between 5 and 2100 sec with 1 sec resolution.

The LTK spectrometer contains: one semiconductor detector - silicon PIN diode of Hamamatsu S2744-08 type with 2 cm² area and 0.3 mm thickness, one low noise hybrid charge-sensitive preamplifier A225F type of AMPTEK Inc., a fast 12 channel ADC, 2 microcontrollers and buffer memory. Pulse high analysis technique is used for measurement of the energy losses in the detector.

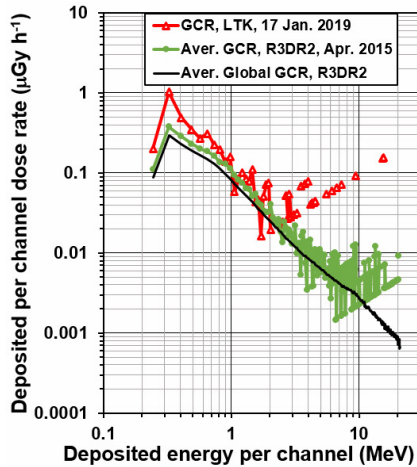


Fig. 5. Comparison of the LTK deposited energy spectrum shape, obtained on 17 January 2019 with averaged spectra, obtained on ISS with R3DR2 instrument.

The semiconductor detector of the LTK instrument is mounted approximately 2 mm below the 0.3 mm thick aluminum cover plate. Furthermore, there is shielding from 0.07 mm copper and 0.2 mm plastic, which provided 0.3 g cm^{-2} of total shielding from the front side. The LTK instrument is additionally shielded by 2 FR-4 (glass epoxy) plates with total thickness of 3.15 mm and by 5.0 mm carbon fiber reinforced polymer (Fajardo et al., 2019, (see Fig. 3b there).

The calculated required kinetic energy of particles arriving perpendicular to the detector is 2.6 MeV for electrons and 62.5 MeV for protons. This means that only electrons and protons with energies exceeding the values listed above can cross the “Liulin Ten-Koh” shielding materials and reach the detector surface. The detector shielding, being larger from the sides and from behind, stops the low energy ORB relativistic electrons, attenuates the lower energy IRB protons, but practically does not change the flux of the primary GCR particles.

Analysis of the first data obtained by “Liulin Ten-Koh Saganti” (flight) instrument

The first command transmission and data downlink with Ten-Koh satellite happen over KIT, Japan on 31 Oct 2018. The first “Liulin Ten-Koh Saganti” spectrum was received on 08 November 2018 at 13:17:00 Japanese Standard Time.

Analysis of the predominant GCR data, obtained on 17 January 2019

Recently, Dachev et al., (2017) confirmed that the best analysis of the radiation sources type could be made from the dose to flux ratio and from deposited energy spectra shape. Very

The main measurement unit in the LTK instrument is the amplitude of the pulse after the preamplifier, generated by particles or quanta, hitting the detector (Dachev et al., 2002). The amplitude of the pulse is proportional by a factor of 240 mV MeV^{-1} to the energy loss in the detector and respectively to the dose. By 12-bit analogue to digital converter (ADC), these amplitudes are digitized and organized in a 256-channel deposited energy spectrum. The dose in the silicon detector D_{Si} [Gy] by definition in System international (SI) is one Joule deposited in 1 kg of matter. The absorbed dose in LTK is calculated by dividing the summarized in 256 channels energy depositions in the spectrum in Joules to the mass of the detector in kilograms.

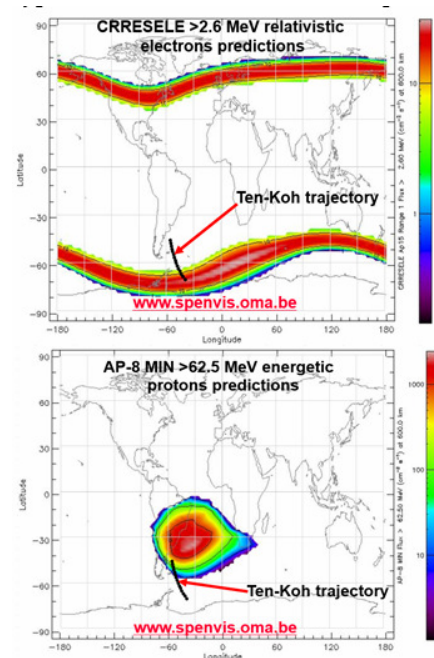


Fig. 6. The Ten-Koh satellite trajectory for 25 December 2019 is plotted over the CRRESELE >2.6 MeV relativistic electrons and AP-8 MIN >62.5 MeV energetic protons at 600 km predicting global maps obtained online from (www.spenvis.oma.be).

briefly, the data can be simply split into two parts by using the dose to flux ratio (D/F) (Heffner, 1971). When the D/F is less than $1.12 \text{ nGy cm}^2 \text{ particle}^{-1}$, the expected predominant type of radiation in the interval of the measurement is ORB electrons. When the D/F is greater than $1.12 \text{ nGy cm}^2 \text{ particle}^{-1}$, the expected type of radiation is IRB or SEP protons (Heffner, 1971, Dachev 2009, Dachev et al., 2012). The GCR source spans the two ranges. The GCR source was identified by the requirements that their dose rates are less than $15 \mu\text{Gy h}^{-1}$. The deposited energy spectra shape depends by the type of radiation and was comprehensively studied by Dachev 2009, Dachev et al., (2012 and 2017).

Further, in the paper we will investigate 3 examples of observations of LTK data with expected predominant GCR, IRB and ORB radiation environment. Because of the very low solar activity, solar energetic protons (SEP) was not observed in the available till now Ten-Koh data

An amount of 14 LTK spectra was received on 17 January 2019. The date, time and geographic coordinates of Ten-Koh satellite normal mode execution is characterized by Mission starting time: 11:15:01 17/01/2019 UTC and mission ending time: 11:21:26 17/01/2019 UTC.

The starting latitude is 33.7149°N , while the starting longitude is 158.3639°W .

The chain of black points in Fig. 3 shows the trajectory of the Ten-Koh satellite on 17 January 2019, plotted over the CRRESELE at 630 km relativistic electrons ($>2.6 \text{ MeV}$) predicting global map, obtained online from (www.spnvis.oma.be). It is seen that the satellite moves in the northern hemisphere out from the predicted ORB maximum and far away from the SAA region in pure GCR environment.

Figure 4 presents the L-value profiles of the GCR flux, dose and dose to flux rate, obtained by the LTK spectrometer on 17 January 2019. It is seen that the flux profile (blue points and line) slowly increase in the range from 0.5 to $2.5 \text{ cm}^{-2} \text{ s}^{-1}$ when the L-value changes from 1.37 to 2.87. The dose profile (red points and line), being in dependence by the deposited in the detector energy, shows relatively small values up to $L=2$ and increase to about $7 \mu\text{Gy h}^{-1}$ in the L-value range above 2.

Geomagnetic shielding, measured by the vertical cutoff rigidity (Smart & Shea, 2005), is the reason for reduced GCR fluxes and dose rates at low L values (Fig. 4) and the slightly rising dose rate toward L values of 2.15. At these increasing L values the vertical cutoff rigidity decreases, and the major amount of the low-energy GCR spectra penetrate down to the Ten-Koh orbit.

The R3DR2 dose rate data (Dachev et al., 2017), obtained in rectangle with coordinates ($180^\circ \div 150^\circ\text{W}$, $33^\circ \div 55^\circ\text{N}$), which include the Ten-Koh trajectory, are plotted with green crosses in Fig. 4. The solar modulation (Potgieter, 2013) of the GCR flux is the reason that the R3DR2 dose rate data are in average ($3.7 \mu\text{Gy h}^{-1}$) smaller than the LTK dose rate data ($4.67 \mu\text{Gy h}^{-1}$). The R3DR2 dose rate data are obtained in 11-20 April 2015 time interval close to the maximum of the 24th solar cycle (<https://www.swpc.noaa.gov/products/solar-cycle-progression>), while the LTK data are obtained in January 2019 in the minimum of the solar cycle.

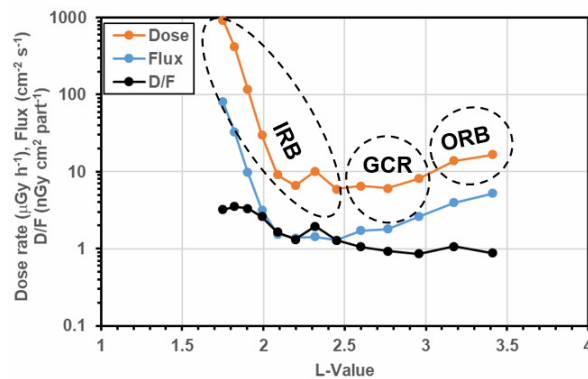


Fig. 7. The L-value profiles of the flux, dose and dose to flux rate, obtained by the LTK spectrometer on 25 December 2018.

The third parameter plotted in Fig. 4 (heavy black points and line for LTK data and magenta crosses for the R3DR2 data) is the dose to flux ratio (D/F). It is seen that in all L range the D/F value for the both instruments is close to $1.12 \text{ nGy cm}^2 \text{ particle}^{-1}$, which verify that the data are obtained in predominant GCR environment.

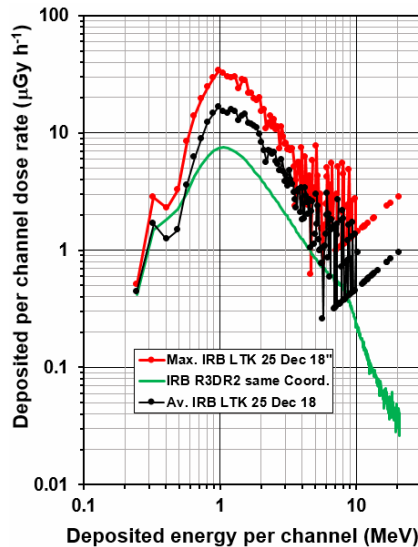


Fig. 8. Comparison of the LTK deposited energy spectrum shape, obtained on 25 December 2018 with averaged IRB spectrum, obtained on ISS with R3DR2 instrument.

R3DR2 instrument April 2015 spectrum (green line and points) and the globally averaged over 3,393,592 R3DR2 measurements in period 24 October 2014-10 January 2016. The shape of this spectrum looks very similar to the R3DR2 spectra and this confirms again that the LTK data are obtained in predominantly GCR environment.

Generally, the Liulin Ten-Koh spectrum is above the R3DR2 spectra because:

- The R3DR2 spectrum represent the global GCR dose rate, which is in average $2.78 \mu\text{Gy h}^{-1}$, while the LTK average spectrum represent relatively high latitude doses with average value of $4.67 \mu\text{Gy h}^{-1}$;
- The higher altitude of the Ten-Koh satellite (~620 km) than ISS (415 km);
- The lower solar activity, which increase the GCR flux in the near Earth radiation environment (Potgieter, 2013).

Analysis of the predominant IRB data, obtained on 25 December 2018

The trajectory of the Ten-Koh satellite on 25 December was very interesting because in its Northern part energetic protons (>62.5 MeV) in the SAA was observed, while the Southern part ORR relativistic electrons (>2.6 MeV) was registered. In the upper and lower frames of Fig. 6 is presented these two cases. As in Fig. 4 the Ten-Koh trajectory is presented with a chain of black points.

Figure 7 presents the L-value profiles of the flux, dose and dose to flux rate, obtained by the LTK spectrometer on 25 December 2018. According to the values of the D/F ratio,

Figure 5 illustrates the different shapes of the deposited energy spectra as obtained by the LTK and R3DR2 instruments. The deposited dose rate is the area between the abscissa and the curve of the deposited energy spectrum.

The LTK average spectrum obtained on 17 January 2019 is presented with red triangles and red line. The shape of this spectrum looks very similar to the R3DR2 spectra up to deposited energy of 2 MeV. Further, the LTK spectrum points, being only single points, depend strongly by the energy depositions in the channel (i.e. channel number) and their values are far above the R3DR2 instrument GCR spectra values.

As explained in previous paragraph, the LTK spectrum are higher than the GCR

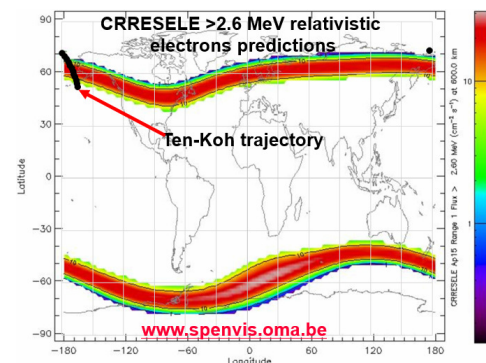


Fig. 9. The Ten-Koh satellite trajectory for 20 December 2018 is plotted over the CRRESELE>2.6 MeV at 630 km relativistic electrons predicting global map, obtained online from (www.spervis.oma.be).

the data are selected in 3 different radiation sources mentioned by labels in the figure. Our major interest is in the first 6 points (from the left) in the dose profile (red points and line) and particularly the first 4 points, where the dose rate is higher than $30 \mu\text{Gy h}^{-1}$ and the D/F ratio is higher than $1.12 \text{ nGy cm}^2 \text{ particle}^{-1}$. These values in L range less than 2 and the picture in the lower frame of Fig. 6 reveal that the predominant radiation source there is energetic protons in the region of the SAA.

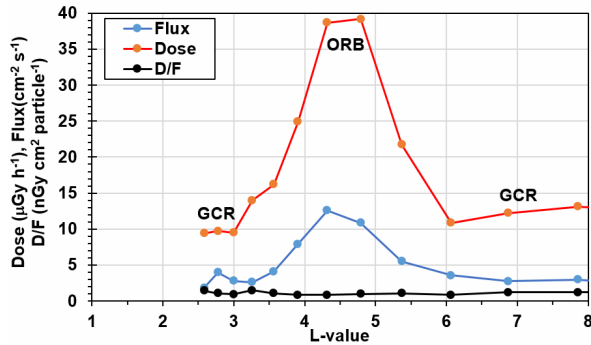


Fig. 10. The L-value profiles of the flux, dose and dose to flux value, obtained by the LTK spectrometer on 20 December 2018.

the detector have energies larger than 300 MeV. More precisely the shapes of the depositing energy spectra in the region of the SAA was studied by Dachev (2009) and by Dachev et al. (2017).

There are 3 different spectra with 3 different depositing energy per channel values in Fig. 8. The highest spectrum presents the data in the first point in Fig. 7 and the dose rate is calculated to be $853 \mu\text{Gy h}^{-1}$. The middle spectrum is obtained, by averaging of all first 3 points in Fig. 7 and the dose rate there is $451 \mu\text{Gy h}^{-1}$. The spectrum from R3DR2 data is the result from averaging of 9,129 spectra obtained between 24 October 2014 and 10 January 2016 in a region with coordinates ($50^\circ \div 60^\circ \text{W}$, $40^\circ \div 50^\circ \text{N}$), which include the Ten-Koh trajectory. The dose rate is $221 \mu\text{Gy h}^{-1}$. Nice coincidence of the shape of the spectra confirm the preliminary expectation that those measurements with the LTK spectrometer was performed in predominant IRB radiation environment.

Analysis of the predominant ORB data, obtained on 20 December 2018

The chain of black points in Fig. 9 shows the trajectory of the Ten-Koh satellite on 20 December 2018, plotted over the CRRESELE at 630 km relativistic electrons ($>2.6 \text{ MeV}$) predicting global map, obtained online from (www.spervis.oma.be). It is seen that the satellite moves in the northern hemisphere crossing first low L GCR source region, next crosses the region of the Northern hemisphere ORB maximum and moves again in the GCR source in the polar cap region.

The L-value profiles of the flux and dose rate in Fig. 10, obtained by the LTK spectrometer on 20 December 2018,

To confirm this, Fig. 8 presents the shapes of the deposited energy spectra as obtained by the LTK on 25 December 2018 and by R3DR2 instrument. The first impression from the deposited energy shapes in Fig. 8 is that they are completely different from these in Fig. 5.

The existence of maximum at higher depositing energies than in Fig. 5 is explained with predominant registration of SAA protons with energies less than 300 MeV (Fajardo et al., 2019, (see Fig. 8b and 8c there), while the GCR protons reaching

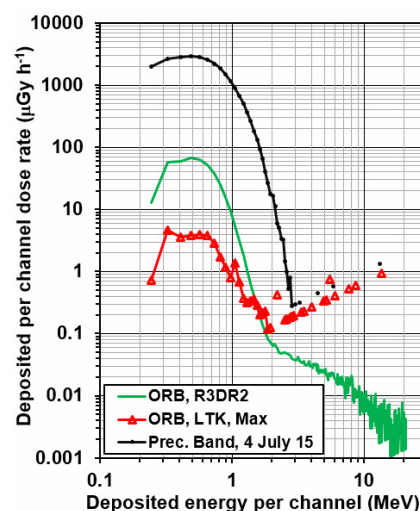


Fig. 11. Comparison of the LTK deposited energy spectrum shape, obtained on 20 December 2018 with averaged ORB spectrum and precipitation band spectrum, obtained on ISS with R3DR2 instrument.

confirm the analysis in the previous paragraph. It is seen that the dose rate and flux profiles first have small values, typical for the GCR region, next with the increase of the L-value, increased to well-formed maxima in the region of the Northern hemisphere ORB maximum and decrease back to low values in the region of the polar cap.

The D/F values in Fig. 5 have values with small exceptions larger than $1.12 \text{ nGy cm}^2 \text{ particle}^{-1}$ for the points mentioned as GCR and fall down below $1.12 \text{ nGy cm}^2 \text{ particle}^{-1}$ for the points mentioned as ORB. This is in agreement with the Heffners (1971) experimental model predictions.

Figure 11 shows 3 deposited energy spectra as obtained by the LTK and R3DR2 instruments. The lowest spectrum with red line and red triangle markers is the LTK for the maximal 2 points in Fig. 10. It is seen that the shape of the LTK spectrum is very similar to other 2 spectra up to 2 MeV.

The green spectrum is obtained by the R3DR2 instrument on ISS in the period 21-30 June 2015, while the black spectrum is the result of averaging of 4 spectra obtained on 4 July 2015 during registration of precipitation band (Dachev et al. 2018).

Conclusions

The paper presents the analysis of the first space radiation data, obtained by Liulin Ten-Koh instrument on the Japanize Ten-Koh satellite. Never the less that the first amount of data from “Liulin Ten-Koh Saganti” spectrometer are relatively limited the comparison with larger amount of R3DR2 data show that they have the expected dose to flux values and shapes of the deposited energy spectral and can be used for the further more comprehensive analysis of the LEO environment at the Ten-Koh satellite.

References

- Badavi, F.F., Validation of the new trapped environment AE9/AP9/SPM at low Earth orbit. *Adv. Space Res.* 54, 917–928, 2014. <http://dx.doi.org/10.1016/j.asr.2014.05.010>.
- Dachev Ts., B. Tomov, Yu. Matviichuk, Pl. Dimitrov, J. Lemaire, Gh. Gregoire, M. Cyamukungu, H. Schmitz, K. Fujitaka, Y. Uchihori, H. Kitamura, G. Reitz, R. Beaujean, V. Petrov, V. Shurshakov, V. Benghin, F. Spurny, Calibration Results Obtained With Liulin-4 Type Dosimeters. *Adv. Space Res.* V 30, No 4, 917-925, 2002. [http://dx.doi.org/10.1016/S0273-1177\(02\)00411-8](http://dx.doi.org/10.1016/S0273-1177(02)00411-8).
- Dachev, Ts. P., B. T. Tomov, Yu.N. Matviichuk, Pl. G. Dimitrov, Vadawale, S. V., J. N. Goswami, V. Girish, G. de Angelis, An overview of RADOM results for Earth and Moon Radiation Environment on Chandrayaan-1 Satellite, *Adv. Space Res.*, 48, 5, 779-791, 2011. <http://dx.doi.org/10.1016/j.asr.2011.05.009>.
- Dachev, T. P., Bankov, N. G., Tomov, B. T., Matviichuk, Y. N., Dimitrov, P. G., Häder, D.-P. & Horneck, G. Overview of the ISS radiation environment observed during the ESA EXPOSE-R2 mission in 2014–2016. *Space Weather*, 15, 1475–1489, 2017. <https://doi.org/10.1002/2016SW001580>.
- Dachev, T.P., J.V. Semkova, B.T. Tomov, Yu.N. Matviichuk, Pl.G. S. Maltchev, R. Koleva, Pl., Dimitrov, N.G. Bankov, V.V., Shurshakov, V.V., Benghin, E.N., Yarmanova, O.A. Ivanova, D.-P. Häder, M.T. Schuster, G. Reitz, G. Horneck, Y. Uchihori, H. Kitamura, O. Ploc, J. Kubancak, I. Nikolaev, Overview of the Liulin type instruments for space radiation measurement and their scientific results, 92–114, 2015. <http://dx.doi.org/10.1016/j.lssr.2015.01.005>.
- Dachev, Ts., G. Horneck, D.-P. Häder, M. Lebert, P. Richter, M. Schuster, R. Demets, Time profile of cosmic radiation exposure during the EXPOSE-E mission: the R3D instrument. *Journal of Astrobiology*, 12, 5, 2012, 403-411. <http://eea.spaceflight.esa.int/attachments/spacestations/ID501800a9c26c2.pdf>.
- Dachev, Ts., G. Horneck, D.-P. Häder, M. Schuster, and M. Lebert, EXPOSE-R cosmic radiation time profile, *Journal of Astrobiology*, 14, 17-25, 2015. <http://dx.doi.org/10.1017/S1473550414000093>.
- Dachev, Ts.P., Characterization of near Earth radiation environment by Liulin type instruments, *Adv. Space Res.*, 44, 1441-1449, 2009. <http://dx.doi.org/10.1016/j.asr.2009.08.007>.
- Dachev, T.P., Relativistic Electron Precipitation Bands in the Outside Radiation Environment of the International Space Station, *Journal of Atmospheric and Solar-Terrestrial Physics*, 177, 247-256, 2018, <https://doi.org/10.1016/j.jastp.2017.11.008>.
- Damasso, M., Dachev Ts., Falzetta G., Giardi M.T., Rea G., Zanini A., The radiation environment observed by Liulin-Photo and R3D-B3 spectrum-dosimeters inside and outside Foton-M3 spacecraft, *Radiation Measurements*, V. 44, NO 3, 263-272, 2009. <http://dx.doi.org/10.1016/j.radmeas.2009.03.007>.

- Fajardo I., A. Lidtke, S.A. Bendoukha, K.-I. Okuyama, D. Faizullin, J. Gonzalez-Llorente, R. Morales, R. Rodríguez, M. Matsuo, N. Urakami, R. Kwauchi, P. Saganti, D. Holland, T. Dachev, S. Tuttle, R. Dudziak, M. Miyazaki, N. Yamagata, K. Hatanaka, F. Abdullah, Challenges, development and operation of a small satellite mission to explore the space environment and its effects on spaceborne platforms, *Acta Astronautica*, 2019. (in print)
- Haffner, J. W., *Yadernoe izluchenie i zashchita v kosmose* (Nuclear Radiation and Protection in Space), pp 115, Atomizdat, Moscow, 1971. (book in Russian)
- Häder, D.P., P. Richter, M. Schuster, Ts. Dachev, B. Tomov, Pl. Georgiev, Yu. Matviichuk, R3D-B2 - Measurement of ionizing and solar radiation in open space in the BIOPAN 5 facility outside the FOTON M2 satellite, *Adv. Space Res.* Volume 43, Issue 8, Pages 1200-1211, 2009. <http://dx.doi.org/10.1016/j.asr.2009.01.021>.
- Nealy, J. E., F. A. Cucinotta, J. W. Wilson, F. F. Badavi, N. Zapp, T. Dachev, B.T. Tomov, E. Semones, S. A. Walker, G. de Angelis, S. R. Blattnig, W. Atwell, Pre-engineering spaceflight validation of environmental models and the 2005 HZETRN simulation code, *Adv. Space Res.*, 40, 11, 1593-1610, 2007. <http://dx.doi.org/10.1016/j.asr.2006.12.030>.
- Okuyama, K.-I., Ten-Koh Development Team, P. Saganti, D. Holland, T. Dachev, R. Dudziak, and S. Tuttle, Observation of Ionospheric Disturbance Near the End of the 24th Solar Cycle Period and Space Deterioration Situation of Advanced Materials Using the Micro-Sat Ten-Koh, 32nd International Symposium on Space Technology and Science, ISTS Japan, June 2019.
- Potgieter, M. S. (2013). Solar modulation of cosmic rays. *Living Reviews in Solar Physics*, 10, 3.
- Slaba, T.C., S.R. Blattnig, F.F. Badavi, N.N. Stoffle, R.D. Rutledge, K.T. Lee, E.N. Zappe, T.P. Dachev and B.T. Tomov, Statistical Validation of HZETRN as a Function of Vertical Cutoff Rigidity using ISS Measurements, *Adv. Space Res.*, 47, 600-610, 2011. <http://dx.doi.org/10.1016/j.asr.2010.10.021>
- Smart, D. F., & Shea, M. A. (2005). A review of geomagnetic cutoff rigidities for Earth-orbiting spacecraft. *Advances in Space Research*, 36, 2012–2020.
- Wilson, J. W., J. E. Nealy, T. Dachev, B.T. Tomov, F. A. Cucinotta, F. F. Badavi, G. de Angelis, N. Leutke, W. Atwell, Time serial analysis of the induced LEO environment within the ISS 6A, *Adv. Space Res.*, 40, 11, 1562-1570, 2007. <http://dx.doi.org/10.1016/j.asr.2006.12.030>.

Parameters of Thermal and Non-thermal X-ray and Gamma Ray Emission of Solar Flares, Observed onboard CORONAS-F

Bogomolov A.V.¹, Myagkova I.N.¹, Miteva R.², Danov D.², Kashapova L.K.²

¹ Skobeltsyn Institute of Nuclear Physics, Moscow State University, Russia

² Space Research and Technology Institute, Bulgarian Academy of Sciences, Bulgaria

³ Institute of Solar-Terrestrial Physics SB RAS, Irkutsk, Russia

E-mail: aabboogg@sinp.msu.ru

Abstract.

Based on data from the SPR-N and SONG multi-channel hard electromagnetic radiation detectors onboard the CORONAS-F space observatory and the X-ray monitors onboard GOES satellites, we have distinguished the thermal and non-thermal components in the X-ray spectrum of a number of powerful flares of 23rd solar activity cycle. Temporal, spectral and energetic parameters of the flares were analyzed using the catalogs of Solar Energetic Particles and Related Phenomena (<http://newserver.stil.bas.bg/SEPcatalog/>).

Introduction

In the comparative analysis of flares with similar characteristics, but with different geoeffectiveness, it was shown that it may be important to take into account the conditions for the release of particles from the flare area (magnetic field topology) [Bogomolov et al., 2018]. The same conditions can affect how much of the energy of the accelerated electrons will be used to heat the solar plasma, and which will leave the flare region along with the accelerated particles.

The experiment

The CORONAS-F observatory was launched on July 31, 2001 into a quasi-circular orbit with an inclination of 82.5°, orbital period of 94.5 min. and an altitude of 507±21 km (by the end of the flight, its orbit dropped to ~ 300 km). The spacecraft ceased to exist on December 6, 2005. The main tasks of the CORONAS-F mission are to study non-stationary processes on the Sun and their effects on the interplanetary medium and the Earth's magnetosphere.

In this work, we used the data of two devices installed on the CORONAS-F. One of them is SPR-N elaborated for studying X-ray radiation from solar flares in the range of 15-100 keV and measuring its linear polarization. In this work, only the SPR-N patrol detector was used. This is a scintillation detector based on CsI (Na) with a diameter of 1.5 cm and a thickness of 0.3 cm, above which is a cylindrical collimator providing a rather narrow field of view of the detector - within 5x5 degrees. To protect against X-rays coming from the spacecraft, lead glass 0.5 cm thick is placed under the CsI (Na) crystal. During the whole experiment with the SPR-N instrument, which began on August 15, 2001, the instrument operated in the monitor mode of continuous measurements. The output parameters of the SPR-N patrol detector are the counting rates in channels 15–40 and 40–100 keV, as well as the counting rate of the anti-coincidence shield from plastic scintillator. The time resolution for the patrol detector of the device was determined by the exposure time, which, as a rule, was equal to 4 seconds.

To obtain the parameters of the bremsstrahlung radiation from solar flares, we used data from the SONG instrument, designed to measure hard X-rays, gamma rays in lines and continuum, as well as neutron and relativistic electron fluxes. Particles are registered in SONG by scintillation detector based on a CsI(Tl) crystal with a diameter of 200 mm and a height of 100 mm, surrounded by an active anti-coincidence shield from a plastic scintillator used for protection against charged particles, as well as for the detection of relativistic electrons. The time resolution of SONG during the experiment ranged from 1 to 4 seconds.

The wide energy range from 30 keV to 200 MeV was divided into 12 channels, the first five of which at the beginning of the experiment had values: 0.03–0.06, 0.06–0.15, 0.15–0.5, 0.5–1.5 and 1.5–4 MeV. During the flight, the threshold values slowly increased, by the end of 2005 the difference was about 1.5 times. A more detailed description of the experiments with SPR-N and SONG can be found in earlier works [Bogomolov et al. 2003, Bogomolov and Myagkova 2017, Kuznetsov et al. 2006, Zhitnik et al. 2006].

Table 1 List of solar flares observed by the SPR-N instrument which can be used to separate the thermal and non-thermal components of X-ray radiation.

DATE	GOES Tbeg-Tmax-Tend	class	Lat	Lon	Backgr	E _{max} SONG	SEP
25.08.2001	16:23 16:45 17:04	X5,3	-17	-34	bCbe	60-100	-
05.09.2001	14:25 14:32 14:34	M6,0	15	31	E	1.3 - 4	-
11.12.2001	7:58 8:08 8:14	X2,8	16	-41	Cbe	7- 15	SEP
20.05.2002	15:21 15:27 15:31	X2,1	-21	-65	Eb	7.7-16.5	SEP
17.07.2002	6:58 7:13 7:19	M8,5	21	17	E	1.6-4.8	-
18.07.2002	3:22 3:37 3:40	M2,2	20	27	E	0.6-1.6	-
20.08.2002	8:22 8:26 8:30	M3,4	-10	38	E	4.8-8.4	SEP
21.08.2002	1:35 1:41 1:45	M1,4	-11	47	E	0.6-1.6	-
21.08.2002	5:28 5:34 5:36	X1,0	-12	51	E	4.8-8.4	-
24.08.2002	0:49 1:12 1:31	X3,1	-2	81	Ebc	4.8-8.4	SEP
30.08.2002	12:47 13:29 13:35	X1,5	15	-74	E	4.8-8.4	-
10.09.2002	14:49 14:56 15:00	M2,9	-10	-43	E	0.6-1.6	-
17.03.2003	18:50 19:05 19:16	X1,5	-14	39	Cbe	5.2-9.1	SEP
09.04.2003	23:23 23:29 23:34	M2,5	-10	78	Eb	0.6-1.6	-
26.04.2003	3:01 3:06 3:12	M2,1	20	69	Eb	1.7-5.2	-
26.04.2003	8:01 8:07 8:09	M7,0	n/d	n/d	Cb	5.2-9.1	-
27.05.2003	22:56 23:07 23:13	X1,3	-7	17	E	5.2-9.1	-
28.05.2003	0:17 0:27 0:39	X3,6	-7	17	bE	5.2-9.1	SEP
29.05.2003	0:51 1:05 1:12	X1,2	-6	37	bCb	5.2-9.1	SEP
23.10.2003	8:19 8:35 8:49	X5,4	-21	-88	bCbe	5.2-9.1	-
24.10.2003	2:27 2:54 3:14	M7,6	-19	-72	Ebc	0.65-1.7	-
28.10.2003	9:51 11:10 11:24	XX17,2	-16	-8	ebCbe	80-130	SEP
29.10.2003	20:37 20:49 21:01	XX10,0	-15	2	bEb	5.2-9.1	SEP
04.11.2003	19:29 19:50 20:06	XX28,0	-19	83	bCbe	130-260	SEP
17.11.2003	8:55 9:05 9:19	M4,2	-1	-33	E	1.7-5.2	-
06.01.2004	6:13 6:29 6:36	M5,8	5	-90	E	1.7-5.2	-
11.04.2004	3:54 4:19 4:35	C9.6	-16	46	E	0.22-0.73	SEP
01.01.2005	0:01 0:31 0:39	X1,7	6	-34	E	2- 6	SEP
20.01.2005	6:36 7:01 7:26	X7,1	14	61	Ebc	90-150	SEP

Data

During the experiment (August, 2001 – end of 2005) we obtained the following data. The X-ray emission with $E > 15$ keV was observed by SPR-N in 159 solar flares. List of the flares observed by SONG includes 105 flares with HXR-emission > 50 keV. 38 of them were observed in the energy channel > 500 keV. In 4 flares gamma-emission with $E > 100$ MeV was detected. Catalog of the flares observed in the experiment with SONG can be found in http://swx.sinp.msu.ru/apps/solar_flares_cat/. For problems of separation of thermal and non-thermal radiation, data of simultaneous measurements with the SPR-N instrument (containing both components of radiation) and SONG (bremsstrahlung, at least three channels) are required. The list of suitable flares is presented in Table 1.

First seven columns of the table are well-known data from the solar event lists: date of the flare, times (start, maximum and end) of soft X-ray emission, observed by GOES, the flare

class (GOES, https://satdat.ngdc.noaa.gov/sem/goes/data/new_full/) and the solar coordinates of the active region. The next column, named ‘backgr’, shows the background conditions at the time of the flare. CORONAS-F operated on the near-Earth polar orbit, thus besides equatorial regions it crossed polar caps and Earth’s radiation belts (ERB). The conditions are shown as the sequence of the letters: e (equator), c (polar cap) and b (ERB). The capital letter indicates the moment of maximum X-ray flux. For example, a sequence ‘bCbE’ means that a flare begins when the satellite was in a ERB, the maximum of flare radiation corresponds to a polar cap, then the satellite again crosses ERB, and the end of the flare is on the equator.

For some time the satellite was in the shadow of the Earth. Flares, for which the Sun was screened by the Earth at the moment of maximum radiation, were not selected for analysis. Three flares, in which during some time (not at the moment of maximum) the satellite was in the Earth’s shadow, are marked with a gray background in the ‘backgr’ cell.

The next column, labeled ‘Emax SONG’, shows the maximum energy channel in which the SONG detected gamma radiation at a level that is significant for this work, i.e. with the ability to include this channel for obtaining the spectral index, as well as for observing the dynamics of gamma radiation during the flare.

The last column (‘SEP’) indicates in which flares presented in the SOHO/ERNE proton event catalog (<http://newserver.stil.bas.bg/SEPcatalog/>) there was a significant flux of protons with energies 17–22 MeV. See the description of the catalog in the paper of Myagkova et al., [2019, this issue].

Results

a) Method

We take into account two components of hard X-ray emission:

- 1) Thermal emission from an optically thin plasma, $I(E, kT) = J_{0th} \exp(-E/kT) / E$
- 2) A power-law bremsstrahlung spectrum, $I(E, \gamma) = J_{0th} E^{-\gamma}$

Other components (gamma ray lines, π^0 -decay etc.) do not yield to the hard X-ray and soft gamma-ray emission.

In the SPR-N channel 40–100 keV only bremsstrahlung component presents. In the SPR-N channel 15–40 keV both thermal and non-thermal components are present. The spectral index in the channel 15–40 keV is the same as in the channel 40–100 keV.

The parameter of thermal radiation kT can be estimated from the ratio of values of the GOES channels 1–8 Å and 0.5–4 Å. At the same time, the contribution of thermal radiation to the SPR-N counting rate in a channel 15–40 keV cannot be estimated accurately only by GOES data. The reason is that the spectrum of thermal radiation in the energy range >15 keV is strongly incident and the error in the energy threshold values even per fraction of keV leads to a difference in counting rates by several times.

We used a different approach. First, an estimate of the bremsstrahlung index γ was made using SONG channels in which the contribution of gamma lines looks insignificant. Thermal radiation in SONG is absent. Then, knowing the γ , we determined the constant J_{0th} from the condition that in the SPR-N channel 40–100 keV the count rates were equal to the observed ones. After this we extrapolate the obtained power-law spectrum to the SPR-N channel 15–40 keV and calculated the expected count rates in it caused only by the bremsstrahlung emission. The remaining part of the count rates ($I(\text{total}) - I(\text{bremsstrahlung})$) is due to thermal component. Finally, we calculate the thermal radiation constant J_{0th} using kT , determined according to the GOES, and the condition that the SPR-N count rates in the 15–40 keV channel expected from the thermal part of the spectrum must be equal to the observed ones. As an example, Fig. 1 shows the results of the calculations described above for the flare 29.10.2003 of class X10.

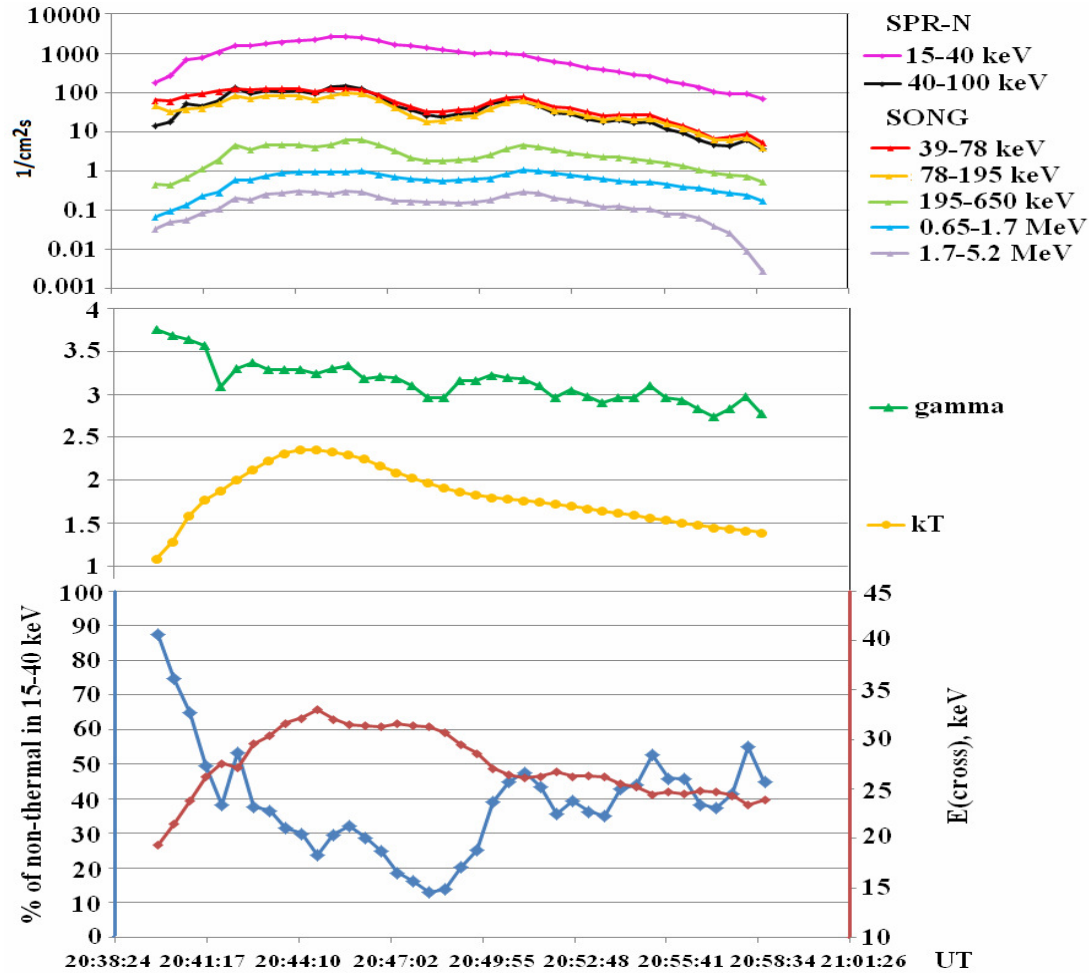


Fig. 1 The SPR-N and SONG count rates, bremsstrahlung spectral index, kT , part(%) of non-thermal emission in the SPR-N channel 15-40 keV and energy $E(\text{cross})$ at which thermal and non-thermal radiation fluxes become equal, obtained for the solar flare X10.0 29.10.2003.

b) Statistical analysis

To search for a possible connection between the characteristics of thermal and non-thermal components of X-ray radiation with SEP and solar wind, we chose the following parameters for the correlation analysis:

- Gamma – Power index of bremsstrahlung (non-thermal radiation);
- kT of thermal emission;
- $E(\text{cross})$ – energy at which thermal and non-thermal radiation fluxes become equal;
- Part (%) of non-thermal radiation, in the beginning, middle and end of a flare;
- GOES class, i.e. flux in soft X-rays 1–8 Å [W/m^2];
- J_p – Peak proton intensity [$\text{protons}/(\text{cm}^2 \cdot \text{s} \cdot \text{sr} \cdot \text{MeV})$] – from SOHO/ERNE catalog;
- J_e – electron fluxes in three bands: 53–103, 103–175 and 175–315 keV (ACE/EPAM);
- CME – linear speed [km/s].

The obtained matrix of the Pearson's correlation coefficients is presented in Table 2. Note that the correlation coefficient R only shows the strength of the linear relationship. In many cases, the relationship may be non-linear. For example, the dependence of energy $E(\text{cross})$ to the flare class in soft X-rays, shown in Fig. 2, is well approximated by a logarithmic line with the coefficient of determination $R^2 > 0.8$.

Table 2. Correlation matrix between the parameters of the flare X-ray emission, proton and electron fluxes and CME speed.

	Jp 17-22 MeV	Je 53-103 keV	Je 103-175 keV	Je 175-315 keV	V(CME)
GOES class	0,59	0,36	0,38	0,37	0,79
Gamma	-0,47	-0,27	-0,31	-0,44	-0,53
kT	0,61	0,40	0,41	0,34	0,65
Ecross	0,55	0,35	0,35	0,28	0,56
Part_start	-0,50	-0,11	-0,14	-0,11	-0,61
Part_mid	-0,68	-0,33	-0,32	-0,23	-0,51
Part_end	-0,37	-0,16	-0,16	-0,20	0,38

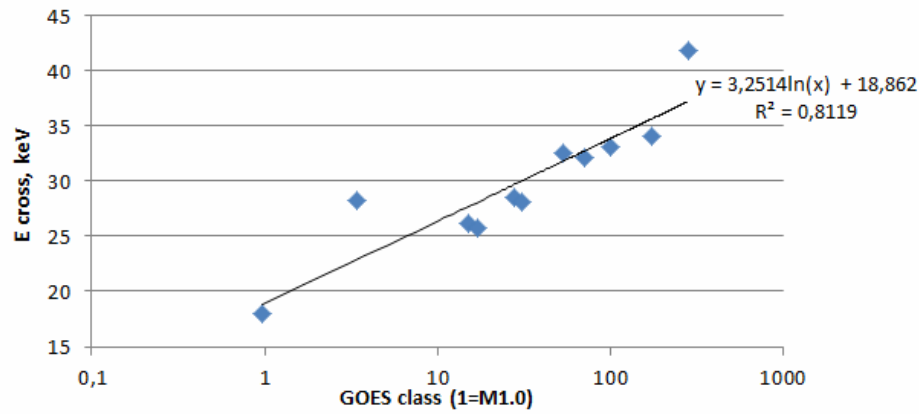


Fig. 2 The relationship of energy at which the thermal and non-thermal components of flare X-rays are equal, and the flare class in soft X-rays.

Discussion

The small statistics of solar flares used in this work allows only to note some general patterns. One of them is the absence of a significant correlation of electron fluxes with all used X-ray and gamma-ray emission parameters. Another statement is the lack of correlation of the spectral index of gamma radiation with particle fluxes.

In the future, it is planned to analyze how the energy of the accelerated electrons and the thermal energy of the flare region change during the flare. All flares from Table 1 are suitable for this analysis, if it is possible to estimate the volume of the flare area and to assume the fraction f of this volume filled with the emitting plasma (filling factor). In Kurt V.G. et al. [2010] these calculations are presented for one of the most powerful flares observed at CORONAS-F on January 20, 2005 (class X7.1). The calculations were carried out using the formulas from Saint-Hilaire P. and Benz A.O. [2005] assuming the passage of electrons through a dense but optically thin plasma. Some of the main results are shown in Fig. 3.

Except for the very beginning of the flare preceding the impulsive phase, the energy deposited by the electrons prevails over the thermal one and is sufficient for plasma heating in the first acceleration pulse in the time interval 06:44–06:46 UT. The kinetic energy of the electrons is close to the thermal one for a filling factor $f=0.4–0.6$ in the remaining time. Thus, it means that in the event 20.01.2005 the electrons accelerated in the pulsed stage of the flare brought enough energy to provide the main heating of the plasma.

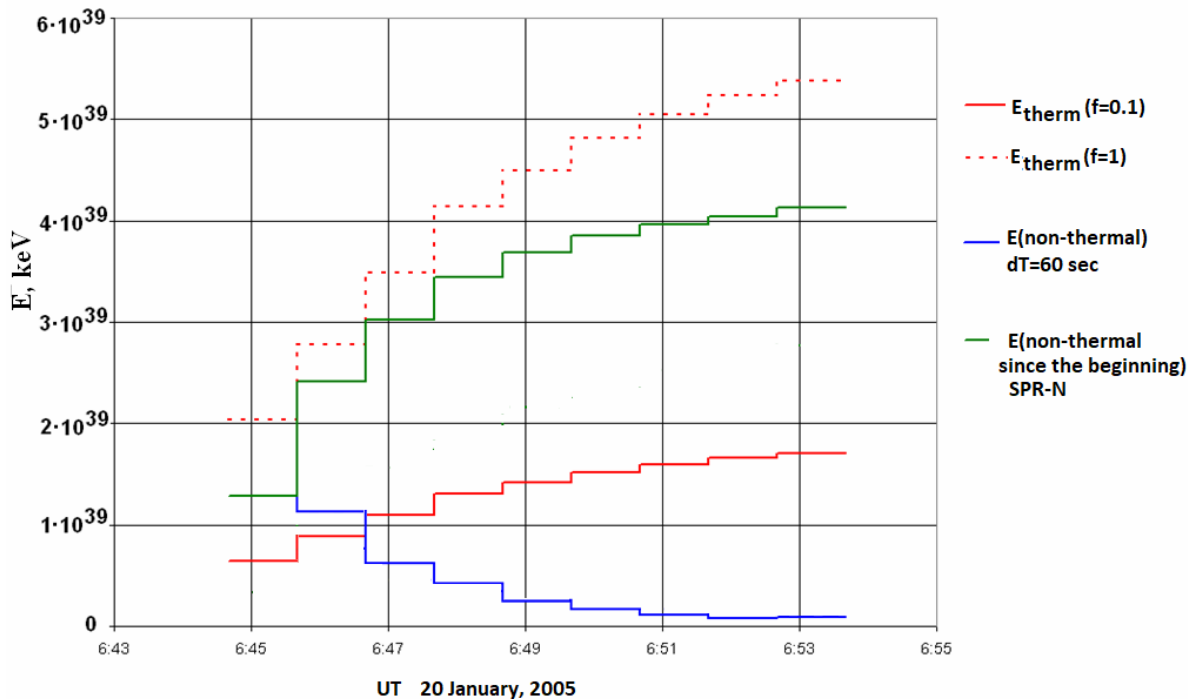


Fig. 3 Energetic parameters of the flare X7.1 20.01.2005 according to Kurt V.G. et al. [2010].

Acknowledgment

This study is supported by the project “The origin on solar energetic particles: solar flares vs. coronal mass ejections”, co-funded by the Russian Foundation for Basic Research with project No. 17-52-18050 and the National Science Fund of Bulgaria under contract No. DNTS/Russia 01/6 (23-Jun-2017).

References

- Bogomolov A.V., Denisov Yu. I., Logachev Yu. I. et al. (2003). Time, spectral and polarization characteristics of hard X-radiation of solar flares observed during the SPR-N experiment onboard the orbital observatory CORONAS-F. *Bulletin of the Russian Academy of Sciences: Physics*, 67, no. 10, 1422-1426.
- Bogomolov, A.V., Myagkova, I.N. (2017). Results of hard X-ray and gamma-ray observations onboard CORONAS-F in the frames of Russian-Bulgarian project “The origin of solar energetic particles: Solar flares vs. coronal mass ejections” *Proceedings of 13th International scientific conference “Space, Ecology, Safety”* (2–4 November 2017, Sofia, Bulgaria), 34-40.
- Bogomolov, A. V., Myagkova, I. N., Myshyakov, I., et al. (2018). Comparative analysis of the proton generation efficiency during 17 March 2003 and 11 April 2004 solar flares. *Journal of Atmospheric and Solar-Terrestrial Physics*, 179, 517-526
- Kurt V.G., Svertilov S.I., Yushkov B.Yu., et al. (2010). Dynamics and energetics of the thermal and nonthermal components in the solar flare of January 20, 2005, based on data from hard electromagnetic radiation detectors onboard the CORONAS-F satellite. *Astronomy Letters*, 36, no. 4, 280–291.
- Kuznetsov S.N., Kurt V.G., Myagkova I.N., et al. (2006). Gamma-Ray Emission and Neutrons from Solar Flares Recorded by the SONG Instrument in 2001–2004. *Solar System Res.*, 40, no. 2, 104-110.
- Myagkova, I. N., Miteva, R., Danov, D., Kashapova, L., Bogomolov, A. V. (2019) Features of solar energetic particles during the 23rd cycle of solar activity and their relationship with solar X-ray, gamma0emiaaion and coronal mass ejections, *Proceedings of the WS-11 workshop, held in Primorsko, Bulgaria* (this issue).
- Saint-Hilaire P. and Benz A.O. (2005). Thermal and non-thermal energies of solar flares. *Astron. Astrophys.* 435, no. 2, 743-752.
- Zhitnik I.A., Logachev Yu. I., Bogomolov A.V., et al. (2006). Polarization, Temporal, and Spectral Parameters of Solar Flare Hard X-rays as Measured by the SPR-N Instrument Onboard the CORONAS-F Satellite // *Solar System Res.* 40, no. 2. 93-103.

Study on the Features of the SEP Solar Origin Based on Microwave Observations

Kashapova L.K.¹, Meshalkina N.S.¹, Miteva R.², Zhukova A.V.³, Myagkova I.N.⁴

¹ Institute of Solar-Terrestrial Physics SB RAS, Irkutsk, Russia

² Space Research and Technology Institute, Bulgarian Academy of Sciences, Sofia, Bulgaria

³ Crimean Astrophysical Observatory RAS, Nauchny, Russia

⁴ Skobelitsyn Institute of Nuclear Physics, MSU, Moscow, Russia

E-mail: lkk@iszf.irk.ru

Abstract.

We present the results on the analysis of microwave (MW) emission in solar flares related to strong solar energetic particle (SEP) events observed during the 23rd solar cycle. The parameters of the MW spectrum were used as indicators of acceleration processes during solar flares. The magnetic topology of the active regions (ARs) that produced the flares were taken into account by the approach suggested by Abramenko et al. [2018]. We found that during their evolution most of the ARs related to proton-rich SEP events violated at least one of the classical sunspot group evolution laws (Hale's law, Joy's law et cetera). However, the statistical study of all ARs of the cycle revealed the domination of normal ARs. The dependences between SEP events and MW indicators of the acceleration process for different groups are studied and discussed.

Introduction

The nature of the solar sources of solar energetic particle (SEP) events has not been fully understood nowadays (see, *Klein and Dalla, 2017*). There is no definitive answer to a very important question – are the charged particles accelerated during flares in the solar atmosphere or on shock waves generated by coronal mass ejections (CME)? Or do both of these mechanisms contribute to acceleration in different ratio? Why some active regions (ARs) are sources of a large number of solar geoeffective events, while others are not? The X-ray and gamma-ray emissions are direct indicators of acceleration processes in the solar atmosphere. But since the sensitivity threshold of modern detectors in these spectral ranges is not sufficient for detecting weak fluxes, information about many events is lost. The alternative to direct observations is the observation of microwave (MW) emission that is more sensitive to mechanisms of emission generated by accelerated electrons. However, applying of this type of observation as indicators of the processes of energy release and acceleration of particles in solar flares faces some problems. The first problem is that MW emission is generated by electrons only while the majority of SEP observations deals with protons. However, *Chertok et al. [2009]* showed the close correlation of the SEP proton fluxes and properties of MW emission. The other problem is that the MW flux distribution with frequency could be influenced simultaneously by several physical parameters. For example, the same flux value at the maximum of the spectrum can result from both the magnetic field value at the source and the density of accelerated electron flux. Thus the statistical analysis could get scattering resulted from non-uniform physical/morphological properties of solar sources.

Also, it is difficult to take into account the magnetic morphology of the emission source both as the magnetic topology of the AR. *Abramenko et al. [2018]* analyzed the violating of the classical sunspot group evolution laws for ARs of the 24th solar cycle. The study was done based on line-of-sight magnetograms provided by HMI/SDO and revealed three groups of ARs. The first group (A) consisted of regular ARs followed all the mean-field dynamo laws. They are about half of all analyzed ARs. The second group (B) was formed from the irregular ARs, violating either Hale polarity law or Joy's law or having the leading spot less

than the main following spot. It turned out that they are about 25 %. The last group consists of unipolar ARs. These results give us some indicator of the AR's magnetic structure. The current study aims are to check the relation of the different groups with solar sources of proton-rich SEP events and to carry out the statistical analysis of MW emission parameters characterizing the acceleration processes.

Data and analysis

The SEP events with significant proton fluxes and solar flare related to these events were chosen using the catalogue of proton events by *Papaioannou et al.* [2016]. We also need to select events with signatures of non-thermal X-ray emission in order to check the properties of the acceleration processes. Thus, the period of selection should be limited by the observation of one instrument observing in this spectral region. We used data by CORONAS/SONG spacecraft for the period 2001–2005 [Kuznetsov et al., 2014]. This instrument obtained 1D and spectral observations but with high sensitivity to weak fluxes in non-thermal X-ray range. We selected the flares with pronounced response in spectral range above 25 keV. These events should also be simultaneously observed by RHESSI for confirmation of the localization. After the cross-check of the lists, we were left with 24 solar flares that satisfied the selected properties.

The catalogue presents SEP event fluxes of protons with energies above 10 MeV, 30 MeV, 60 MeV and 100 MeV. To increase the statistics, we used the information on the ratio of the maxima of the flux of particles with energies above 10 MeV and 30 MeV. The lower value means a higher amount of more energetic protons.

The selected events should also have a response in the MW range. The parameters of the MW spectra were analyzed based on observations of the Radio Telescope Network (RSTN). RSTN [Guidice et al. 1981] obtains radio data with a time resolution of 1 s at eight selected frequencies and provides quasi-continuous data coverage over the day. If possible, the Nobeyama radio polarimeters data [Torii et al., 1979; Nakajima et al., 1985] were used for improving the spectral resolution of MW spectra. We used the values of the peak frequency and the electron spectral index as indicators of acceleration processes. The peak frequency is the frequency at which the flux value reaches a maximum. The electron spectral index δ was calculated by the formula $\delta = 1.1 * (\alpha - 1.2)$ [Dulk, 1985], where α is the MW photon spectral index estimated as the slope of the spectrum at frequencies above the peak frequency.

To study the peculiarities of the AR we used the line-of-sight magnetograms and white-light observations by SOHO/MDI [Scherrer et al., 1995] and EUV observations by SOHO/EIT [Moses et al., 1997]. The considered events took place in 22 ARs during the 23rd cycle and had various topology of the magnetic field. We used criteria which allow us to take into account the peculiarities of the AR's evolution based on the magnetic-morphological classification of ARs. The classification relates to the agreement of bipolar ARs to the basic laws of the mean-field dynamo theory: the polarity law (Hale's law), the law of the tilt latitudinal dependence (Joy's law) and the rule about the ratio of magnetic fluxes/areas of leading and following sunspots. The criteria distribute the ARs into the same groups as it was in Abramenko et al. [2018].

We carried out, both, analysis of all ARs of the 23rd solar cycle and of the selected ARs. The results are presented as diagrams in Fig. 1. One can see that the distribution between the different groups (A, B and U) is the same as it was during the 24th solar cycle [Abramenko et al., 2018]. However, most of ARs that were related to SEP events occurred among the ARs violating at least one law (group B). The physical reason for such distribution could be that ARs violating the classic laws should have more complicated magnetic topology. This feature is well known as a factor promoting flare and CMEs productivity of ARs and SEP events as well.

To compare the indicators of acceleration in solar flares according to the MW emission with the ratio of SEP proton fluxes, we divided the events in two groups, A+U and B. The events of the first group occurred in regular ARs, which followed all laws or are unipolar (as rule the remains of leading spots of regular ARs). The magnetic structure in their ARs should be close to classical bipolar or unipolar. The other group consisted of events which turned out in ARs-"violators". Figure 2 presents the plots of the ratio of the maximum of proton flux above 10 MeV to the maximum of proton flux above 30 MeV relative to the peak frequency in GHz of the MW spectrum of the related flare. We can see that events related to ARs from groups A and U show some trend of this ratio to the peak frequency. The SEP events with more energetic protons correspond to the higher value of the peak frequency. The higher peak frequency could be a result of the higher magnetic field in the emitting source or larger fluxes of accelerated electrons. Anyway, this fact confirms the close relationship between acceleration processes in the solar atmosphere during flares and proton abundance of SEP events. But the plot for group B does not show a strong correlation.

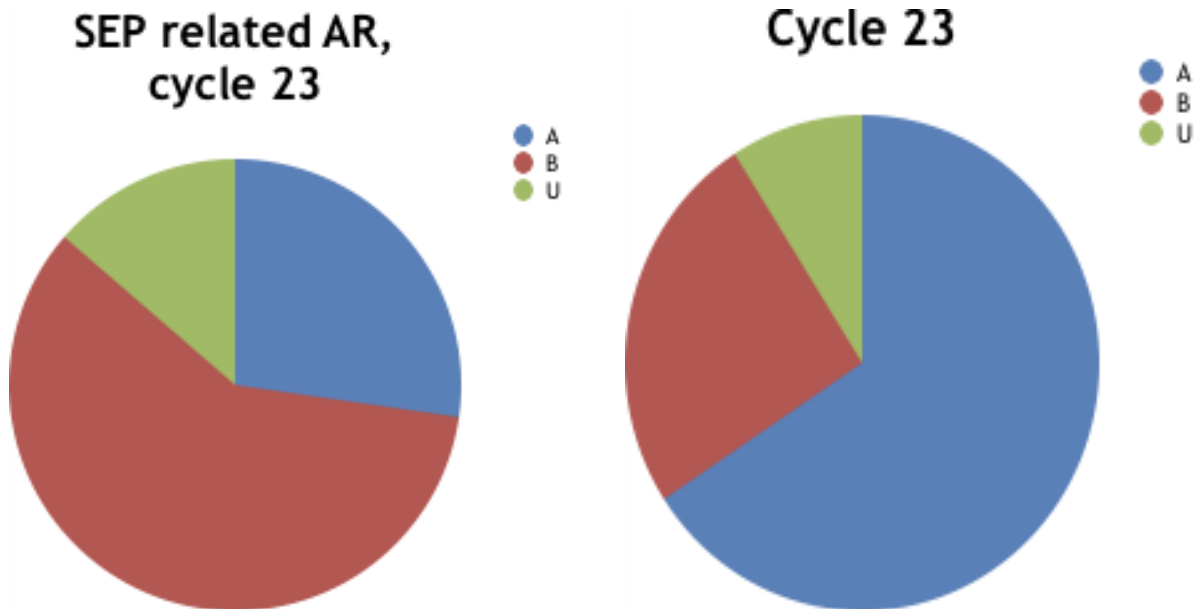


Fig. 1 The diagrams show the ratio of regular active regions (A), the active region violating at least one of the laws (B) and unipolar active regions (U). The left panel shows the ratio for all groups of the 23rd solar cycle. The right panel shows the ratio for active regions related with SEP events with proton fluxes.

The comparison of proton flux ratio in SEP events relative to the electron spectral index is shown in Figure 3. One can see that events related to ARs from group A and U demonstrate some correlation or tendency while the SEP events related to ARs from group B did not. We note that the tendency seen on the left panel of Fig. 2 is in good agreement with results obtained by *Daibog et al.* [1993]. The authors explained the relation of more proton-rich events to solar flares with the soft spectral index by the better possibility of the particle to escape from the higher loops where spectral index should be softer.

We also compared the photon flux ratio in SEP events and CME speed for the same groups (see, Fig. 4). Most of the CME speeds associated with the events of group A and U had the speed of about 1500 km/s and did not show a dependence with the ratio. The behavior of the events related to group B looked complicated and should be studied more carefully.

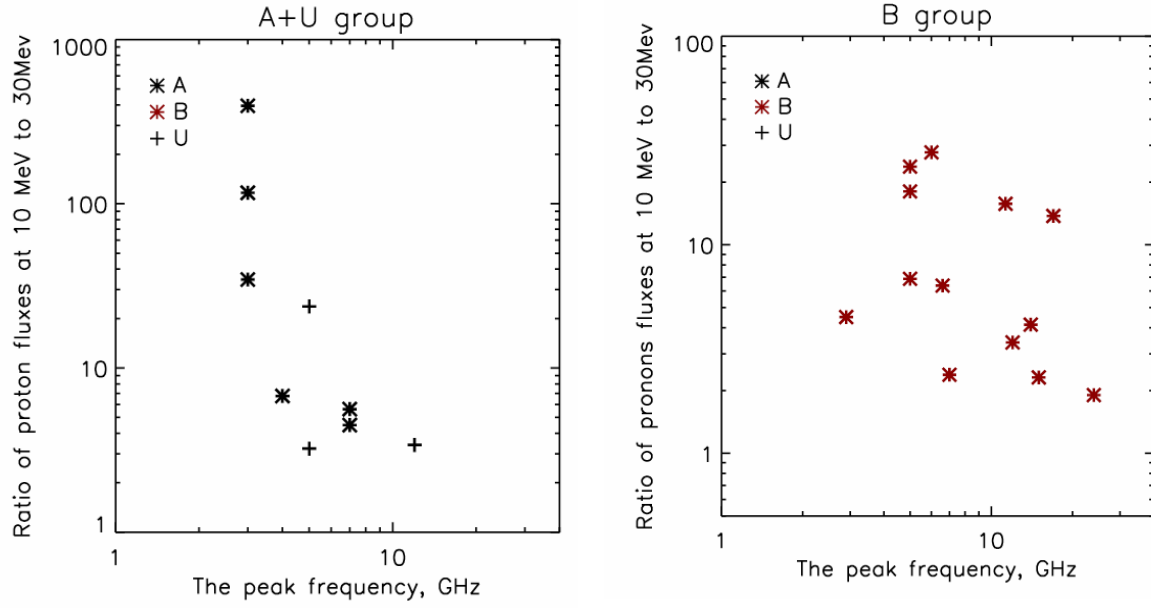


Fig. 2 The ratio of the fluxes at the maximum for protons with energies above 10 MeV to the fluxes of protons with energies above 30 MeV relative to the peak frequency for groups A and U (right panel) and group B (left panel), respectively.

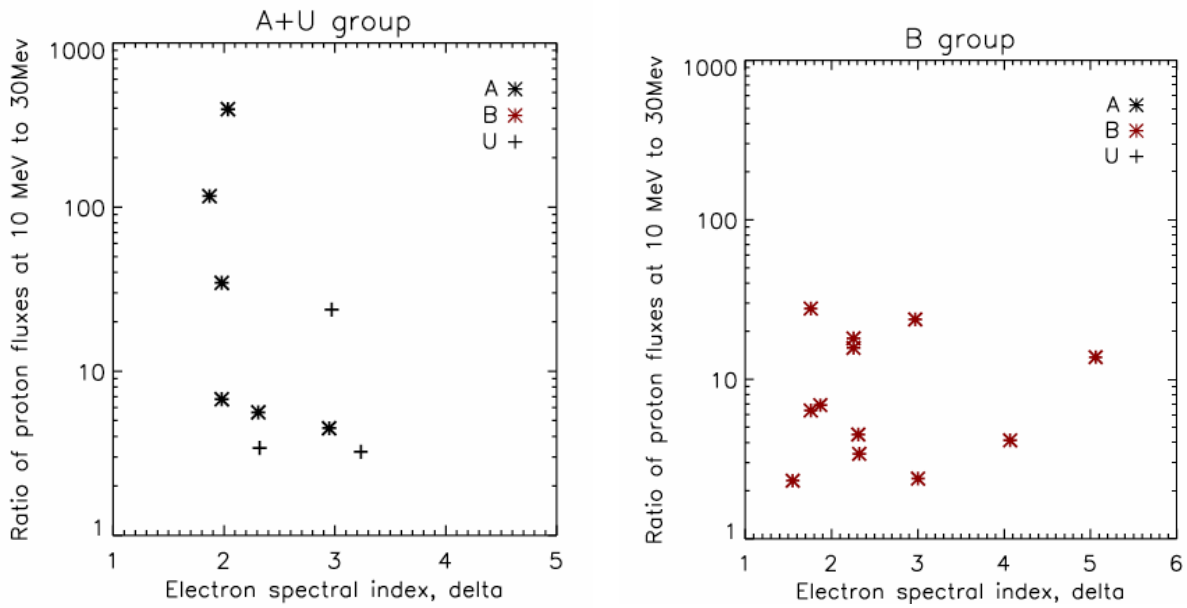


Fig. 3 The ratio of the fluxes at the maximum for protons with energies above 10 MeV to the fluxes of protons with energies above 30 MeV relative to the electronic spectral index for groups A and U (right panel) and group B (left panel), respectively.

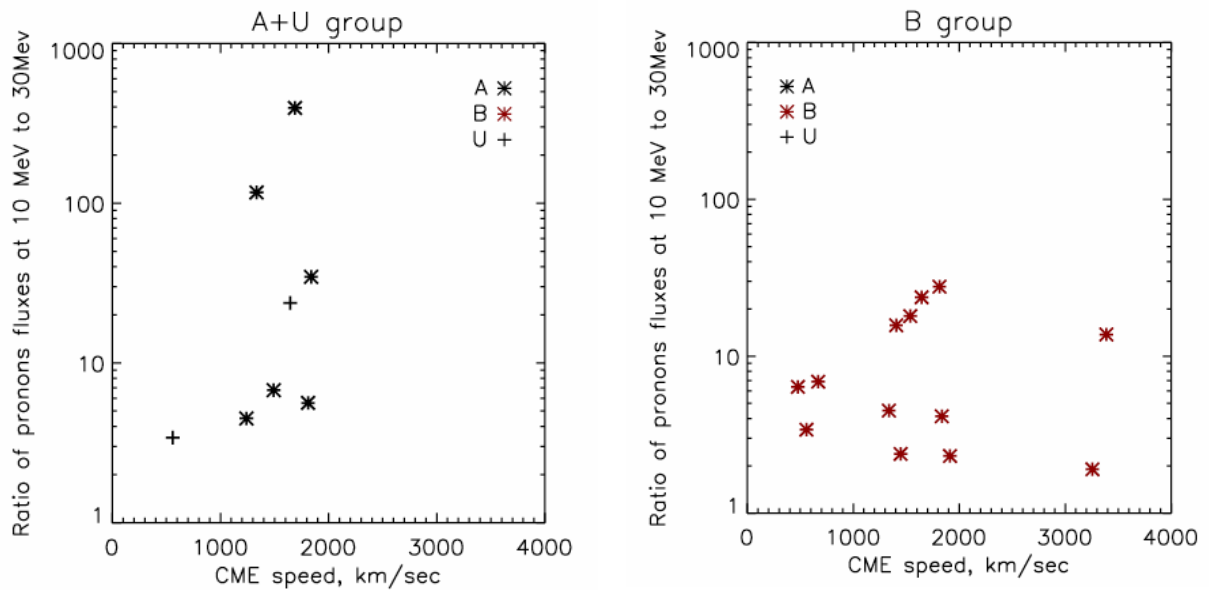


Fig. 4 The ratio of the fluxes in the maximum for protons with energies above 10 MeV to proton fluxes with energies above 30 MeV relative to the projected velocity of CMEs (https://cdaw.gsfc.nasa.gov/CME_list/) for groups A and U (right panel) and groups B (left panel), respectively.

Conclusions

Based on the analysis we make the following conclusions:

Most of ARs related to proton-rich events SEP events occurred in the ARs violating at least one of the classical mean-field dynamo laws (group B). But the statistical study of all ARs of the 23rd solar cycle showed the domination of normal ARs (group A).

Events associated with groups A and U show dependences on the peak frequency and spectral index, predicted by solar flare models and previously obtained by other authors (see, for example, *Daibog et al.*, [1993]).

Events related with ARs of group B do not show any clear dependencies on both the peak frequency and spectral index.

We expect that most of the methods developed based on the “standard flare” model will work for prediction of the SEP productivity of ARs of groups A and U. However, these results require additional statistical study.

Acknowledgment

This study is supported by the project 'The origin on solar energetic particles: solar flares vs. coronal mass ejections', co-funded by the Russian Foundation for Basic Research with project No. 17-52-18050 and the National Science Fund of Bulgaria under contract No. DNTS/Russia 01/6 (23-Jun-2017). LK and NM thank the budgetary funding of Basic Research program II.16 for partial support.

References

- Abramenko V.I., Zhukova A.V., Kutsenko A.S. (2018) Contributions from Different-Type Active Regions Into the Total Solar Unsigned Magnetic Flux. *Geomagnetism and Aeronomy*, 58, no 8, 1159–1169
- Chertok I.M., Grechnev V.V., Meshalkina N.S. (2009) On the Correlation between Spectra of Solar Microwave Bursts and Proton Fluxes near the Earth *Astronomy Reports*, Vol. 53, No. 11, 1059–1069.
- Klein, K.-L., Dalla S. (2017) Acceleration and Propagation of Solar Energetic Particles. *Space Science Reviews*, Volume 212, Issue 3–4, 1107–1136
- Daibog E. I., Melnikov V. F., Stolpovskii V. G. (1993) Solar energetic particle events from solar flares with weak impulsive phases of microwave emission. *Solar Physics*, 144, 361–372
- Dulk G. A. (1985), Radio emission from the sun and stars. *Annual review of astronomy and astrophysics*, 23, 169–224.
- Guidice D. A., Cliver E. W., Barron W. R., Kahler S. (1981) The Air Force RSTN System. *Bulletin of the American Astronomical Society*, 13, 553.
- Kuznetsov, S.N., Kurt, V.G., Myagkova, I.N., Yushkov, B.Y., Kudela, K., (2006) Gamma-ray emission and neutrons from solar flares recorded by the SONG instrument in 2001–2004. *Solar System Research*, 40, 104–110.
- Nakajima, H.; Sekiguchi, H.; Sawa, M.; Kai, K.; Kawashima, S. (1985) The radiometer and polarimeters at 80, 35, and 17 GHz for solar observations at Nobeyama. *Astronomical Society of Japan, Publications*, 37, 163–170.
- Moses D., et al. (1997) EIT Observations of the Extreme Ultraviolet Sun.. *Solar Phys.* 175, 571–599
- Papaioannou A.; Sandberg I., Anastasiadis A., Kouloumvakos A., Georgoulis M.K., Tziotziou K., Tsiropoula G., Jiggins P., Hilgers A. (2016) Solar flares, coronal mass ejections and solar energetic particle event characteristics. *Journal of Space Weather and Space Climate*, 6, 29.
- Scherrer, P. H et al. (1995) The Solar Oscillations Investigation - Michelson Doppler Imager. *Solar Physics*, 162, 129–188.
- Torii C., Tsukiji, Y., Kobayashi S., Yoshimi N., Tanaka H., Enome S. (1979) Full-automatic radiopolarimeters for solar patrol at microwave frequencies. *Nagoya University, Research Institute of Atmospherics, Proceedings*, 26, 129–132.

Radio Signatures of in Situ Observed ACE/EPAM Electron Fluxes

Miteva R.¹, Samwel S. W.²

¹ Space Research and Technology Institute, Bulgarian Academy of Sciences (SRTI-BAS),
Sofia, Bulgaria

² National Research Institute of Astronomy and Geophysics (NRIAG), Helwan, Cairo, Egypt
E-mail: rmiteva@space.bas.bg

Abstract.

We present the preliminary results on a correlation study between RSTN radio flux and the peak intensity of ACE/EPAM 103–175 and 175–315 keV solar energetic electrons. Data over the period 1997–2017 is considered. For this analysis, we collected the reported radio flux at all eight RSTN frequencies (in the range 245 MHz–15.4 GHz), usually at the time of the identified flare origin. Pearson correlation coefficients are calculated between the reported radio flux at each frequency and the identified by us electron amplitude. Thus, for the first time the remotely observed radio signatures of electrons can be directly compared with the in situ observed electron flux over nearly two solar cycles. Comparison of the results with SOHO/ERNE protons over several energy channels is also presented and discussed.

Introduction

The aim of this work is the comparison of the space weather conditions before the onset of Solar energetic particles (SEPs) are in situ observed fluxes in the range 10–100s of keV for the electrons, from few to 100s of MeV for the protons and heavy ions that are originally accelerated in the solar corona and/or (re-accelerated) in the interplanetary (IP) space. SEP events are considered an important ingredient of space weather research [Schwenn 2006]. Improved knowledge of the particle acceleration, escape, transport and detection is needed to successfully forecast the particles in order to mitigate not only the technological risk [Pulkkinen 2007], but also the radiation hazard for future space travelers to Mars [Semkova *et al.* 2018]. The above chain of phenomena, which SEPs undergo from the Sun to the particle detector, is currently difficult to simulate. Thus, numerous proxies are utilized to quantify the observed particle flux from the properties of their solar origin, namely solar flares (SFs) and coronal mass ejections (CMEs).

The classical approach is to use the SEP peak identity and to perform Pearson correlation coefficients with the parameters of the SEP-associated SFs and CMEs. On the particle side, the majority of the statistical reports in the literature deal with energetic protons [Miteva *et al.* 2018]. Due to its long-term availability, GOES flare soft X-ray emission, so-called flare class, is primarily used to quantify the flare contribution to SEPs. Reports considering radio emission do exist (e.g. Miteva *et al.* [2017] and the references therein), however they always relate in situ observed protons with the remote signatures of electrons (e.g. radio flux). For the CMEs, their projected linear speed, angular width, acceleration, etc. are among the investigated quantities.

For the first time here, we start with the identification of in situ electrons and perform the correlations with the flare radio emission signatures using data over nearly two solar cycles. For that purpose, ACE/EPAM electron and RSTN metric to microwave (MW) radio wavelengths are selected. GOES flare class and CME linear speed are also used. Additionally, we compare the results with protons from the SOHO/ERNE instrument, in order to relate the obtained results to other studies.

Data selection and analysis

In this study we use electron data from ACE/EPAM [Gold *et al.* 1998] and proton data from SOHO/ERNE [Torsti *et al.* 1995] instruments as provided during solar cycles 23 and 24.

Solar electron events in the 103–175 (low) and 175–315 keV (high) ACE/EPAM energy channels are identified and the background-subtracted flux of the in situ observed electrons is calculated. These are in fact the preliminary results from the ACE/EPAM electron catalog, currently under completion (<http://www.nriag.sci.bg/aceepam-electron-event-catalog-2/>).

Similar procedure is applied for the proton events using the preliminary results from the SOHO/ERNE catalog (<http://newserver.stil.bas.bg/SEPcatalog/>) in five energy channels: 17–22, 26–32, 40–51, 64–80, 101–131 MeV.

The association between SEPs and their solar origin is performed following the widely-adopted guidelines: the closest in time before the SEP onset at 1 AU and the strongest in SXR intensity/speed SF/CME pair is pre-selected. In case of eastern origin events (indicated by a slowly rising SEP profile) or when an alternative origin is indicated by the occurrence and strength of the accompanied type III radio bursts, a correction in the solar origin selection is performed.

GOES flare information is used from the flare reports, https://hesperia.gsfc.nasa.gov/goes/goes_event_listings/ and the CME speed is adopted from the SOHO/LASCO CME catalog, https://cdaw.gsfc.nasa.gov/CME_list/.

Finally, for the RSTN radio emission, we used the NOAA-SWPC daily reports on the edited events (<ftp://ftp.swpc.noaa.gov/pub/warehouse>) that include also radio fluxes in 8 frequencies: 245, 410, 608 (606 in solar cycle (SC) 23, 610 in SC24), 1415, 2695, 4995, 8800, 15400 MHz.

Results

During the investigated period 1997–2017, we identified ~1240 ACE/EPAM electrons in the low energy channel and ~990 in the high energy channel, respectively. Solar origin is associated for 70–80 % of them.

The results for the Pearson correlations between the electron flux and the reported radio flux are listed in Table 1 for the two electron channels. In addition, the results are given graphically in Fig. 1, denoted with red for the low and blue color for the high energy channel, as a function of the RSTN frequencies. The vertical bars at each data point represent the uncertainties based on 1000 calculation using the bootstrapping method. The obtained trends rise to a maximum at about 2695–4995 MHz and then follows a decline. With horizontal lines are given the averaged value for the correlations with SFs and CMEs, denoted in the plot. They are based on 0.40 ± 0.03 (897) and 0.38 ± 0.04 (727) for the SF class and 0.43 ± 0.04 (766) and 0.40 ± 0.04 (625) for the CME speed for the low and high electron energy channels, respectively. In brackets are given the respective sample size for each calculation. In general, the results for the two electron energy channels are rather close in value.

Table 1. Pearson correlation coefficients and its bootstrapping uncertainty between the election peak intensity at two energy channels and the RSTN radio flux. In brackets are given the sample size over which the respective correlation is made.

Electron flux	245 MHz	410 MHz	608 MHz	1415 MHz	2695 MHz	4995 MHz	8800 MHz	15400 MHz
103–175 keV	0.25 ± 0.07 (426)	0.32 ± 0.05 (361)	0.40 ± 0.05 (307)	0.43 ± 0.05 (328)	0.51 ± 0.05 (339)	0.52 ± 0.04 (355)	0.50 ± 0.04 (351)	0.43 ± 0.04 (766)
175–315 keV	0.26 ± 0.06 (371)	0.34 ± 0.05 (324)	0.39 ± 0.05 (280)	0.44 ± 0.05 (301)	0.54 ± 0.05 (312)	0.53 ± 0.04 (328)	0.51 ± 0.04 (324)	0.40 ± 0.04 (625)

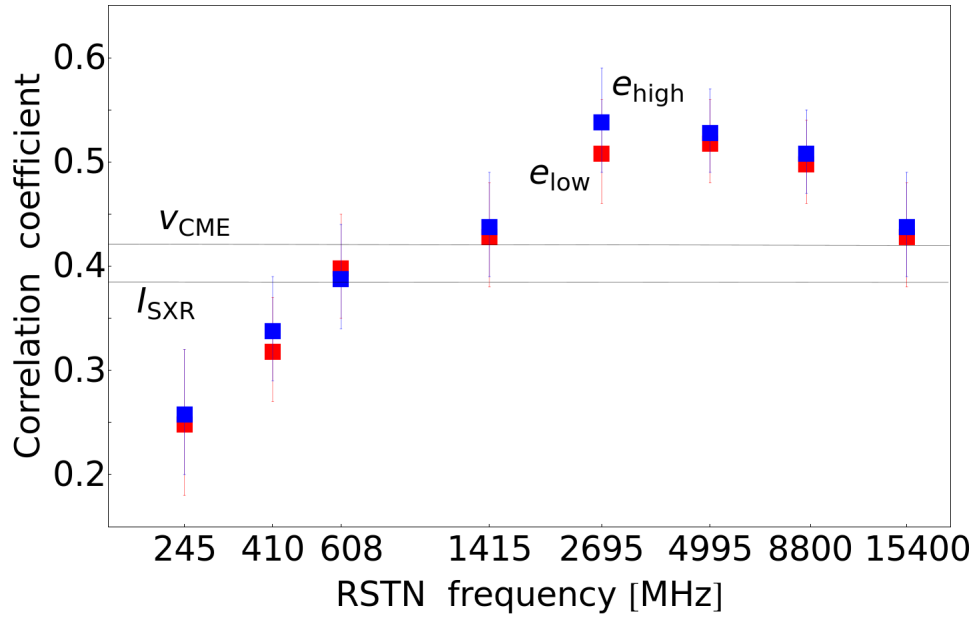


Fig. 1 Dependence of the correlation coefficients between the in situ electrons and the RSTN radio emission plotted as a function of the RSTN radio frequency, in MHz. Color code used: red: 103–175 keV electrons, blue: 175–315 keV electrons.

For comparison, we perform the similar correlation study using the SOHO/ERNE protons. We calculate the respective correlations with the RSTN radio flux for each of the 5 proton energy channels, denoted in different color, and present the results as a function of the radio frequency only graphically, see Fig. 2. Similar trend, compared to the electrons is observed, with the exception of the correlation at 245 MHz which is enhanced.

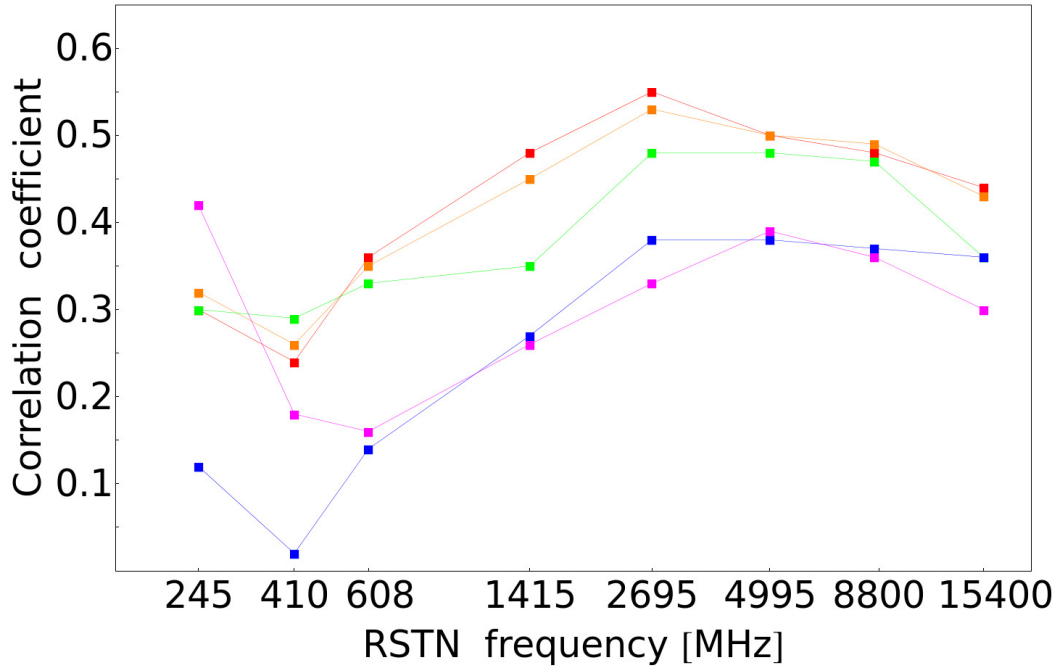


Fig. 2 Dependence of the correlation coefficients between the in situ protons and the RSTN radio frequency plotted as a function of the RSTN radio frequency, in MHz. Color code used: red: 19.5 MeV, orange: 29 MeV, green: 45.5 MeV, blue: 72 MeV, purple: 116 MeV.

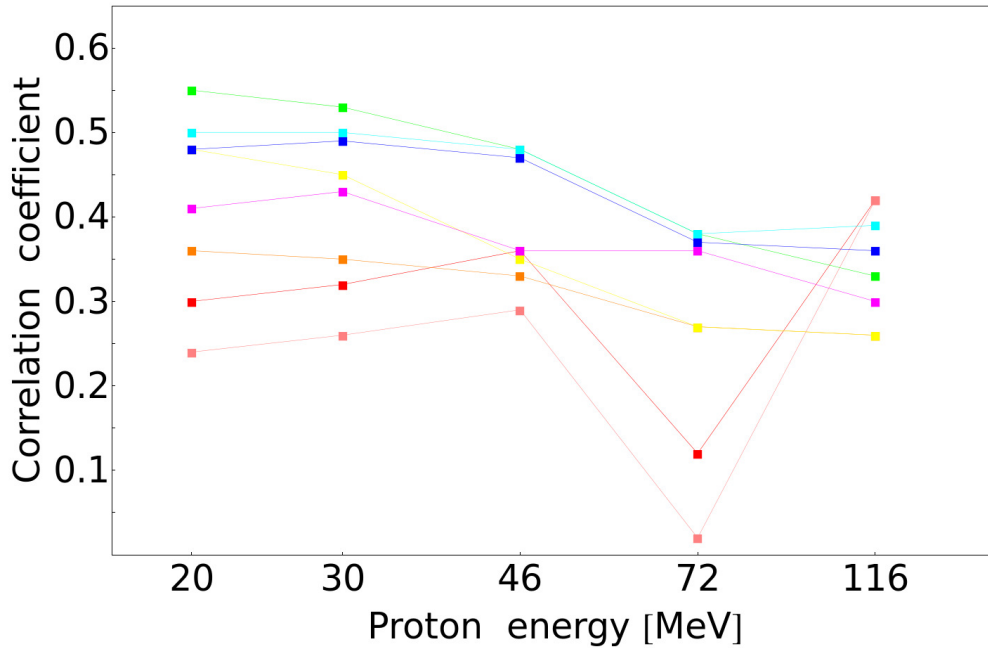


Fig. 3 Dependence of the correlation coefficients between the in situ protons and the RSTN radio frequency plotted as a function of the proton energy, in MeV. Color code used: red: 245 MHz, pink: 410 MHz, orange: 608 MHz, yellow: 1415 MHz, green: 2695 MHz, cyan: 4995 MHz, blue: 8800 MHz, purple: 15400 MHz.

Finally, we show alternative representation of the above results, this time as a function of the proton energy, in each of the five channels, Fig. 3. A slightly declining trend is noticed for all 8 RSTN frequencies (plotted with different colors), with a steep drop at 64–80 (~72) MeV channel for some of the frequencies.

Summary and discussion

We perform, for the first time, correlation analysis between in situ observed electron fluxes and the remote electron signatures in terms of radio emission from RSTN stations in solar cycles 23 and 24. Apart from the 15.4 GHz we obtain an increasing trend of the Pearson correlation coefficients with the increase of the radio emission frequency of the electron related flares. The correlations for the 2695–8800 MHz emission are statistically larger compared to the cases when GOES SXR flare class and CME projected speed are considered. The trend is kept when the correlations are done both for low and high energy electron fluxes. The differences between low (245 MHz) and higher frequencies (2695–8800 MHz) are statistically significant.

With respect to the protons, similar trend with a peak at 3 GHz is obtained, although the steady increase starts from 410 MHz. In contrast to the two electron channel where no difference is noticed, there is a slightly decreasing trend (with a steep drop at 64–80 MHz) of the correlations with the increase of the proton energy.

This analysis will be repeated when the background subtracted radio flux is carefully analyzed by us for each event.

Acknowledgment

The authors are thankful to the grant provided from VarSITI ISEST/Minimax 24 for the project ‘Solar energetic electrons and radio emission signatures’. RM acknowledges also support from the projects ‘The origin on solar energetic particles: Solar flares vs. coronal mass ejections’, co-funded by the National Science Fund of Bulgaria under contract No. DNTS/Russia 01/6 (23-Jun-2017) and Russian Foundation for Basic Research with project No. 17-52-18050 and ‘An investigation of the early stages of solar eruptions – from remote observations to energetic particles’ co-funded by the National Science Fund of Bulgaria contract No. NTS/AUSTRIA 01/23 (28.02.2017) and Austria OeAD Project No. BG 11/2017.

References

- Gold, R. E., Krimigis, S. M., Hawkins, S. E., III, Haggerty, D. K., Lohr, D. A., Fiore, E., Armstrong, T. P., Holland, G., Lanzerotti, L. J. (1998) Electron, Proton, and Alpha Monitor on the Advanced Composition Explorer spacecraft, *Space Science Reviews*, Vol. 86: 1/4, pp. 541–562.
- Pulkkinen, T. (2007) Space Weather: Terrestrial perspective, *Living Reviews in Solar Physics*, Vol. 4: 1, article id. 1, 60 pp.
- Miteva, R., Samwel, S. W., Krupar, V. (2017) Solar energetic particles and radio burst emission, *Journal of Space Weather and Space Climate*, Vol. 7, id. A37, 15pp.
- Miteva, R., Samwel, S. W., Costa-Duarte, M.-V. (2018) The Wind/EPACT proton event catalog (1996–2016), *Solar Physics*, Vol. 293: 2, article id. 27, 44pp.
- Schwenn, R. (2006) Space weather: The solar perspective, *Living Reviews in Solar Physics*, Vol. 3: 1, article id. 2, 72 pp.
- Semkova, J., Koleva, R., Benghin, V., Dachev, Ts., Matviichuk, Y., Tomov, B., Krastev, K., Maltchev, S., Dimitrov, P., Mitrofanov, I., Malahov, A., Golovin, D., Mokrousov, M., Sanin, A., Litvak, M., Kozyrev, A., Tretyakov, V., Nikiforov, S., Vostrukhin, A., Fedosov, F., Grebennikova, N., Zelenyi, L., Shurshakov, V., Drobishev, S. (2018) Charged particles radiation measurements with Liulin-MO dosimeter of FREND instrument aboard ExoMars Trace Gas Orbiter during the transit and in high elliptic Mars orbit, *Icarus*, Vol. 303, pp. 53–66.
- Torsti, J., Valtonen, E., Lumme, M., Peltonen, P., Eronen, T., Louhola, M., Riihonen, E., Schultz, G., Teittinen, M., Ahola, K., Holmlund, C., Kelhä, V., Leppälä, K., Ruuska, P., Strömmer, E. (1995) Energetic Particle Experiment ERNE, *Solar Physics*, Vol. 162: 1–2, pp. 505–531.

EVE Flare Diagnostics of in situ Observed Electron Events

Miteva R.¹, Samwel S. W.², Veronig A.^{3,4}, Koleva K.¹, Dechev M.⁵, Dissauer K.³,
Temmer M.³, Kozarev K.⁵, Zabunov S.¹

¹ Space Research and Technology Institute, Bulgarian Academy of Sciences (SRTI-BAS),
Sofia, Bulgaria

² National Research Institute of Astronomy and Geophysics (NRIAG), Helwan, Cairo, Egypt

³ Institute of Physics, University of Graz, Graz, Austria

⁴ Kanzelhöhe Observatory for Solar and Environmental Research, University of Graz, Austria

⁵ Institute of Astronomy with National Astronomical Observatory, Bulgarian Academy of
Sciences (IA-NAO BAS), Sofia, Bulgaria

E-mail: rmiteva@space.bas.bg

Abstract.

We present a comparative study between SDO/EVE flare intensity and the peak intensity of solar energetic electrons and protons over solar cycle 24 (2010–2017). For the analysis we selected flare emission in three EUV wavelengths: 94, 133 and 304 Å. Data from 103–175 and 175–315 keV ACE/EPAM energy channels are used to identify and analyze the flux of the in situ observed electrons. SOHO/ERNE data in five energy channels (17–22, 26–32, 40–51, 64–80, 101–131 MeV) is used for the proton signatures of the so-identified electron events. We calculated Pearson correlation coefficients between the electron and proton particle fluxes and the flare EUV intensities, and compare the results with the respective correlations between particle flux and the solar flare GOES class and speed of the coronal mass ejections.

Introduction

Solar energetic particles (SEPs) – in situ observed 10–100s of keV electrons up to several 100s of MeV protons and heavy ions that propagate from the Sun into the interplanetary space – are an important aspect of space weather research [Schwenn 2006]. Nowadays, the SEP fluxes are accepted to be energized due to the acceleration processes taking place in solar flares (SFs) and coronal mass ejections (CMEs), regarded as the solar origin of the particles [Bazilevskaya 2017]. The negative effects of SEPs to various technological system, both ground-based and space-born, is now well established [Pulkkinen 2007]. Furthermore, the planning and carrying out of human flights to the Moon and Mars require an improved knowledge and successful forecasting of the energetic protons and electrons released from the Sun due to the potential radiation risk they carry [Semkova et al. 2018]. And since the electron component arrives first, it can be used as an early warning for the approaching protons [Posner 2007].

The standard approach is to use GOES soft X-ray (SXR) flare class and CME projected speed while quantifying the SFs or CMEs, respectively, as contributors to the SEP acceleration. Moreover, in the majority of the reports in the literature, proton particle fluxes are used. In our recent work [Miteva et al. 2018], we also used proton events but performed the correlations with hard X-rays (HXR). The selection criterion there was the visibility of events in the RHESSI HXR instrument [Lin et al. 2002]. Extreme ultraviolet (EUV) channels were not in the focus.

In the present study, we expand this line of analysis by utilizing solar flare emission in various EUV wavelength channels from the SDO/EVE instrument [Woods et al. 2012]. Here, we present for the first time the correlation study using the peak intensity of in situ solar energetic electrons in solar cycle 24. The time period is specified by the data availability from the SDO/EVE instrument.

Data selection and analysis

For the current analysis we use data from SDO/EVE, ACE/EPAM [Gold *et al.* 1998] and SOHO/ERNE [Torsti *et al.* 1995] instruments as provided during solar cycle 24. We select flare emission in three EUV wavelengths available from the SDO/EVE instrument since mid-2010: 94, 133 and 304 Å. However, the EVE instrument has a data gap after May 2014, thus limiting the event sample. Background subtraction of the flare emission is performed for each case and the peak amplitude is further used for the correlation analysis.

Solar electron data from 103–175 (low) and 175–315 keV (high) ACE/EPAM energy channels are used to identify and analyze the background-subtracted flux of the in situ observed electrons. These are preliminary results adopted from the ACE/EPAM electron catalog, currently under completion

(<http://www.nriag.sci.bg/aceepam-electron-event-catalog-2/>).

Proton data from the SOHO/ERNE catalog (<http://newserver.stil.bas.bg/SEPcatalog/>) is used in five energy channels: 17–22, 26–32, 40–51, 64–80, 101–131 MeV as the proton signatures of the electron events. Also the proton fluxes are background subtracted ones.

The association between SEPs and their solar origin is performed following a standard set of criteria: the closest in time before the SEP onset at 1 AU and the strongest in SXR intensity/speed SF/CME pair is pre-selected. Correction in the selection is possible in case of eastern events (indicated by a slowly rising SEP profile) or when an alternative origin is indicated by the occurrence and strength of the accompanied type III radio burst.

Results

During the period of SDO/EVE data availability, we identified more than 200 ACE/EPAM electron events in the low energy channel and about 170 in the high energy channel, respectively. The solar origin (flare and coronal mass ejection, CME) is identified for the majority of the SEP events. Finally, we calculated the \log_{10} – \log_{10} Pearson correlations between the electron and proton fluxes and flare EUV intensities, and compared the results with the respective correlation with the GOES 1–8 Å flare peak flux (GOES flare class) (https://hesperia.gsfc.nasa.gov/goes/goes_event_listings/) and the SOHO/LASCO CME projected speed (https://cdaw.gsfc.nasa.gov/CME_list/). The results are listed in Table 1, where the uncertainties are calculated based on the bootstrapping method over 1000 calculations. In brackets we give the respective sample size for each case.

Table 1. Pearson correlation coefficients and their uncertainties for different samples of SEP and flare/CME characteristics, as given in the respective columns and rows.

The sample size is given in brackets.

SEP flux/ solar origin	ACE/ EPAM electron flux: 103– 175 keV	ACE/ EPAM electron flux: 175– 315 keV	SOHO/ ERNE proton flux: 17–22 MeV	SOHO/ ERNE proton flux: 26–32 MeV	SOHO/ ERNE proton flux: 40–51 MeV	SOHO/ ERNE proton flux: 64–80 MeV	SOHO/ ERNE proton flux: 101–131 MeV
EUV 94 Å	0.38±0.10 (127)	0.38±0.11 (111)	0.60±0.08 (68)	0.56±0.08 (64)	0.57±0.08 (56)	0.50±0.14 (31)	0.41±0.18 (17)
EUV 133 Å	0.40±0.09 (110)	0.39±0.10 (99)	0.53±0.08 (66)	0.52±0.09 (64)	0.50±0.10 (56)	0.29±0.17 (29)	0.40±0.23 (15)
EUV 304 Å	0.17±0.11 (85)	0.15±0.12 (76)	0.33±0.09 (50)	0.37±0.10 (48)	0.34±0.12 (44)	0.27±0.19 (25)	0.12±0.36 (13)
GOES class	0.32±0.07 (203)	0.30±0.08 (171)	0.46±0.08 (79)	0.45±0.08 (74)	0.45±0.09 (65)	0.40±0.15 (33)	0.29±0.18 (18)
CME speed	0.36±0.08 (150)	0.41±0.08 (126)	0.57±0.07 (79)	0.44±0.09 (74)	0.55±0.07 (65)	0.68±0.09 (33)	0.39±0.20 (18)

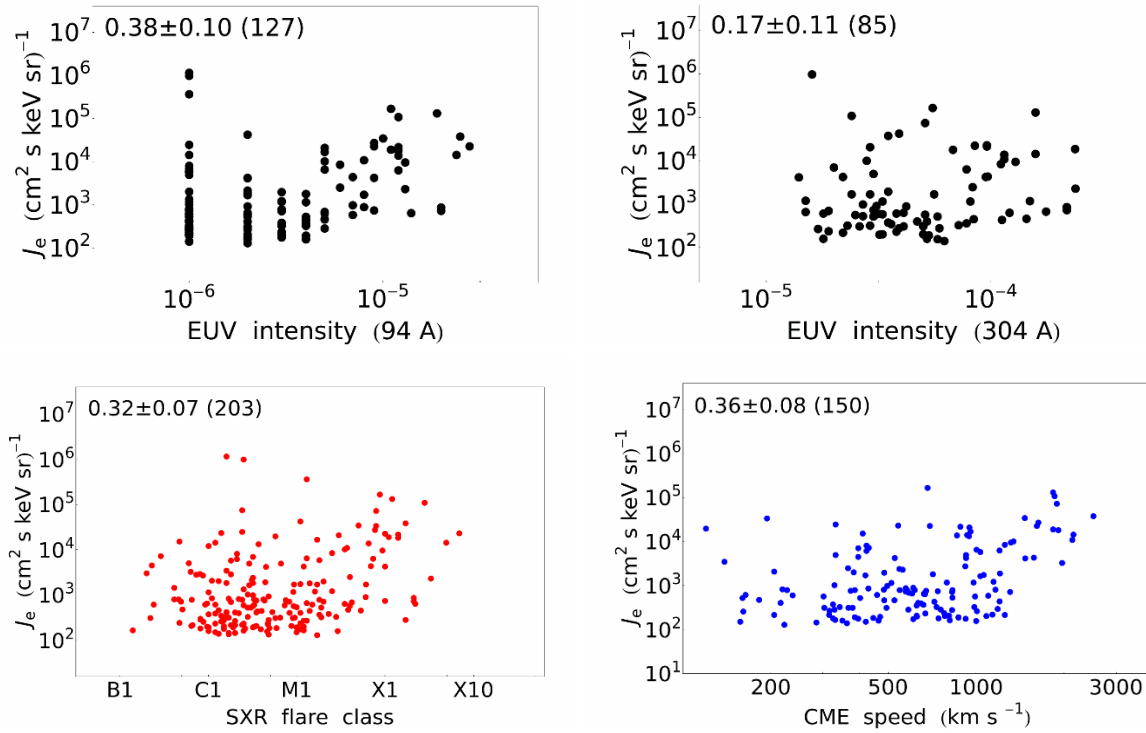


Fig. 1 Scatter-plots between the 103–175 keV ACE/EPAM electron peak intensity and the flare emission in EUV 94 Å, 304 Å, GOES SXR 1–8 Å or CME projected speed, respectively. The Pearson correlation coefficient is given on each plot. In brackets is shown the sample size.

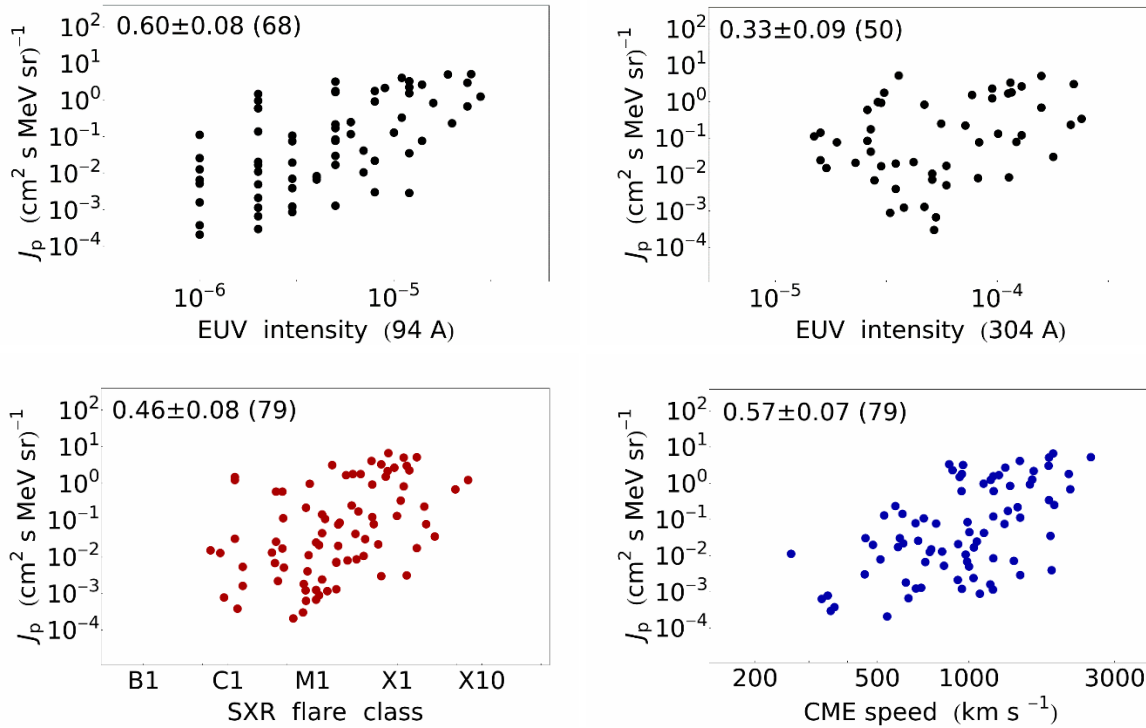


Fig. 2 Scatter-plots between the 17–22 MeV SOHO/ERNE proton peak intensity and the flare emission in EUV 94 Å, 304 Å, GOES SXR 1–8 Å or CME projected speed, respectively. The Pearson correlation coefficient is given on each plot. In brackets is shown the sample size.

For illustration, in Figs. 1 and 2 we show representative scatter plots for some of the correlations of the electrons and proton fluxes with the flare and CME properties, respectively.

The following trends are obtained:

- The two electron energy channels give consistent results for the correlation coefficients.
- For all tested relationships, the correlation coefficients decrease when the energy of the proton increases.
- The highest correlation coefficient of the flare EUV emission is smaller for the electron flux (0.4) than for the proton flux (0.6).
- For both electrons and protons the correlation coefficients are higher with the SDO/EVE 94 Å wavelength than the GOES class.
- The differences between the correlation coefficients for GOES class vs. electron fluxes and the EUV fluxes vs. electron fluxes are small and not statistically significant. Similar trends are obtained when the correlations are done between the electrons and CME speed.
- When proton fluxes are used instead, the correlations with some EUV flare emission wavelengths and SXR can differ up to twice the uncertainty value, however the differences are again not statistically significant. The correlations with the CME speed and protons can be larger for specific proton energies.
- The correlations with 304 Å are systematically lower compared to the other two EUV wavelengths, 94 and 133 Å.

Summary and discussion

We perform, for the first time, correlation analysis between in situ observed electron fluxes above 100 keV with parameters of solar flares (GOES class, EUV intensity) and CMEs (projected speed). For the statistical study we use the available data from SDO/EVE (2010–2014) and preliminary ACE/EPAM electron and SOHO/ERNE proton lists.

The correlation coefficients between the SOHO/ERNE proton peak intensities and the flare emission from the EUV channels 94 and 133 Å are always larger or similar to the respective values when GOES flare class and LASCO projected CME speed are used instead. The opposite result is found when 304 Å data is used.

With the increase of the SOHO/ERNE proton energy we obtained a declining trend for the correlations between the proton peak fluxes and flare emission (both EUV and SXR) and the CME speed. The first part is in contrast to the result reported by *Dierckx et al.* [2015] between SEP-EM protons (based on GOES and IMP-8 data) and the SXR flare emission, where a rising trend with respect to proton energy was obtained. The declining trend of the correlations with the CME speed is confirmed using an alternative source of proton data. Although the SOHO/ERNE proton data is known to have some saturation effects for large intensity events, the selective discrepancy of the flare correlation trend needs further research.

For all cases, we obtain lower Pearson correlation coefficients when using electron fluxes, compared with the commonly used proton fluxes.

We find that final conclusions made for the flare vs. CME origin of SEP events are sensitive on the selection of electron vs. proton events and also on the chosen wavelength of flare emission. This reflects the contradicting reports in the literature on the SEP-productivity of SFs vs. CMEs.

Acknowledgement

This study is supported by the projects ‘An investigation of the early stages of solar eruptions – from remote observations to energetic particles’ co-funded by National Science Fund of Bulgaria contract No. NTS/AUSTRIA 01/23 (28.02.2017) and Austria OeAD Project No. BG 11/2017; ‘The origin on solar energetic particles: Solar flares vs. coronal mass ejections’, co-funded by the Russian Foundation for Basic Research with project No. 17-52-18050 and the National Science Fund of Bulgaria under contract No. DNTS/Russia 01/6 (23-Jun-2017) and the VarSITI ISEST/Minimax 24 project ‘Solar energetic electrons and radio emission signatures’.

References

- Bazilevskaya, G. A. (2017) Once again about the origin of solar cosmic rays, *Journal of Physics: Conference Series*, Volume 798: 1, article id. 012034.
- Dierckxsens, M., Tziotziou, K., Dalla, S., Patsou, I., Marsh, M. S., Crosby, N. B., Malandraki, O., Tsiropoula, G. (2015) Relationship between Solar Energetic Particles and Properties of Flares and CMEs: Statistical Analysis of Solar Cycle 23 Events, *Solar Physics*, Vol. 290: 3, pp. 841–874.
- Gold, R. E., Krimigis, S. M., Hawkins, S. E., III, Haggerty, D. K., Lohr, D. A., Fiore, E., Armstrong, T. P., Holland, G., Lanzerotti, L. J. (1998) Electron, Proton, and Alpha Monitor on the Advanced Composition Explorer spacecraft, *Space Science Reviews*, Vol. 86: 1/4, pp. 541–562.
- Lin, R.P, Dennis, B. R, Hurford, G. J and 63 more (2002) The Reuven Ramaty high energy solar spectroscopy images (RHESSI), *Solar Physics*, Vol. 210: 1, pp. 3–32.
- Miteva, R., Koleva, K., Dechev, M., Veronig, A., Kozarev, K., Temmer, M., Dissauer, K., Duchlev, P. (2018) Hard X-ray Diagnostic of Proton Producing Solar Flares Compared to Other Emission Signatures, *Publications of the Astronomical Society “Rudjer Boskovic”*, Vol. 18, pp. 117–125.
- Posner, A. (2007) Up to 1-hour forecasting of radiation hazards from solar energetic ion events with relativistic electrons, *Space Weather*, Vol. 5: 5, CiteID 05001.
- Pulkkinen, T. (2007) Space Weather: Terrestrial perspective, *Living Reviews in Solar Physics*, Vol. 4: 1, article id. 1, 60 pp.
- Schwenn, R. (2006) Space weather: The solar perspective, *Living Reviews in Solar Physics*, Vol. 3: 1, article id. 2, 72 pp.
- Semkova, J., Koleva, R., Benghin, V., Dachev, Ts., Matviichuk, Y., Tomov, B., Krastev, K., Maltchev, S., Dimitrov, P., Mitrofanov, I., Malahov, A., Golovin, D., Mokrousov, M., Sanin, A., Litvak, M., Kozyrev, A., Tretyakov, V., Nikiforov, S., Vostrukhin, A., Fedosov, F., Grebennikova, N., Zelenyi, L., Shurshakov, V., Drobishev, S. (2018) Charged particles radiation measurements with Liulin-MO dosimeter of FRENDO instrument aboard ExoMars Trace Gas Orbiter during the transit and in high elliptic Mars orbit, *Icarus*, Vol. 303, pp. 53–66.
- Torsti, J., Valtonen, E., Lumme, M., Peltonen, P., Eronen, T., Louhola, M., Riihonen, E., Schultz, G., Teittinen, M., Ahola, K., Holmlund, C., Kelhä, V., Leppälä, K., Ruuska, P., Strömmer, E. (1995) Energetic Particle Experiment ERNE, *Solar Physics*, Vol. 162: 1–2, pp. 505–531.
- Woods, T.N, Eparvier, F.G, Hock, R., Jones, A.R., Woodraska, d., Judge, D., Didkovsky, L., Lean, J., Mariska, J., Warren, H., McMullin, D., Chamberlin, P., Berthiaume, G., Bailey, S., Fuller-Rowell, T, Sojka, J., Tobiska, W.K, Viereck, R. (2012) Extreme Ultraviolet Variability Experiment (EVE) on the Solar Dynamics Observatory (SDO): Overview of Science Objectives, Instrument Design, Data Products, and Model Developments, *Sol. Phys.*, Vol. 275: 1–2, pp. 115–143.

Features of Solar Energetic Particle Events During the 23rd Cycle Of Solar Activity and Their Relationship with Solar X-ray, Gamma-Emission and Coronal Mass Ejections

Myagkova I.N.¹, Miteva R.², Kashapova L.³, Bogomolov A.V.¹, Danov D.²

¹ Skobeltsyn Institute of Nuclear Physics, MSU, Moscow, Russia

² Space Research and Technology Institute, Bulgarian Academy of Sciences, Sofia, Bulgaria

³ Institute of Solar-Terrestrial Physics SB RAS, Irkutsk, Russia

E-mail: irina@srd.sinp.msu.ru

Abstract.

The study on the relationship of solar cosmic ray events (in particular, the ratio of the maximum between the proton and electron fluxes) with X-ray and gamma radiation from solar flares, as well as with parameters of coronal mass ejections was carried out. It was done on the basis of SOHO/ERNE proton event catalog (<http://newserver.stil.bas.bg/SEPcatalog/>) and Solar Flares Catalog based on measurements of X- and gamma-emission (>50 keV) detected by SONG (CORONAS-F – Russian solar observatory) from August, 2001 till December, 2003 (http://swx.sinp.msu.ru/apps/solar_flares_cat/index.php). Solar electron flux (> 300 keV) were measured in the polar caps by MKL-instrument on board CORONAS-F satellite.

Introduction

Solar energetic particles (SEPs) – electrons, protons and heavy nuclei at energies from the keV up to the GeV range – together with X-ray and gamma-ray flares and coronal mass ejections (CMEs) are important components of space weather and topic of ongoing research [Lanzerotti, 2001, Jiggins et al., 2014]. The aim of this work is the comparison of the ratio of the maximum proton and electron fluxes of SEPs with the soft X-ray (SXR), hard X-ray (HXR) and gamma-ray flare intensity and the projected velocity of CME.

Experiments

The CORONAS-F Russian space solar (Complex **OR**bital **O**bservation in Near-Earth space **A**ctivity of the **S**un) observatory was launched on July 31, 2001, and operated until the end of 2005. At the beginning of its flight CORONAS-F had a quasi-circular orbit, with initial parameters: altitude 507±21 km, inclination 82.5 degrees, and period of revolution 94.5 min. The primary goal of the CORONAS-F experiment was to investigate nonstationary processes on the Sun and their impact on the interplanetary medium and the Earth's magnetosphere [Kuznetsov et al., 2014].

It is very important that on CORONAS-F observatory both neutral solar emission and charged particles were detected. Solar neutrons were measured on the lighted side of the Earth outside of the Earth's radiation belts, solar particles – both protons and electrons – in polar caps.

In the SONG (SOlar Neutrons and Gamma-quants) instrument CsJ-crystal is used for X-ray and gammas detection: it has rather smaller energy resolution comparing with NaJ, but impulse shape depends on specific ionization of the particle, therefore it is possible to differ impulses produced by gammas and neutrons. More detail the SONG instrument description you can find in Kuznetsov *et al.* [2014] and in the same Proceedings, paper of Bogomolov A. *et al.* [2019, this issue].

The MKL instrument which detected charged particles, both solar protons and electrons, consists of one block with radiation detectors, pulse generators, gate circuits, and voltage converters for the detectors and electronics along with a device for information output to the telemetry inside it.

Spectra of electron flux with energies of E_e 0.3–12 MeV and proton flux with energies of E_p 1–5 MeV are measured by means of telescopic system consisting of three detectors (see Fig. 1). Dt.3 is a thin n-p-detector of 10 mm diameter and 50 mkm thickness; Dt.4 is a thick n-p-detector of 12 mm diameter and 2,000 mkm thickness; Dt.5 is a jointed scintillation detector of Phoswich type. It consists of CsJ crystal of 10 mm diameter and height. CsJ has a higher density comparing with Si-detectors and allows to measure electrons with higher energy [Kuznetsov et al., 2014].

Data

In this work we used the peak flux of solar electrons with the energy 0.6–1.5 MeV from MKL instrument. For the solar proton peak flux we have used the reported values from the catalog lists the proton enhancements from the High Energy Detector (HED) aboard SOHO/ERNE instrument identified during solar cycle (SC) 23 (1996÷2008) and SC24 (2009÷2018),

<http://newserver.stil.bas.bg/SEPcatalog>.

The catalog lists the peak intensity for the solar proton events in the different HED energy channels (in the range 14÷131 MeV) and additional information (GOES SXR flare class, linear speed of the CME in km s^{-1}) organized in table-form separately for SC23 and SC24. Proton peak was identified at the maximum of the particle profile (local enhancements are not considered). Onset time was identified as the time of 3-sigma intensity value above pre-event level. Peak time was considered as the time at the peak proton intensity. The peak proton intensity (J_p) was given after subtraction of the pre-event level in protons/($\text{cm}^2 \cdot \text{s} \cdot \text{sr} \cdot \text{MeV}$). The reported there onset/peak times and J_p are based on 5-min averaged data.

We used the reported peak fluxes of solar protons from the SOHO/ERNE catalog and not measured by an MKL device, as was done for electrons, because SOHO/ERNE instrument has much higher sensitivity, which gave us the opportunity to analyze weak SEP events that were of considerable interest to us.

We compared the peak flux of solar protons with energies 17–22 MeV according to the SOHO/ERNE catalog, with the ones of solar electrons (J_e) with energies of 0.6–1.5 MeV according to the MKL instrument.

For 125 SEP events from September 9, 2001 to December 2, 2003, peak proton (17–22 MeV) and electron (0.6–1.5 MeV) fluxes were analyzed, as well as the properties of the SEP solar origin: CME speeds, class of the X-ray flare, flare heliographic coordinates and gamma fluences with energies above 500 keV. We found that for 34 of these 125 proton events, the flux of solar electrons was not observed – probably due to insufficient sensitivity of the MKL device for weak events. For the remaining 91 events, we analyzed the ratio of the fluxes of solar protons and electrons.

Results and discussion

The correlation plot between the peak fluxes of solar protons with energies 17–22 MeV according to SOHO/ERNE catalog vs. the peak flux of solar electrons with energies of 0.6–1.5 MeV according MKL data is presented in Fig. 2.

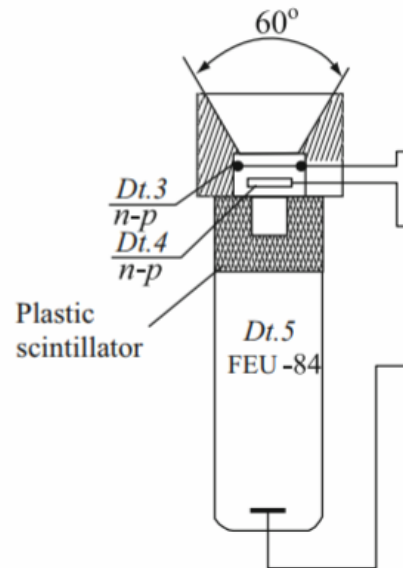


Fig. 1. Schematic arrangement of part of MKL instrument intended for the high-energy electron detection.

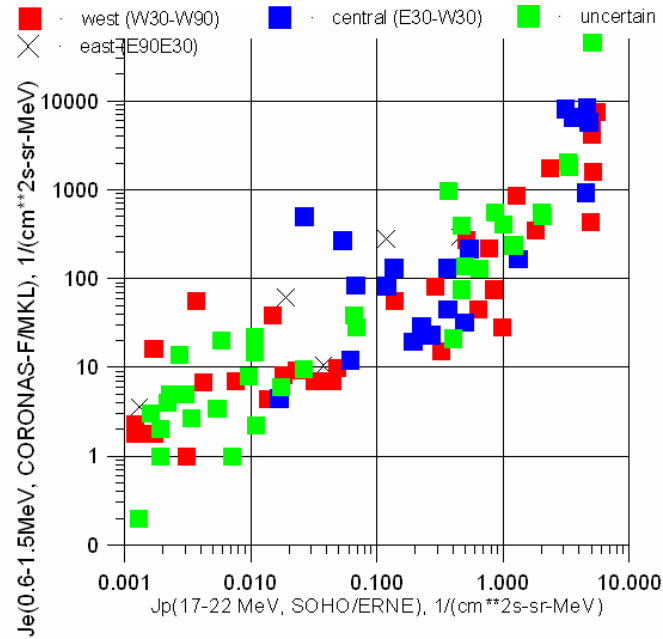


Fig. 2 Correlation plot between the peak flux of solar protons with energies 17–22 MeV according to SOHO/ERNE catalog vs. the peak flux of solar electrons with energies of 0.6–1.5 MeV according MKL data. For color code see text.

Different colors represent events depending on the localization of the SEP-related solar flare on the solar disk according to the SOHO/ERNE catalog: west events (W90–W30 degrees) in red color, central events (W30–E30 degrees) – green, east events (E30–E90 degrees) – oblique crosses. Events for which localization by the SOHO/ERNE catalog has not been determined in Fig. 2 (and in all next figures) are shown in green. From Fig. 2 it is clearly seen that there is a number of non-localized events, especially among the weak SEP events (with proton flux in 17–22 MeV less than 0.01 particles per $\text{cm}^2\text{-s-sr-MeV}$).

Figure 2 also shows that there is a linear relationship between the maximum intensity of proton and electron fluxes in SEPs, both for western and central flares as well as strong non-localized ones, except for a few events.

In order to investigate this feature in more detailed, we have analyzed the dependence of the ratio of peak flux of protons and electrons (J_e/J_p) on the flux of protons (left panel of Fig. 3) and electrons – right panel of Fig. 3).

As can be seen from the left panel of Fig. 3, in the case of dependence on the proton flux, a declining trend is obtained: for a higher proton flux – a lower ratio J_e/J_p was observed, except for four events.

As for the dependence of the ratio J_e/J_p on the peak solar electron fluxes, there is a more complex relationship. In the right panel of Fig. 3, two branches are visible. The first is a linear relationship at high peak electron fluxes, where the ratio 100–1000 is obtained, which includes events generated primarily by central and western flares. The second is also linear, but with medium peak solar electron fluxes (<100 particles per $\text{cm}^2\text{-s-sr-MeV}$), and the ratio is substantially higher, with most events being the result of western or non-localized flares.

It is possible that there are at least two types of flares for which the conditions for acceleration and escape from the Sun of protons and electrons are different. Namely, there are a number of relatively weak events, where the flux of solar electrons is nevertheless significant. Since among such events there are practically no events generated by central flares, it can be assumed that in such cases it is more difficult for solar protons to reach Earth orbit than for the electrons originated in the same flare.

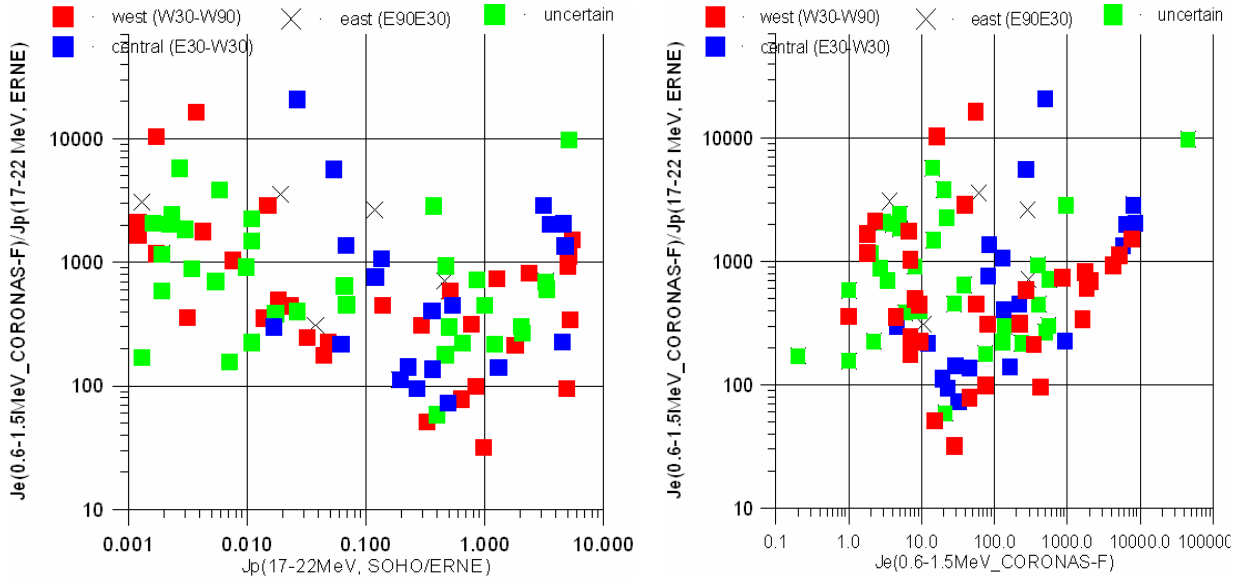


Fig. 3. Correlation plots between the ratio of the peak flux of protons and electrons on the proton flux (left panel) and electron flux (right panel).

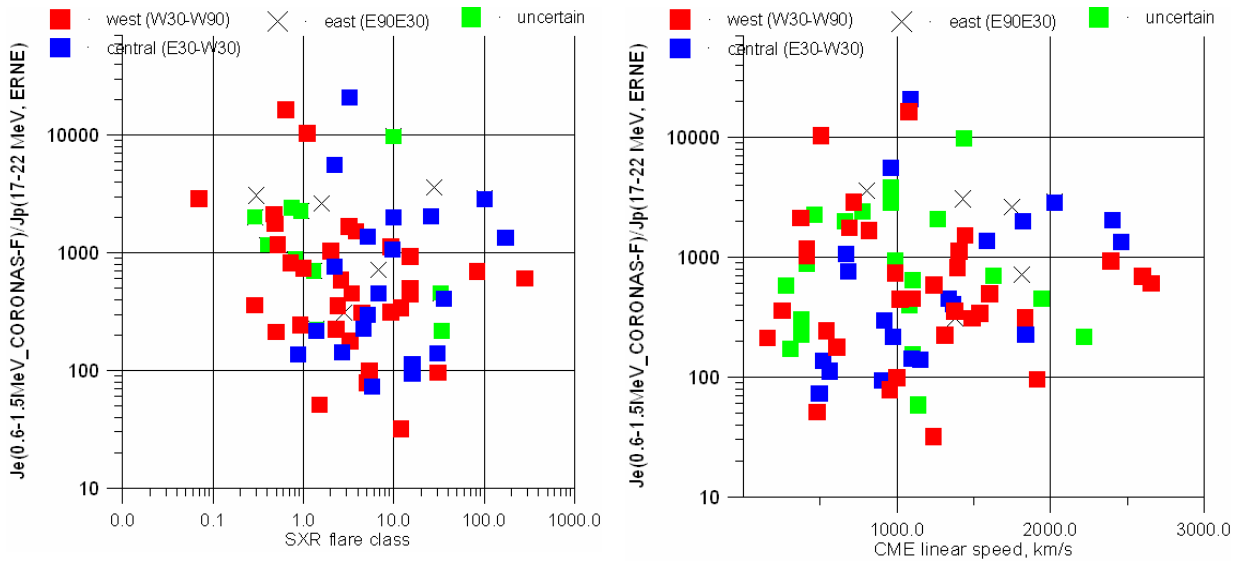


Fig. 4. Dependences of the ratio of the peak flux of protons and electrons (J_e/J_p) on the SXR flare class (left panel) and on the CME speed (right panel).

Our next step was to study the dependence of the J_e/J_p ratio on (a) the class of the parent flare in SXR (left panel of Fig. 4) and b) on the speed of the CME associated with this SEP event (right panel of Fig. 4). The values for both the flare class and the speed of the CME were taken from the SOHO/ERNE catalog.

As it can be seen from both panels of Fig. 4, it is difficult to make any definite conclusions. For the left panel in Fig. 4 it is possible to see a growth in the ratio of J_e/J_p with the decrease in the SXR flare class (which coincides with the conclusions from the left panel of Fig. 3, since the higher peak proton flux more often corresponds to the higher class of the flare in SXR). There is no correlation between the ratio of J_e/J_p and the linear velocity of the CME, at least for these data.

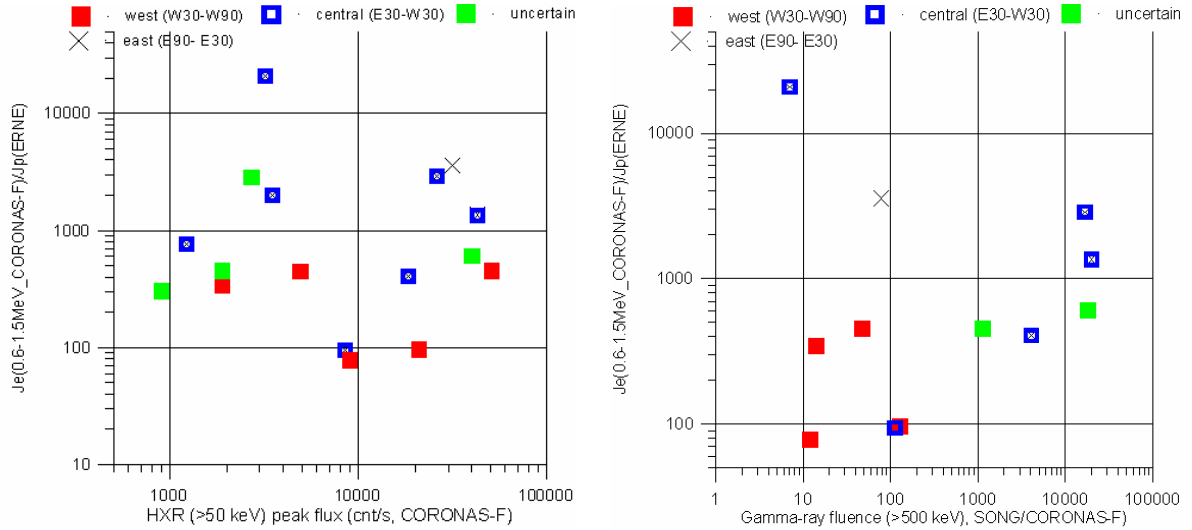


Fig. 5. Dependences of the ratio of the peak flux of protons and electrons (Je/Jp) on HXR (>50 keV) peak flux from SONG (CORONAS-F), left panel, and on gamma-emission fluence >500 keV from SONG (CORONAS-F), right panel.

Our last attempt to find a relationship of Je/Jp with parameters of the parent flares was to perform the correlation with the peak HXR fluxes with energy > 50 keV (left panel) and gamma fluence > 500 keV (right panel) both according to SONG (CORONAS-F). The results are presented in Fig. 5.

Among 70 flares in which the SONG instrument measured the HXR flux, only 17 of them were followed by SEP events, and only in 12 of these 17 flares the gamma-emission flux with the energy >500 keV was measured, which made it possible to calculate their gamma-fluence (the total number of photons with energies above 500 keV recorded during the flare). Figure 5 shows that there is no correlation between the peak of the HXR emission and Je/Jp . In the case of flare gamma-fluence, there is a tendency of increase of the ratio flux Je/Jp with the increase of gamma-fluence, which is expected, since the main part of gamma radiation belonged to the energy range up to 10 MeV, which corresponds to the acceleration of flare electrons.

Conclusions

The Je/Jp ratio in SEP events during 2001–2003 years was analyzed.

For the higher flux of the protons – lower ratio Je/Jp was obtained, except for four events.

The dependence of the ratio Je/Jp on the peak flux of solar electrons is complex – we have found two branches of this dependence, so it is possible that there are at least two types of flares for which the conditions for acceleration and escape from the Sun of protons and electrons are different. This deserves further investigation.

No clear correlations were found between the ratio Je/Jp with flare class, CME velocity and HXR peak flux.

Acknowledgment

This study is supported by the project 'The origin on solar energetic particles: solar flares vs. coronal mass ejections', co-funded by the Russian Foundation for Basic Research with project No. 17-52-18050 and the National Science Fund of Bulgaria under contract No. DNTS/Russia 01/6 (23-Jun-2017). LK and NM thank the budgetary funding of Basic Research program II.16 for partial support.

References

- Bogomolov, A., Myagkova I., Miteva R., Danov D., Kashapova L. (2019) Parameters of Thermal and Non-thermal X-ray and Gamma Ray Emission of Solar Flares, Observed onboard Coronas-F, Proceedings of the WS-11 workshop, held in Primorsko, Bulgaria (this issue).
- Jiggins, P., Chavy-Macdonald, M.A., Santin, G., Menicucci, A., Evans, H., Hilgers, A. (2014) The magnitude and effects of extreme solar particle events. *Journal of Space Weather and Space Climate* 4, A20. doi:10.1051/swsc/2014017.
- Lanzerotti, L. J. (2001) Space weather effects on communications, in *Space Storms and Space Weather Hazards*, NATO Sci. Ser. II: Math., Phys. and Chem., vol. 38, edited by I. Daglis, 313 pp., Kluwer Acad., Dordrecht, Netherlands.
- Kuznetsov, S.N., Bogomolov, A.V., Galkin, V.I., Denisov, Y.I., Podorolsky, A.N., Ryumin, S.P., Kudela, K., Rojko, J. (2014) Scientific Set of Instruments "Solar Cosmic Rays", in: Kuznetsov, V. (Ed.), *The Coronas-F Space Mission*, p. 289. doi:10.1007/978-3-642-39268-9_9.

STEREOCat Speed de-projection of SEP-Related CMEs

Tsvetkov Ts.¹, Miteva, R.², Temmer, M.³, Petrov, N.¹

¹ Institute of Astronomy and National Astronomical Observatory, BAS, Bulgaria

² Space Research and Technology Institute, BAS, Bulgaria

³ Institute of Physics, University of Graz, Austria

E-mail: tsvetkov@astro.bas.bg

Abstract.

Particles accelerated to high energies by solar eruptive phenomena can reach the Earth moving along the interplanetary magnetic field lines. We use a list of 156 SOHO ERNE 20 MeV solar energetic particle (SEP) events from solar cycle 24 (2009–2017) with identified solar origin (e.g. flares and CMEs). The aim of this study is to evaluate the 3D parameters of SEP-related CMEs and estimate if they can give us a better insight of SEP production than the previously used 2D velocities. The 3D kinematic properties of the CME set are explored using observations from STEREO SECCHI and SOHO LASCO coronagraphs based on the STEREOCat analysis tool.

Introduction

CMEs are changes in coronal structure including appearance and ejection of bright formation of plasma that can be observed at various wavelengths (white-light, soft X-ray, EUV, etc.). Usually their speeds are estimated in the plane of the sky (which is a projection of their real velocities) and have typical values in the range between 20 and 2000 km s⁻¹. Occasionally it may reach values up to 3500 km s⁻¹ [Chen P. F., 2011]. The mean CME speed varies between 300 km s⁻¹ (near solar minimum) and 500 km s⁻¹ (near maximum of the solar cycle) [Yashiro S., et al., 2004].

CME parameters are important part of all CME propagation models as initial conditions. Such models help to estimate the CME path and arrival time at various locations, which requires precise evaluation of CME parameters.

Solar energetic particles (SEPs) are the in situ observed electrons, protons and ions of solar origin that were accelerated by processes taking place at solar eruptive phenomena and propagated through the interplanetary space to spacecraft outside Earth magnetosphere. SEP events constitute an important space weather component that carry technological and biological risks [Pulkkinen T., 2007; Semkova J., et al., 2018]. Mitigation procedures start with an improved forecasting of the phenomena that involves better knowledge on their connection to solar eruptive events. Generally, when quantifying the relationship between SEP intensity and solar flare flux and CME speed, one used Pearson correlation analysis. Apart from selected event cases described by Park et al. [2017], only SOHO/LASCO CME projected speeds were used previous papers. In this study, we expand the sample size by covering solar cycle 24.

Data

CMEs are visible in white light as bright structures moving away from the Sun in coronagraphs. The best observations of CMEs nowadays are provided by SOHO and STEREO missions. For the analysis performed in this study, we used data from the following coronagraphs:

- Sun Earth Connection Coronal and Heliospheric Investigation (SECCHI) COR 2 on board both the STEREO Ahead & Behind spacecraft (FOV – out to 15R☉).
- Large Angle and Spectrometric Coronagraph (LASCO) C3 – SOHO with FOV 3.7÷32R☉ above the solar limb.

The analysis presented in this study is done using the StereoCat tool. Related SEP events are explored using data from SOHO/ERNE ~20 MeV energy channel.

The aim is to estimate “true” 3D velocities of SEP-related CMEs and compared it with 2D speeds, provided by SOHO LASCO CME Catalog.

Results

a) Velocity distributions of SEP-related CMEs

A list of 156 solar energetic particle (SEP) events was obtained for the period of solar cycle 24 (2009–2017). All events were associated with CMEs and 112/156 events were also linked with solar flares.

We estimated the “true” velocities of SEP-related CMEs with STEREOCat tool, which allows common measurements using only 2 spacecraft data at once. Depending on visibility of eruptions by different instruments we made measurements with all possible combinations of telescopes. 41/156 CMEs were observed simultaneously by the 3 instruments and we estimated 3 values for their 3D speeds (STEREO A + LASCO C3; STEREO A + STEREO B; LASCO C3 + STEREO B). Since no STEREO Ahead data is available for the period 2014 July–2015 November and after October 2014 STEREO Behind is out of order, measurements for 28/156 events observed in this periods are impossible. 8/156 CMEs are only observed simultaneously by STEREO B and C3 (in the period of STEREO A data gap) and in other 9 cases the only possible combination includes STEREO A and C3 data (after communications with STEREO B dropped down).

Finally, we have 64 measurements by the pair STEREO A and LASCO C3, 56 calculations by STEREO A and STEREO B and 53 – by LASCO C3 and STEREO B. We plotted the distributions of the 3D velocities by each pair (Figure 1a, b, c) as well as the distribution of 2D velocity quantified by LASCO CME Catalog (Figure 1d).

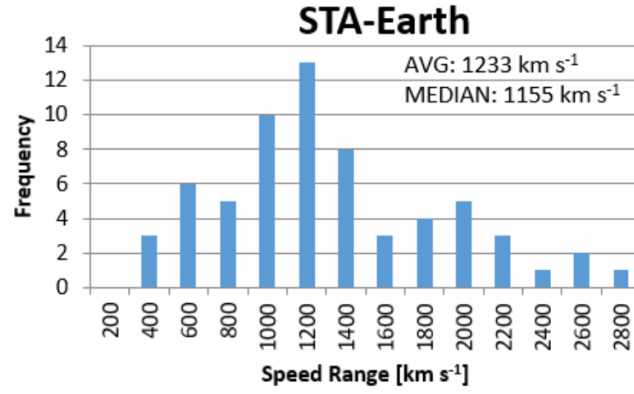
The average and median velocities in each case show that we have similar values from the 3 different combinations of instruments that estimate 3D speeds (average velocities between 1220 and 1273 km s⁻¹ and median velocities 1148–1156 km s⁻¹), but they differ from the values obtained by the 2D sample (average and median speeds, 1003 km s⁻¹ and 928 km s⁻¹, respectively).

b) Comparison between measured 3D and 2D velocities

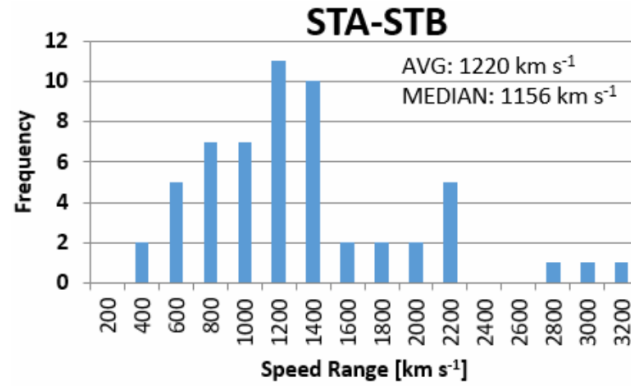
To compare the calculated velocities with LASCO 2D CME speeds we plotted the dependence and estimated Pearson product-moment correlation coefficient r for each plot (values are given in Table 1). The most powerful relation with 2D speeds seems to be with the velocities measured by STEREO A + LASCO C3 pair, although other pairs also show high positive correlation with 2D velocities. The uncertainties are calculated using bootstrapping method based on a sample of 1000 calculated correlations. Coefficients of determination (r^2) for each pair is also estimated and listed in Table 1.

Table 1. Pearson product-moment correlation coefficients r and coefficients of determination for 3D velocities measured by each pair of instruments with 2D LASCO speeds.

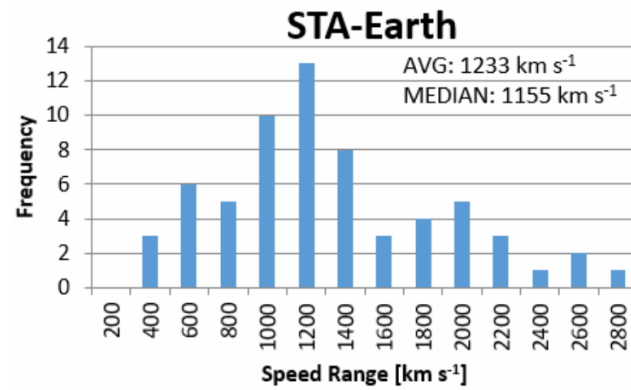
Pair of instruments	r	$r^2 \times 100$ [%]
STEREO A + C3	0.86 ± 0.04	74
STEREO A + B	0.78 ± 0.08	61
C3 + STEREO B	0.83 ± 0.05	69



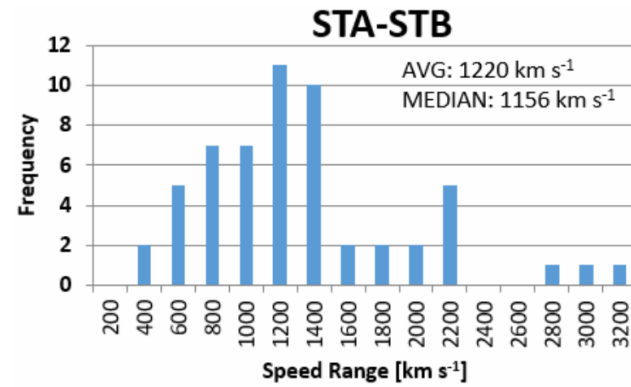
a)



b)



c)



d)

Fig. 1 Distribution of the velocities of SEP-related CMEs according to the pair of instruments used for the measurements. STA denotes STEREO A, STB – STEREO B, Earth - SOHO.

Pearson correlation coefficient is also calculated to reveal a relation between a characteristic of SEP-related event (CME or flare) and peak intensity of SEP event, detected on 20 MeV by SOHO/ERNE. Results are listed in Table 2.

The highest correlation again is with 2D LASCO speeds, although STEREO A combinations with C3 and STEREO B also give close value.

Table 2. Pearson product-moment correlation coefficients r and coefficients of determination for relations of different properties (2D and 3D CME speeds, and flare class) with peak intensity of the associated proton event on 20MeV.

	Properties	No. of events	r	$r^2 \times 100$ [%]
20 MeV protons SOHO/ERNE peak intensity vs.	Flare class	112	0.42 ± 0.07	18
	2D LASCO CME speed	156	0.55 ± 0.05	30
	ST A+C3 CME speed	64	0.47 ± 0.09	22
	ST A+ST B CME speed	56	0.47 ± 0.11	22
	C3+ST B CME speed	54	0.42 ± 0.11	18

Conclusions

We present a study of “true” 3D velocities of CMEs related with the SEP events from solar cycle 24.

Our results show that 3D speeds are in general larger than the SOHO/LASCO projected speeds. Correlation coefficients while using the 3D speed are smaller than those when using 2D speeds, although the differences are within the statistical uncertainty. Thus, LASCO CME speeds tend to overestimate the relevance of CMEs as the origin of SEP events, at least in a statistical sense.

Acknowledgment

This study is supported by the National Science Fund of Bulgaria with contracts No.: DNST/Russia 01/6 (23-Jun-2017), KP-06-H28/4, NTS/AUSTRIA 01/23 (28.02.17) and Austria OeAD Project No. BG 11/2017.

References

- Chen, P. F. (2011). Living Rev. in Solar Physics, 8, 1.
- Park, J., Moon, Y.-J., Lee, H. (2017). Dependence of the peak fluxes of solar energetic particles on CME 3D parameters from STEREO and SOHO, *ApJ*, Vol. 844: 17 (6pp.).
- Pulkkinen, T. (2007). Space Weather: Terrestrial perspective, *Living Reviews in Solar Physics*, Vol. 4: 1, article id. 1, 60 pp.
- Semkova, J., Koleva, R., Benghin, V., Dachev, Ts., Matviichuk, Y., Tomov, B., Krastev, K., Maltchev, S., Dimitrov, P., Mitrofanov, I., Malahov, A., Golovin, D., Mokrousov, M., Sanin, A., Litvak, M., Kozyrev, A., Tretyakov, V., Nikiforov, S., Vostrukhin, A., Fedosov, F., Grebennikova, N., Zelenyi, L., Shurshakov, V., Drobishev, S. (2018). Charged particles radiation measurements with Liulin-MO dosimeter of FRENDO instrument aboard ExoMars Trace Gas Orbiter during the transit and in high elliptic Mars orbit, *Icarus*, Vol. 303, pp. 53–66.
- Yashiro, S., Gopalswamy, N., Michalek, G., St Cyr, O.C., Plunkett, S.P., Rich, N.B. and Howard, R.A. (2004). *J. Geophys. Res.*, 109, 7105.

About Productivity of the Solar Energetic Particle Events

Zhdanov D.A.¹, Kashapova L.K.¹, Myshyakov I.I.¹, Miteva R.²

¹ The Institute of Solar-Terrestrial Physics, SB RAS, Irkutsk, Russia

² Space Research and Technology Institute – Bulgarian Academy of Sciences, Sofia, Bulgaria
E-mail: zhdanov@iszf.irk.ru

Abstract.

We present an analysis of 22 SEPs events related to flares that demonstrate significant microwave emission. We analyzed the microwave burst parameters characterizing acceleration processes for each event. In some events, despite the significant microwave signatures, powerful SEPs were not produced.

The current study aimed to check the correlation of the SEP event productivity of active regions based on features of their magnetic field topology and the presence of type III radio bursts as an additional indicator of open magnetic field lines. The magnetic field during the pre-flare stage was extrapolated by a potential approximation. The obtained results are discussed.

Introduction

Solar energetic particles (SEPs) relate with one of the most important aspects of space weather. The electrons, protons and ions observed in situ on the terrestrial orbit present a real hazard to humans and technological devices. The problem of physical understanding of the processes of acceleration, escape and transport from the solar source to the particle detector has been still actual nowadays (see, for example, *Klein and Dalla, 2017*). There are no doubts that the solar origins of SEP events relate to solar flares and coronal mass ejections (CMEs), but the role distribution between these phenomena is unclear. One of the studied problems is on the indicators of acceleration processes. Emission generated by electrons could be directly observed both in X-rays and microwaves. However, the emission generated by protons is observed very rarely because of the low flux level of emission and the insufficient threshold of the current instruments. There are several approaches based on observational and theoretical studies. For example, *Chertok et al. [2009]* demonstrated the close relation of the SEP proton fluxes and properties of microwave non-thermal gyrosynchrotron emission. Also, it is not clear what the importance of particle acceleration is over their escape to interplanetary (IP) space.

The SEP events may not be related to powerful soft X-ray solar flares. But on the other hand, weak flares may be associated with prominent SEP events. In the work by *Bogomolov et al. [2018]* a comparison between the characteristics of two flares was carried out. These flares show very close characteristics of the acceleration processes. It is turned out that the flare related to the proton-rich SEP event took place in the active region where 3D reconstruction of magnetic field lines demonstrated the presence of a fan of high loops associated with open magnetic field lines. Moreover, the flare was associated with the type III radio burst that is also evidence of the presence of open magnetic field lines during the solar flare and nearby the flare location.

Based on these results we could make the assumption and show that one of the indicators of the existence of advanced possibilities for proton escaping could be the domination of open magnetic field lines in the active region producing the event. This hypothesis should be checked on a more statistically representative set of data. Microwave emission properties could be an indicator of the presence of acceleration process.

And the type III radio bursts will be an additional indicator of existing of open magnetic field lines nearby the flare location.

Data and analysis

We used the catalog of the SEP events detected by the Wind/EPACT instrument over the period 1996–2016 [Miteva *et al.* 2018]. Microwave data was obtained by the Badary Broadband Microwave Spectropolarimeter (BBMS) located in Radio Astrophysical Observatory of the Institute of Solar-Terrestrial Physics, Russia [Zhdanov *et al.* 2011].

We considered two groups of SEP events. The first group consisted of solar flares associated with proton events, the second group consisted of solar events without protons. Table 1 shows a list of 18 proton-rich events and 3 non-proton-rich events. We had described the microwave properties of the first group (№1-18) in Zhdanov *et al.* [2018].

The second group contains solar flares which had a radio flux higher than 500 sfu at two or more frequencies simultaneously in the range from 3.7 to 17 GHz, but were not followed by significantly enhancement in the proton flux. We used the Nobeyama radio polarimeter catalog of radio fields to find such events in the period 2010–2017. We chose only the events that were simultaneously observed by the BBMS also. Thus, we could found only 3 events (№19-21).

Table 1 List of SEP events with properties of the associated phenomena.

№	Date (yyyy-mm-dd)	Start time (UT)	GOES class	Radio Flux _{max} at F _{max}	Radio F _{max}	Proton flux 28-72 MeV	Flare Position	CME Speed km/s	Magnetic configuration	type III radio bursts	
				(sfu)	(GHz)					Learmonth catalogue	Wind/WAVES
5	2012-03-07	01:05	X1.3	7000	9.4	9.591/106851	N22E12	1825	closed	No	Yes
4	2012-01-23	03:38	M8.7	8000	4.0	9.455/196610	N28W21	2175	closed	No	Yes
6	2012-05-17	01:25	M5.1	600	5.0	1.357/1296	N11W76	1582	-	No	Yes
2	2011-06-07	06:16	M2.5	800	6.5	0.3390/7315	S21W54	1255	open-closed	No	Yes
3	2011-08-09	07:48	X6.9	2000	10.0	0.1270/284	N17W69	1610	open-closed	No	Yes
8	2013-05-15	01:25	X1.2	1600	7.0	0.0352/484	N12E64	1366	closed	No	Yes
11	2014-02-20	07:26	M3.0	500	6.0	0.0309/272	S15W73	948	open-closed	Yes	Yes
13	2015-06-18	00:33	M1.2	60	2.0	0.0252/296	S16W81	1714	-	No	Yes
14	2015-06-21	02:06	M2.6	1100	7.5	0.0203/266	N13E10	1366	closed	No	Yes
10	2013-11-02	04:40	C8.2	80	4.0	0.0142/326	S23W04	828	closed	No	Yes
15	2015-06-25	08:02	M7.9	4500	9.0	0.0142/1093	N09W42	1627	closed	No	Yes
9	2013-06-21	02:30	M2.9	110	4.7	0.0073/153	S16E73	1900	-	No	Yes
1	2011-02-15	01:44	X2.2	1000	8.0	0.0037/84	S20W10	669	closed	No	Yes
16	2016-03-16	06:34	C2.2	12	7.0	0.0024/14	N12W88	592	-	No	Yes
12	2014-12-17	04:25	M8.7	800	7.0	0.0016/107	S20E09	587	closed	Yes	Yes
17	2016-04-18	00:14	M6.7	350	6.0	0.0007/u	N12W62	1084	closed	No	Yes
7	2013-03-15	05:46	M1.1	120	1.5	0.0004/u	N11E12	1063	open-closed	No	Yes
18	2016-07-23	05:00	M7.6	700	7.0	0.0004/u	N05W73	835	-	No	Yes
19	2013-11-10	05:12	X1.0	550	8	-	S13W14	682 no cme	closed	No	Weak
20	2014-10-22	01:39	M8.7	1000	9.4	-	S12E21		closed	No	No
21	2015-03-10	03:21	M5.1	1100	17	-	S16E34	1040	open	No (V type)	Weak

The magnetic field was reconstructed using data, provided by Heliospheric and Magnetic Imager (HMI) [Schou *et al.* 2012] instrument onboard Solar Dynamics Observatory (SDO) spacecraft [Pesnell *et al.* 2012]. We reconstructed a coronal magnetic field in a potential approximation for the all events from two groups. The coronal magnetic field was calculated in a potential approximation using a method, based on Green's function approach.

The applied method works in a spherical geometry. Distribution of the radial magnetic component over the photosphere level, calculated from SDO/HMI vector magnetograms with resolved pi-ambiguity, is used as input boundary conditions. The height of the computational domain is 150 Mm that defines the maximum height of the reconstructed loops up to 0.2 solar radii. We considered force lines to have either a closed configuration or an open configuration. Table 1 shows the result of determining the magnetic field configuration for all events. The presence of the type III radio bursts we checked by two ways. We used the information from Learmonth radio spectrograph (25–180 MHz) catalogue of radio bursts (http://www.sws.bom.gov.au/World_Data_Centre/) by Automated Radio Burst Identification System (ARBIS 2) based on the algorithm by Lobzin *et al.* [2009]. Information about the presence of the burst at lower frequencies we obtained from the Wind/WAVES data.

Discussion and conclusion

Initially, we checked the presence of open magnetic field line configuration in active regions as factor that leads to more proton-rich event. However, we found the closed configuration of the magnetic field in most of the active regions associated with the solar origins of proton-rich SEP events. Figure 1 shows the open-closed magnetic field configuration in event SOL2012-01-23.

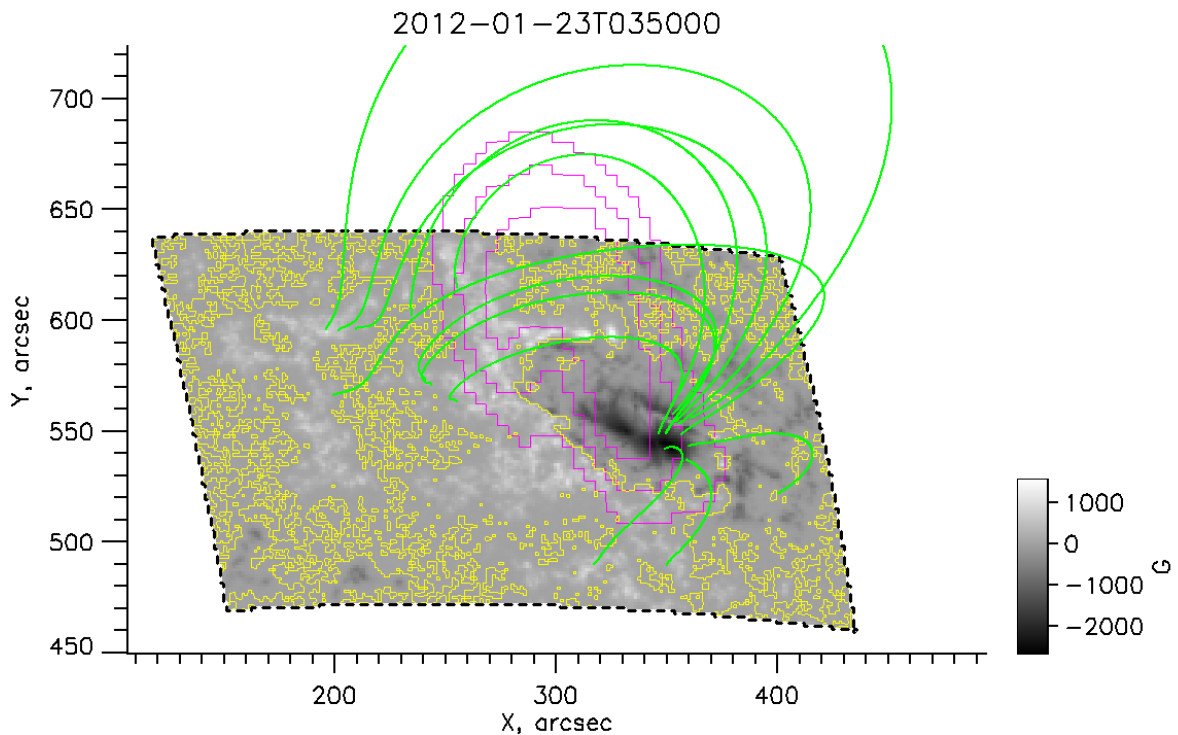


Fig. 1 Example of closed magnetic field configuration in the event SOL2012-01-23, green lines – force lines, purple contour – the 17 GHz radio source by Nobeyama Radioheliograph (NoRH). Contour levels – 0.7, 0.8, 0.9 from of the maximum.

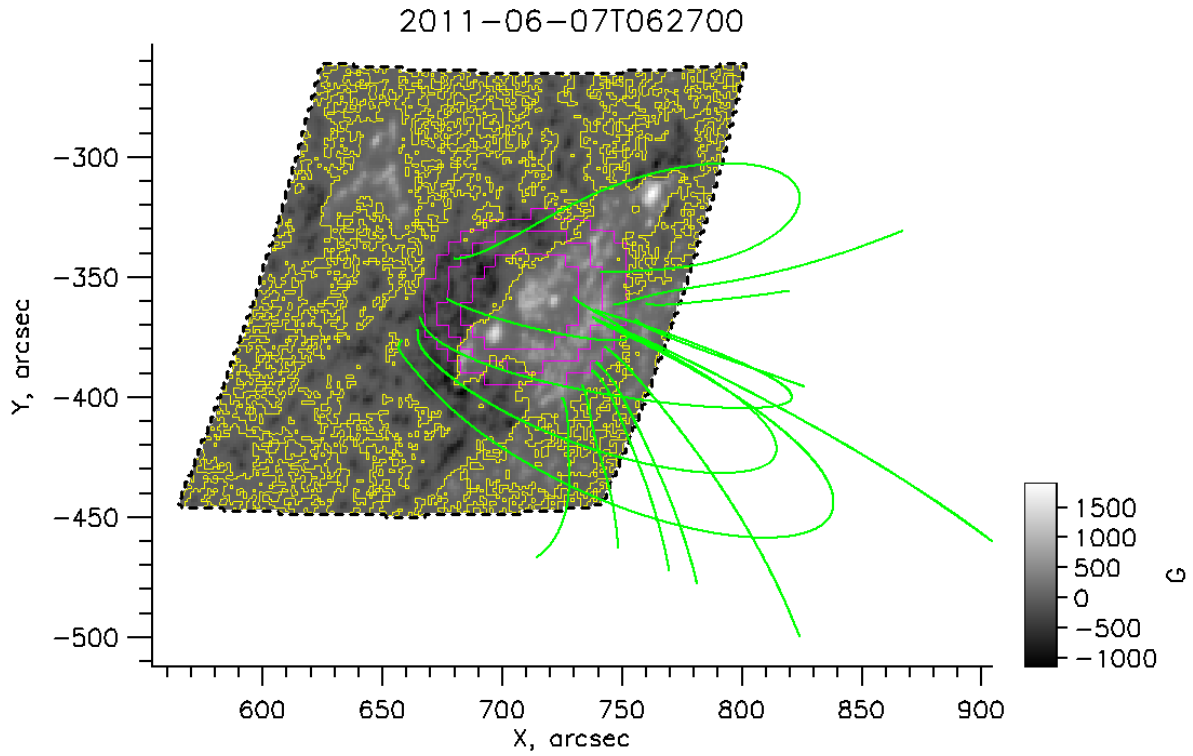


Fig. 2 Example of open-closed magnetic field configuration in the event SOL2011-06-07, green lines – force lines, purple contour – the 17 GHz radio source (NoRH). Contour levels – 0.7, 0.8, 0.9 from of the maximum.

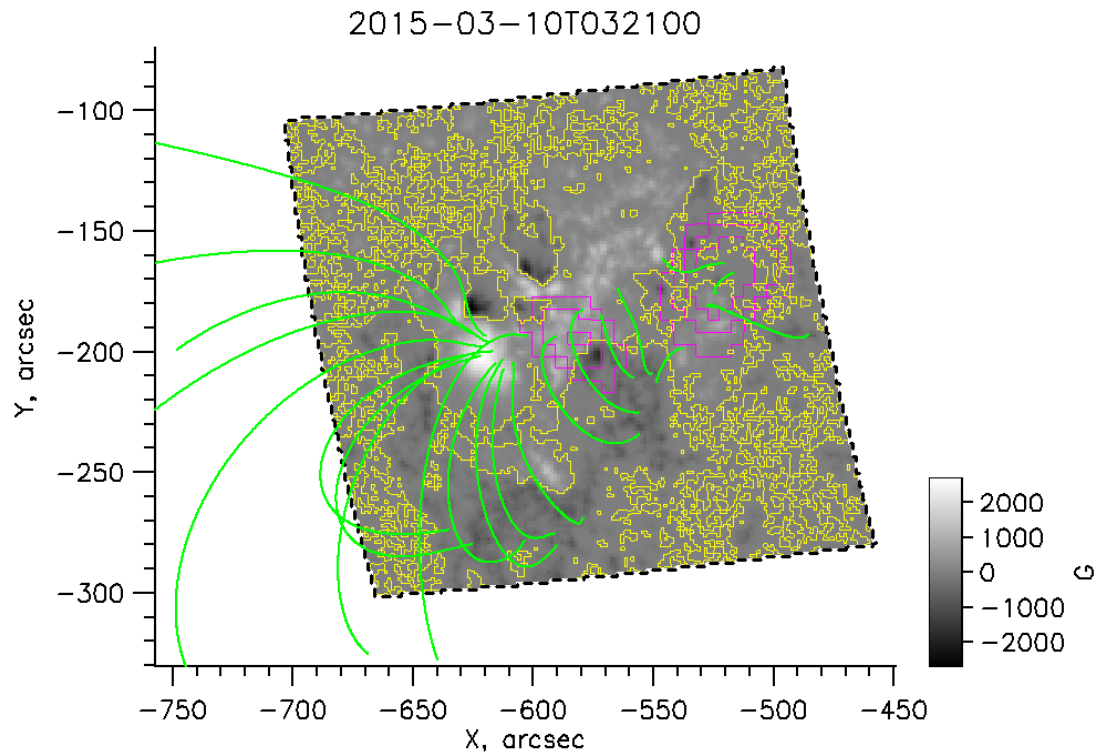


Fig. 3. Example of open magnetic field configuration in the event SOL2015-03-10, green lines – force lines, purple contour – the 17 GHz radio source (NoRH). Contour levels – 0.85, 0.9, 0.95 from of the maximum.

We did not find clear evidence of open magnetic configurations in the active regions related to the studied proton events. Conversely, some configurations look like an open-closed configuration. Figure 2 shows the open-closed magnetic field configuration in the active region where the event SOL2011-06-07 occurred. We found the open-closed configuration of the magnetic field in active regions associated with 4 proton events out of 17 only.

Only one flare was in active region where the magnetic field configuration was clearly open. But this flare is associated with unproductive proton events. Figure 3 shows the open magnetic field configuration in event SOL2015-03-10. But the catalogue of Learmonth spectrograph showed presence the type V during the corresponding flare. If the burst identification is correct, it means that accelerated electrons escaping from the solar atmosphere were captured by high closed magnetic field lines. The presence of the low-frequency type III bursts indicates open magnetic field lines extend from 0.5 solar radii into IP space [Cane *et al.* 2002]. Our method allowed reconstructing the magnetic field lines up to 0.2 solar radii. The presence of type V instead the type III could mean that the used approach for estimation is not working properly.

Moreover, we were faced with uncertainties with the detection of type III radio bursts. For most of the events where the Learmonth catalogue did not reveal the type III presence, the WIND/Waves observations showed the presence of type III at lower frequencies. The visual inspection of the Learmonth dynamic spectra also reveal type III-like activity at the time of interest. The events without proton fluxes demonstrated weak evidence or absence of type III.

Thus, the approach taking into account the configuration of magnetic field lines in the active regions associated with the SEP event should be improved based on the results obtained in the current study.

Acknowledgement

This study is supported by the project 'The origin on solar energetic particles: Solar flares vs. coronal mass ejections', co-funded by the Russian Foundation for Basic Research with project No. 17-52-18050 and the National Science Fund of Bulgaria under contract No. DNTS/Russia 01/6 (23-Jun-2017). The results were obtained using the equipment of Center for Common Use «Angara» <http://ckp-rf.ru/ckp/3056/>. DZ and LK thank the budgetary funding of Basic Research program II.16 for partial support.

References

- Bogomolov, A.V., Myagkova, I.N., Myshyakov, I., et al. (2018). Comparative analysis of the proton generation efficiency during 17 March 2003 and 11 April 2004 solar flares. *J Atmospheric and Solar-Terrestrial Physics*, 179, 517-526.
- Cane, H.V., Erickson, W.C., Prestage, N.P., (2002). Solar flares, type III radio bursts, coronal mass ejections, and energetic particles. *Journal of Geophysical Research (Space Physics)* 107, 1315.
- Chertok I.M., Grechnev V.V., Meshalkina N.S. (2009) On the Correlation between Spectra of Solar Microwave Bursts and Proton Fluxes near the Earth *Astronomy Reports*, 2009, Vol. 53, No. 11, 1059–1069.
- Klein, K.-L., Dalla S. (2017). Acceleration and Propagation of Solar Energetic Particles. *Space Science Reviews*, Volume 212, Issue 3-4, 1107-1136
- Lobzin, V. V., I. H. Cairns, P. A. Robinson, G. Steward, and G. Patterson (2009), Automatic Recognition of Type III Solar Radio Bursts: Automated Radio Burst Identification System Method and First Observations, *Space Weather*, 7, S04002, doi: 10.1029/2008SW000425.
- Miteva R., Samwel S. W., Costa-Duarte M. V. (2018), The Wind/EPACT Proton Event Catalog (1996 - 2016), *Solar Physics*, 293, no. 2, article id. 27, 44 pp.
- Pesnell, W. D., Thompson, B. J., Chamberlin, P. C. (2012). The Solar Dynamics Observatory (SDO). *Solar Physics*, 275, no. 1-2, 3-15.
- Reames D. V. (2015), What Are the Sources of Solar Energetic Particles? Element Abundances and Source Plasma Temperatures, *Space Science Reviews*, 194, no. 1-4, 303-327
- Schou, J., Scherrer, P. H., Bush, R. I., et al. (2012). Design and Ground Calibration of the Helioseismic and Magnetic Imager (HMI) Instrument on the Solar Dynamics Observatory. *Solar Physics*, 275, no. 1-2, 229–259.
- Zhdanov D.A., Zandanov V.G. (2011), Broadband microwave spectropolarimeters, *Central European Astrophysical Bulletin*, 35, 223-227.
- Zhdanov, D., Kashapova, L.K., Miteva, R. (2018). Results of comparative analysis of the SEP events and the microwave bursts observed by 2-24 GHz and 4-8 GHz spectropolarimeters in 2010-2016. Tenth Workshop Solar Influences on the Magnetosphere, Ionosphere and Atmosphere», proceedings of the conference held 4-8 June, 2018 in Primorsko, 105-108.

Author's index

A - C

Atanassov A. 147;
Bankov N. 31; 77;
Bazilevskaya G.A. 01;
Benghin V. 31; 77;
Bershadskaia I.N. 101;
Bogomolov A.V. 179; 201;
Bojilova R. 71;
Brazhenko A. 40;
Burnecki K. 44;
Chapanov Ya. 152; 158;
Chernouss S.A. 123;

D

Dachev T. 77; 171;
Daibog E.I. 01; 07;
Danov D. 179; 201;
Dashkevich Zh.V. 129; 134;
Dechev M. 13; 196;
Derevyagin V.G. 84;
Despirak I.V. 89; 123;
Dimitrov P. 77; 171;
Dissauer K. 196;
Dodin A.V. 139;
Dorovskyy V. 40;
Drobishev S. 31;
Duchlev P. 13;

E - G

Efishov I.I. 123;
Fainshtein V.G. 65;
Fajardo L. 171;
Fedorenko Yu.V. 119;
Filatov M.V. 123;
Frantsuzenko A. 40;
Ginzburg E.A. 01;
Gromov S.V. 95; 107;
Gromova L.I. 95; 107; 113; 119;
Guineva V. 147;

H - J

Holland D. 171;
Ishkov V.N. 01; 17;
Ishkova L.M. 101;
Ivanov E. 56;
Ivanov V.E. 129; 134;
Janczura J. 44;
Jordanova M. 77;

K - M

Kashapova L.K. 139; 179; 185; 201; 211;
Kecskemety K. 07;
Kilcik A. 23; 28; 35; 143;
Kirillov A. 147;
Kleimenova N.G. 89; 95; 107; 113; 119;
Koleva K. 13; 196;
Koleva R. 31; 77;
Konovalenko A. 40;
Kozarev K. 196;
Krastev K. 31;
Kravetz R.O. 84;
Kupryakov Yu.A. 139;
Lazutina L.L. 01;
Lebed O.M. 119;
Logachev Yu.I. 01; 07;
Lubchich A.A. 89;
Lytvynenko O.A. 84;
Magdalenic J. 40;
Malysheva L.M. 95; 107;
Manninen J. 113; 119;